3-D STRUCTURE IN SOUTHERN ONTARIO VIA RECEIVER FUNCTION IMAGING

BY

JINLING ZHANG

张金玲

A thesis
Submitted to the Faculty of Graduate Studies
in Partial Fulfillment of the Requirements
for the Degree of

MASTER OF SCIENCE

Department of Geological Sciences
University of Manitoba
Winnipeg, Manitoba

THE UNIVERSITY OF MANITOBA

FACULTY OF GRADUATE STUDIES

*****

COPYRIGHT PERMISSION

3-D STRUCTURE IN SOUTHERN ONTARIO VIA RECEIVER FUNCTION IMAGING

BY

JINLING ZHANG

A Thesis/Practicum submitted to the Faculty of Graduate Studies of The University of Manitoba in partial fulfillment of the requirement of the degree

Of

MASTER OF SCIENCE

Abstract

A detailed image of the 3-D crustal and upper mantle architecture of the Grenville province in southern Ontario (a complex orogenic belt of circa 1.1 billion years in age) was achieved in this study by applying common-conversion-point (CCP) stacking and scattering tomography techniques to a set of teleseismic receiver functions recorded by 29 three-component broadband stations deployed by the POLARIS (Portable Observatories for Lithospheric Analysis and Research Investigating Seismicity) array and CNSN (Canadian National Seismograph Network).

Results from CCP stacking clearly delineate the crust-mantle boundary, the Moho, at a depth of ~ 41-52 km. A sub-crustal negative-polarity arrival at ~ 60-100 km, as well as a sub-OBG negative polarity arrival immediately beneath the positive Moho arrival near or beneath the OBG are also visible in CCP images. The former feature might be correlated with remnants of subduction occurring during orogeny, while the latter might be correlated with the formation of the graben.

Higher resolution images of crustal structure were obtained using scattering tomography. Besides the Moho discontinuity, two other crustal discontinuities, the upper crust to mid-crust discontinuity (UMD) at a depth of ~10-15 km, and the middle to lower crustal discontinuity (MLD) at a depth of ~20-30 km, are clearly shown by positive S-wave velocity perturbations. These two velocity anomalies appears to be weaker and less continuous within the Central Metasedimentary Belt (CMB) than the anomalies within the adjacent Central Gneiss Belt (CGB). Within the crust, a southeast-dipping feature (25^{o}-30^{o}) is found beneath the Grenville Front Tectonic Zone (GFTZ) and northwest of

the nearby Britt domain. A weaker SE-dipping feature observed beneath the CMB and CMBbz might be attributed to tectonically imbricated rock units. The cross-section images both in CCP and in scattering show that the crust beneath the Ottawa-Bonnechere Graben has been thinned as much as 11 km relative to its neighboring blocks by normal faulting. A linear, cohesive, NW-striking low-velocity S-wave anomaly, which is oriented parallel to the OBG along its SW edge, is clearly shown in a depth slice (at 20 km) in the scattering image. A similar feature is visible in the travel-time model of Aktas and Eaton (2005) at much greater depth, suggesting that the graben is associated with a mantle structure possibly attributed to the Great Meteor hotspot track (Rondenay 2000).

Two lines across the Mississauga domain (MD), southwest of tectonic boundary-Central Metasedimentary Belt Boundary thrust zone (CMBbz) were examined in detail. Along Line-7 (oriented NW-SE), the MLD is disrupted twice beneath the MD, however a similar feature has not found along Line-2 (oriented SW-NE), indicating that a mixed reverse-slip and strike-slip sense of displacement occurred in the MD. The CMBtz might be split into two branches beneath this domain. This finding is consistent with a ENE oblique geometry of internal magnetic anomaly fabrics extended in this domain as well as high frequency of seismicity in this domain, suggesting that the Mississauga domain is a tectonic active area, which strongly support that the buried trace of CMBbz is located parallel to, and west of Lake Ontario as described by O'Dowd et al. (2004), rather than across western Lake in NNE direction as interpreted by other authors.

Acknowledgments

I would like to thank my advisor, Dr. Andrew Frederiksen, for his guidance, generous support during my thesis research, and for providing, and assisting with, the scattering tomography code as well as patiently correcting my thesis grammar.

I sincerely thank Dr. Ian Ferguson for kindly and patiently reviewing my thesis, and providing constructive comments and advice. I also thank Professor John Page for serving on my committee.

Thanks to Dr. Bill Brisbin and all the faculty from the Department of Geological Sciences, who were always willing to offer advice and helpful suggestions.

I thank POLARIS and CNSN for the teleseismic data used in the thesis study.

Table of Contents

List of Figures

List of Tables

List of Abbreviations

1-D	one Dimension
3-D	three Dimensions
2-D	two Dimensions
CCP	Common Conversion Point
CCPscat	Common Conversion Point (Scattering) software package
CGB	Central Gneiss Belt
CMB	Central Metasedimentary Belt or Core-Mantle Boundary
CMBbz	Central Metasedimentary Belt Boundary zone
CMP	Common Middle Point
CNSN	Canadian National Seismography Network
COCORP	Consortium for Continental Reflection Profiling
EM	ElectroMagnetic
GF	Grenville Front
GFBF	Grenville Front Boundary Fault
GFTZ	Grenville Front Tectonic Zone
GLIMPCE	Great Lakes International Multidisciplinary Program on Crustal Evolution
GSC	Geological Survey of Canada
IASP91	standard 1-D Earth model (Kennett 1991)
LSQR	Least-Squares solution
MD	Mississauge domain

MLD	Middle to Lower crustal Discontinuity
Moho	crust-mantle boundary
NE	Northeast
NW	Northwest
OBG	Ottawa-Bonnechere Graben
PACES	Pan American Center for Earth and Environmental Studies
PKS	P wave bottoming in the core and converting to S at the CMB
POLARIS	Portable Observatories for Lithospheric Analysis and Research Investigating Seismicity
Pp*p	incident teleseismic P wave which converts to downgoing P wave at the free surface, encounters a scatterer, and is back scattered to the receiver as a P wave
PpPs	generated from incoming P converted as P at a discontinuity, reflected downward as P at the earth's free surface
PR	Pattern Recognition approach
Ps	P-to-S converted phase
Ps*p	incident teleseismic P wave which converts to downgoing S wave at the free surface, encounters a scatterer, and is back scattered to the receiver as a P wave
Ps*s	incident teleseismic P wave which converts to downgoing S wave at the free surface, encounters a scatterer, and is back scattered to the receiver as a S wave

PsSs+PsPs	resulted from incoming P-wave, converted as P or S at a discontinuity, reflected downward as P or S at the earth's free surface, and then reflected upwards at S at disconituities
RF	Receiver Function
R-T-Z	Radial-Transverse-Vertical
SE	Southeast
SKKS	S wave reflected once from inner side of the CMB
SKS	S wave traversing the core as acoustic wave
SNR	Signal to Noise Ratio
SOSS	South Ontario Seismic Survey
SV-RF	Vertical Shear wave-Receiver Function
SW	Southwest
T-to-D	Time-to-Depth
TWT	Two Way Time
UMD	Upper to Middle crustal Discontinuity

List of Symbols

Vp or α	P velocity
Vs or β	S velocity
ρ	density
u	displacement
U_R, U_T & U_z	ground displacement vector in R-T-Z components
w	wave field
F^1	inverse Fourier transformation
f	frequency
ω	angular frequency ($2 \times \pi \times f$)
$S_n(\omega)$, $P_n(\omega)$	S wave component (either SV or SH) and P wave component of motion from the nth seismogram
$P_n^*(\omega)$	complex conjugate of $P_n(\omega)$
δ	a regularization parameter which adjusts the trade-off between model variation and data misfit.
Z	depth of the discontinuity
T_s & T_p	S- and P-wave travel times along the discontinuity
$\delta t_p, \delta t_s$	P and S travel times to account for their different pierce points at the interface, using the point immediately below the station as a reference.
Δt	travel-time between P and P-to-S converted phase
r_S	horizontal distance between P and P-to-S converted phase

θ	incident angle or back azimuth
x_0, y_0, z_0	offset of receiver in X, Y, and Z directions
λ & μ	Lame parameters.
∂	partial derivative operator
∇	gradient operator
∇^2	second gradient operator
Q	body force
k	wave number
a	length of heterogeneity
$\hat{\mathrm{N}}, \hat{\Gamma}$ & $\hat{\mathrm{P}}$,	unit vectors in the incidence, departure and incident polarization directions
V	volume of the inhomogeneity
$\lambda = 2\pi / k$	wavelength
t_{S-R}	total travel time from source to receiver
t_{S-D}	travel time from a plane wave (P or S wave) to a diffractor or scatterer
t_{D-R}	travel time from the diffractor to the receiver.
c	P or S wave velocity
X, Z	horizontal and vertical distance
d^i_α, d^i_β & d^i_ρ	scattered trace generated by perturbing the α, β and ρ properties of the i^{th} scatter
A	partial derivative matrix
$\tilde{d}_i$	scattered data set

I	identity matrix
λ	weighting factor
S	a Gaussian smoother
$\sum$	summation operator
p	ray parameter
a_A^S	Amplitude of P wave converted, at point 'A' of the free-surface
a_A^P	Amplitude of the converted phase, P-to-S, at point 'A' of the free-surface
${}^{S}{}_{u}{}^{P}$	displacement from an incident S wave scattered as an P wave
${}^{P}{}_{u}{}^{P}$	displacement from an incident P wave scattered as an P wave
${}^{S}{}_{u}{}^{S}$	displacement from an incident S wave scattered as an S wave
$1/r$	geometry spreading factor

Chapter 1

Introduction

1.1 Study Area

The study area of this thesis is southern Ontario which geographically covers the area from Ottawa to London and from Niagara to Georgian Bay, i.e., from (42.5°N, 82°W) to (46.803°N, 74.21°W), roughly 600 by 500 km (see Figure 1.1).

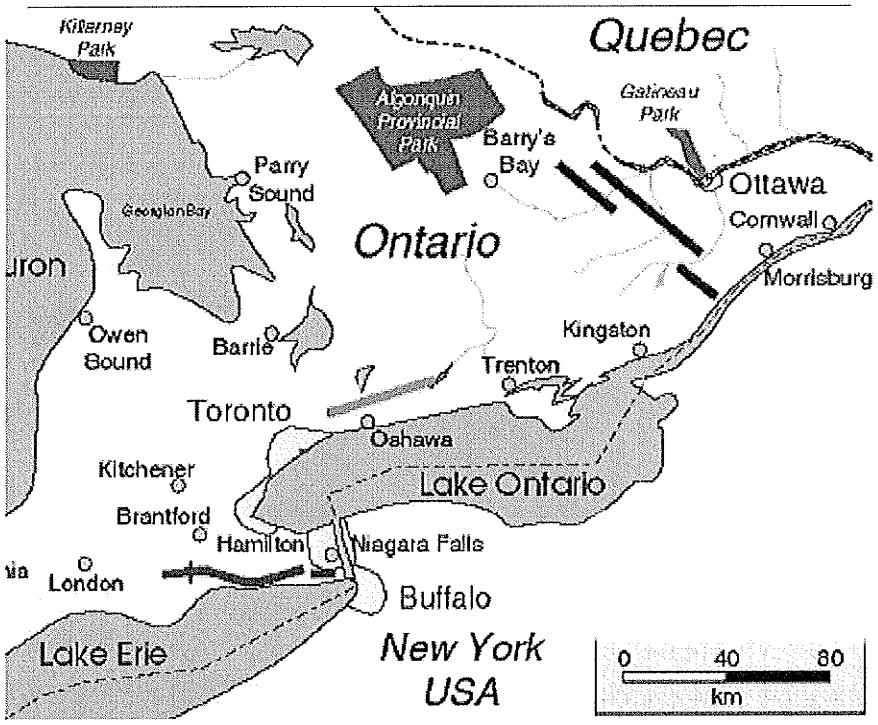

Figure 1.1. Location of study area: southern Ontario covering from (42.5°N, 82° W) to (46.803° N, 74.21°W), roughly around 600 by 500 km. (Modified from http://www.lithoprobe.ca/transe_cts/soss/) [accessed on Sep. 27, 2005].

The Precambrian bedrock in southern Ontario forms the southwest part of the Grenville Province. The Grenville Province is a complex orogenic belt, ~ 1.1 billion years old, which truncates several older geological provinces. Recorded within the Grenville Province is the tectonic evolution of the southeast margin of Laurentia during the Mesoproterozoic, and this orogen has overprinted the structural trends and metamorphic effects of the Archean and Paleoproterozoic geologic provinces of Laurentia (Easton, 1992).

The Grenville in this region is composed of two major divisions: the Central Gneiss Belt and Central Metasedimentary Belt, separated by the Central Metasedimentary Belt Boundary Zone. The Grenville is bounded at northwest by the Grenville Front Tectonic Zone, which includes deformed and metamorphosed rocks derived from the Archean Superior and Paleoproterozoic Southern provinces, and the Killarney Magmatic Belt (see Figure 2.2, Easton, 1992).

The Central Gneiss Belt consists mainly of Archean crust with 1740 and 1450 Ma plutons and 1800-1680 Ma supracrustal rocks with ca. 1450 Ma continental arc granitoid rocks. The tectonic history includes ca. 1700 Ma and 1450 Ma episodes of deformation, metamorphism, and magmatism (Carr et al., 2000).

The Central Metasedimentry Belt Boundary Zone, subparallel with the Grenville Front Tectonic Zone, marks the boundary between the Central Gneiss Belt and the allochthonous terranes of the Central Metasedimentary Belt, it is several kilometers wide, which is characterized by strongly deformed rocks with northeasterly trending, moderately to shallowly southeast-dipping tectonic layers and southeast-plunging mineral lineations. Both zones have pronounced seismic expressions extending to the Moho

(Easton, 1992). The growing evidence shows that the Central Gneiss Belt and the Central Metasedimentary Belt are allochthonous and only became attached to each other during the Grenville Orogeny, but the Central Gneiss Belt may have served as basement to the supracrustal rocks of the Central Metasedimentary Belt (Easton, 1992).

The Central Metasedimentary Belt consists dominantly of <1300 Ma volcanic, plutonic, volcaniclastic, carbonate, and siliciclastic rocks, as well as supracrustal rocks and orthogneiss assemblages, which include 1300-1240 Ma and 1180-1155 Ma calc-alkaline arc rocks, ca. 1130 Ma anorthosite and associated mangerite-charnockite-granite suite granitoid rocks (Carr et al., 2000).

Most structural and metamorphic features within the Grenville Province were previously thought to result from the ca. 1.0 billion-year-old Grenville Orogeny. Subsequent Rb-Sr and U-Pb geochronologic studies showed that two orogenies are present within the Central Metasedimentary Belt, an older (ca. 1230 to 1180 Ma) "Elzevirian Orogeny" and a younger (ca. 1120 to 1050 Ma) "Ottawan Orogeny" or "Grenville Orogeny". A variety of events affected the Grenville Province subsequent to the Ottawan Orogeny and prior to deposition of the Paleozoic sedimentary succession, including injection of mafic dikes into the crust between ca 1140 to ca 420 Ma. and alkalic and carbonatitic magmatism at ca 1050 to ca 180 Ma. Many of these dike swarms and alkalic events are related to development of, and latter reactivation along, the Ottawa-Bonnechere graben system (Easton, 1992).

1.2 Objectives of the Research

During the past three decades, a variety of geophysical studies have greatly increased our knowledge of crustal and lithospheric evolution in the Grenville orogen in southern Ontario. Seismic reflection profiles have shed some light on the tectonic evolution of the crust and uppermost mantle (Rondenay 2000), and seismic refraction profiles conducted over the same regions have provided well-constrained velocity models (White et al. 2000). Gravity has contributed to understanding the tectonic interpretation in terms of crustal variation and density distribution (Easton 1992, Rondenay 2000). Results obtained from teleseismic and MT studies have provided an evidence for an anisotropic, laterally heterogeneous lithosphere and provided further constraints on lithospheric evolution in this region (Rondenay 2000).

In comparision with other geophysical methods, earthquake seismology can provide the widest range of information on the deep structures of the upper mantle (Rondenay 2000). Furthermore, due to the lower frequency signal (~1 Hz) from teleseismic earthquakes, it is relatively insensitive to small-scale crustal heterogeneities (Zhu 2000). This may lead to improved Moho images, which are often poorly defined in seismic reflection profiles in the study area possible due to intrusion of upper mantle material into the crust.

As part of the Polaris project, there are 30 three-component broadband seismographs currently operating in the southern Ontario and adjacent regions (see Figure 5.1 for station locations). The available data which was collected from this dense array of recording equipment for many years makes it possible to improve our understanding of lithospheric structures in the upper few hundred km of the Earth in

relation to the tectonic evolution of the Grenville orogen and Paleozoic rifting, as well as assisting in identifying potential zones of crustal weakness (Eaton et al, 2000).

The direct purpose of this research is to use the available data from these stations to characterize crust and upper mantle structure and interpret them in three dimensions. In order to achieve this goal, two complimentary approaches (Common Conversion Point – CCP, stacking and scattering tomography) are applied (Dueker and Sheehan 1997, and Frederiksen and Revenaugh 2004). Higher resolution crustal images can be expected from scattering tomography, and images to greater depth can be achieved by CCP stacking. Based on available receiver function data, computer resources (hardware and programming tools), and codes (Dr. Frederiksen's scattering code), the following six intermediate research objectives were established to meet the project goal:

1. determine 1-D base model (P-wave, S-wave velocities and density, as well as Vp/Vs ratio) using previous geophysical studies, especially models from seismic reflection and refraction profiles as well as standard Earth models (IASP91, Kennett 1991) to compute teleseismic ray geometries and delay-times.
2. develop a CCP stacking software package using Matlab. Use this software to calculate and stack P-to-S converted phases based on teleseismic receiver functions; determine the CCP stacking parameters; visually analyze the stacking fold distribution; and generate any-angle 2-D cross-sections or 3-D images for both CCP stacking results and resultant scattering models (P, S or density);
3. apply scattering tomography to the same receiver function data. Preprocess the data to meet computer memory requirements and determine and test the scattering parameters to get good-quality models.

4. perform a checkerboard resolution test to check the accuracy in recovering models in terms of both the geometry (depth, volume and dip) of discontinuities and the amplitude of associated material property perturbation.
5. integrate and compare these two images (CCP stacking and scattering tomography).
6. interpret images in three dimensions in the light of known geology, gravity, and magnetotelluric studies as well as results from coincident seismic reflection and seismic refraction profiles.

1.3 Outline of this Thesis

In Chapter 1, I have briefly introduced the geology of study area and research objectives.

Chapter 2 discusses the geological background of the Grenville orogen in southern Ontario, including the major subdivisions, and major crustal scale structures. The regional geological setting and the distinctive lithotectonic terranes within each subdivision are also discussed.

Chapter 3 presents a review of previous geophysical studies deployed in or vicinity of the study area, including controlled-source seismic reflection and refraction, teleseismic, deep electromagnetic, gravity, heat flow, seismicity and stress field studies.

Chapter 4 discusses the methodology. Three approaches used for this research, including receiver function methods, CCP stacking methods as well as scattering tomography methods are discussed in detail in terms of their mathematical principles and geometries and data processing.

Chapter 5 introduces the data and analysis, which includes data acquisition, event selection and waveform cross-correlation. Receiver function analysis is also described based on a few examples from single stations.

Chapter 6 presents the results achieved in this study based on ten 2-D cross-sections and 3-D depth slices. A 1-D base model used to calculate travel-time and ray geometries, and the most important stacking or scattering parameters and processes of determining these parameters are also introduced. A resolution test and the limits of resolution for different imaging methods are discussed as well.

Chapter 7 discusses the differences and similarities between the images obtained using CCP stacking and scattering tomography, as well as results achieved using the above two methods in this study and other geophysical studies.

Chapter 8 contains summarized observations and interpretations, and suggestions for future research.

There are three appendices in this thesis. Appendix A lists the earthquakes used and recorded by the POLARIS and CNSN stations used in this study. Appendix B contains instructions for use of the 'CCPscat' software package developed in this study. Appendix C consists of P-velocity perturbation images from scattering tomography.

Chapter 2

Geology of Southern Ontario

2.1 Introduction

The Precambrian bedrock in southern Ontario makes up the southwest part of the Grenville Province. The Grenville Province has been affected by a circa 1230 to 1050 Ma year old orogenic event, the Grenville Orogeny, resulting from the tectonic evolution of the southeast margin of Laurentia during the Mesoproterozoic. This orogen has overprinted the structural trends and metamorphic effects recorded in the Archean and Paleoproterozoic geologic provinces of Lautentia and involved northwest-directed thrusting and imbrication of the entire crust.

The Grenville orogen is separated from older units, including: the Superior and Southern provinces, the Killarney Magmatic Belt, the Eastern Granite-Rhyolite Province and the Midcontinent Rift (Williams et al., 1992), to the North and Northwest by the Grenville Front (GF) (Figure 2.1).

There are two major divisions of the Grenville Province in southern Ontario, the northern part being the Central Gneiss Belt (CGB) and the southern part constituting the Central Metasedimentary Belt (CMB). The part of the CGB within 20 to 30 km of the GF is termed Grenville Front Tectonic Zone (GFTZ), (cf., Wynne-Edwards 1972, Lumbers 1975, 1978, Rivers et al. 1989). It includes the Grenville Front Boundary Fault (GFBF), and consists of deformed and metamorphosed rocks derived from the Southern and Superior provinces. The Central Metasedimentary Belt Boundary Zone (CMBbz), several

kilometers wide and subparallel with GFTZ in Ontario, separates the CGB from the allochthonous terranes of the CMB (Figure 2.2), which have been thrust onto the CGB from the southeast. Within the CGB and CMB, there are similar subparallel zones of intense deformation on a smaller scale associated with boundaries between lithotectonic terranes and domains (Figure 2.2). Mylonites are locally developed. Marble tectonic breccias, containing fragments of metasedimentary, plutonic and amphibolite rock are common within, and adjacent to, the eastern margin of the CMBbz (Easton 1992).

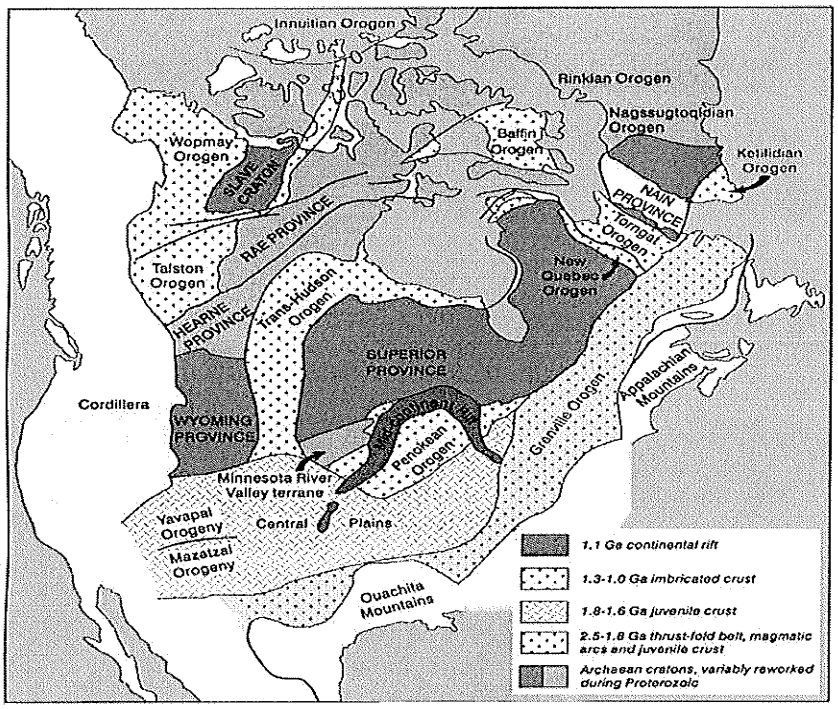

Figure 2.1. Location of the Grenville orogen which was highlighted in yellow color relative to the regional tectonic elements of North America (modified from Hoffman, 1989).

The GFTZ and CMBbz are two major shear zones characterized by strongly deformed rocks with northeasterly trending, slightly to shallowly southeast-dipping tectonic layering and southeast-plunging mineral lineation. Both GFTZ and the CMBbz

have pronounced seismic expressions (Green et al. 1989; White et al. 1991a, 1992; Pratt et al. 1989; Easton 1992) and extend to the Moho.

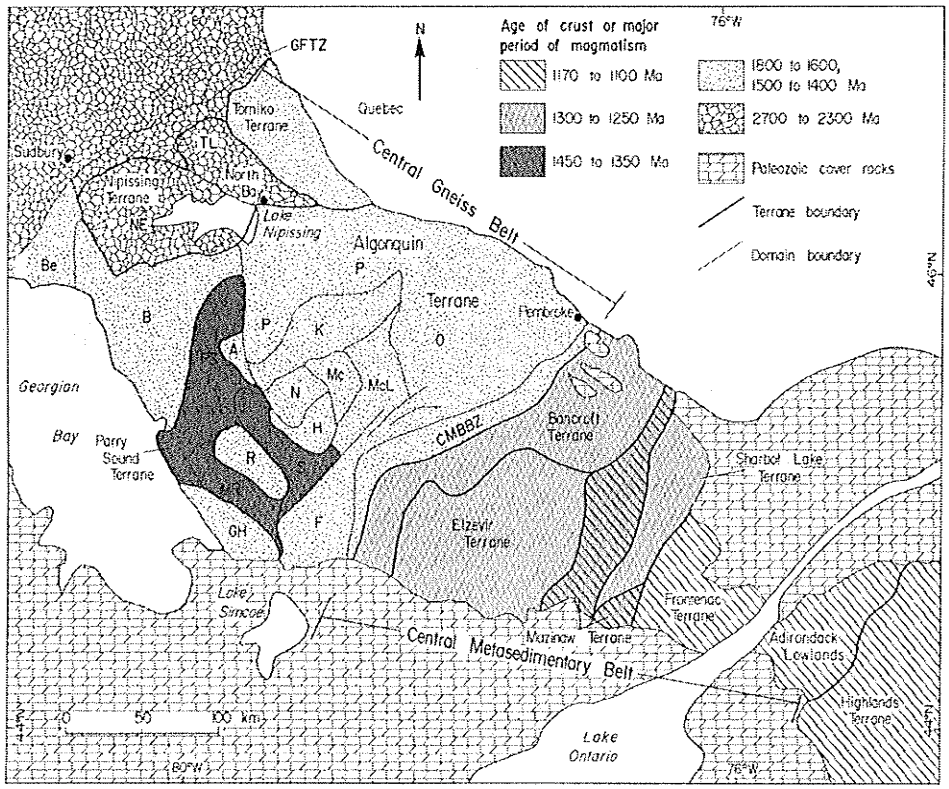

Abbreviations

A	Ahmic Domain	GH	Go Home Domain	NE	Nepewassi Domain
B	Britt Domain	H	Huntsville Domain	O	Opeongo Domain
Be	Beaverstone Domain	K	Kiosk Domain	P	Powassan Domain
CMBBZ	Central Metasedimentary Belt Boundary Zone	Mc	McCraney Domain	PS	Parry Sound Domain
		McL	McClintock Domain	R	Rosseau Domain
F	Fishog Domain	MR	Moon River Domain	S	Seguin Domain
GFTZ	Grenville Front Tectonic Zone	N	Novar Domain	TL	Tilden Lake Domain

Figure 2.2. Lithotectonic terranes, domains and crustal ages within the Central Gneiss Belt and Central Metasedimentary Belt in Ontario. The Alqonquin Terrane consists of the Ahmic, Britt, Fishog, Go Home, Huntsville, Kiosk, McCraney, McClintock, Novar, Opeongo, Powassan and Rosseau domains (modified from Easton 1986a, 1992).

2.2 Central Gneiss Belt

The Central Gnesis Belt consists of a variety of Archean to Mesoproterozoic crustal segments, which are generally flat-lying, amphibolite-granulite-facies, quartzofeld spathic genisses, mainly of igneous origin with subordinate paragneiss, all of which are highly strained throughout, and have been affected by the Grenville orogeny (Easton 1992).

The CGB rocks are bounded to the northwest and southeast by southeast-dipping ductile thrust (or) normal shear zones developed during ca 1120-1040 Ma motion (e.g., Grenville Front Tectonic Zone (GFTZ), CMBbz (Carr et al. 2000, White et al. 2000). The dominant structural trend is northeasterly for CGB rocks in Ontario, but northwesterly trends occur along Georgian Bay. Subordinate domains, and distinctive lithotectonic terranes within the Central Gneiss Belt (see Figure 2.2) are bounded by several kilometer wide deformation zones (Davidson 1984a, Rivers et al. 1989). The lithotectonic terranes are distinguished by differences in rock type, internal structure, metamorphic grade, geologic history and geophysical signature in southern Ontario (Carter and Easton 1990) where they influenced Paleozoic deposition.

Rocks of three main ages are present in the Central Gneiss Belt (see Figure 2.2, Easton 1986a, Dickin et al. 1990). North of the French River, Archean and Paleoproterozoic gneisses of the Nipissing Terrane are intruded by Mesoproterozoic (1700 to 1350 Ma) plutonic rocks, with largely granitic and monzonitic rocks. Most of the Central Gneiss Belt (Algonquin and Tomiko terranes) consists of 1.8 to 1.6 billion-year-old Mesoproterozoic gneisses invaded by 1.5 to 1.4 billion-year-old granitic and monzonitic plutons that may represent an extension of the Eastern Granite-Rhyolite

Province across the Grenville Front. The Tomiko Terrane may consist entirely of Mesoproterozoic rocks allochthonous to the adjacent Nipissing Terrane. The Algonquin Terrane probably represents a section of 1.8 to 1.6 billion-year-old crust extensively intruded by granitic magmas of the Eastern Granite-Rhyolite Province (Easton 1992). Although later imbricate thrusting occured, the Algonquin Terrane is probably parautochthonous (Rivers et al. 1989). The Parry Sound Terrane consists of mafic to intermediate rocks extracted from the mantle at about 1450 to 1350 Ma (Dickin and McNutt 1989a) and in contrast to the adjacent Algonquin Terrane, it consists entirely of juvenile crust.

2.3 Central Metasedimentary Belt

The Central Metasedimentary Belt (also termed as the Compsite Arc Belt) to the southeast is bounded by ductile and brittle-ductile thrust and normal faults, i.e., the Central Metasedimentary Belt Boundary Zone (Carr et al. 2000, White et al. 2000). It is a major Mesoproterozoic accumulation of supracrustal rocks consisting of marble, volcanic rocks and clastic metasedimentary rocks. These rocks have been intruded by compositionally variable plutons of syntectonic, late tectonic and posttectonic age. The entire succession of CMB has been metamorphosed at grades varying from greenschist to granulite facies and it has the most mineral deposits of any region within the Grenville Province of Ontario (Easton 1992). In contrast to the strongly deformed gnesses of the CGB, the rocks of the CMB are dominated by structural polyfolded domains with complex geometry, and are considered to have been at middle to upper crustal levels during the Grenville orogeny (White et al. 2000).

The Central Metasedimentary Belt can be divided into several lithotectonic terranes in terms of differences in rock type, geologic history, structural history, and ages of metamorphism and plutionism (see Figure 2.2). The Bancroft Terrane, metamorphosed at middle to upper amphibolite facies, consists mainly of deformed carbonate metasedimentary rocks with minor volcanic rocks invaded by nepheline syenites and syenites at circa 1270 to 1220 Ma (Miller 1983). The Elzevir Terrane, including the classical Grenville Supergroup, is distinguished by volcanism and sedimentation between 1300 and 1250 Ma, and was subjected to plutonism and metamorphism at 1250 to 1230 Ma and at 1130 to 1070 Ma. In large areas of the south-central and eastern Elzevir Terrane, sedimentary and volcanic textures are locally well-preserved at greenschist facies (Easton 1992).

The Mazinaw Terrane includes the classical Grenville Supergroup overlain by a young (ca. 1155 Ma) metamorphosed and deformed Flinton Group which are believed to be derived partially from weathering of Frontenac Terrane plutonic and metamorphic rocks. The terrane consists of marbles, calc-alkalic metavolcanic rocks and clastic metasedimentary rocks, which were deposited on a basaltic-tonalitic basement. The Mazinaw Terrane has a intense and prolonged structural and metamorphic history which is similar to that present in the Frontenac Terrane (Kinsman and Parrish 1990).

The Sharbot Lake Terrane, located between the Mazinaw and Frontenac terranes, consists of upper greenschist- to lower amphibolite-facies carbonate and mafic metavolcanic rocks. Although geographically separated, it appears to be closely related to Elzevir Terriane in rock type and structural and metamorphic history.

The Frontenac terrane consists of a sequence of marbles, quartzites and quartzofeldspathic gneisses, that were intruded by plutonic rocks and subjected to metamorphism at about 1170 to 1160 Ma. It is distinguished from the above terranes in terms of composition, in that lacks volcanic rocks. The Frontenac Terrane is preserved at granulite facies in contrast to the lower grade Bancroft and Elzevir terranes to the north, and the Adrondack lowlands to the south (Easton 1992).

2.4 Other Tectonic Elements

2.4.1 Grenville Front and Grenville Front Tectonic Zone

The Grenville Front (GF) is the boundary between the Grenville province and older structural provinces to the west and northwest (Wynne-Edwards 1972). It marks the northwest limit of the tectonic reworking of rocks of the older provinces during the Grenville orogeny and has long been recognized as the surface expression of a major crustal discontinuity generally considered to have formed between 1300 and 1000 Ma (see Figure 2.3).

A major fault or mylonite zone marks the Grenville Front, while faults, foliations and lineations are commonly steep and inclined to the southeast (Davidson 1986c). Varying metamorphic grades of the metamorphism of the older orogens to the northwest are in contrast with the uniformly high grade on the Grenville side of the front, suggest that Grenville side of the front has been uplifted with respect to the northwest side. The Grenville province is also characterized by reset potassium argon and argon isotopic systems (Stockwell 1964; Harper 1967; Easton 1986a, York et al. 1991).

The rocks are overprinted by metamorphism that all of the rocks north of the Grenville Front Boundary Fault become increasingly deformed near it and overall reaches lower at the south of the Grenville Front and increases toward to fault (Dressler 1979, Lumbers 1975 and Davidson 1986c). Grenville Front-related metamorphism is also recognized by the association and orientation of minerals expressed as a south-east-dipping, front-parallel foliation and with downdip lineation. (Lumbers 1978, Dressler 1979, Davidson 1986c, Easton 1992).

An earlier stage of ductile deformation occurred prior to brittle deformation in some areas along the Grenville Front (Davidson 1986c). This ductile deformation is not necessarily associated with the Grenville Orogeny. North of the Grenville Front Boundary Fault, rocks are clearly recognizable as being Killarnean, Huronian or Archean when metamorphosed and deformed. In contrast, south of the Grenville Front Boundary Fault, the nature of the protolith is much more difficult to establish, although some distinctive rock units occur south of the boundary fault (e.g., River Valley Anorthosite).

The Grenville Front Tectonic Zone (GFTZ) is a prominent southeast-dipping zone of amphibolite-facies rocks and northeast-trending cataclastic foliation up to 30 km across with transitional boundaries. The zone underwent ductile thrusting at ca. 1000 Ma. It lies mainly south of, but parallels, the Grenville Front Boundary Fault (Easton 1992), and overprints earlier structures of the Grenville, Southern and Superior Provinces (Lumbers 1978). The zone also includes rocks north of the Grenville Front Boundary Fault that underwent Grenville metamorphism and contain a southeast-plunging lineation as part of the Grenville Front Tectonic Zone.

The GFTZ can be divided into three broad lithologic segments corresponding to three segments of the Grenville Front Boundary Fault: the Killarney-Sudbury Segment (including the Beaverstone Domain), the Sudbury-River Valley Segment, and the River Valley-Temagami Segment.

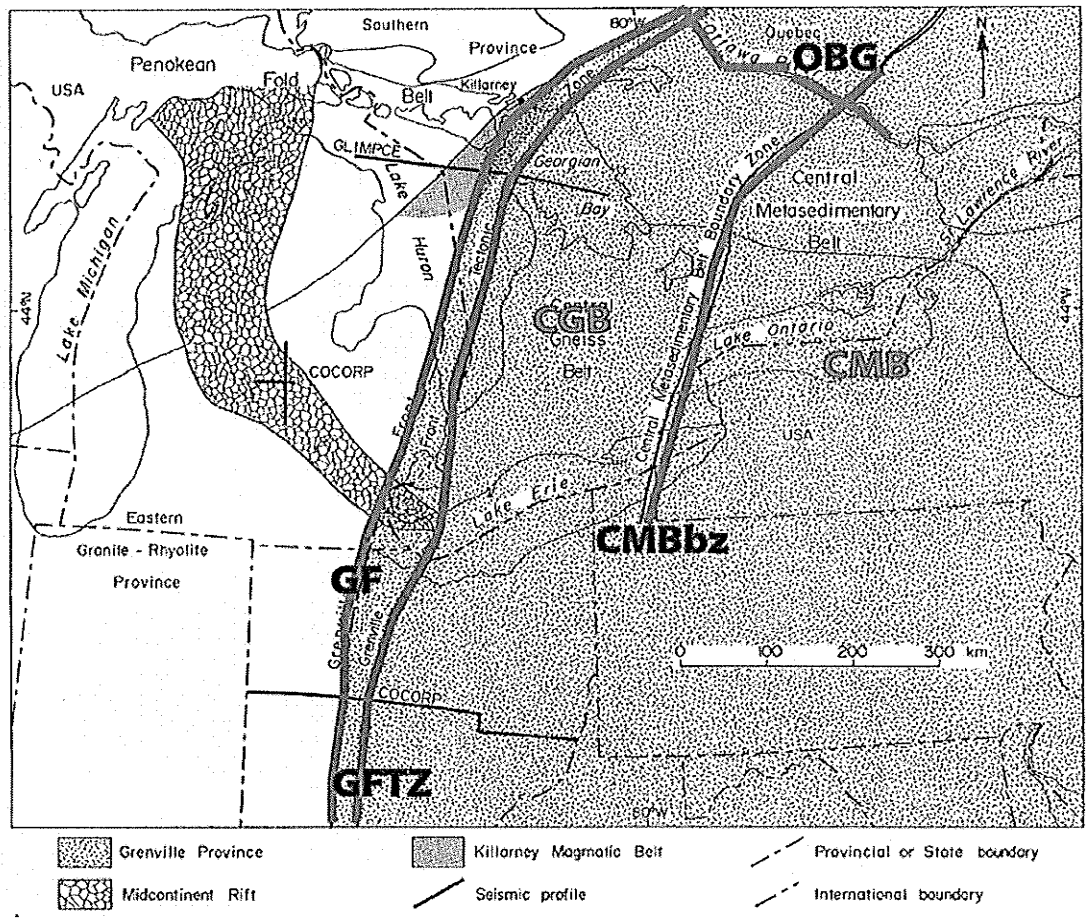

Figure 2.3. Principal subdivisions of the Precambrian rocks in central and southern Ontario and adjacent areas, showing location of GLIMPCE and COCORP deep seismic profiles. Positions of the Grenville Front Tectonic Zone, Central Metasedimentary Belt Boundary Zone and the southeastern extension of the Midcontinent Rift in the areas covered by Paleozoic rocks are interpretations (from Carter and Easton 1990).

2.4.2 Central Metasedimentary Belt Boundary Zone (CMBbz)

The Central Metasedimentary Belt Boundary Zone (CMBbz), separating the Central Gneiss Belt from the Central Metasedimentary Belt, is a north to northeast-trending zone of cataclastic and tectonically disrupted quartzofeldspathic gneisses and northwest-directed ductile thrusts that carried rocks of the Central Metasedimentary Belt northwestward over rocks of the Laurentian margin (White et al. 2000). Most CMBbz rocks are tectonites, including transposed, straight and porphyroclastic gneiss. The tectonites dip along most of its length shallowly to the south-southeast at 20° to 40° (Easton 1992).

In the westernmost part of the CMBbz, the tectonites appear to be derived from Fishog Domain gneisses. In the Minden area, the CMBbz is a 2 to 6 km wide tectonic zone (Easton 1992, Figure 2.4). In the middle of the CMBbz, the protolith is indeterminate. The eastern contact of the CMBbz is sharp, with a granitoid straight gneiss in fault contact with marble tectonic breccia of the Denna Lake Structural Complex (Easton 1992). North of Haliburton, the CMBbz changes orientation from north to northeast, and several large thrust complexes of circa 1340 Ma tonalitics gneisses are interleaved with the taconites. Several large thrust sheets also occur in the CMBbz in the Pembroke area. Because of interleaved marble tectonic breccia and thrust nappes, it is difficult to define the boundary with the Bancroft Terrane between Haliburton and Minden (Easton 1992).

The ages of movement from the CMBbz coincide with ages from the Huntsville area, suggesting early (1180 to 1140 Ma) and late (1070 to 1060 Ma) movement on ductile Central Gneiss Belt thrusts (Easton 1992).

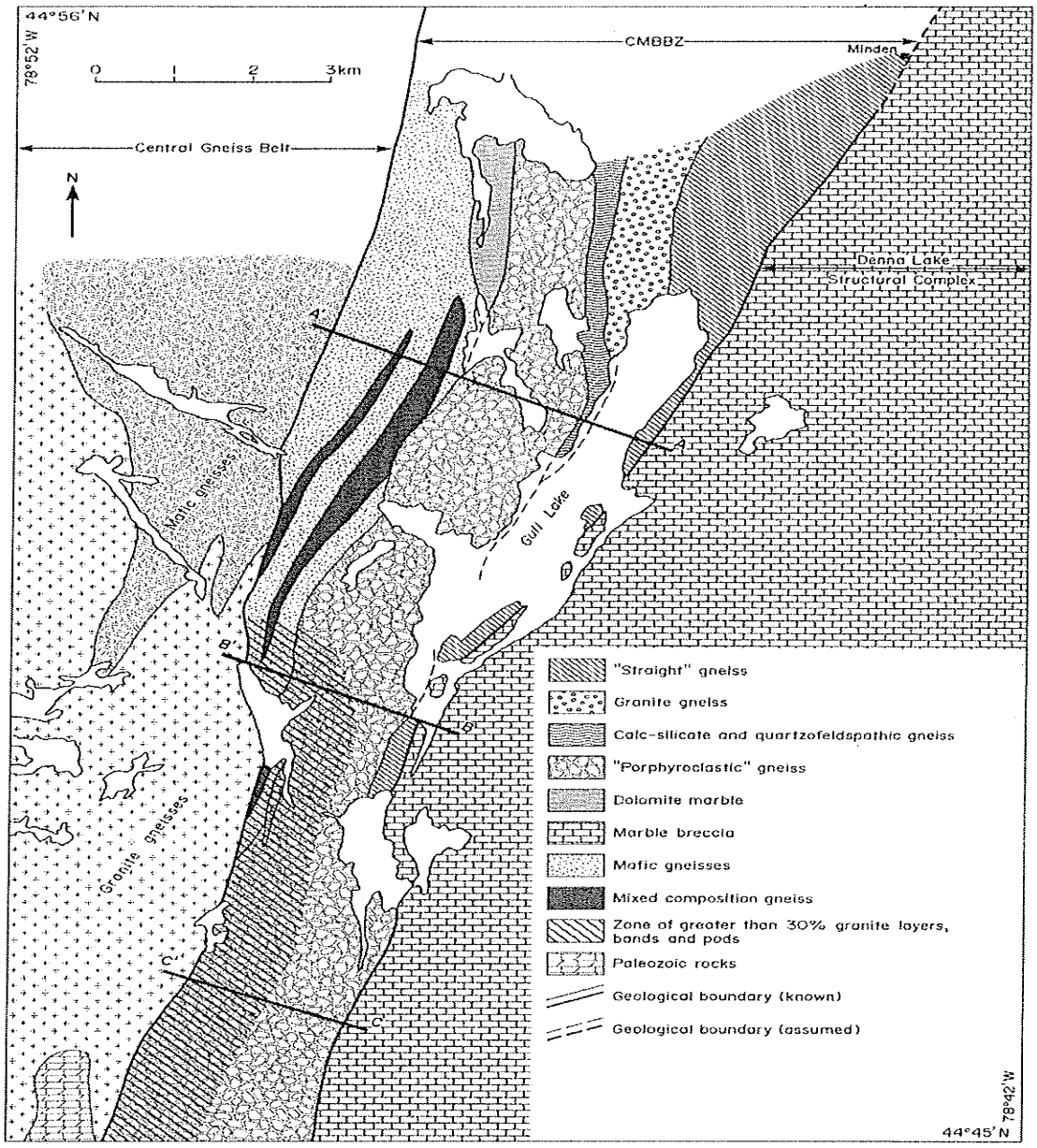

Figure 2.4. Lithotectonic subdivisions of the Central Metasedimentary Belt Boundary Zone (CMBbz) in the Minden area (from Easton 1992).

2.4.3 Ottawa-Bonnechere Graben (OBG)

The Ottawa-Bonnechere Graben lies along the Ontario-Quebec border and is approximately 60 km wide. Along the graben, lamprophyre dikes are common, while at the southern end of the Ottawa-Bonnechere Graben, in the region where it joins with the St. Lawrence Graben System (on the Quebec side of the Ontario-Quebec border), numerous small carbonatite intrusions are present. Therefore, the Ottawa-Bonnechere Graben may be associated with Mesozoic lamprophyric dikes and Paleozoic alkalic-carbonatite intrusions, and preserves a number of lower Paleozoic outliers along the Ottawa River valley and Lake Nipissing areas (Easton 1992).

Faults, and extension-related alkalic and kimberlitic plutonism occur in the Lake Timiskaming and Ottawa-Bonnechere Graben in Ontario, suggest that the graben was undergoing an overall extensional regime associated with the opening of the Atlantic Ocean during the Mesozoic. However, Paleozoic age alkalic-carbonatite intrusions in the Ottawa-Bonnechere Graben indicate that it may be a pre-Mesozoic structure. More significant igneous intrusions associated to Mesozoic rifting occur in Quebec and New England (Easton 1992).

As a consequence of rifting, divergent tectonism (i.e., midocean ridge spreading) created the Atlantic Ocean and the subsequently stress regime in the North American plate became compressional. This compressional regime, with maximum principal horizontal stress oriented NE to ENE, is evidenced by significant, historical, intraplate seismic activity (Easton 1992).

Chapter 3

Review of Previous Geophysical Studies

3.1 Introduction

In the past two to three decades, a large number of geological and geophysical surveys and networks, including the Great Lakes International Multidisciplinary Program on Crustal Evolution (GLIMPCE), the Abitibi-Grenville LITHOPROBE transect survey, Lake Ontario industry exploration surveys, the 1988 Grenville-Appalachian Seismic refraction (GRAP-88) experiment, Portable Observatories for Lithospheric Analysis and Research Investigating Seismicity (POLARIS) as well as the South Ontario Seismic Survey (SOSS) have been oriented towards understanding either the lithospheric architecture in relation to the tectonic evolution of the Grenville orogen and adjoining southeastern Superior Province, or seismicity and earthquake hazards in Ontario (Eaton 2005, White et al. 2000). Among the different geophysical methods that have been employed, controlled-source seismic, magnetotelluric, gravity and teleseismic surveys have contributed most to the study of the crustal and lithospheric architecture of the Grenville orogen in Southern Ontario and surrounding areas, therefore the following five sections discuss the results obtained from those methods.

3.2 Seismic Reflection

Figure 3.1 shows most of the controlled-source seismic surveys which have been conducted in or near the study area over the past 20 years.

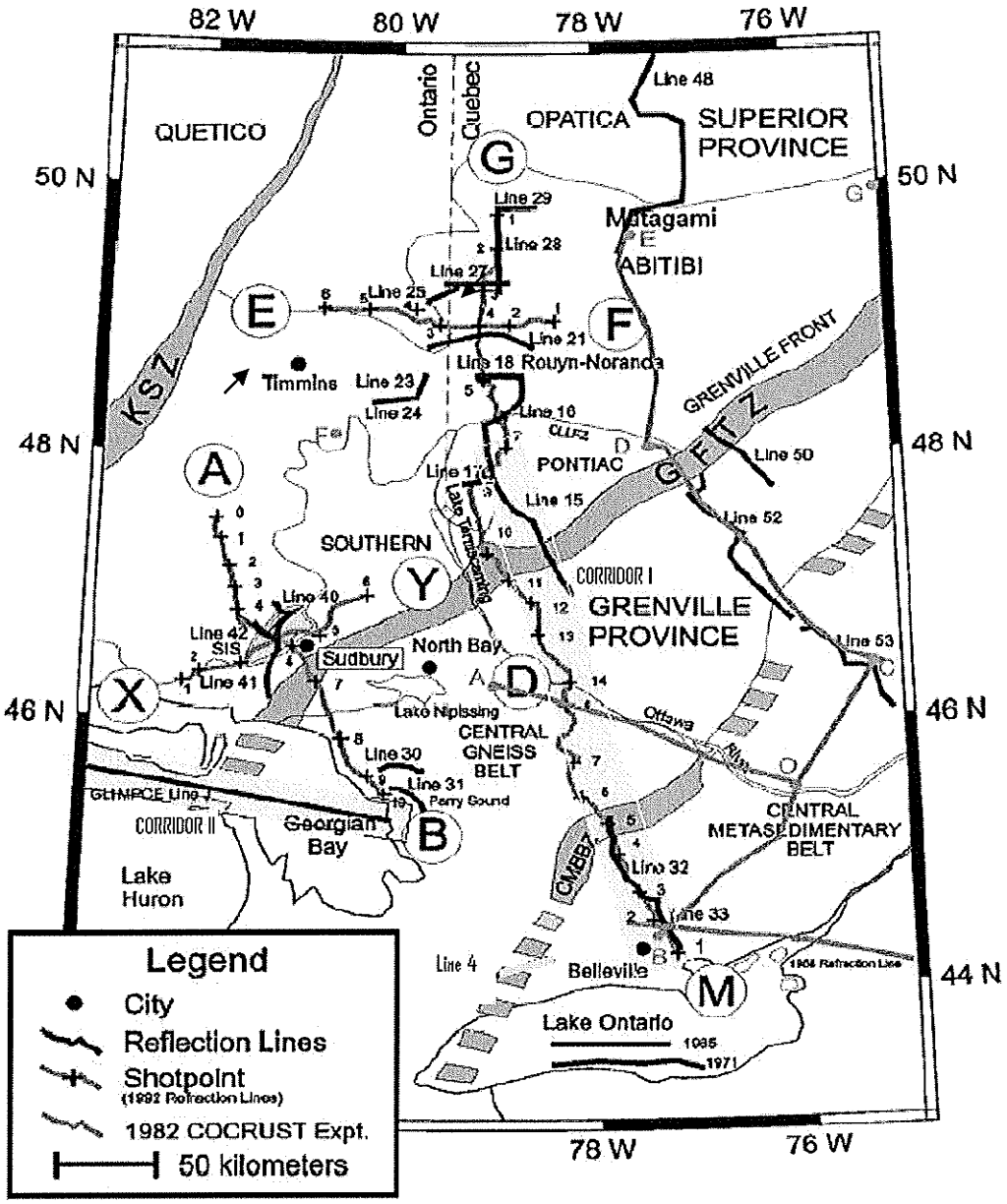

Figure 3.1. Simplified tectonic map of the study area, showing most of the controlled-source seismic lines over the past 20 years. Corridor I and II as well as SOSS-line 4 were highlighted in yellow color which will be discussed in detail in the text. Corridor I (referred to in the text) includes AGT92-line 15, AGT90-lines 31, 32 and 33, and line 71, as well as wide-angle refraction experiment AG92-WAR, and the GRAP-88 experiment. Corridor II consists of GLIMPCE-line J; GFTZ – Grenville Front Tectonic Zone; CMBbz – Central Metasedimentary Belt Boundary tectonic zone (modified from Roy and Mereu 2000).

In 1986, two multichannel seismic reflection profiles in Lake Huron were carried out by GLIMPCE. One of these profiles (GLIMPCE-Line L) and its interpretation are shown in Figure 3.2. The most distinct features in this profile are 32 km wide, east-dipping zone of reflectors which coincide with GFTZ. These strongly east-dipping reflectors can be traced to greater than 14 s, indicating that the GFTZ extends throughout the crust. The steep western boundary of the zone delineates the GFBF mylonite zone at depth and sharply truncates by geologic structure from the west. However, the Moho is poorly defined in these profiles (Green et al. 1989, Easton 1992).

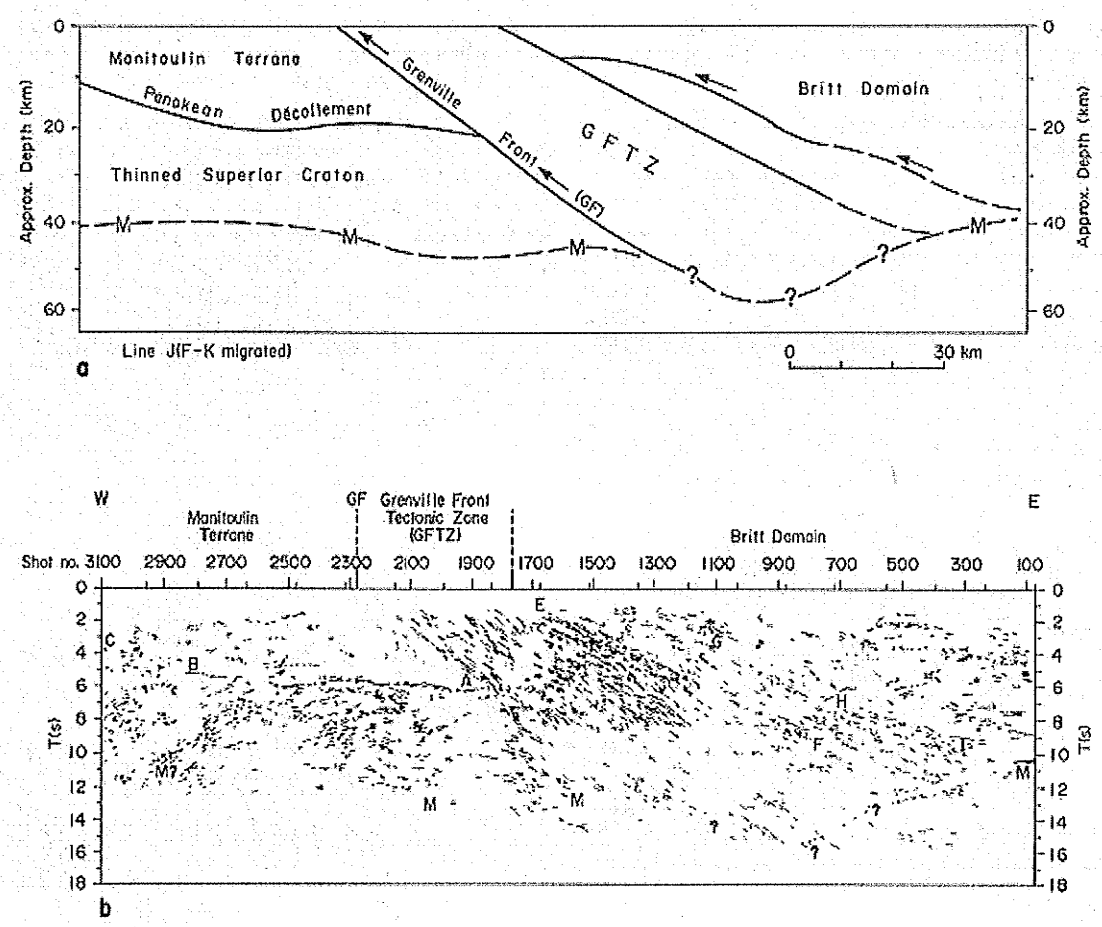

Figure 3.2. GLIMPCE-Line L seismic profile (below) and the interpretation of the various reflectors (top) (modified from Green et al. 1989, Easton 1992).

In 1991, as part of the Abitibi-Grenville LITHOPROBE project, seismic reflection lines (Line 32 and Line 33, see Figure 3.1) were run through the Bancroft terrane, Elzevir terrane and Mazinaw terrane within the CMB, extending roughly ~130 km in a NW-SE direction, perpendicular to the major shear zones in the CMB (Roy and Mereu 2000).

Roy and Mereu (2000) reprocessed the seismic profiles of Line 32 and 33 by using a pattern recognition approach (PR). Results from Line 32 and 33 (see Figure 3.3 and Figure 3.4) show that crustal-scale shear zones in the CMBbz (event A, Figure 3.3) are characterized by bands of SE dipping shallow reflectors extending to mid-crustal depths of 25-30 km. These are analogous to the GFTZ and support models of NW-directed crustal shortening during the Grenville orogen. These reflection features are steep at the surface and become listric at depth, as determined by mylonitic fabrics and the orientations of nappes within the CMBbz. They do not penetrate the Moho, as indicated by the absence of any major relief of the Moho topography in the CMB and CGB. Several other reflectors (e.g., event C and D in Figure 3.3) dip ~ 20^{o} towards the southeast, which were interpreted to represent Elzevir terrane rocks thrusted northwestwards above the Bancroft terrane.

Major seismic boundaries coincide with the terrane boundaries (e.g., Elzevir-Mazinaw boundary, Easton 1992, Roy and Mereu 2000). The overall structure and reflection geometry determined from the reprocessed data agree well with those presented by White et al. (1994).

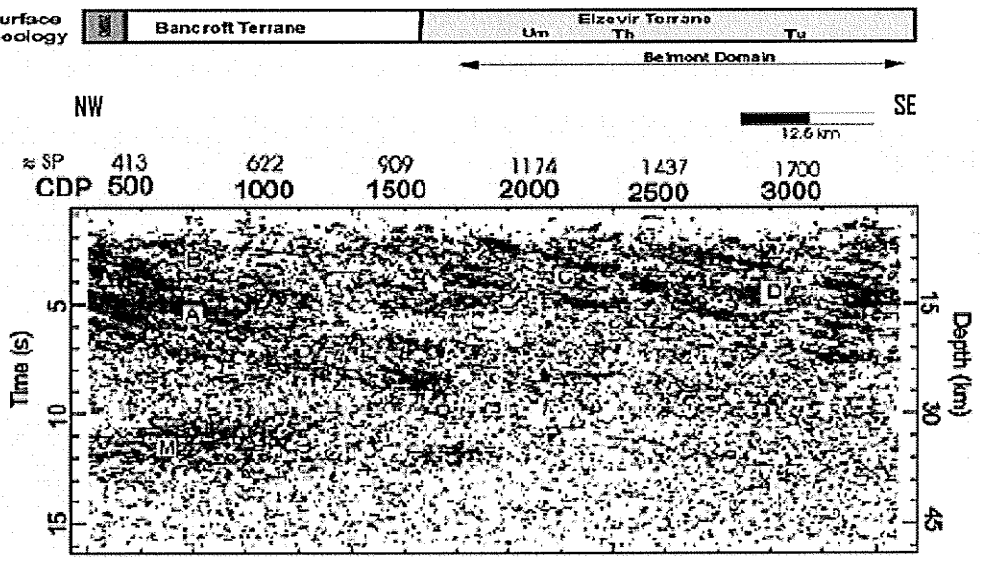

Figure 3.3. Coherency filtered, migrated stacked section from Line 32 processed using the PR approach. Major SE-dipping reflectors can be observed from 0-8 s two-way travel time. The Moho signature is poor except in the northern part of Line 32 (modified from Roy and Mereu 2000).

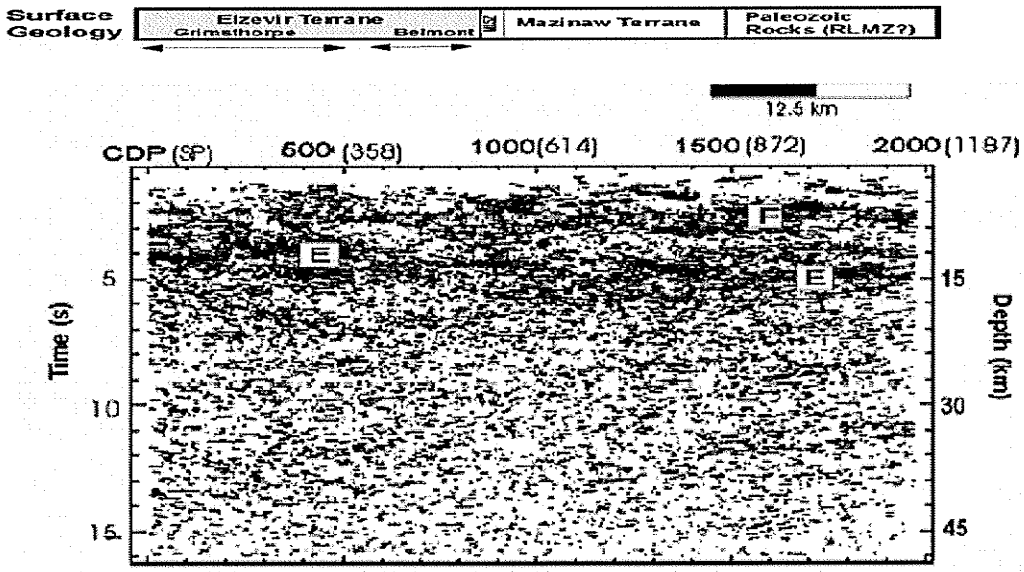

Figure 3.4. Coherency filtered, migrated stacked section from Line 33 processed using the PR approach. The reflectors are more gently dipping than those observed on Line 32. The lower crust is less reflective and a clear Moho signature is absent; RLMZ- the Robertson Lake Mylonite Zone (modified from Roy and Mereu 2000).

Most recently, O'Dowd et al. (2004) published their study on the crustal structure of a buried segment of the Grenville orogen near Toronto, Canada, situated between the Lithoprobe's Abitibi-Grenville transect north of Lake Ontario (White et al., 2000) and COCORP profile south of Lake Erie (Pratt et al. 1989) (see Figure 3.1, Line 4). It is a 75-km Lithoprobe reflection profile, traversing the CMBbz.

Figure 3.5 shows the resulting seismic profile. An approximately horizontal but discontinuous reflection at ~0.4 s correspond to the contact between Pleistocene deposits of the Oak Ridges Moraine and the underlying Paleozoic rocks dominated by limestone and shale. Beneath this layer, Precambrian bedrock in the upper ~21 km (7 s two-way-time -TWT) of the crust is visible as a coherent reflection fabric with apparent southeast-dipping reflections with strike and dip of ~N13°E and 25° respectively, which truncates and/or overprints a subhorizontal band of reflectivity at ~21 km depth with rough strike and dip of ~N65°E and 20° eastward dip, penetrating to the CMBbz (O'Dowd et al. 2004).

A similar dipping reflection feature can be observed along Lithoprobe line 32 (White et al., 2000), it appears to indicate tectonically imbriacted units of the CMB and CMBbz.

The Moho is poorly defined with minimal topography but visible at 12.5 s TWT along the eastern two-thirds of the profile. O'Dowd et al. explained this weak Moho reflection might result from high attenuation in the thick Quaternary section. However, since other Lithoprobe seismic lines in the area also show a similar weak Moho (White et al., 2000), it is likely to be a local characteristic of lower crust and Moho (O'Dowd et at. 2004).

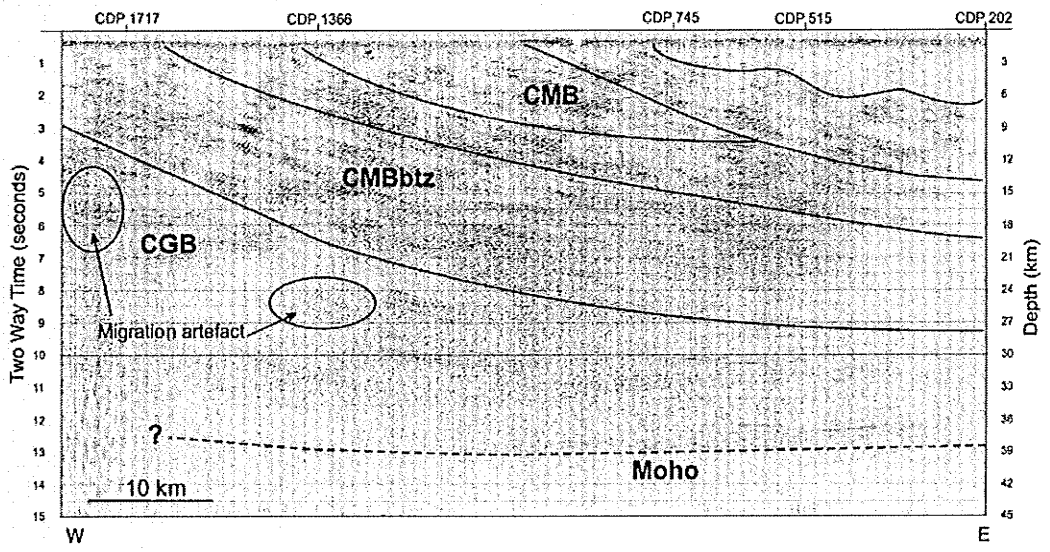

Figure 3.5. SOSS Line 4, migrated seismic profile. Section is plotted with no vertical exaggeration for a crustal velocity of 6.0 km/s. Total line length is 75 km. CGB – Central Gneiss Belt, CMB – Central Metasedimentary Belt, other abbreviations are the same as in Figure 2.1 (modified from O'Dowd et al. 2004).

3.3 Seismic Refraction

In 1982, a seismic refraction experiment was conducted across parts of the Grenville Province by Canadian Consortium for Crustal Resonnaissance using Seismic Techniques (COCRUST) (Mereu et al., 1986a, 1986b). Although the profiles (Figures 3.6 and 3.7) have not shown any evidence of a mid-crustal discontinuity on these lines, the velocity gradient model for line CD (see Figure 3.7a) indicates that the crust on the west side of the CGB is more homogeneous than the east side of CMB. It also shows that southeast of Quebec, the Grenville Front at depth is marked by a significant thickening (more than 5 km) of the crust to the south of the Grenville Front and a substantial change in the character of the velocity gradient within the crust (see Figure 3.7a; Mereu et al. 1986a, 1986b). Mereu et al. (1986a) suggest that the Superior Province was cooler and

more rigid than the Grenville Province rocks to the south and that a depression formed on the Moho, northwest of the Grenville Front is similar to the depression present along the CMBbz (Easton, 1992).

The Moho depth profile along line QP (see Figure 3.7b) reveals that the crust is thicker on the southeast side of CMBbz than beneath the CGB, indicating that the surface shear zones in the CMBbz may extend throughout the crust forming a depression the Moho, agreeing with the preliminary data obtained from the Abitibi-Grenville LITHOPROBE seismic reflection lines (e.g., White et al, 1991a, 1992). Another Moho depth model along line QR across the Ottawa-Bonnechere Graben finds the Moho to be poorly defined (Mereu et al, 1986a, 1986b), possibly due to intrusion of upper mantle material into the lower crust, which is consistent with suggestions that the graben is an ancient rift (Easton 1992).

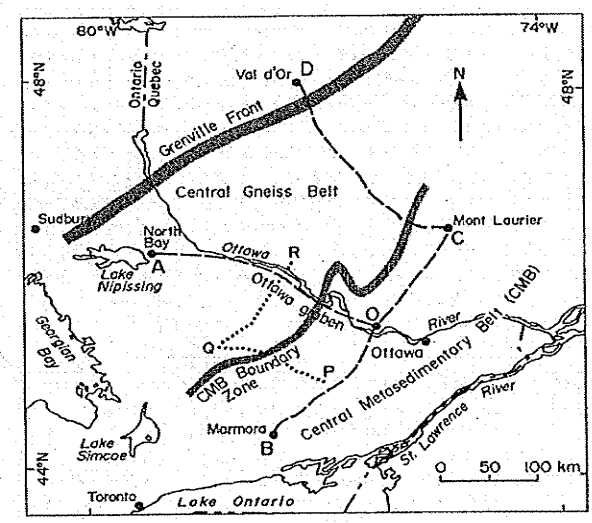

Figure 3.6. Map showing the location of the 1982 COCRUST experiment. Seismic refraction profiles are shown in Figure 3.7. Shot points A,B,C,D and lines AO,BO,OC and CD belong to the Ottawa-Bonnechere Graben experiment. Line QP indicates the location where the wide-angle reflected waves sampled the Moho, for the fan experiment, in which shot B was recorded along line AO (Modified from Mereu et al. 1986a, Easton 1992).

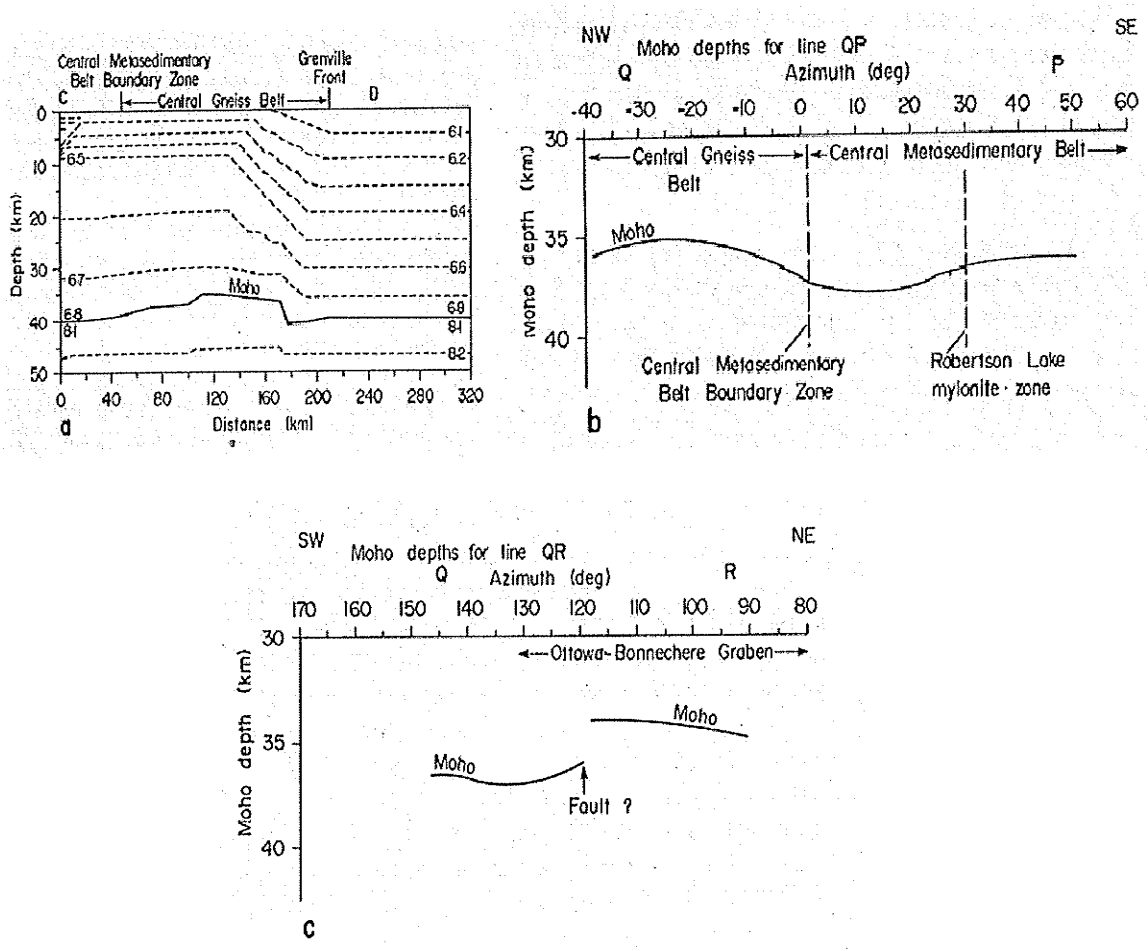

Figure 3.7. seismic refraction profiles for the 1982 COCRUST seismic survey. Location of lines are shown in Figure 3.6. Dashed lines in figure (a) are velocity contour lines showing velocities in km/s. a) Velocity gradient model for line CD. b) Moho depth profile along line QP across the CMBbz. c) Moho depth profile along line QR across the Ottawa-Bonnechere Greben (modified from Mereu et al. 1986a, Easton 1992).

In 2000, White et al. presented a cross-section based on seismic reflection data and wide-angle refraction as well as results complied from many previous publications which included GLIMPCE line J (Green et al. 1989); AGT90 Lines 31, 32, and 33 (White et al., 1994); AGT92 line 15 (Kellet et al., 1994); 1971 Lake Ontario data, (Forsyth et al., 1994a) (see Figure 3.1). These data were acquired over a period spanning 21 years.

The results (see Figure 3.8 and Figure 3.9) show that a significant variation in crustal thickness occurs in the vicinity of the Grenville Front. The crust thickens from 32-33 km in the foreland (Southern and Superior provinces) to at least 40 km thickness at 30 km southeast of the Grenville Front along Corridor II (see Figure 3.1), whereas along Corridor I (see Figure 3.1), the crust thickens from 38 to 42 km. A local crustal thinning occurs further east along lines 52, 53 and 54, where the apparent crustal thickness is 44 km beneath the Grenville Front, thins rapidly to 36 km some 60 km to the southeast and reaches a maximum apparent crustal thickness of 50 km, 250 km further to the southeast within the Grenville Province (White et al. 2000). Their velocity model was used as our base model, and will be discussed in detail in later chapters.

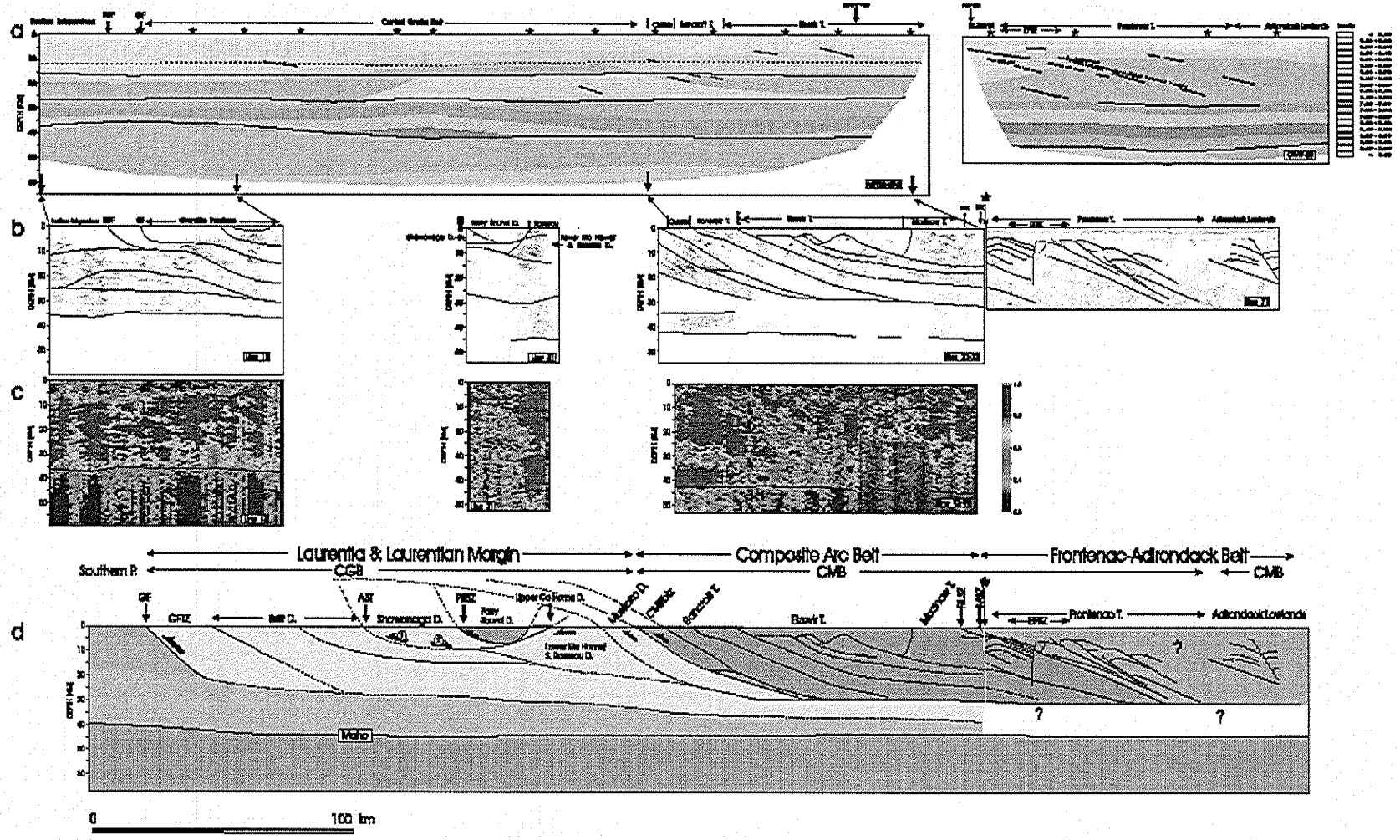

Figure 3.8. Corridor I: (a) Seismic refraction velocity model. ☆. shot point. (b) Depth-migrated seismic reflection data with an overlay of interpretation lines (blue): style of line (solid or dashed) is intended to convey confidence level of interpretation. (c) Seismic reflection amplitude attribute calculated using unmigrated data. The attribute values are normalized using the maximum value. The reflection Moho is indicated by the dashed line. (d) Interpretational cross-section. The asterisk (*) emphasizes the location of an 80 km gap between line 33 and 71, BGF, Baie Gilles fault: other abbreviations are the same as in Figure 3.1 (modified from White 2000).

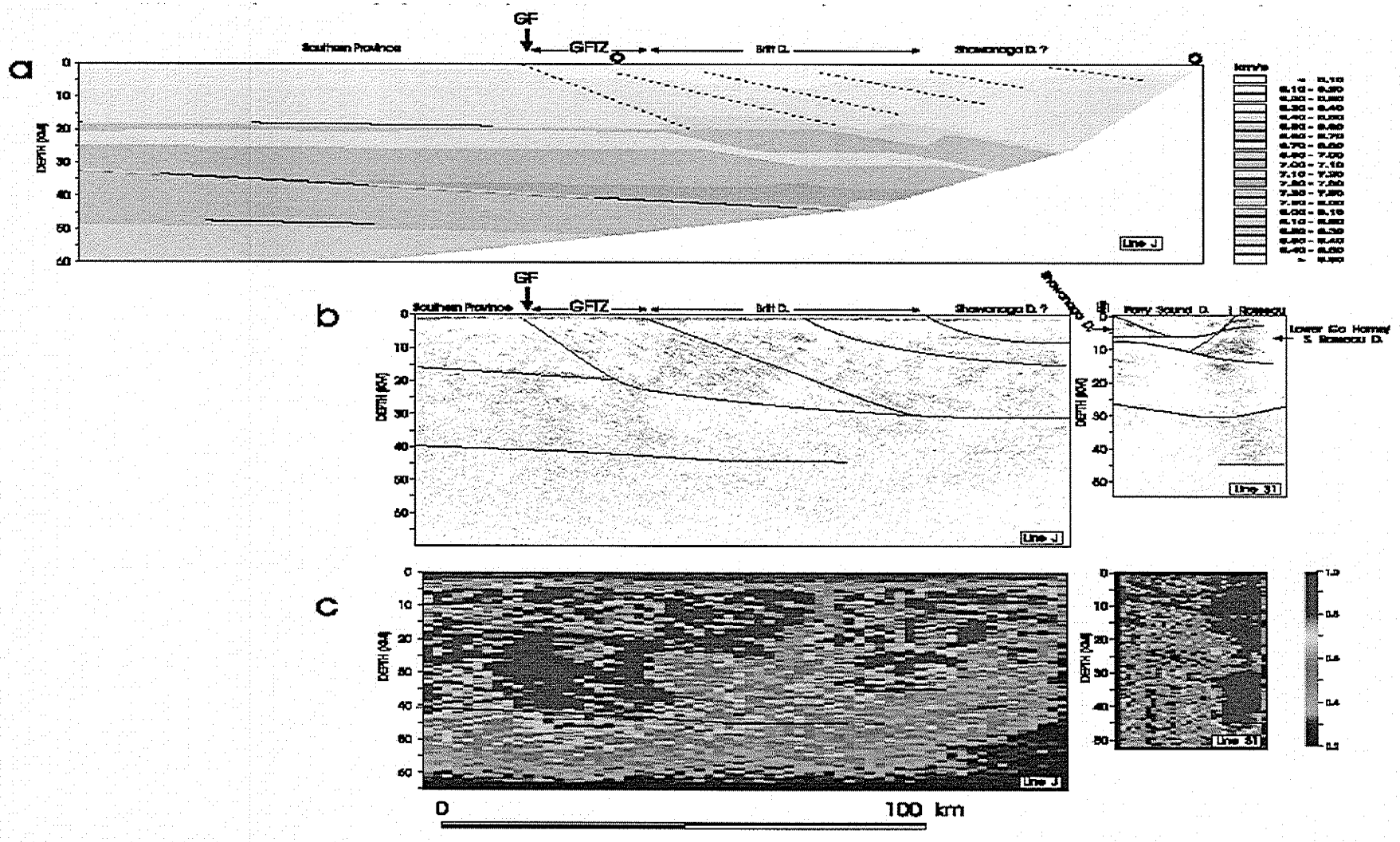

Figure 3.9. Corridor II: (a) Seismic refraction velocity models. ◯, denotes receiver location. (b) Depth-migrated seismic reflection data with an overlay of interpretation lines (blue): style of line (solid or dashed) is indented to denote confidence level of interpretation. Moho depth shown is taken from the velocity model in (a). (c) Seismic reflection amplitude attribute calculated using unmigrated data (line J). The attribute values are normalized using the maximum value. The dashed line (line J) is the Moho depth (a). Abbreviations are the same as in Figure 3.1 (modified from White 2000).

3.4 Teleseismic Studies

A shear-wave splitting study analyzed core-refracted phases SKS, SKKS and PKS with the particle-motion method of Silver and Chan (1991) in the lower Great Lakes region (Eaton et al. 2004). This study involved 27 broadband seismograph stations extending across a low-velocity anomaly in the lithospheric mantle.

Their observations shown in Figure 3.10 reveal three distinct anisotropic domains in the lower Great Lakes region. A shear-wave velocity map for 210 km depth from model NA00 (Van der Lee, 2002) is also superimposed in this figure. A distinctive feature in this figure is the aforementioned low-velocity region, which is centered on the Lake Ontario. This feature was interpreted by Fouch et al (2000) as a divot in the North American lithospheric root. Zone 'A', the failed rift zone, shows uniform SW-trending fast splitting vectors which overlap and consistent with the results of Rondenay et al (2000). In zone 'B', located further west, most of the splitting vectors are approximately aligned with the WSW direction of absolute plate motion, with maximum splitting times near the center of the low-velocity feature. Zone 'C', comprising stations around Georgian Bay, with the least number of shear-wave observations, exhibits considerable scatter. Eaton et al. (2004) concluded that spatial variability in the direction and magnitude of splitting are consistent with a flow regime influenced by basal topography of the lithospheric keel.

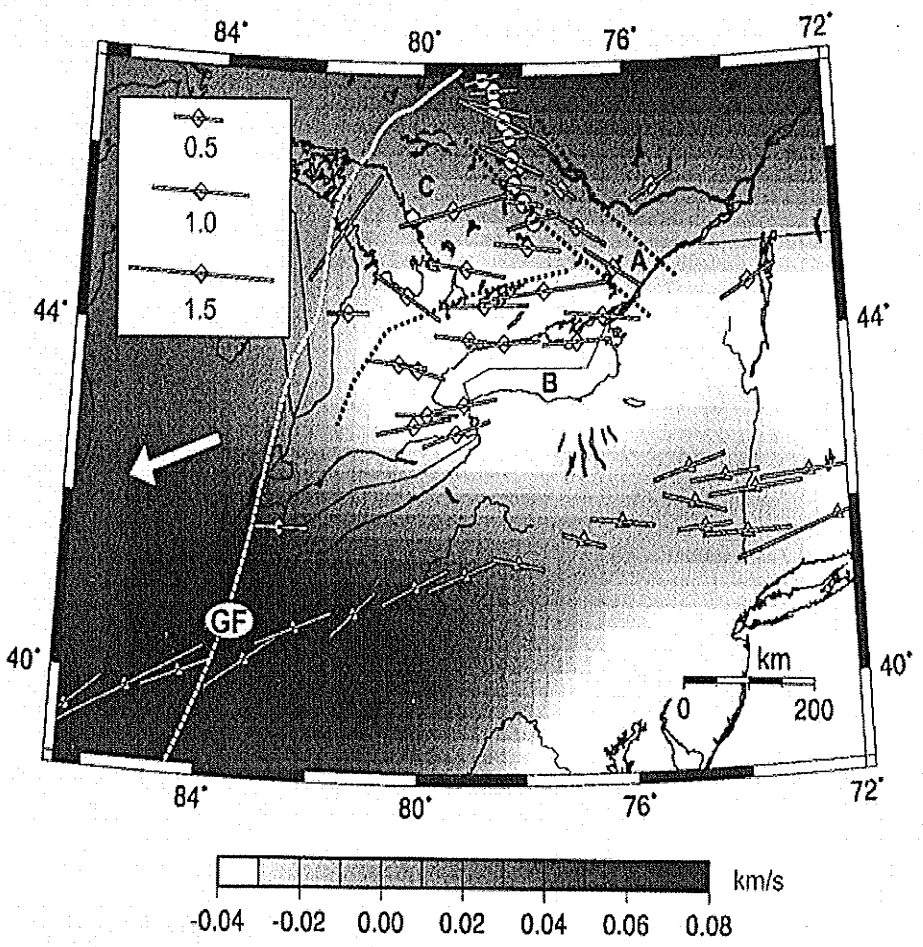

Figure 3.10. Multi-event splitting vectors superimposed on shear-wave velocity anomaly at 210 km depth, from model NA00 (Van der Lee, 2000). Large arrow shows absolute plate motion direction. Diamonds denotes stations from Eaton et al (2004); circles are from Rondenay et al. (2000); triangles are from Fouch et al. (2000). GF-Grenville Front; zones A, B, and C are discussed in the text (modified from Eaton et al., 2004).

Aktas and Eaton (2005) performed P and S-wave tomographic traveltime inversion in the lower Great Lakes region. Two salient features were detected in 3-D models (Figure 3.11): 1) a steep SE-dipping, slab-like high-velocity feature which strikes parallel to tectonic belts in the Grenville Province imaged on both the P- and S- wave velocity models. This feature extends to as deep as 350 km and was interpreted as a relict

slab correlated with 1.25 Ga subduction beneath the CMB. 2) a SW-plunging, ribbon-like low-velocity anomaly shown in the S-wave model, which projects up-dip to a seismically active area in western Quebec. A similar feature was also observed by Rondenay et al. (2000). This low velocity anomaly may be associated with the Cretaceous passage of North America over the Great Meteor hotpot. Atkas and Eaton (2005) attribute the non-vertical attitude of the inferred plume anomaly to interaction of the hotspot with dipping zones of weakness in the North American lithospheric root.

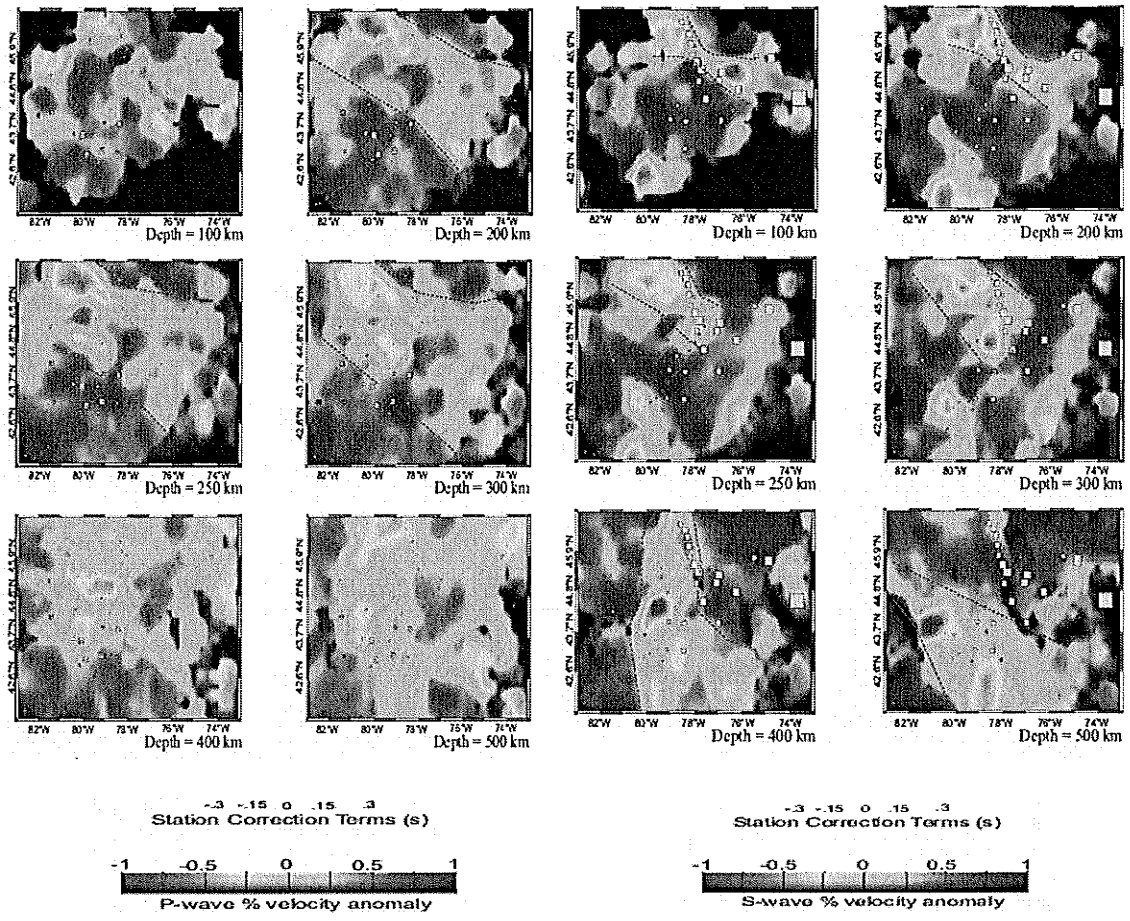

Figure 3.11. P-wave travel-time inversion results (left) and S-wave travel-time inversion results (right). The color scale gives percent velocity anomaly with respect to IAS91 (from Atkas and Eaton, 2005).

3.5 Deep Electromagnetic Studies

Electromagnetic (EM) studies have shown that the Phanerozoic sedimentary rocks of the Southern Ontario have relatively high conductivity and a strong influence on the EM response. In contrast, the upper crust in Precambrian Shield areas has a much lower conductivity. The resistivity of individual sedimentary units ranges from <10 Ω.m for shale and sandstones to >1000 Ω.m for carbonates and evaporates. Individual sedimentary units may increase this conductivity greatly. A conductivity of 10-20 S/m has been reported in one Ordovician black-shale unit near the base of the Whitby Formation, which is comparable to the conductivity of the mid-crust and restricts the resolution of conductivity structure of the crust (Mareschal et al. 1991).

Overall EM survey results from Ontario and Quebec show a globally-observed decrease in resistivity of the mid-crust (to values less than 300 Ω.m). There are some studies that have reported higher values of 1000-3000 Ω.m (Kurtz et al. 1993). In some models resistivity values exceed 10,000 Ω.m (Bailey et al. 1989). Due to the relatively high conductance of the mid-crust, MT can not provide good resolution of the lower crust (>25 km depth). However, long-period MT soundings can provide good resolution of the mantle resistivity beneath Ontario and Quebec. The results from Schultz et al. (1993) suggest that in the Kapuskasing area of the Superior Province upper mantle resistivity increases from 1000 Ω.m near the top of the mantle to around 1500 Ω.m at a depth of about 100 km. The resistivity decreases at depth greater than 100 km.

Anisotropic electromagnetic responses have been observed in a number of studies in, or adjacent to, the present study area (e.g., Ji et al., 1996; Mareschal et al., 1995; Kellett et al., 1994; Boerner et al., 2000, Kurtz, 1982, Eaton et al., 2004, Frederiksen et

al., 2005). A significant anisotropic response in the middle crust to upper mantle across the Grenville Front was observed by most MT studies.

A comparative study of electrical and seismic anisotropies in the vicinity of Grenville Front was presented by Rondenay et al. (2000). Their results are shown in Figure 3.12. For electrical measurement (MT), the electrical anisotropy indicates a fairly uniform orientation of N80°E. The direction of maximum conductivity is generally E-W, being parallel to the lineations defined by the major Precambrian deformation zones. For the teleseismic SKS splitting data, the average direction of fast polarization is $N101^{\circ}E \pm 10^{o}$, and average splitting is $1.46 \pm 0.21s$. Over the study area, the direction of seismic anisotropy correlates well with the calculated direction of electrical anisotropy. There is a 20 degree obliquity observed between the two anisotropies, which may reflect a dextral shear sense in the mantle, which is in agreement with the last cycle of regional deformation inferred from the surface geology (Ji et al., 1996).

A compilation of older Lithoprobe and new POLARIS MT results (Figure 3.13) by Frederiksen et al. (2005) shows that a relatively uniform electrical anisotropy near the Grenville Front that is subparallel to crustal tectonic features, indicating a relationship with Grenvillian orogeny. In contrast, responses oriented at a relatively high angle to the tectonic fabric are observed at many MT sites in the Grenville Province, suggesting that the lithospheric mantle beneath the Grenville Province has undergone significant deformation postdating the Grenvillian Orogeny. The source of the anisotropic response is still under debate. Kellett et al. (1994) suggests that it might have resulted from Archean rocks of the southern Superior Province extending southwards at depth into the Grenville Province. Boerner et al. (2000) also suggest that the observed anisotropy near

the Grenville Front may be a consequence of Archean aged rocks rather than younger crust. Some researchers also suggest that it may be caused by an anistropic upper mantle (Frederiksen et al., 2005).

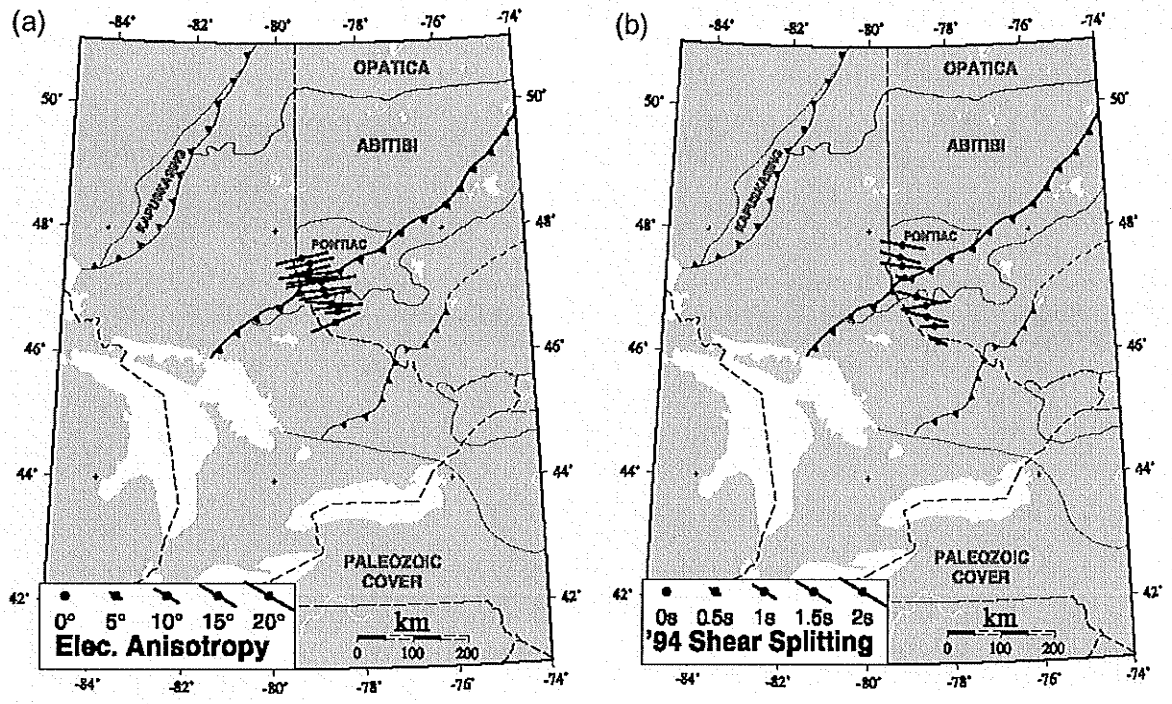

Figure 3.12. Azimuths and amplitudes of (a) electrical anisotropy and (b) shear-wave splitting near the study area (modified from Rondenay et al. 2000).

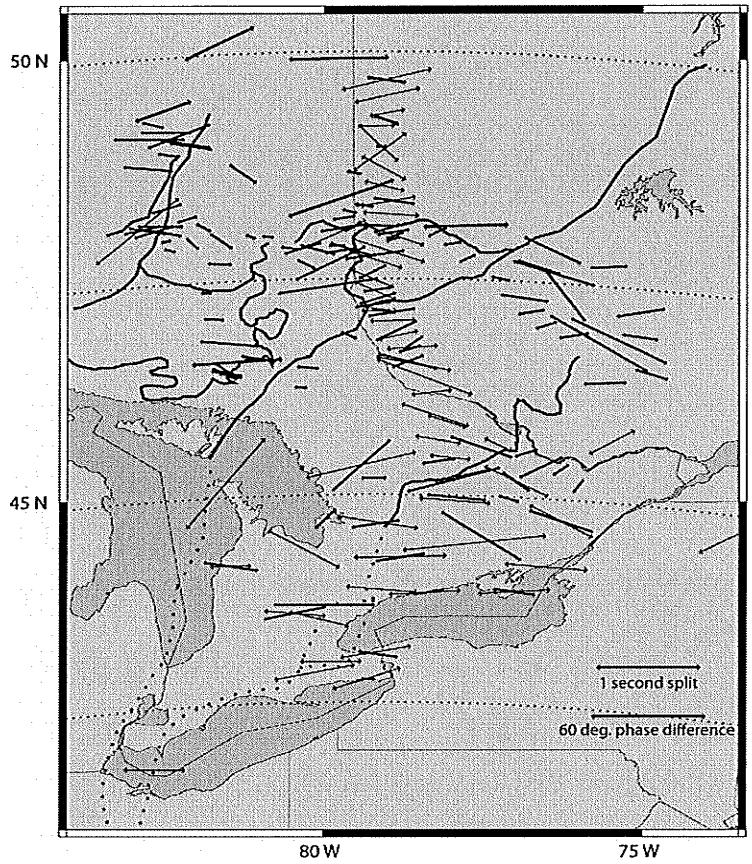

Figure 3.13. Diagram showing comparison of MT strike direction and SKS fast directions. The MT strike azimuth is shown in the direction closest to SKS fast direction at nearby sites (from Frederiksen et al., 2005).

3.6 Gravity

The results from gravity can help constrain and improve the tectonic interpretations obtained from other methods by providing information on crustal composition and thickness (through modeling) (Rondenay, 2000). Prominent features of the gravity response in Ontario are Bouguer gravity low along the Grenville Front in the Killarney area which is associated with the Killarney Magmatic Belt; and prominent high anomalies in the Parry Sound Domain and Nepewassi Domain, particularly the

northwestern half of the domains. A prominent, east-trending low between North Bay and Mattawa does not correlate with any single geological feature (Easton 1992).

The gravity modeling results from Roy and Mereu (2000) (see Figure 3.14 and 3.15) show that density is higher below the Elzevir and Mazinaw terranes than beneath the Bancroft terrane. There is a very gradual increase in density of the CGB from 0-40 km depth, indicaties that internal structure of the CGB rocks is relatively homogeneous. This result coincides with the relatively non-reflecting crust in the CGB as seen on Lines 30 and 31 (White et al. 1994). The higher-density of CMB rocks, in contrast with the lower-density footwall rocks of the CGB, supports the suggestion that mid-crustal exhumation has occurred along regional-scale decollement zones, i.e. the CMBbz. Density images also show the amalgamation of two different crustal units – the CMB and the CGB – to the NW, augmenting the current idea of NW-directed tectonic transport during the Grenville orogeny. The presence of an anomalous density distribution up to lower crustal level between the CGB and CMB suggests that this movement and accretion of the two units was a crustal-scale process (Roy and Mereu 2000).

Most recently, a new tentative gravity model based on mapping both crustal thickness variation and density variation in the lower crust of southern Ontario has been derived by Bank et al. (2005). The results are obtained by using complete Bouguer gravity values from the Geological Survey of Canada (GSC) and Pan American Center for Earth and Environmental Studies (PACES) constrained by semblance-weighted receiver function analysis and seismic refraction studies. The results reveal a large crustal variation between ~30 km beneath the mid-continent rift (around 78°W, 44.8°N) and ~48 km on either side, the thickness being ~45 km at the Ottawa-Bonnechere Graben and in

the Composite Arc Terrane of the CMB of the Grenville orogen. These results are not totally in agreement with seismic estimates of crustal thickness. The inverted density variations show a clear distinction between dense lower crust of the CGB and less dense lower crust of CMB to the northwest and southeast of the Grenville Orogen, respectively. Crustal thickness variations are not reflected in the general flat surface topography of the area. The increase in the density of the lower crust might indicate that Moho topography of orogenic belts can be sustained long after tectonic activity has ceased (Bank et al., 2005).

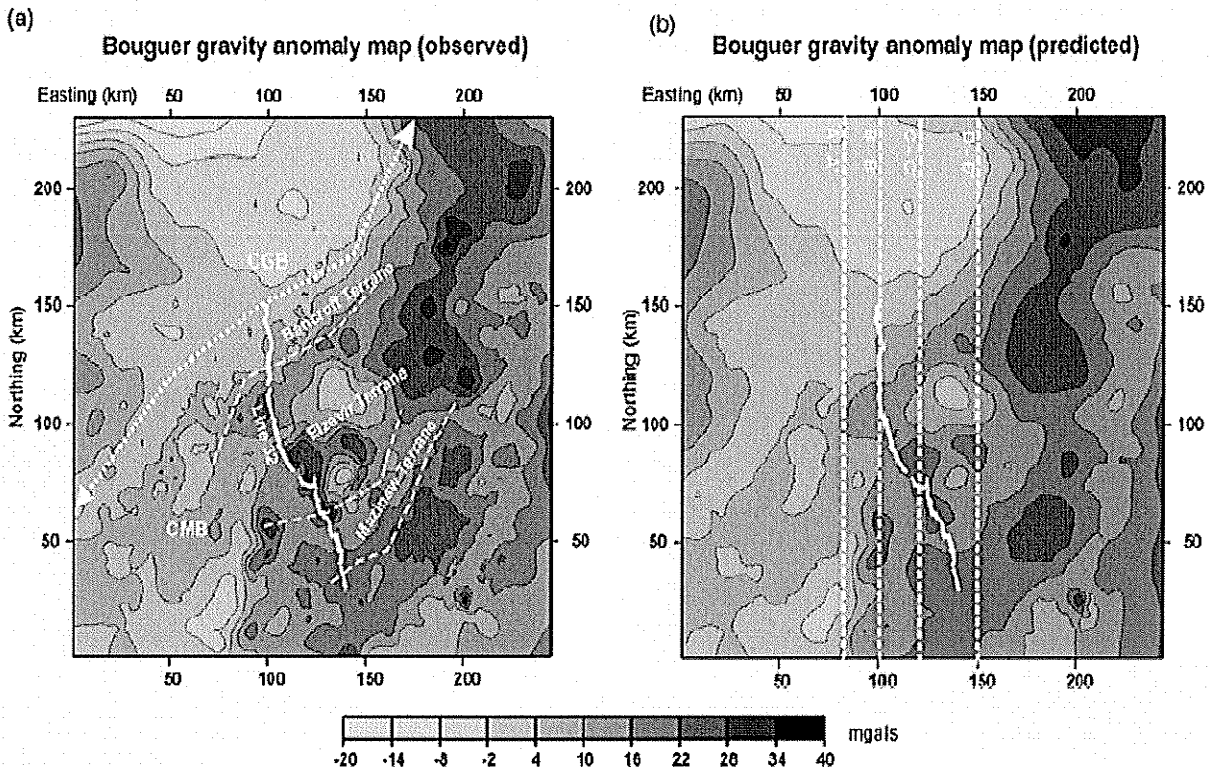

Figure 3.14. (a) Observed Bouguer anomaly data along with location of Lines 32 and 33. The approximate location of the boundary between the CGB and CMB has been marked. (b) Predicted gravity data from the 3-D inversion. Note the similarity between (a) and (b). Vertical lines indicate N-S depth sections shown in Figure 3.15 (modified from Roy and Mereu 2000).

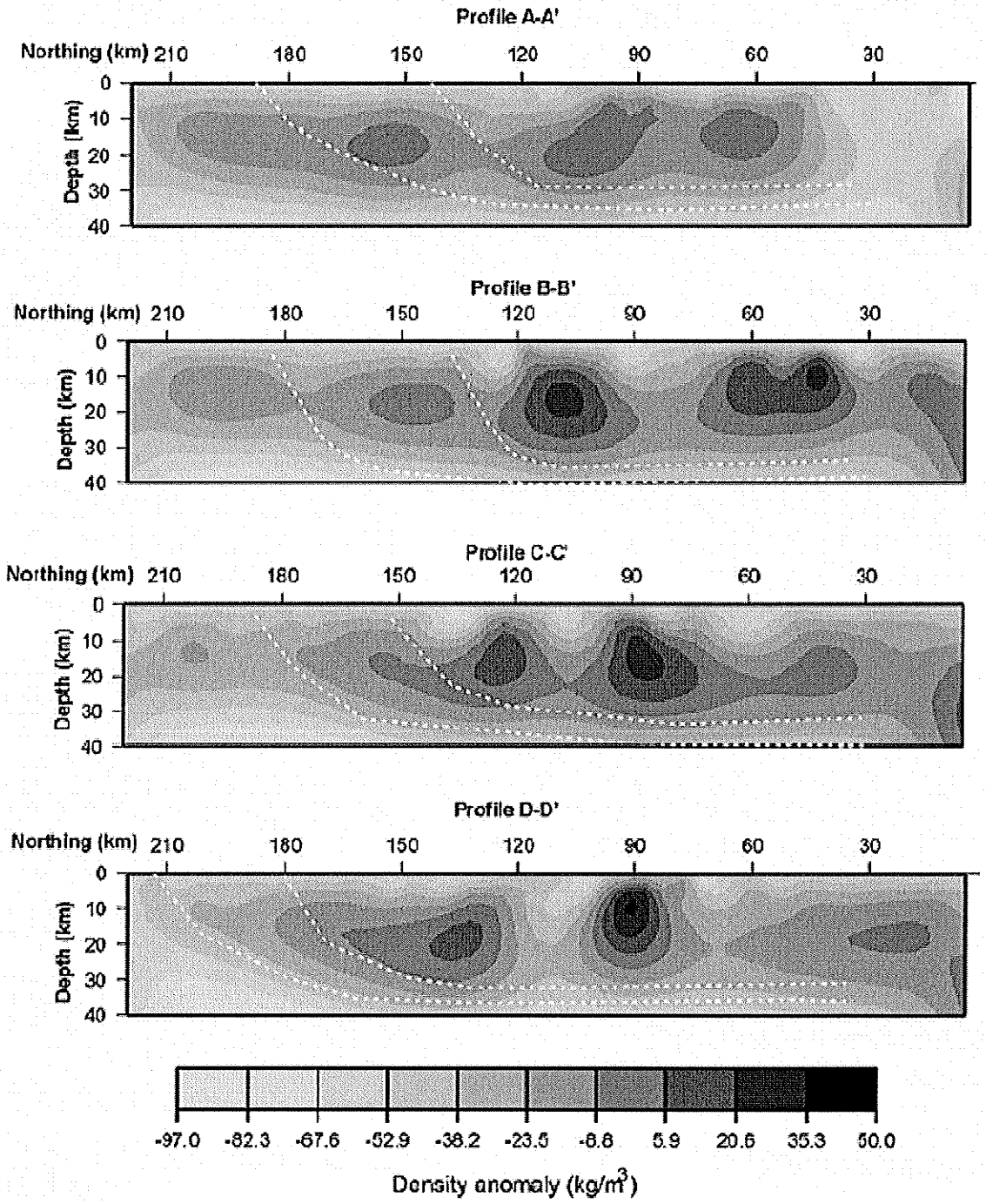

Figure 3.15. Vertical cross-sections from the 3-D inversion volume along profiles A-A', B-B' and D-D' as marked in Figure 3.14(b). Clearly higher densities are observed in the CMB as compared to the CGB at mid-crustal depths. Dashed lines indicate the probable decollement zones along which uplift has taken place. The sections do not reflect the true dip of the structures since they are oblique to the strike (modified from Roy and Mereu 2000).

3.7 Heat Flow

Heat flow and deep thermal structure in and adjacent to the study area have been discussed by Mareschal et al. (2000). The average heat flow in the Grenville Province, at the intermediate age of 1.0 Ga, is low ~ 38 $mW.m^{-2}$ compared with adjacent older Superior Province (2.7 Ga, 42 $mW.m^{-2}$) and younger Appalachians (0.4 Ga, 58 $mW.m^{-2}$). Heat-flow trends are continuous across the Grenville Front. This large variation in heat flow has been attributed to changes in crustal composition. Mareschal et al. (2000) summarized available knowledge of crustal structure in five different areas based on a combination of seismic studies, laboratory measurements of rock physical properties, and geological constraints (Figure 3.16). From these model, it is clear that heat flow is high wherever there is a significant amount of granitic rock, regardless of age. The western Abitibi, of Archean age, has heat-flow values in excess of 50 $mW.m^{-2}$ and is characterized by a thick layer of trondhjemite-tonalite-granodiorite (TTG) rock. The Appalachian Province, which is much younger, has many highly enriched granitic plutons emplaced in gneissic upper crust and a mean heat flow of 55 $mW.m^{-2}$. In contrast, the Grenville Province has low heat flow where granitic rocks are rare. Mareschal et al. (2000) also found that heat is not sensitive to crustal thickness. Low heat-flow values are found in the Kapuskasing region in Grenville province where the crust is thicker than 50 km, whereas high heat-flow values are obtained for the much thinner (36-40 km) Appalachian crust.

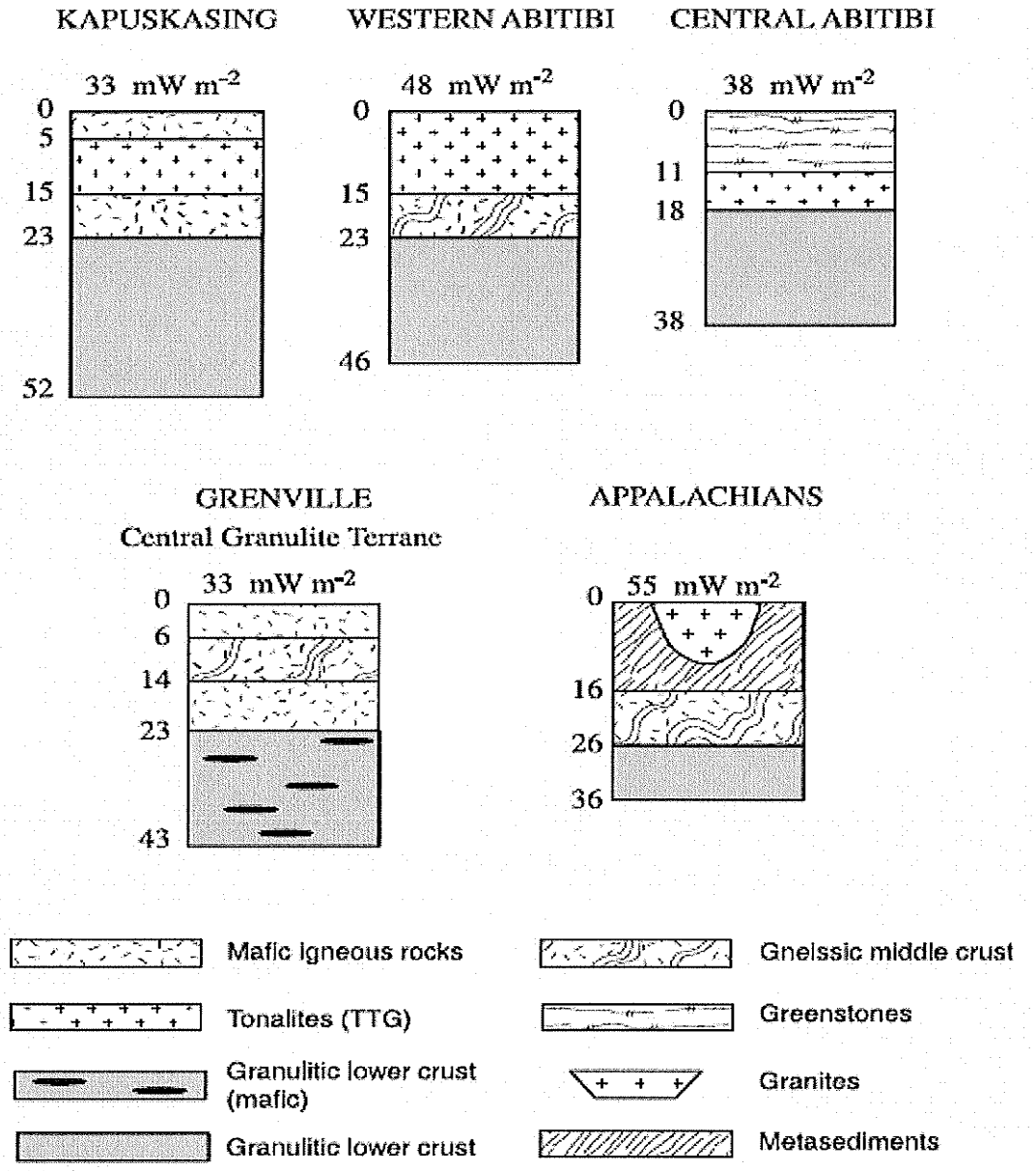

Figure 3.16. Diagram showing comparison between heat-flow and crustal sections inferred from seismic data in different regions: Kapuskasing Structure Zone (Boland and Ellis, 1989), western Abitibi (Boland and Ellis, 1989), central Abitibi (Green at al., 1990), central Granulite Terrane in the Grenville Province (Musacchio et al., 1997), and Appalachian Mountains in Quebec (Musacchio et al., 1997). TTG, trondhjemite-tonalite-granodiorite (modified from Mareschal et al., 2000).

3.8 Seismicity

Western Ontario and the surrounding area experience moderate to large earthquakes, despite being an intraplate region. Wallach et al. (1998) conducted seismic hazard assessments in this area. Figure 3.17 shows epicenters of all earthquakes known to have occurred in the region of western Lake Ontario, recorded since 1991. Most of the events in this area are less than $M = 4$; however, the Lockport and Attica earthquakes in western New York State are as big as $M \geq 5.0$, and the Leroy earthquake in northeastern Ohio was of magnitude $M_b = 5.0$. There was an earthquake of $M = 6.25$ at Temiscamingue, Quebec, and $M_L = 4.5$ in Georgian Bay.

Epicenters of four small earthquakes indicate a linear trend parallel and close to the magnetic signature of the Niagara-Pickering linear zone near the intersection of 45°N and 79°W (Figure 3.17). Other epicenters lie along or near the segment of the Niagara-Pickering linear zone which extends southward from the southern part of Lake Ontario to Lake Erie. Evidence of brittle faulting, repeated fault activity, and movement compatible with the current stress field, indicate that the Niagara-Pickering linear zone is tectonic active. The 1986 $M_b = 4.9$ Leroy earthquake and its focal mechanism are spatially associated with the Akron magnetic boundary, suggesting that the Akron magnetic boundary is a seismigenic source. Some epicenters of low-to moderate-magnitude earthquakes appear to be spatially related to the Georgian Bay linear zone, with the most evident being the north-northwest-oriented linear pattern adjacent to, and beneath Lake Ontario. In addition, there is the Hamilton – Lake Erie lineament, that is parallel and proximal to a possible fault and coincides with a linear array of small to moderate

earthquakes. All three lineaments have a higher frequency of seismicity than adjacent areas, thus the western Lake Ontario is a tectonically active area (Wallach et al., 1998).

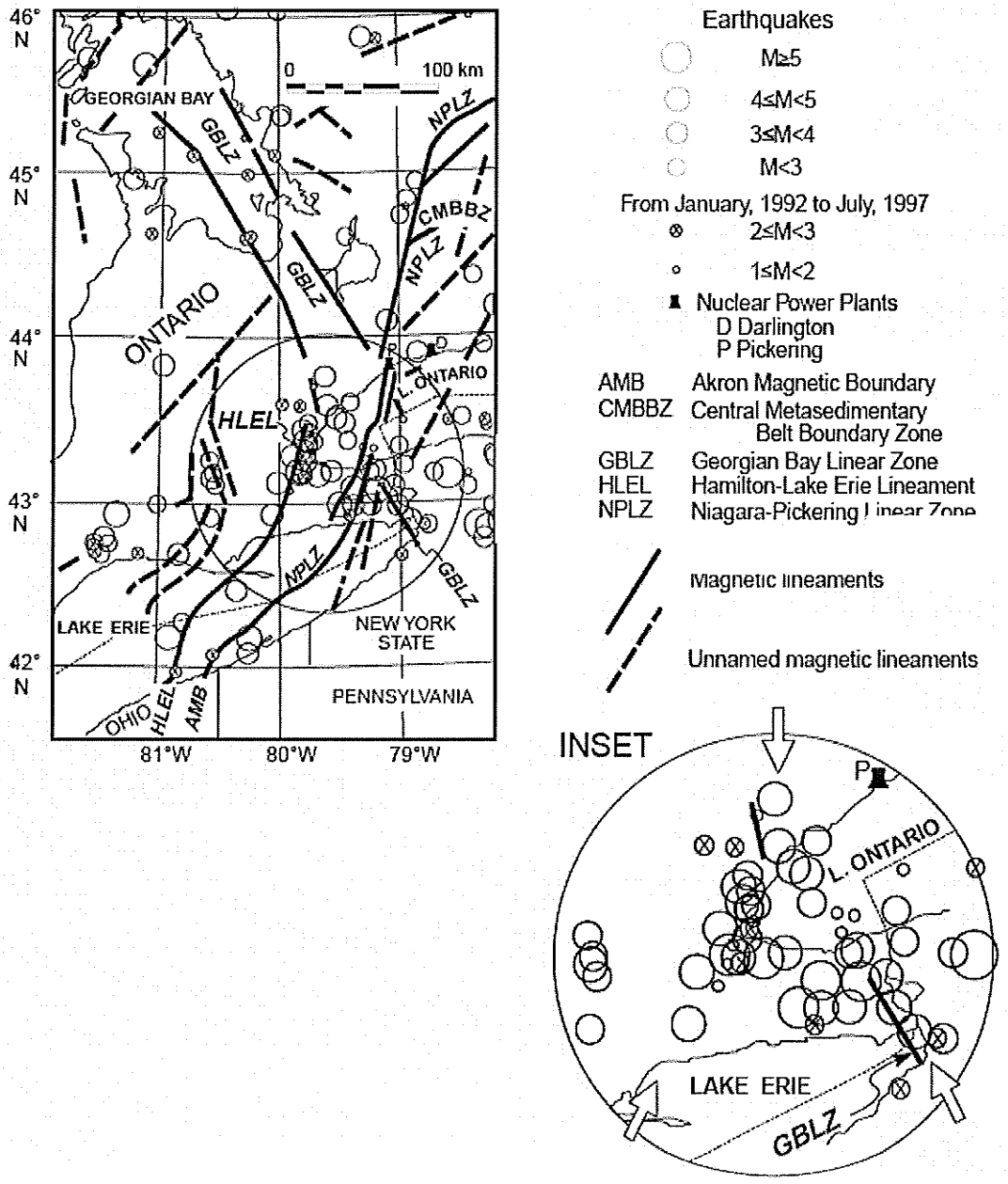

Figure 3.17. Maps showing seismicity in the western Lake Ontario – Lake Erie – Georgian Bay region, and its relationship to the total-field magnetic components of the Georgian Bay linear zone, Hamilton – Lake Erie lineament, and Niagara-Pickering linear zone. Inset shows two well-defined linear trends, indicated by the arrow (from Wallach et al., 1998).

Another area stands out as being concentrations of usually intense seismicity within the study area, the western Quebec seismic zone (Figure 3.18). In general, these active regional structures are features left over from previous continental rifting episodes. Adams and Basham (1991) speculated that the seismicity along the St. Lawrence rift system in Quebec might be connected southwest through Lakes Ontario and Erie and from there southwest through Ohio and Indiana to the New Madrid seismic zone (Ebel and Tuttle, 2002).

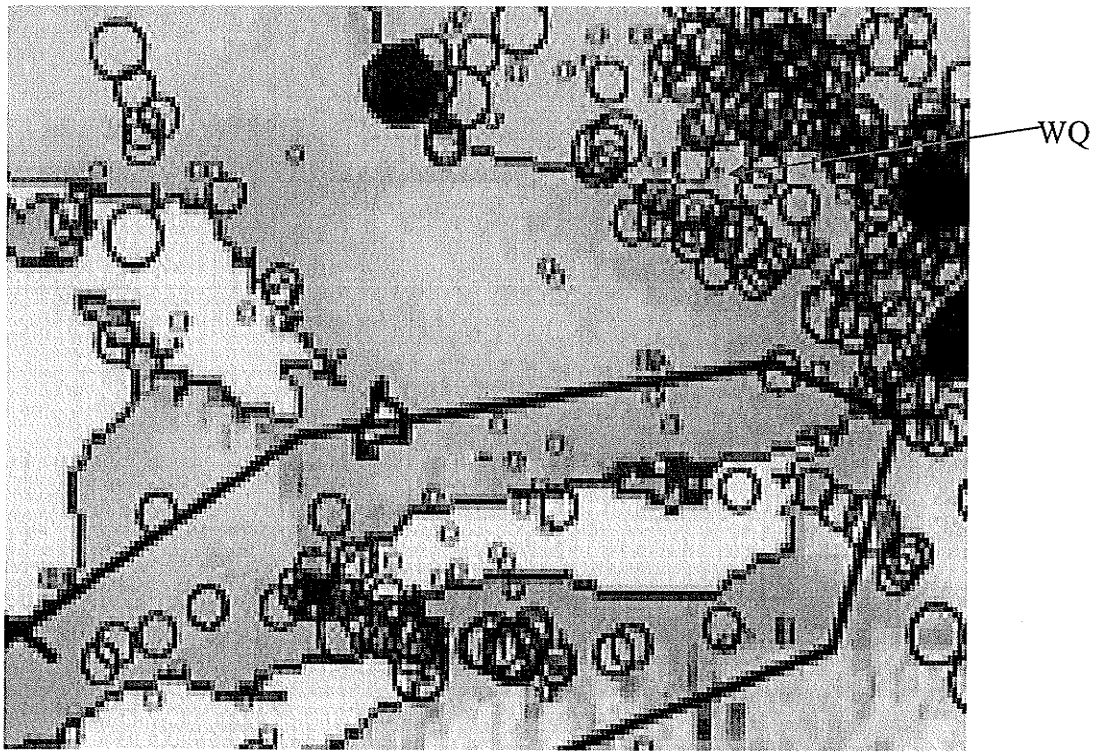

Figure 3.18. Seismicity of southern Ontario; WQ-the western Quebec seismic zone (modified from Ebel, J.E. and Tuttle, M., 2002).

Chapter 4

Methodology

4.1 Introduction

As discussed in Chapter 4, since the 1980's a variety of geophysical methods have been carried out to probe and reveal crustal and lithospheric structure in the Grenville orogen in southern Ontario, including controlled-source seismic methods, teleseismic, gravity, heat flow, magnetotelluric sounding and so on. Among all geophysical methods, controlled source seismic profiles and teleseismic techniques are the most important methods for investigating the Earth's architecture.

Although controlled source seismic reflection and refraction can provide high resolution images of Earth structures, the high cost of surveys limits the spatial coverage of the study area. In addition, due to the high frequency signals (~200 Hz), the methods are relatively more sensitive to small-scale crustal heterogeneities and may have insufficient signal penetration depth. In contrast, low-cost earthquake seismology can provide the widest range of information on the deep structures of the upper mantle (Rondenay 2000).

In this study, we focus on studying the 3-D structure of the crust and mantle in southern Ontario using teleseismic (earthquake) data recorded at three-component seismic broad-band stations. The receiver function technique is the basic method used for this research. This technique was developed in the 1970s (Langston, 1979), and has become a popular tool to estimate Moho depth, crustal velocity models and depths to

mantle discontinuities (e.g. Dueker and Sheehan, 1997, Zhu, 2000). To enhance the signal to noise ratio, receiver functions will be sorted and stacked into common conversion point bins (CCP stacking). A three-dimensional image of the Moho and upper-mantle structure is constructed by finding discontinuity depths within each column of bins. We also generate an image of the crust by using a scattering tomography technique based on the Born approximation. Hopefully a whole picture of a three dimensional structure image of study area will be achieved by combining these two results, along with information from previous work as well as local geology. The following three sections will discuss the three teleseismic methods used in detail.

4.2 Receiver Function

4.2.1 Introduction

When teleseismic P-waves travel through the Earth, part of the P-wave energy will convert into S-waves energy at various velocity discontinuities. Four converted phases are commonly observed: Ps, PpPs, and PpSs+PsPs (see Figure 4.1). Naming of these phases follows the conventions of Bath and Steffanson (1966), in which lowercase letters represent upgoing travel paths, while uppercase letters denote downgoing paths except for the first segment. For example, Pp, the direct P arrival, is a prominent pulse; Ps, P-to-S conversion, produced at a discontinuity (such as the Moho); PpPs, resulting from incoming P which remains P at a discontinuity, reflected downward as P at the Earth's free surface, and converted to upgoing S at a discontinuity; multiple PpSs+PsPs, observed from incoming P-wave, converted as P or S at a discontinuity, reflected

downward as P or S at the earth's free surface, and then reflected upwards as S at discontinuities.

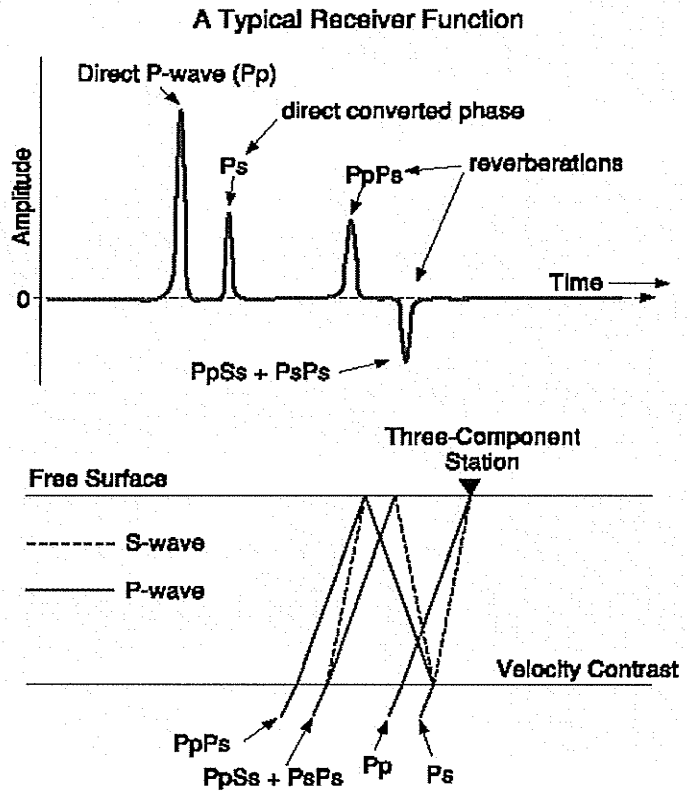

Figure 4.1. (top) A typical receiver function; (bottom) corresponding ray paths (modified from http://eqseis.geosc.psu.edu/~cammon/HTML/RftnDocs/rfref01.html) [accessed on Sep. 27, 2005].

Owing to the fact that S waves travel slower than P waves, the converted wave, i.e. Ps, and multiples, for instances, PpPs, PsSs+PsPs, arrive at stations within the P wave coda after the direct P wave (Figure 4.1 (top)). The crustal thickness or depth of discontinuity interfaces can be estimated by measuring the time separation between the direct P- arrival and converted phase (Ps) or multiples.

Receiver functions are generally obtained by deconvolution of the vertical component from the radial component in order to remove earthquake source and instrument response effects (Ammon 1991). This process can be done either in time

domain, for example, using the spiking deconvolution method (Kind et al, 1995) or in the frequency domain (Zhu 2000).

In this study, receiver functions are calculated by using the least squares simultaneous deconvolution method which was introduced by Gurrola et al. (1995). This method involves using several wave field-decomposed seismograms to estimate a single impulse response. The receiver function processing for this research was conducted in several steps. First, selected high quality seismograms are rotated from the three-component coordinate system (North-East-Vertical) into the ray coordinate system (Radial-Transverse-Vertical) in an attempt to separate the primary P wave, vertically polarized shear SV-wave and the horizontally polarized SH-waves, and then free surface transformation is performed to maximize the projection of the shear waves on the S component. Thirdly, binning is performed for a common-receiver gather in terms of slownesses and back azimuths of different events to enhance signal and reduce noise. And finally, deconvolution is performed to remove the effect of different source time functions.

4.2.2 Rotation

After the data have been inspected and selected, before obtaining the receiver function, the data must be rotated from the three-component recording system (N-E-Z) into the ray coordinate system (R-T-Z). The three-component seismograms recorded in North, East, and vertical directions (see Figure 4.2), are rotated into ray coordinate system, which includies the radial (R) component, which is in the direction towards the source, the transverse (T) component, which is perpendicular to the radial direction and horizontal, and the vertical (Z) direction. The reason for this is to isolate different types

of waves, such as the direct P wave, the vertically polarized shear SV-wave, and the horizontally polarized SH-wave.

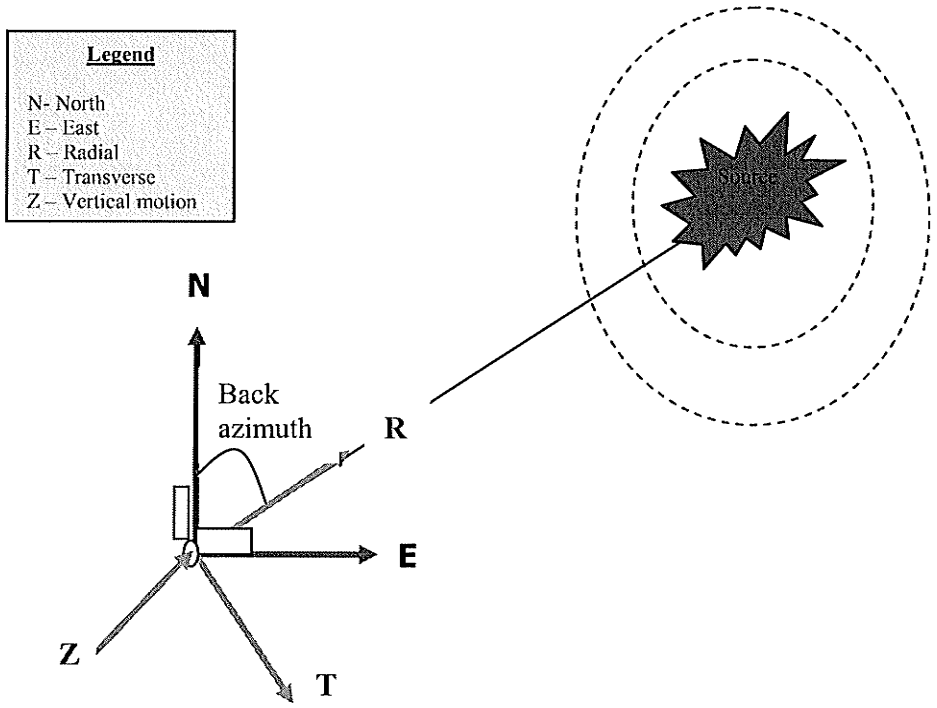

Figure 4.2. Three component recordings and ray coordinate system

In the case of flat lying and isotropic structure, the direct P-wave can be found in the Z and R components, the converted phase, Ps and multiples can be observed primarily in the R component, and no energy should be seen on the T component. However in reality, completely isotropic and laterally homogeneous structures do not exist, and weak energy may be observed on the T component. Hence, the T component usually is used to study dipping and anisotropic structures.

4.2.3 Free-surface Transformation

A more accurate receiver function may be obtained by applying the free surface transformation method developed by Kennett (1991). A relationship between the ground displacement vector $u = [U_R, U_T, U_Z]^T$ and the upgoing wave field $w=[P,SV,SH]^T$ was given by Kennett (1991) through a transfer matrix M by assuming the zero traction boundary condition and isotropic media. This explicit relation is:

$$\begin{pmatrix} P \\ SV \\ SH \end{pmatrix} = \begin{pmatrix} p\beta^2/\alpha & 0 & \dfrac{\beta^2 p^2 - 1/2}{\alpha q_\alpha} \\ \dfrac{1/2 - \beta^2 p^2}{\beta q_\beta} & 0 & p\beta \\ 0 & 1/2 & 0 \end{pmatrix} \begin{pmatrix} U_R \\ U_T \\ U_Z \end{pmatrix} \tag{4.1}$$

where p is the ray parameter, α, β are P-wave and S-wave velocities, respectively, $q_\alpha = \sqrt{\alpha^{-2} - p^2}$ and $q_\beta = \sqrt{\beta^{-2} - p^2}$.

Note that rotation and free surface transformation can be done in one matrix transformation, as described elsewhere (Kennett 1991).

4.2.4 Binning

Binning is performed once wave field decomposition is completed. Data from 29 stations cover a fairly broad range of back-azimuths and slownesses. For each station, events generated from nearby locations can be sorted and binned together in terms of the back azimuth, which defines the direction of the epicenter, and slowness, which is directly related to depth and distance of the earthquake, as shown in Figure 4.3(a).

Back azimuths are calculated according to spherical geometry, given the location (Latitude, Longitude and Elevation) of stations and events. A simplified geometry for this

calculation is shown in Figure 4.3(b). The slowness is calculated by using the Tau-P toolkit program, which uses a standard 1-D Earth model (IASP91), with the known distance (degrees) and source depth (km).

(a)

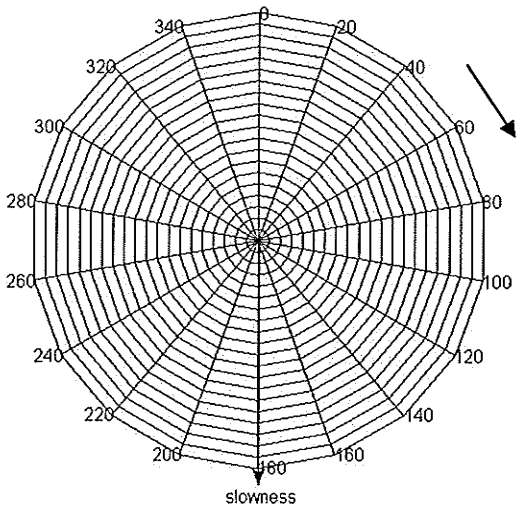

(b)

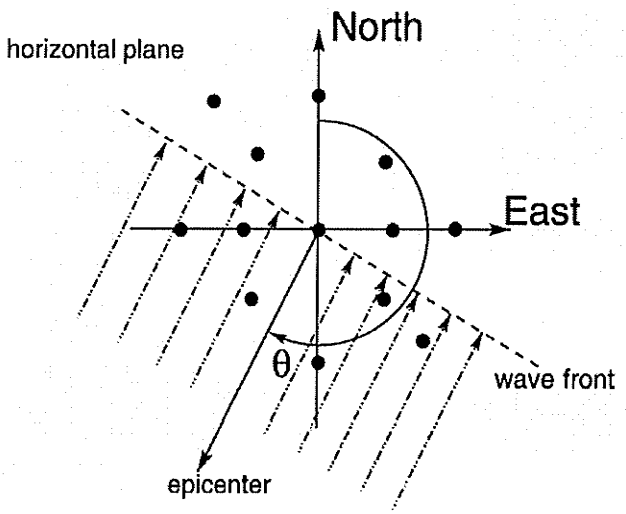

Figure 4.3. (a) Transformed data stacked in 20° back azimuth and 0.02 s/km (0.02x112 s/deg) slowness bins and ordered by back azimuth (numbers on the circle showing the value of backazimuth). (b) Geometry of the horizontal plane of an incident plane wave arriving with a back azimuth (θ; modified from Rost and Thomas 2002).

4.2.5 Deconvolution

Receiver functions are then obtained by the using least-squares simultaneous deconvolution method (Gurrola et al. 1995) which is based on using wave-field decomposed seismograms to estimate a single impulse response *g(t)*.

For all *N* seismograms in the frequency domain, it is given as

$$g(t) = F^{-1}[G(\omega)] = F^{-1}\left[\frac{\sum_n^N S_n(\omega)P_n^*(\omega)}{\sum_n^N P_n(\omega)P_n^*(\omega)+\delta}\right] \tag{4.2}$$

here, F^{-1} denotes inverse Fourier transformation; ω denotes angular frequency ($2\times\pi\times f$); $S_n(\omega)$ and $P_n(\omega)$ represent the S wave component (either SV or SH) and P wave component of motion from the *n*th seismogram, respectively; $P_n^*(\omega)$ is the complex conjugate of $P_n(\omega)$, and δ is a regularization parameter which adjusts the trade-off between model variation and data misfit. Golub et al. (1979) obtained δ by minimizing the general cross validation function *GCV(*δ*)*:

$$GCV(\delta) = \frac{\sum_n^N \sum_m^M (S_n(\omega_m) - P_n(\omega_m)G(\omega_m))^2}{\left(NM - \sum_m^M X(\omega_m)\right)^2} \tag{4.3}$$

where $$X(\omega) = \frac{\sum_n^N P_n(\omega)P_n^*(\omega)}{\sum_n^N P_n(\omega)P_n^*(\omega)+\delta} \tag{4.4}$$

and *M* is the number of frequencies represented in the discrete Fourier transform. This estimation for δ makes the model $G(\omega)$ more reasonably predict the data $S_n(\omega)$ (cf. Oldenburg 1981, Bostock 1998).

Instead of using the δ parameter, many authors use what is called the water-level parameter to avoid dividing by a zero or a very small number due to low values of

$|P(\omega)|^2$ in the above equation (e.g. Ammon 1991, Zhu 2000). As the consequence of water level is an attenuation of frequencies for which the vertical component has a small amplitude, as seen in Figure 4.4, the values used should be as small as possible. The appropriate water-level fraction is determined by the nature of the vertical component seismogram and signal to noise ratio. Typical values are in the range of 0.0001 to 0.1; a water-level value of 1.0 produces a scaled version of the cross-correlation of the horizontal and vertical seismograms rather than the desired deconvolution. Choosing acceptable noise levels produced by water-level in the corresponding receiver function is important (Ammon 1991).

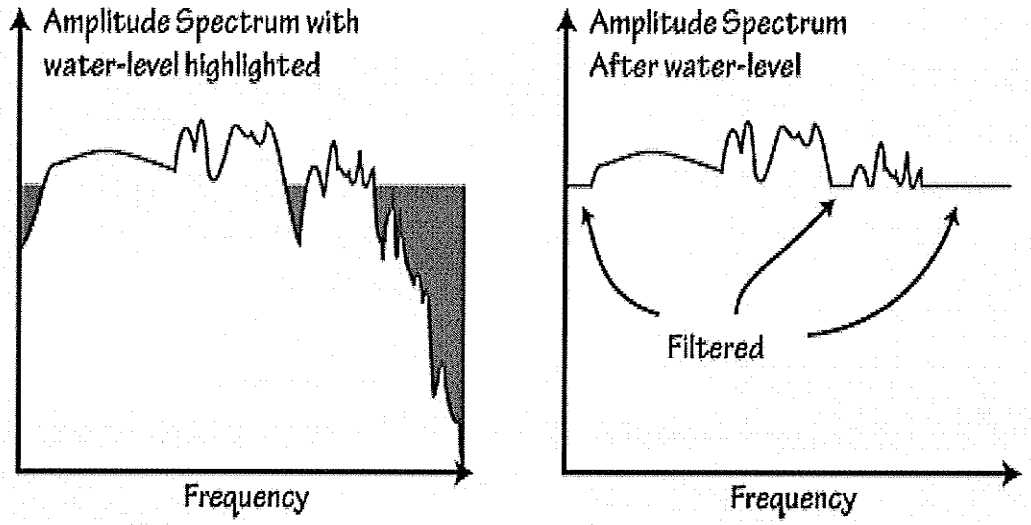

Figure 4.4. Effects of water level in the receiver function (modified from http://eqseis.geosc.psu.edu/~cammon/HTML/RftnDocs/rfref01.html) [accessed on Sep. 27, 2005].

Whereas Gurrola 's filter is consistent with application of linear inverse theory to a linear problem and allows automated recovery of correct damping, while the water level has to be hand-tuned. Gurrola 's filter outperforms the operation of replacing small values

of the amplitude spectrum used in water-level deconvolution (Knapmeyer and Harjes 2000). More detailed information on receiver function computation may be found elsewhere (Langston 1979, Owens et al 1984).

4.3 Common Conversion Point (CCP) Stacking

4.3.1 Introduction

Structural investigation using a single receiver function has been done since the 1970s' (e.g., Langston, 1979). However, in real situations, identifying Ps conversions and multiples from the Moho and other interfaces, and measuring their arrival times on a single receiver function trace can be very difficult due to background noise, scattering from crustal heterogeneities, and the low amplitudes of some converted arrivals. In addition, only local and one-dimensional images can be obtained from solitary stations.

To image three dimensional structure of the study area using receiver functions, and to improve the signal-to-noise ratio, CCP stacking is used in this study. Stacking techniques were developed in the 1960's to help to lower the detection threshold of global earthquakes and nuclear explosions and improve the resolution of the fine structure of the Earth's interior (Rost and Thomas 2002). The direct benefit of stacking compared to a single seismic recording is the improvement of the signal-to-noise ratio (SNR). A good approximation of the improvement of the SNR in terms of amplitude of the array, S, in comparison with the SNR of the single array station, s, is $S = s\sqrt{M}$ for M traces which contributed to the stack. Stacking is a common method used to refine velocity models of the Earth's interior (e.g. Karason and Van der Hilst 2001), to detect small-scale structures in the Earth's mantle (e.g., Castle and Creager 1999, Kruger et al

2001) and crustal and mantle boundaries (Zhu 2000) and to investigate heterogeneities in the Earth (e.g., Vidale and Earle 2000).

CCP receiver function stacking has been recently developed for investigation of 3-D structure, and has been successfully applied to data from the Yellowstone hot spot track (Dueker and Sheehan 1997), the slab beneath western Crete (Knapmeyer and Harjes 2000), the San Andreas Fault (Zhu 2002), Japan (Ham et al. 2004) and the Great Basin, Colorado (Gilbert and Sheehan, 2004).

CCP stacking borrows the ideas of Common Middle Point (CMP) stacking and migration in exploration seismology, though instead of reflected waves and two-way-traveltime we are dealing with transmitted waves and one-way-traveltime. It focuses on mapping the location where the P-to-S conversion took place from multiple SV-RF waveforms and a pre-existing basic velocity model.

In this section, the principle and implementation of the receiver function CCP stacking algorithm are described, the geometries are explained in detail, and finally we show how to generate 3-D images using this method.

4.3.2 Travel-time Calculation

For a single, horizontal, homogeneous layer (Figure 4.5), assuming the incident P wave to be a plane wave (which is acceptable in receiver function studies when the epicentral distance is greater than 30°), the travel time difference between the direct P arrival and Ps conversion arrival is given as:

$$\Delta t = T_s + (-\delta t_s + \delta t_p) - T_p \tag{4.6}$$

where T_s and T_p are the travel times along the paths above the discontinuity, and $\delta t_p, \delta t_s$ are corrections to the P and S travel times to account for their different pierce points at the interface, using the point immediately below the station as a reference.

Assuming the ray parameters for the direct P wave and Ps conversion are the same, according to geometry, we can derive this delay time in terms of thickness of interface, Z, ray parameter p_x as follows:

$$\frac{\delta l}{r} = \sin\theta_0 = \alpha_0 p_x \tag{4.7}$$

$$\delta t = \frac{\delta l}{\alpha_0} = r p_x, \qquad \text{where } p_x = \frac{\sin\theta}{c} \tag{4.8}$$

$$\Delta t = \frac{l}{c} = \frac{\sqrt{r^2 + z^2}}{c} \qquad (c : \alpha \text{ or } \beta) \tag{4.9}$$

$$t = \Delta t - \delta t = \frac{\sqrt{r^2 + z^2}}{c} - r p_x = r\left(\frac{\sqrt{1 + z^2/r^2}}{c} - p_x\right) \tag{4.10}$$

$$\text{now} \quad \frac{r}{z} = \tan\theta, \quad \text{so} \quad \frac{z}{r} = \cot\theta = \frac{\sqrt{1-\sin^2\theta}}{\sin\theta} = \frac{\sqrt{1 - c^2 p_x^2}}{c p_x} \tag{4.11}$$

$$1 + z^2/r^2 = \frac{1}{c^2 p_x^2} \tag{4.12}$$

$$\text{So, } t = r p_x \left(\frac{1}{c^2 p_x^2} - 1\right) \tag{4.13}$$

$$\text{and since } \quad r = z\tan\theta = \frac{z\sin\theta}{\sqrt{1-\sin^2\theta}} = \frac{z c p_x}{\sqrt{1 - c^2 p_x^2}} \tag{4.14}$$

$$t = \frac{z c p_x^2}{\sqrt{1 - c^2 p_x^2}} \left(\frac{1 - c^2 p_x^2}{c^2 p_x^2}\right) = z\sqrt{\frac{1}{c^2} - p_x^2} = z p_z \tag{4.15}$$

$$t_p = z\sqrt{1/\alpha^2 - p_x^2}; \qquad t_s = z\sqrt{1/\beta^2 - p_x^2} \tag{4.16}$$

$$t_s - t_p - = z(p_z^{(\beta)} - p_z^{(\alpha)}) \tag{4.17}$$

$$\Delta t(Ps) = t_s - t_p = Z(\sqrt{1/\beta^2 - p_x^2} - \sqrt{1/\alpha^2 - p_x^2}) \quad (4.18)$$

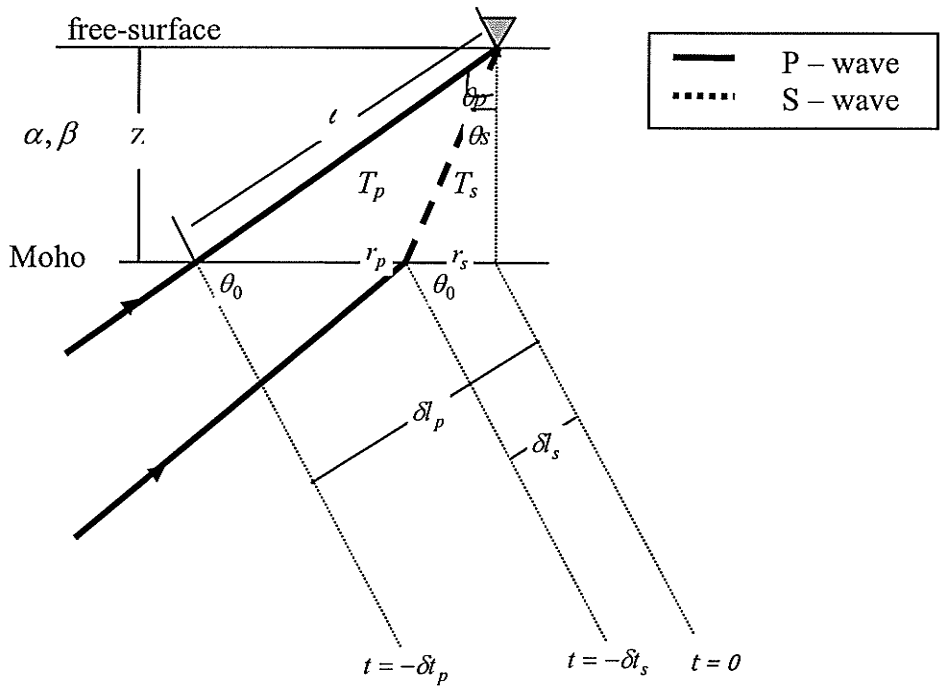

Figure 4.5. The ray paths of direct P and Ps arrivals for a single, horizontal and homogeneous layer. Z is the thickness of the layer, Ts and Tp are the travel times of the P and S arrival above the interface, $\delta t_p, \delta t_s$ are the P and S travel times along the path before reaching the interface.

Similarly, delay travel times for multiples are defined by equation (4.19-4.21):

$$\Delta t(PpPs) = Z(\sqrt{1/\beta^2 - p_x^2} + \sqrt{1/\alpha^2 - p_x^2}) \quad (4.19)$$

$$\Delta t(PpSs/PsPs) = 2Z(\sqrt{1/\beta^2 - p_x^2}) \quad (4.20)$$

$$\Delta t(PsSs) = Z(3\sqrt{1/\beta^2 - p_x^2} + \sqrt{1/\alpha^2 - p_x^2}) \quad (4.21)$$

For multiple layers (see Figure 4.6), the equation for the travel-time distance between the direct P arrival and Ps conversion arrival can be derived as

$$\Delta t = t_s - t_p = \sum_{i=1}^{N} Z_i(\sqrt{1/\beta_i^2 - p_x^2} - \sqrt{1/\alpha_i^2 - p_x^2}) \quad (4.22)$$

where subscript 'i' denotes the number of the layer from the free-surface to the bottom, Z_i represents the thickness of a layer, and α_i, β_i are P and S wave velocity for the ith layer, respectively (Frederiksen and Bostock, 2000).

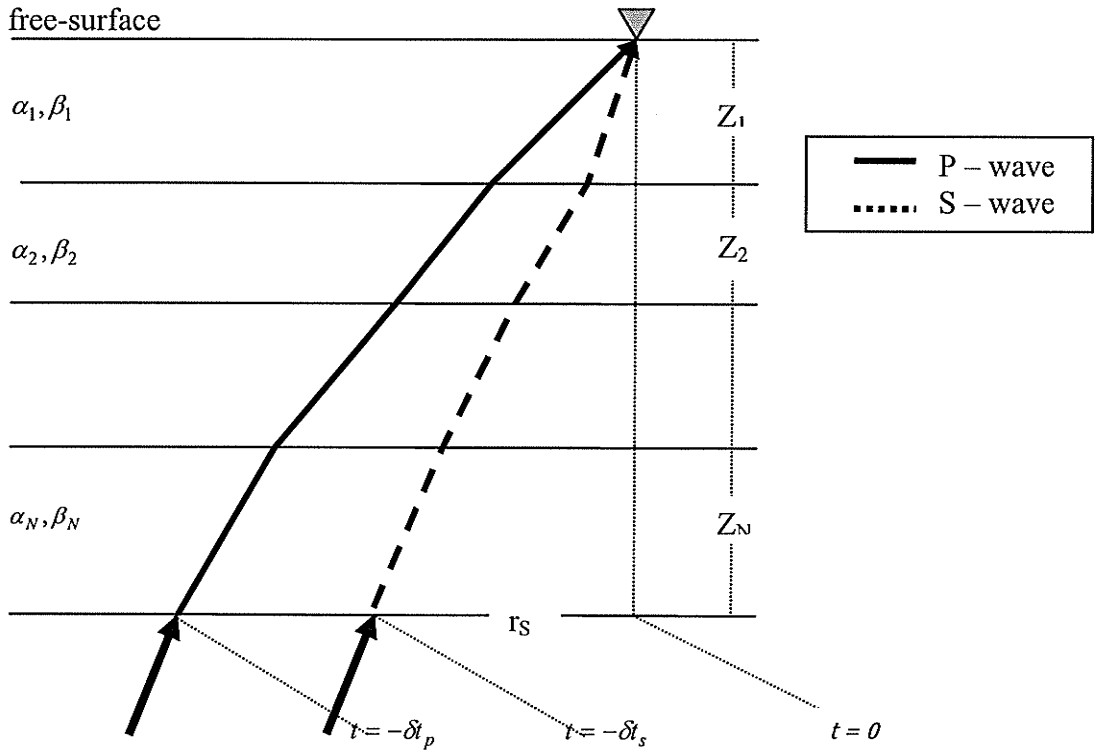

Figure 4.6. The ray paths of direct P and Ps arrival for the case of multiple layers. Subscript 'i' denotes the number of the layer, Z_i is the thickness of a interface, and α_i, β_i are the P and S velocity for a specific layer.

4.3.3 Migration

From equation (4.18) above, it is clear that the thickness (Z) of layers is a function of the travel-time difference between the P wave and P-to-S conversion ($\Delta t(Ps)$), the ray

parameter, p_x, as well as a 1-D velocity base model (α,β, the base model used in this study will be discussed in chapter 6). The explicit relationship is:

$$Z = \sum_{i=1}^{N} Z_i = \Delta t / \sum_{i=1}^{N} (\sqrt{1/\beta_i^2 - p_x^2} - \sqrt{1/\alpha_i^2 - p_x^2}) \tag{4.23}$$

The horizontal distance between the conversion point and the instrument (r_S) can be also derived from the geometry as.

$$r_S = \sum_{i=1}^{N} z_i \tan\theta_s^i = \sum_{i=1}^{N} \frac{z_i \beta_i p_x}{\sqrt{1-\beta_i^2 p_x^2}} \tag{4.24}$$

Given a ray-parameter calculated using the tau-p method and a pre-existing 1-D velocity model, a Time-to-Depth (T-to-D) table showing the travel-time difference between P and Ps as well as the P and S ray-path can be easily computed by programming. For any conversion depth (z), the differential travel-time between P and P-to-S converted phase ($\Delta t(Ps)$) and horizontal distance (r_S) of the conversion point in the crust/mantle from the instrument are derived from this table.

Since the S component contains the clearest observation of P-to-S conversion and multiples, RF migration is usually applied to the SV seismograms given a one dimensional base velocity model.

4.3.4 Stacking

Figure 4.7 - 4.9 are schematic diagrams showing how the 3-D CCP stacking method is designed. The study volume is divided into 3-D cells with varied size bins in an X-Y-Z (East-North-Elevation) coordinate system with the origin in the southwest corner. Based on a T-to-D table, the East (X) and North (Y) coordinates can be derived from r_S together with the back azimuth using simple triangle relations.

$$x' = r_s \cos(\theta), \quad y' = r_s \sin(\theta) \tag{4.25}$$

Note that this location should be corrected by adding the offset of the receivers (x_0, y_0, z_0) as

$$x = x_0 + x', \quad y = y_0 + y' \tag{4.26}$$

The location of the grid cells in the crust/mantle where P-SV conversion took place is determined by the coordinates of this point. Assuming every amplitude of the SV-RF waveform is produced by a primary P-to-S conversion at the calculated depth and amplitude, reflecting the impedance contrast at that conversion point, all points of all SV-RF waveforms which took place in the same bin are stacked to produce a cell of the 3-D structure image.

The resolution of the image depends on the density of spatial sampling of the available seismograms and quality of signal of events. There is a trade-off between the resolution of models and stacking fold number (the number of contributing the same common conversion point) which is determined mostly by the size of cells. For this research, the coverage of study area is about $(600 \times 500 \times 420)$ km, containing 29 stations, with a total of 398 events data. So grid cells of $60 \times 50 \times 3$ km would be a reasonable size, as I discuss in detail in the following chapter.

In summary, several steps are taken for migration and stacking: (1) generating a time-to-depth conversion table; (2) dividing the 3-D volume of study area into cells with varied bin size; (3) determining conversion points according to this T-to-D table; (4) stacking all amplitudes of SV-RF waveforms which contribute to the same bins; (5) constructing a 3-D image of normalized stacking amplitude by dividing by stacking fold number.

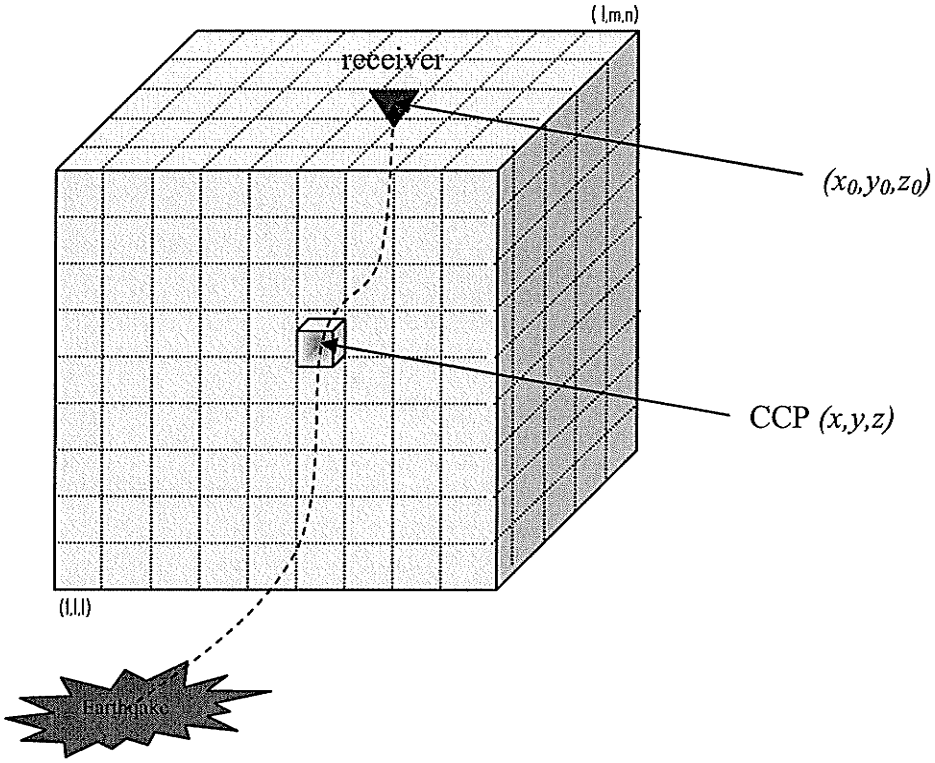

Figure 4.7. schematic diagram for 3-D common conversion point (CCP) binning.

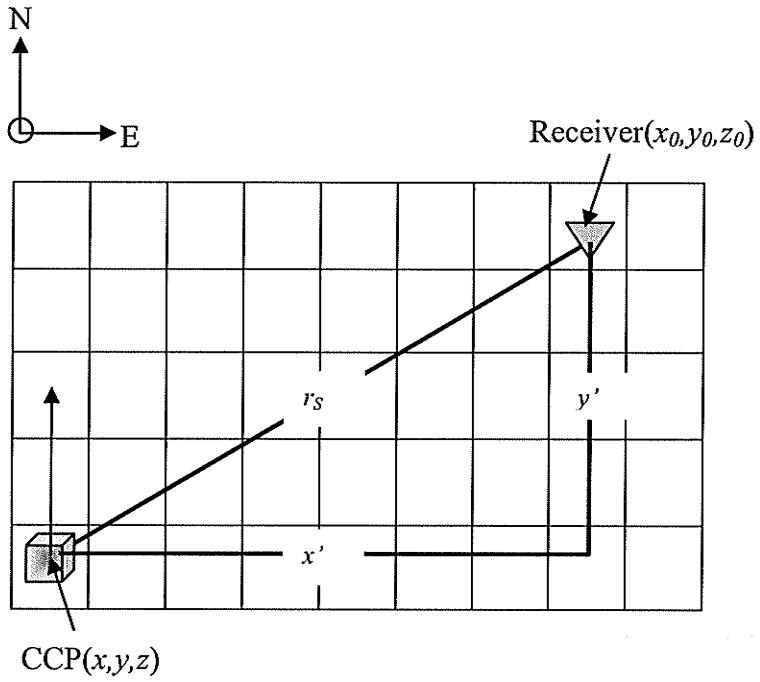

Figure 4.8. Plan view of 3-D CCP binning scheme.

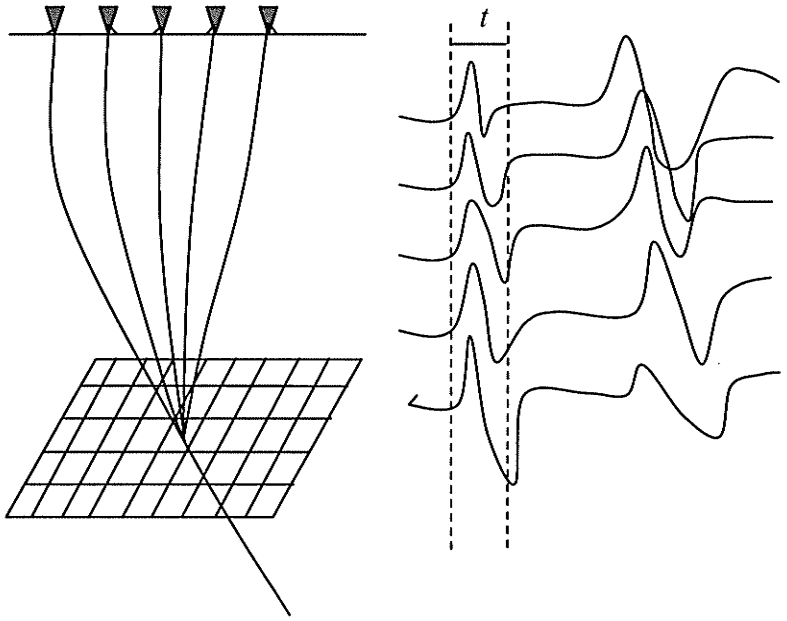

Figure 4.9. Schematic diagram for CCP binning (Modified from Rost and Thomas, 2002).

4.4 Scattering Tomography

4.4.1 Introduction

The receiver function CCP stacking described above is based on ray theory. We assume that when an interface is curved, we only have to select a portion sufficiently small that it can be considered as planar. However, such a simplification is not always possible, for example, when the radius of curvature of an interface is less than a few wavelengths, or the reflector is terminated by a fault, pinch out, unconformity and so on. In such cases, Snell's law is no longer adequate because, given that the seismic wavelengths are often 2 km or more, many geological features give rise to diffraction. Figure 4.10 shows diffracted wavefronts for a faulted bed situation; from this figure, it is clear that at the fault point, the energy is diffracted rather than reflected or refracted.

Huygens' principle can be used to explain scattering phenomena. Based on Huygens' principle, any point of a wavefront may be treated as a source point which generates a secondary wave. Under this assumption, a reflector is constructed of a series of point scatters, each producing a diffraction hyperbola (see Figure 4.11). Huygens' principle is applicable to any wave propagation problem, and provides a simple explanation for the behavior of scatted waves in a qualitative sense, but it does not tell anything about what amplitude the secondary waves should have or how their "radiation pattern" might vary as a function of ray angle in a quantitative sense.

To date, there are many mathematical approaches applied to study scattered waves, including Kirchoff-Helmholtz integration (Neuberg and Pointer, 1995); the finite-element method (Lysmer and Drake 1972), the finite difference method (Fehler and Aki 1978); the integral representation method (Van der Hijden and Neerhoff 1984); generalized ray theory (Achenbach et al. 1982); the Born approximation (Wu and Aki, 1985) and so on. Most of the theoretical studies on elastic wave scattering assume the incidence of plane waves and each method has its own advantages and disadvantages. In this study, the first order Born approximation theory is introduced to account for the effects of scattering and to model observed coda characteristics resulting from receiver-side structure of the Earth.

In the first-order Born approximation, the coda wave field is formulated in terms of scattering by a primary wavelet interacting with inhomogeneities; the equation of motion is expressed in the unperturbed medium except at the scattering point; and the body force equivalent to the scattering source is presented in a convenient form involving

the perturbations in wave velocities and the gradient of density perturbations (Aki and Richards 1980, Wu and Aki 1985).

The advantage of the first order point scattering Born approximation over other techniques lies in its simplicity and fast computation speed owing to its linearized inversion problem. It is accurate for weak scattering and at low frequency, i.e., Rayleigh scattering, when the wavelength is much larger than the size of inhomogeneity. To study more complex models with receiver functions, and to fill the gap between the high resolution images from controlled source seismic profiles and the low resolution but deeper lithospheric images from receiver function CCP stacking, scattering tomography (Frederiksen and Revenaugh, 2004) is applied for this research. Scattering tomography on receiver functions is similar to a seismic migration technique, being designed to properly move seismic trace energy (e.g., P-to-S scattered amplitudes in receiver function) to their true subsurface positions in the time or depth domain.

Several authors have attempted to image structure of Earth based on seismic scattering using teleseismic waves. For example, Revenaugh (1995b) retrieves scatterers using stochastic Kirchhoff migration in the lithosphere beneath the San Jacinto fault region (southern California); Mohan and Rai (1992) use the semblance method to image a strong scatterer in the lower crust and upper mantle west of the Gauribidanaur (India) array; Frederiksen and Revenaugh (2004) image lithospheric structure beneath southern California; Poppeliers and Pavlis (2003) construct a 3-D structure using distorted Born theory in northwest Colorado; and Rondenay et al (2001) applied the Born approximation and a generalized Radon transform method to the Cascadia 1993 data set.

Mathematical methods and seismic data processing techniques vary between different authors according to their specific problems. For instance, migration generally requires closed-spaced receivers. Poppeliers and Pavlis (2003) use interpolation to compensate for sparse data. Scattering tomography uses a formal inverse instead of a migration to compensate sparse density data. However, the basic ideas are similar to exploration seismology, placing grids into the region of interest and treating them as the secondary source. For each cell, the travel time is calculated based on ray theory, geometry and other previously known information. The traces are then back shifted with these travel times for each cell. The amplitude of traces at the same cells are stacked and normalized, and mapped onto the corresponding cells (Rost and Thomas 2002).

In this section, besides explaining first order Born approximation theory, the geometry of a point scatter is given to help for calculation of travel times and amplitude of scattered waves; and forward modeling and inversion methods are introduced to explain how to image subsurface structure using teleseismic data based on the Born approximation.

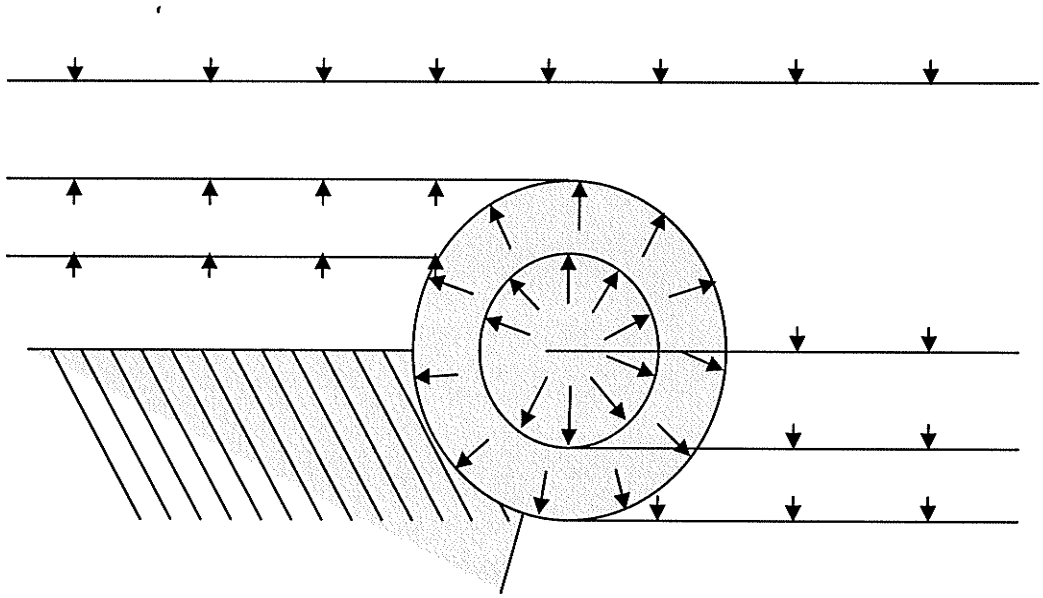

Figure 4.10 Sketch showing diffracted wavefronts for a faulted bed (after Sheriff and Geldart, 1982).

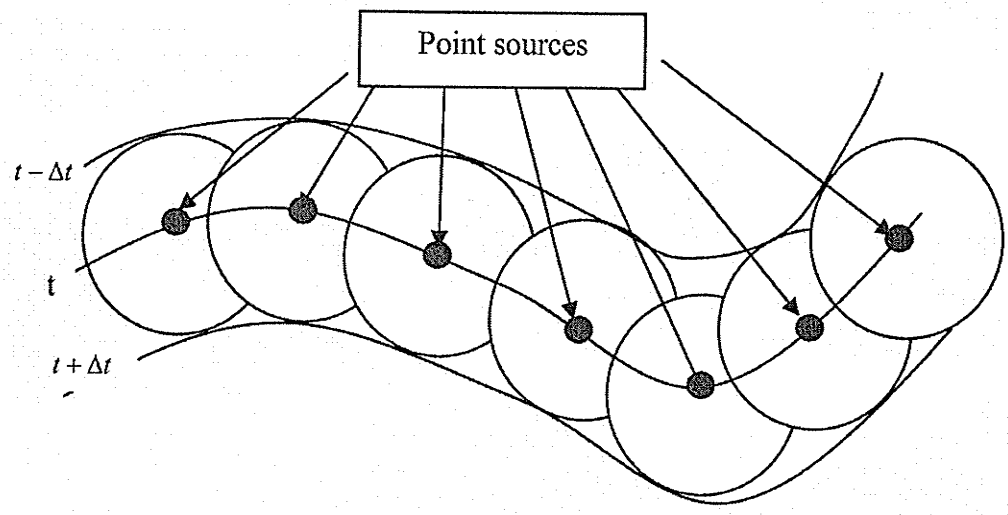

Figure 4.11 Sketch showing how Huygens' principle reconstructs the wavefronts (after Lowrie 1997).

4.4.2 First Order Born Scattering Theory

In weak scattering, the short scale-length perturbations of velocity and density compared with the mean values are small, typically a few percent or less. Therefore, it is possible to represent the total wave field as the sum of the primary wave field (waves that would exist in the medium without any perturbations) and the scattered wave field (waves generated by the primary wave interaction with perturbations). Multiply scattered waves are neglected. The wavefield is defined:

$$u_i = u_i^0 + u_i^s \tag{4.27}$$

where u_i^0 is the ith component of incident, unperturbed wavefield in the absence of the scatterers, and u_i^s is ith the component of the secondary, scattered wavefield that is generated at "sources" corresponding to the heterogeneities through scattering of the background wavefield.

Based on the above assumption, Aki and Richards (1980) derived an expression for scattered wave field as follows. Start off with the wave equation,

$$\rho \ddot{u}_i = \partial_i(\lambda \partial_k u_k) + \partial_j[\mu(\partial_i u_j + \partial_j u_i)] \tag{4.28}$$

where u is the displacement vector, ρ is density, λ and μ are the Lame parameters.

For a finite volume of weak inhomgeneity, the partial derivatives on the wavefield will ve applied to Lame's moduli λ and μ, and density ρ in the form:

$$\rho = \rho_0 + \delta\rho$$

$$\lambda = \lambda_0 + \delta\lambda$$

$$\mu = \mu_0 + \delta\mu \tag{4.29}$$

where ρ_0, λ_0 and μ_0 are density and Lame parameters for the unperturbed medium (base model), and $\delta\rho$, $\delta\lambda$ and $\delta\mu$ are for the perturbations ($\delta\lambda << \lambda$, $\delta\mu << \mu$, $\delta\rho << \rho$).

Substituting (4.29) into (4.28) one obtain

$$(\rho_0 + \delta\rho)\ddot{u}_i = \partial_i[(\lambda_0 + \delta\lambda)\partial_k u_k] + \partial_j[(\mu 0 + \delta\mu)(\partial_i u_j + \partial_j u_i)] \quad (4.30)$$

Since the spatial derivatives of ρ_0, λ_0 and μ_0 are zero, the equation of motion becomes

$$\rho_0\ddot{u}_i - (\lambda_0 + \mu_0)\partial_i(\nabla \cdot u) - \mu_0\nabla^2 u_i = -\delta\rho\ddot{u}_i + (\delta\lambda + \delta\mu)\partial_i(\nabla \cdot u) + \quad (4.31)$$

$$\delta\mu\nabla^2 u_i + (\partial_i\delta\lambda)(\nabla \cdot u) + (\partial_j\delta\mu)(\partial_i u_j + \partial_j u_i)$$

where we have used $\partial_k u_k = \nabla \cdot u$ and $\partial_j\partial_j = \nabla^2$.

As u^0 is an unperturbed wavefield, it obeys the wave equation itself.

$$\rho_0\ddot{u}_i^0 - (\lambda_0 + \mu_0)\partial_i(\nabla \cdot u_0) - \mu_0\nabla^2 u_i^0 = 0 \quad (4.32)$$

In practice, u^0 may be found using ray theory. If we consider only single scattering and neglect any higher order scattering, one obtains.

$$\rho_0\ddot{u}_i^s - (\lambda_0 + u_0)\partial_i(\nabla \cdot u_s) - \mu_0\nabla^2 u_i^s = Q_i \quad (4.33)$$

$$Q_i = -\delta\rho\ddot{u}_i^0 + (\delta\lambda + \delta\mu)\partial_i^0(\nabla \cdot u_0) + \delta u\nabla^2 u_i^0 + (\partial_i\delta\lambda)(\nabla \cdot u^0) + (\partial_i\delta\mu)(\partial_i u_j^0 + \partial_i u_i^0) \quad (4.34)$$

Equation (4.33) is the equation of motion for the scattered wavefield u^s in a homogeneous isotropic medium with body force Q that results from the local interaction of the heterogeneity with the primary wavefield u^0.

4.4.3 A point scatterer

4.4.3.1 Theory

The properties of the scattered wave field are determined by the wavelength of primary waves, $\lambda(=2\pi/k$, where k is the wavenumber); and the scale length of heterogeneity, a. When $ka << 1$, the heterogeneity appears as essentially a point scatterer (Rayleigh scattering). From the equivalent point source in the Rayleigh domain, Wu and Aki (1985) derived the scattered P-wave and S-wave in spherical coordinates.

By replacing $\delta\lambda$ and $\delta\mu$ to first order by $\delta\alpha, \delta\beta$ and $\delta\rho$ as

$$\delta\lambda = 2\rho_0(\alpha_0\delta\alpha - 2\beta_0\delta\beta) + \delta\rho(\alpha_0^2 - 2\beta_0^2) \tag{4.35}$$

$$\delta\mu = 2\rho_0\beta_0\delta\beta + \beta_0^2\delta\rho \tag{4.36}$$

we obtain the expression for scattered displacement amplitude for incident P-wave and S-wave at unit distance from the scatterers and frequency in terms of velocities and density.

In the case of plane P-wave incidence.

$${}^{P}u^{P} = \frac{\hat{\Gamma}V\omega^2}{4\pi\alpha_0^2}\left[\frac{\delta\rho}{\rho_0}(1-2\frac{\beta_0^2}{\alpha_0^2}) - \frac{2}{\alpha_0}(\delta\alpha - \frac{\beta_0}{\alpha_0}\delta\beta) + \frac{\gamma_n\delta\rho}{\rho 0} - \frac{2\gamma_n^2}{\alpha_0^2}(2\beta_0\delta\beta + \beta_0^2\frac{\delta\rho}{\rho_0})\right] \tag{4.37}$$

$${}^{P}u^{S} = \frac{\hat{\Theta}V\omega^2}{4\pi\beta_0^2}\left[\frac{\delta\rho}{\rho_0}\sqrt{1-\gamma_n^2} + \frac{2}{\alpha_0\beta_0}(2\rho_0\delta\beta + \beta_0\delta\rho)\gamma_n\sqrt{1-\gamma_n^2}\right] \tag{4.38}$$

In the case of plane S-wave incidence,

$${}^{S}u^{P} = \frac{\hat{\Gamma}V\omega^2}{4\pi\alpha_0^2}\gamma_p\left[\frac{\delta\rho}{\rho_0} - \frac{2\gamma_n}{\alpha_0}(2\delta\beta + \beta_0\frac{\delta\rho}{\rho_0})\right] \tag{4.39}$$

$${}^{S}u^{S} = \frac{V\omega^2}{4\pi\beta_0^2}\left[(\hat{\mathrm{P}} - \gamma_p\hat{\Gamma})\frac{\delta\rho}{\rho_0} + (2\hat{\Gamma}\gamma_n\gamma_p - \hat{\mathrm{N}}\gamma_p - \hat{\mathrm{P}}\gamma_n)(\frac{2\delta\beta}{\beta_0} + \frac{\delta\rho}{\rho_0})\right] \tag{4.40}$$

where $\hat{\mathrm{N}}, \hat{\Gamma}$ and $\hat{\mathrm{P}}$, are unit vectors in the incidence, departure and incident polarization directions, respectively (Figure 4.12), $\gamma_n = \hat{\Gamma}\cdot\hat{\mathrm{N}}$ and $\gamma_p = \hat{\Gamma}\cdot\hat{\mathrm{P}}$, and $\hat{\Theta} = (\hat{\mathrm{N}} - \gamma_n\hat{\Gamma})/\sqrt{1-\gamma_n^2}$ is in the latitudinal direction, V represents the volume of the inhomogeneity, and the physical-property perturbations are taken to be averages over the volume V. The frequency dependence ω^2 is the same for all phases (Frederiksen and Revenaugh 2004).

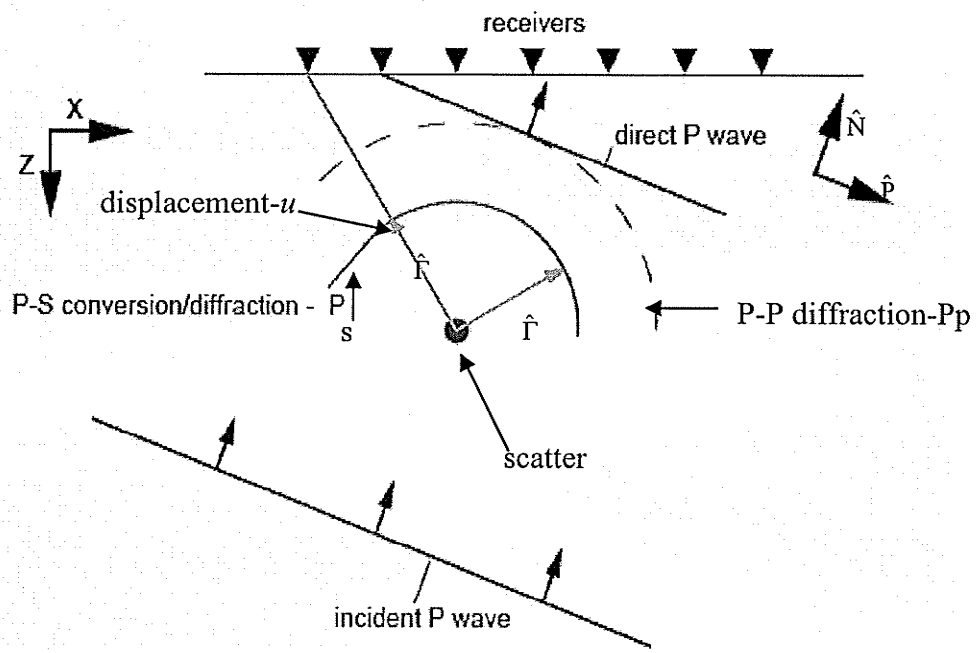

Figure 4.12 Sketch showing the coordinate system used for calculation of amplitude of scattered wave. The phases generated by a point scatter for a plane P-wave incidence are also given.

4.4.3.2 Geometry

The geometries of the backward scattered phases and forward scattered phases produced by a single point scatter are given in Figure 4.13. Consider the P-wave as a plane wave with a known incidence angle. Four phases: Pp∗p, Pp∗s, Ps∗p and Ps∗s could potentially be generated by backward scattering as shown in Figure 4.13a. For forward scattering, there are two possible scattered phases generated: P∗p, P∗s as shown in Figure 4.13b; The symbol, ∗ represents the scatterer, for example, Ps∗s represents an incident teleseismic P wave which converts to a downgoing S wave at the free surface, encounters a scatterer, and is back scattered to the receiver as a S wave (Frederiksen and Revenaugh, 2004).

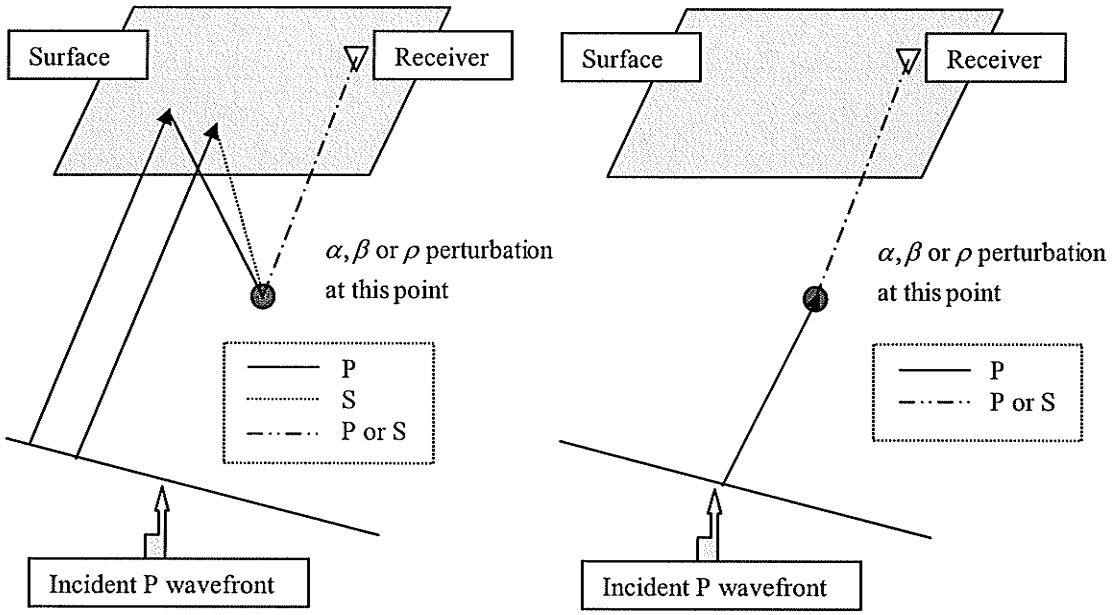

Figure 4.13. Geometry of scattered phases produced by a single point scatter (a) backward scattered phases (b) forward scattered phases (modified from Frederiksen and Revenaugh, 2004).

4.4.3.3 Travel Time

The travel time for a point scatter is calculated based on the geometry of scattered phases and ray theory. Figure 4.14 shows a cross section of scattered phase Ps*p, which is used as an example. The total travel time of a point scatter from a source to a receiver can be given as the sum of the two parts (see Figure 4.14):

$$t_{S-R} = t_{S-D} + t_{D-R} \tag{4.41}$$

where, t_{S-R} denotes the total travel time from source to receiver, t_{S-D} represents the travel time from a plane wave (P or S wave) to a diffractor or scatterer, and t_{D-R} represents the travel time from the diffractor to the receiver.

The first part of the travel time t_{S-D}, can be calculated based on Snells' law using the known incident plane wave slowness, assuming a set of scatterer locations and base model velocities (α_0, β_0).

The second part of the travel time, t_{D-R}, is determined by the location of the scatterers and receivers, as well as plane wave slowness, and can be expressed approximately as:

$$t_{D-R} = 1/c\sqrt{X^2 + Z^2} \tag{4.42}$$

where c denotes P or S wave velocity, and X and Z represent horizontal and vertical distance from a diffractor to a receiver as shown in Figure 4.14. Obviously $t_{D\text{-}R}$ is a diffraction hyperbola.

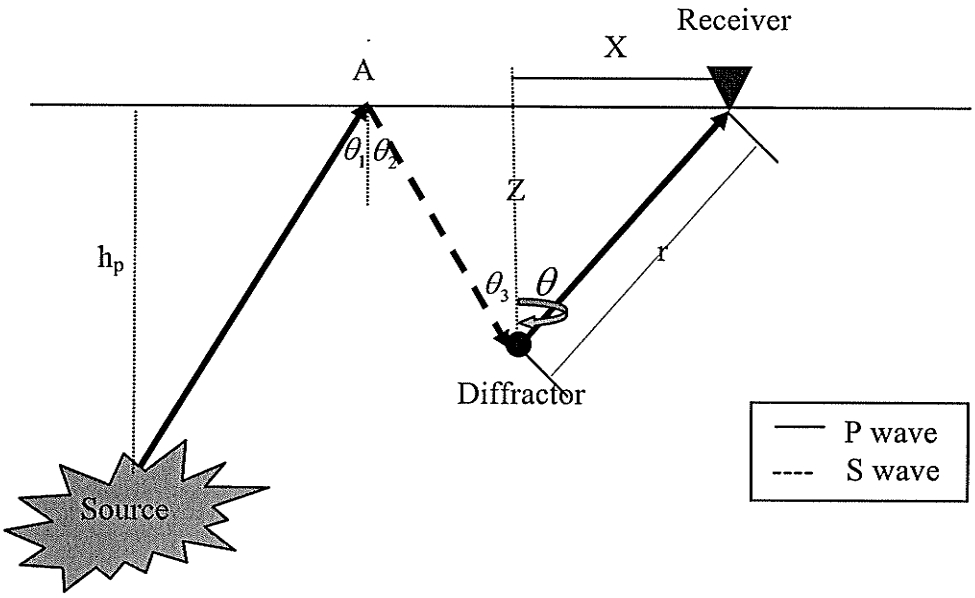

Figure 4.14. Cross-section of scattered wave phase- Ps•p used as an example of travel-time and amplitude calculations.

4.4.3.4 Amplitude of Scattered Wave

We normalize the incident P wave to unit amplitude by dividing by itself, $a^P / a^P = 1$, where a^p may be derived from equation (4.32) based on the base model. A specific amplitude of a point scattering wave phase, for example, Ps*p, from a source to a receiver may be calculated as:

$$a(Ps_*p) = 1 \times a_A^S \times {}^S u^P \times 1/r \times 1 \tag{4.43}$$

where a_A^S represents the amplitude of the converted phase, P-to-S, at point 'A' of the free-surface (see Figure 4.14), which is determined by the free-surface reflection coefficient and depends on near-surface impedances; ${}^S u^P$ represents the displacement from an incident S wave scattered as an P wave which is using equation 4.39; and $1/r$ is a simplified geometrical spreading factor for the wave paths from a scatterer to a receiver.

Similarly, the amplitude for other scattered wave phases can be given as:

$$a(Pp_*p) = 1 \times a_A^P \times {}^P u^P \times 1/r \times 1 \tag{4.44}$$

$$a(Pp_*s) = 1 \times a_A^P \times {}^P u^S \times 1/r \times 1 \tag{4.45}$$

$$a(Ps_*s) = 1 \times a_A^S \times {}^S u^S \times 1/r \times 1 \tag{4.46}$$

$$a(P_*s) = 1 \times {}^P u^S \times 1/r \times 1 \tag{4.47}$$

$$a(P_*p) = 1 \times {}^P u^P \times 1/r \times 1 \tag{4.48}$$

4.4.4 Forward Modeling

Following the method in the above section, given travel time and amplitude, a scattered synthetic seismogram (receiver function) from a single scatter may be generated by convolving a source wavelet with this time series. Under the first order Born

approximation, for weak scattering, the secondary wavefield generated by scatterers is not subject to secondary scattering, making the scatterers independent of each other. Based on this assumption, by dividing the region of interest into a 3-D grid of cells of a dimension, a, with $a < \lambda/10$ so that it satisfies the Rayleigh-scattering approximation, the total scattered wavefield then can be expressed as the sum of wavefields for perturbations to each parameter in each cell. If d represents the primary- removed SV-receiver function data for all traces and all components, using the Born approximation and ray theory, for N cells, we have

$$d = \sum_{i=1}^{N} d_{\alpha}^{i} + \sum_{i=1}^{N} d_{\beta}^{i} + \sum_{i=1}^{N} d_{\rho}^{i} \tag{4.49}$$

where d_{α}^{i}, d_{β}^{i} and d_{ρ}^{i} denotes the scattered trace generated by perturbing the α, β and ρ properties of the i^{th} scatter, respectively.

Let m be a 3N-length vector where cell m_{3j} contains the j^{th} α-perturbation, m_{3j+1} contains the j^{th} β-perturbation, m_{3j+2} contains the j^{th} ρ-perturbation, and the total number of model elements M is determined by cells in x $\times$ cells in y $\times$ cells in z $\times$ properties $[\alpha, \beta, \rho]$.

Then let $\tilde{d}_i$ be the scattered data generated by the perturbation m_i=1 (all other m elements are zero). For non-unit perturbation,

$$d_i = \tilde{d}_i m_i, \tag{4.50}$$

$$\text{then: } A = \begin{pmatrix} \hat{d}_1^1 & \hat{d}_2^1 & \dots & \hat{d}_{3N}^1 \\ \hat{d}_1^2 & \hat{d}_2^2 & \dots & \hat{d}_{3N}^2 \\ \dots & \dots & \dots & \dots \\ \hat{d}_1^m & \hat{d}_2^m & \dots & \hat{d}_{3N}^m \end{pmatrix} \tag{4.51}$$

where A is the partial derivative matrix, and has dimensions of $[3N, M]$, and a single element of A is derived in the manner of a point scatterer (see section 4.3.3).

For general m,

$$d = Am \tag{4.52}$$

4.4.5 Migration and Inversion

Migration attempts to produce a true image of structures within the Earth using a known seismic wavefield. It can be treated as an approximate solution to the general elastic wavefield inversion problem.

By approximately inverting equation (4.52) using the transpose:

$$m = A^T d \tag{4.53}$$

the properties (velocities and density) are mapped back from data samples to their 3-D cells.

To obtain a more accurate solution, the inversion problem is posed as a minimization

$$\min(Am - \lambda I) \tag{4.54}$$

where I is an $M \times M$ identity matrix which represents simple uniform damping and λ is a weighting factor determined by the quality of data. We solve this equation using a standard least-squares solution (LSQR) (Menke 1989, Paige and Saunders, 1975).

To increase the coherency and interpretability of the results, the model is smoothed by posing

$$m=Sx \tag{4.55}$$

where S is a Gaussian smoother and

$$d=ASx=Bx \tag{4.56}$$

and then we rewrite the minimization as

$$min(Bx - \lambda I) \tag{4.57}$$

and therefore the inversion gives damped x and so smoothed m (Frederiksen and Revenaugh 2004).

The resolution of the migration is determined mainly by the number of events and their directional distribution. It also depends on the size of cells and the range of slownesses. The former is usually limited by the computational costs, while the latter is related to incidence angle. For a small slowness, i.e., steep incident angle, the depth resolution will be poorer compared with phases with a large slowness as the delay times between the stations will not differ much for different depths, given steep angles of incidence of a phase (Rose and Thomas 2002).

Chapter 5

Data and Analysis

5.1 Introduction

Due to the presence of local seismicity, density of population and concentration of economic facilities, 30 broadband three component stations have been deployed in southern Ontario, recording data for as long as a decade (Eaton et al. 2000). As a consequence, 3-D structural images of the region may be obtained from this extensive teleseismic data collection. This study employed three component data from 29 stations to construct 3D structure images using CCP stacking and scattering tomography starting from teleseismic receiver functions. The collected raw data need to be preprocessed before applying receiver function analysis, CCP stacking and scattering tomography. In this chapter, I will focus on discussing these steps which were applied prior to receiver function processing and I will give a few receiver function examples from single stations.

5.2 Data Acquisition

Data acquisition for this thesis study involves two different seismic networks. 26 broadband seismograph stations belong to the recently deployed POLARIS (Portable Observatories for Lithospheric Analysis and Research Investigating Seismicity) array; three permanent broadband stations of the Canadian National Seismography network (CNSN) were also used (Figure 5.1).

The POLARIS project is a multi-institutional project funded by the Canadian Foundation for Innovation, Provincial Governments and Universities, as well as private industry across Canada. The POLARIS infrastructure is designed to comprise a total of 90 three-component broadband seismographs and 30 magnetotelluric (MT) mobile field systems which use satellite telemetry to broadcast their data to central locations in Ontario and British Columbia: most of their data are obtainable via internet. The initial targets of the POLARIS network include three-dimensional imaging of the deep structure of the Slave Province in Canada's NWT and earthquake hazards studies in the populated regions of southern Ontario and southwest British Columbia (Cassidy et al. 2003).

As one of three subarrays of POLARIS, 30 three component broadband stations have been installed in southern Ontario and adjacent areas and each will record at least until the end of the four-year deployment. The first six three component stations (BRCO, WLVO, PKRO, ACTO, TYNO, and STCO) were upgraded from short period systems to three component broad band systems in fall 2001. Another fourteen POLARIS stations comprising ELGO, HGVO, PTCO, LINO, PECO, DELO, BANO, MPPO, CLPO, PEMO, ALGO, KLBO, CLWO, and TOBO) were added into the network in 2002 and 2003. By the middle of 2005, ALFO, BRPO, BUKO, OTT, SUNO, PLIO were also deployed. Since station PLIO is far away from the other stations, we cut off this station, and limited our study area is the rectangle from (42.5N, 82W) to (46.8N,74.21W), around 600 by 500 km.

CNSN stations have been recording earthquakes since the 1990s. Three permanent CNSN stations: KGNO, SADO and GAC, are situated in our study area and are included in this study, increasing our data coverage significantly. The average

distance between these 29 three component stations is about 50 km~60 km. This spacing leads to a quite good and uniform coverage of the study area except in the southeast corner of the area (see figure 5.1).

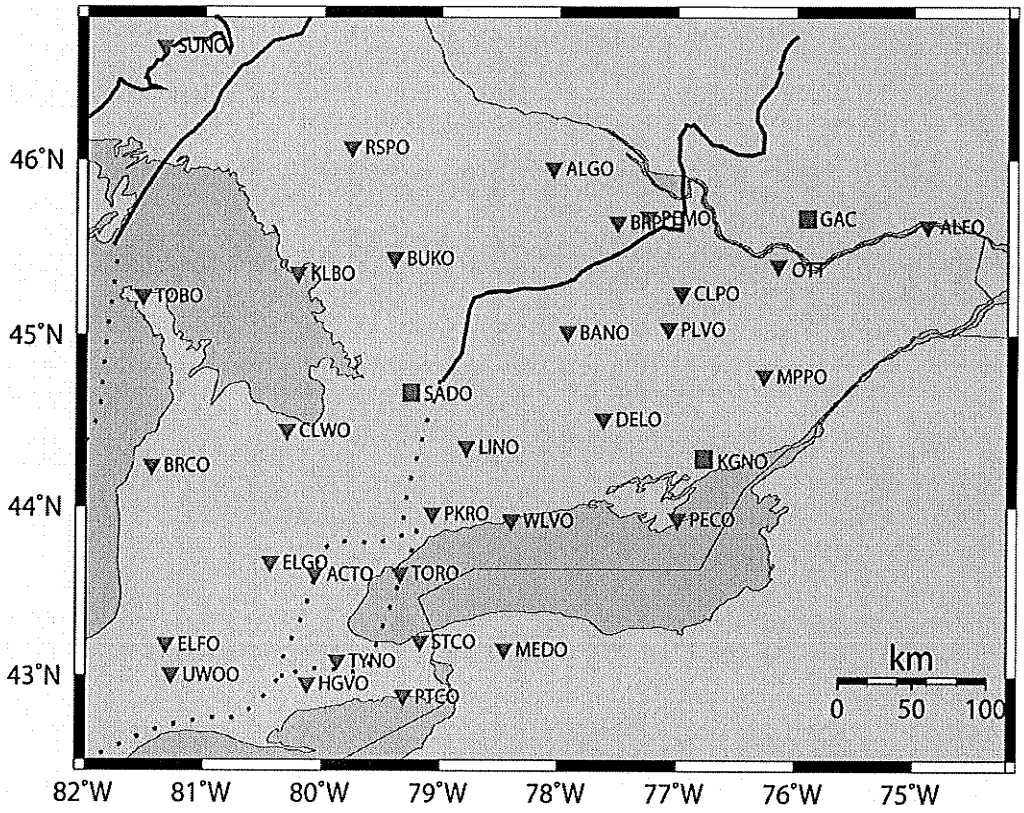

Figure 5.1. Map of broadband three component stations comprising networks in Southern Ontario used in this study. Triangles: stations used in the POLARIS network; Squares: stations from in the CNSN network.

5.3 Data Selection

During a decade (1994-2005), a total around 470 global earthquake events, recorded by these 29 broadband three component stations, are available from data achieves at the POLARIS and CNSN. The number of events for individual station varies

from two (UWOO) to 149 (GAC) depending on the length of recording period and background noise level.

Events that have been used for this study were selected under the following criteria:

First, only teleseismic earthquakes with magnitude greater than 5.5 and some smaller events with deep foci, were examined. Most events with magnitude smaller than 5 are generally hard to observe in the data, given the signal-to-noise ratio in southern Ontario.

Second, events with epicentral distance ranging from 30° to 100° to the center of the network were inspected. Events further than 100° are usually not used to obtain receiver functions as there is no direct P at this distance, the incidence angle of PKP is too close to vertical, resulting in P to SV conversion coefficients very close to zero, and P_{diff} is usually very weak (Knapmeyer and Harjes, 2000).

In order to avoid including bad traces and to enhance SNR, plots of the events satisfying the above two critera were inspected, and only events with clear records of P onsets with good quality were selected for further processing.

This processing left 2370 seismograms for processing receiver function, comprising 120 events in the POLAIS array, 114 events from GAC, 27 from KGNO, 27 from OTT, and 110 events from SADO. Some of them overlap, but all data were used for receiver functions. The selected events from Polaris and CNSN stations SADO and GAC are listed in Table 1, Table 2 and Table 3 in Appendix A, and Figure 5.2 (a-c) are plots of the event locations. An event appearing in those plots is used by at least one of the stations.

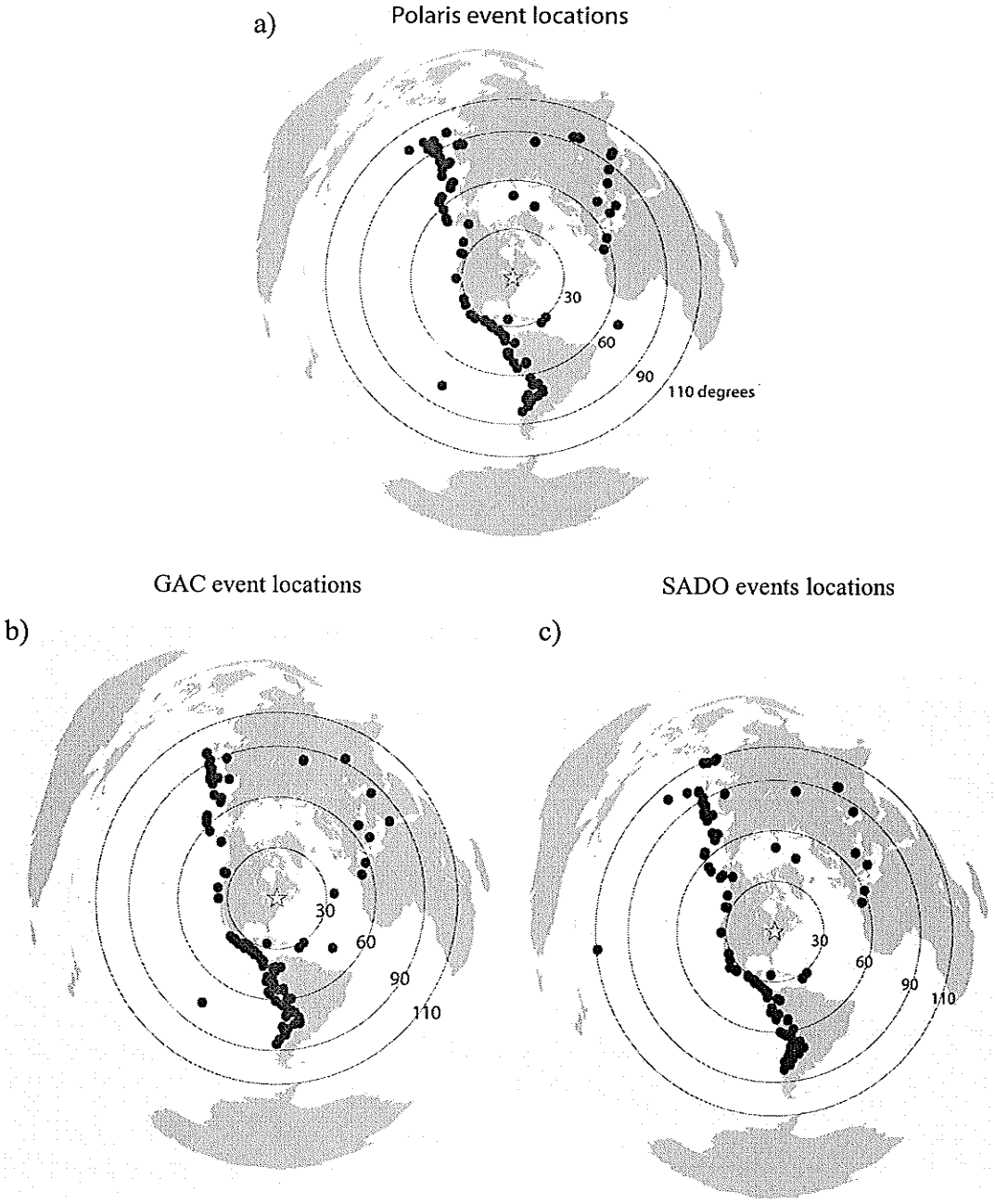

Figure 5.2. Event locations in azimuthal projection. Filled red circles denote event locations, yellow star denotes the central location of the network. An event appearing in this map is used by at least at one of the stations. (a) POLARIS event locations, (b) GAC event locations, (c) SADO event locations.

5.4 First-arrival Picking

Travel-time picking is used to locate the first P-arrival and correct for small time shifts caused by 3-D Earth architecture. Figure 5.3 demonstrates this method: first, we calculated the first arrival time predicted by the IASP91 model (using the Tau-P Tookit), it is marked as 'IASP' on the plot. We next visually pick the P-arrival time near the theoretical position, given that P-waves are normally the first noticeable pulse of the seismogram (see mark 'A'). Then the seismograms for a given event were examined, aligned on the P-wave arrival time and windowed from 10 s before the P arrival to 50 s after the P arrival, using a sample interval of 0.025 s.

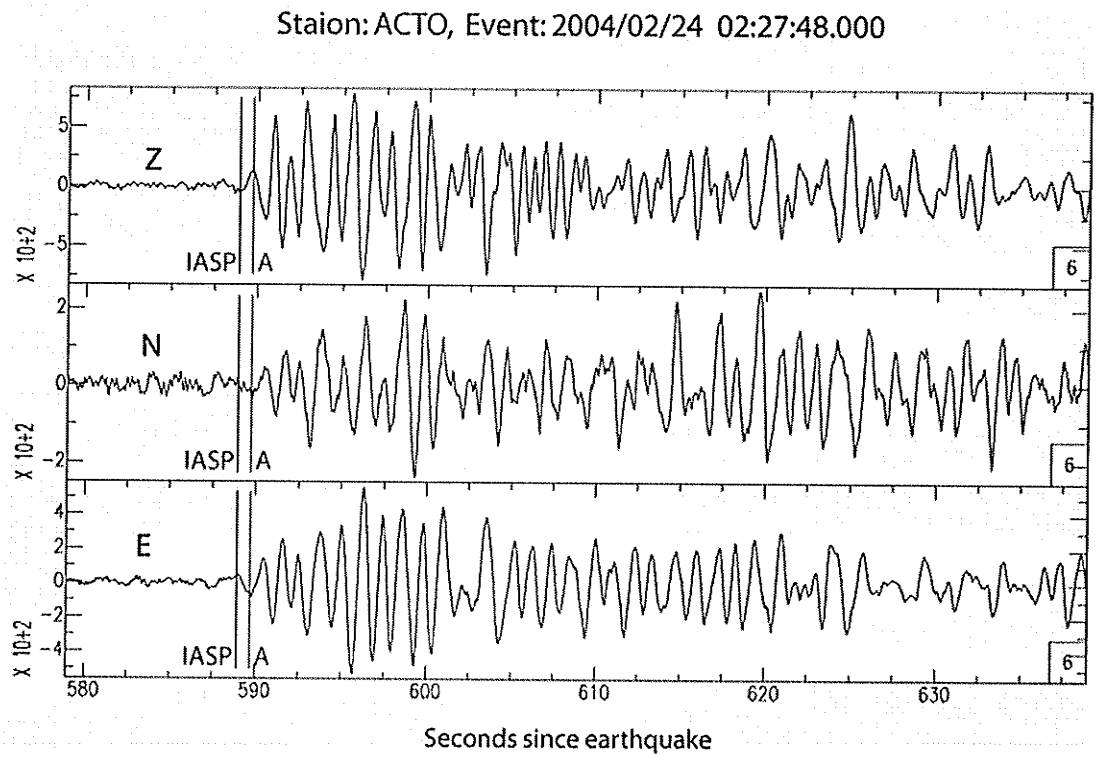

Figure 5.3 is an example of picking the first P-arrival. Blue line denotes the theoretical P arrival (marked 'IASP'), red line is hand picked P-arrival (marked 'A').

5.5 Receiver Function Analysis

The next processing step is receiver function processing, in which the aligned and windowed raw seismograms are first rotated into ray coordinates, the wave field decomposition is performed by free surface transformation, the traces are binned to enhance SNR, and finally the receiver function is obtained by using least-squares simultaneous deconvolution. Receiver function processing and calculation have been discussed in detail chapter 4. Here I give some examples from POLARIS and CNSN stations to demonstrate the processing steps from teleseismic events to receiver functions, and Earth structure information observable from receiver functions.

Figure 5.4 is an example from station ACTO showing the receiver function processing procedure. After deconvolution of the source function (P component), the individual seismic phases (P, Ps and multiples) are well separated on the radial or SV component (see (d) and (e); P, Ps, and Moho multiples are marked on the figures); the self-deconvolved P or Z component shows a spike-like waveform; the SH or T component is the tangential receiver function used for studying anisotropy. A better receiver function is obtained by performing wave field decomposition and damped deconvolution (see (e)) compared with the receiver function obtained by water level method based on ray coordinates (see (d)).

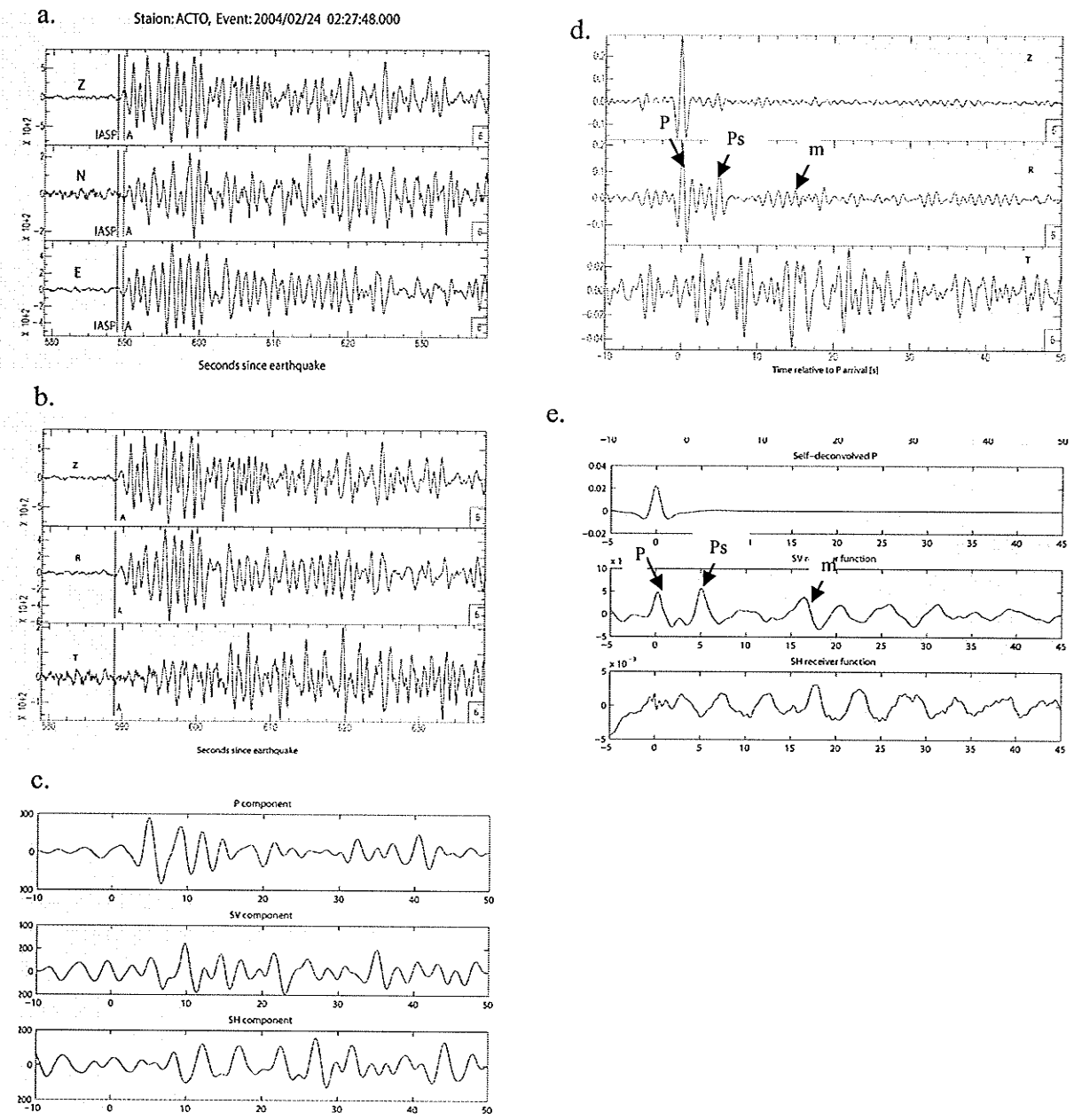

Figure 5.4. Receiver function processing. The data are from station ACTO, event 2004/02/24 (M=7, epicentral distance 84.7°, back azimuth 28.5°), where P, Ps and m denote the P-arrival, P-to-S converted arrival and multiples, respectively. (a) Raw event seismograms in ZEN coordinates; (b) raw event seismograms rotated into ZRT coordinates; (c) raw data surface transformation into P-SV-SH wavefield; (d) receiver function in ray (R-T-Z) coordinates generated by water-level method; (e) receiver function in wave-field coordinates (P-SV-SH) produced by least-squares damped deconvolution.

As discussed earlier, in order to improve the quality of the receiver functions, the events were sorted and stacked in bins with bin size of 20° in back azimuth and 0.02 s/km in slowness for each single station. Figure 5.5 (a-f) shows the stacked receiver functions for six stations: PTCO, HGVO, ELGO, SADO, MPPO and GAC. Their binned event distribution plots are given in Figure 5.6 (a-f). The order of stacked traces is arranged in terms of location of the bins determined in terms of back azimuth from 0° to 360°. In each back azimuth, bins are ordered from minimum slowness to maximum slowness (see Figure 5.6 (e)).The data for the other stations were analyzed in the same way.

A strong coherent phase around 0 s can be clearly observed at stations ELGO, HGVO, GAC and PTCO, which results from a residual P-primary arrival. The free surface transformation is performed to separate P and Ps arrivals. Therefore at some stations, for example, MPPO and SADO, this P arrival is successfully removed, but this method did not work as well at some other stations, for instance HGVO, GAC and so on. The second prominent positive coherent phase, the P-to-S conversion (Ps) from the Moho, around 5 s is clearly shown at all stations. The first Moho multiple, i.e., *PpPs*, is clearly observable around 15 s to 16 s at stations GAC and SADO, and is visible at stations SADO and HGVO.

A clear negative peak is present at about 20 s at stations GAC and SADO, which is associated with the second Moho multiple, i.e., (*PsSs+PsPs*) due to the fact that S waves travel slower than P waves. Another interesting feature around 10 s, parallel to the Moho multiple can be seen at stations ELGO and GAC (marked by a yellow ellipse). This coherent phase can be interpreted as either a multiple of lower crustal origin or a primary conversion from upper mantle structure. Since there is no similarly coherent

feature present between 0 s to 5 s, i.e., between the surface and the Moho, our interpretation is that it is a multiple from lithospheric structure below the Moho.

In general, at stations with more reocorded events and larger fold numbers in each bin (see Figure 5.6), higher quality stacked receiver functions can be expected (Figure 5.5). For example, the SNR of SADO and GAC are obviously higher than the SNR from PTCO and ELGO.

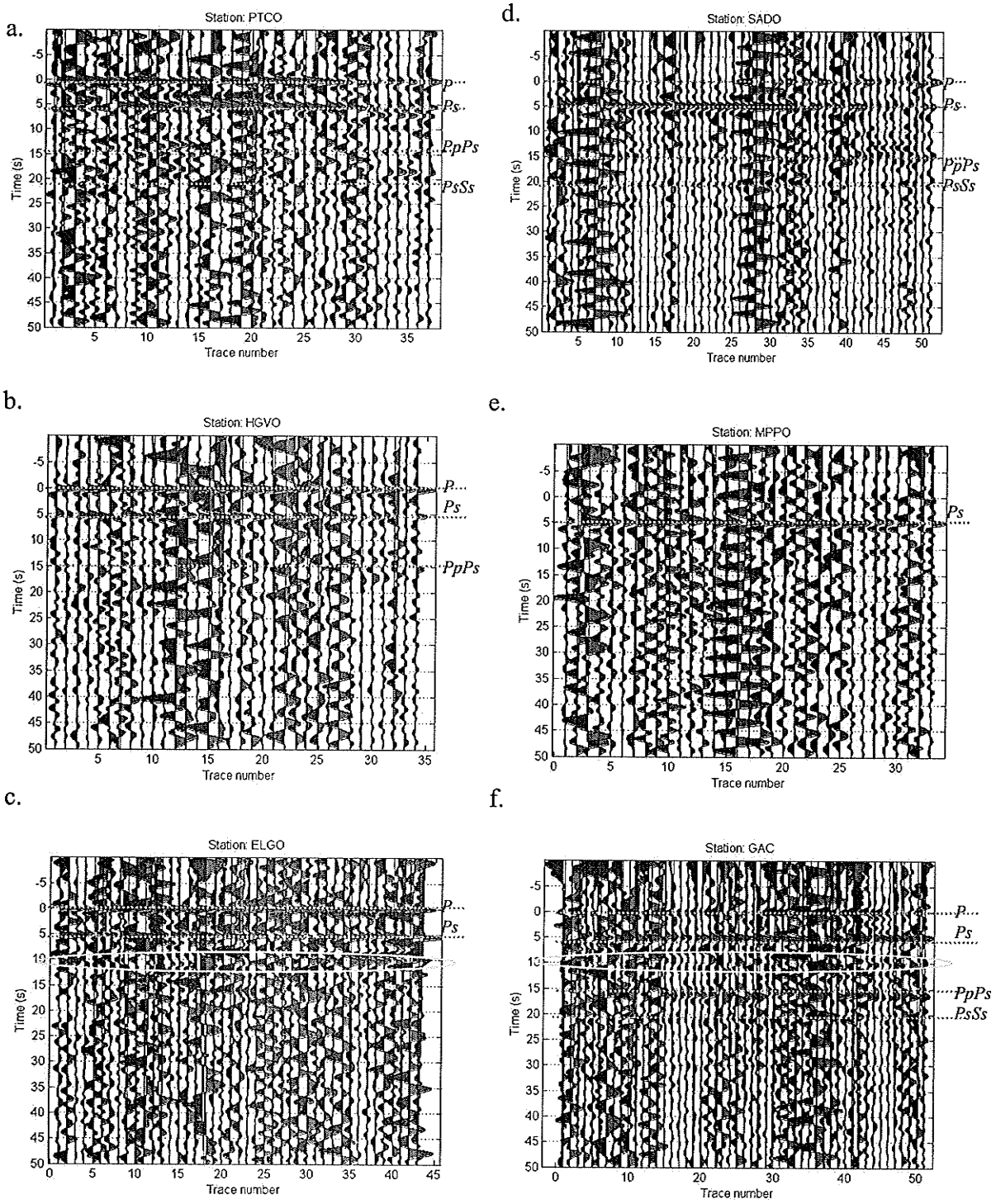

Figure 5.5. Stacked receiver functions for stations PTCO, HGVO, ELGO, SADO, MPPO and GAC ordered according to latitude from south to north (see Figure 5.1 for the station locations). Time is labeled as delay time relative to first P arrival. The Ps (Moho), and Moho multiples are marked on the figures. The yellow ellipse represents additional signal rising from upper mantle structure.

a.

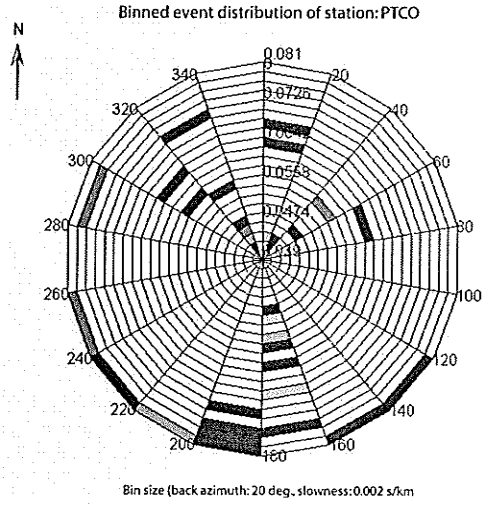
Binned event distribution of station: PTCO
N
0.081
0.0726
0.0558
0.0474
0
20
40
60
80
100
120
140
160
180
200
220
240
260
280
300
320
340
1
2
3
4
5
6
Bin size (back azimuth: 20 deg., slowness: 0.002 s/km

d.

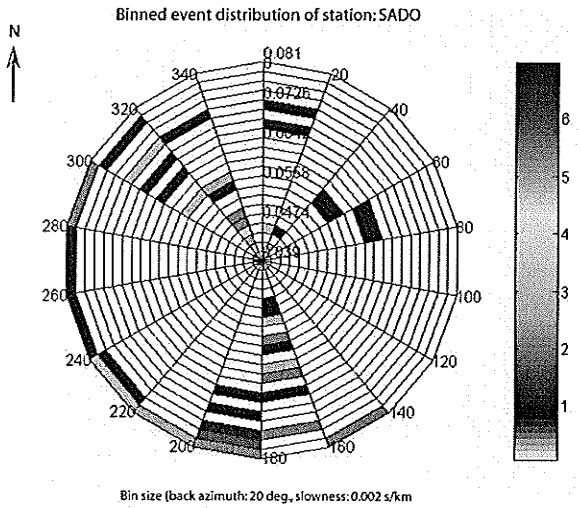
Binned event distribution of station: SADO
N
0.081
0.0726
0.0558
0.0474
0
20
40
60
80
100
120
140
160
180
200
220
240
260
280
300
320
340
1
2
3
4
5
6
Bin size (back azimuth: 20 deg., slowness: 0.002 s/km

b.

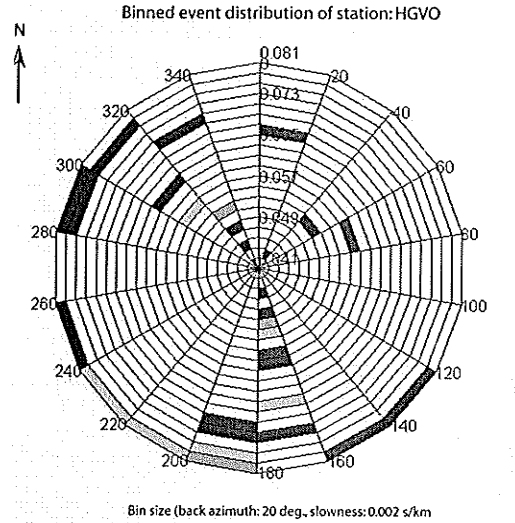
Binned event distribution of station: HGVO
N
0.081
0.073
0.051
0.043
0
20
40
60
80
100
120
140
160
180
200
220
240
260
280
300
320
340
1
2
3
4
5
Bin size (back azimuth: 20 deg., slowness: 0.002 s/km

e.

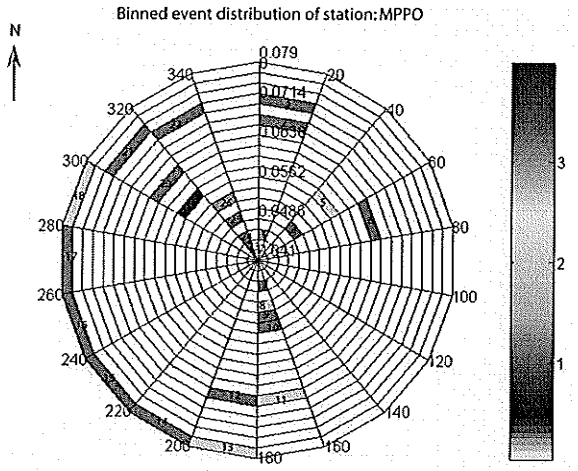
Binned event distribution of station: MPPO
N
0.079
0.0714
0.0638
0.0562
0.0486
0
20
40
60
80
100
120
140
160
180
200
220
240
260
280
300
320
340
1
2
3
Bin size (back azimuth: 20 deg., slowness: 0.002 s/km

c.

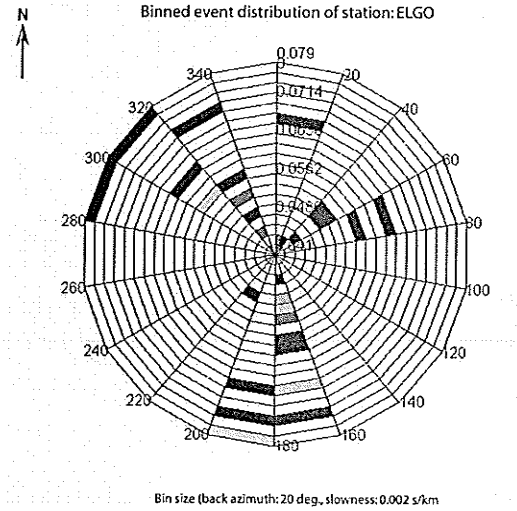
Binned event distribution of station: ELGO
N
0.079
0.0714
0.0562
0
20
40
60
80
100
120
140
160
180
200
220
240
260
280
300
320
340
1
2
3
4
5
6
7
Bin size (back azimuth: 20 deg., slowness: 0.002 s/km

f.

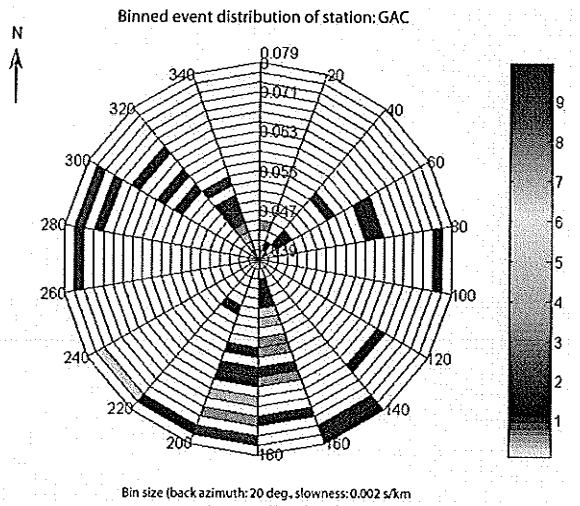
Binned event distribution of station: GAC
N
0.079
0.071
0.063
0.055
0.047
0
20
40
60
80
100
120
140
160
180
200
220
240
260
280
300
320
340
1
2
3
4
5
6
7
8
9
Bin size (back azimuth: 20 deg., slowness: 0.002 s/km

Figure 5.6 (a-f). Binned event distribution for stations: ELGO, HGVO, GAC, MPPO, SADO, and PTCO. The numbers labeled on each bins on figure (e) represent the order of traces in the stacked data. The bin size is 20 degrees of back azimuth and 0.002 s/km of slowness, the angle is the event back azimuth from 0 to 360 degrees with respect to North, and the radius is the event slowness labeled at zero back azimuth. The color represents the number of traces used in each bin.

Chapter 6

Results

6.1 Introduction

In this chapter, I apply the CCP stacking and scattering tomography methods to radial receiver functions to image three dimensional velocity structures beneath the study area. I will discuss these two applications in separate sections, each section having the following structures: Starting from the 1-D base model, the travel-time and ray geometries are calculated. Next, important stacking or scattering parameters and the processes used to determine these parameters are introduced. Then, the resolution tests and limitations of resolution for the two imaging methods are discussed separately. Finally, several observations of major structures obtained from CCP stacking and scattering tomography are shown and illustrated seperately. In the last section, I will summarize the results and interpretations obtained using these two methods.

6.2 Results from CCP Stacking

I developed an interactive 3-D CCP stacking software package using Matlab for computing common conversion points with user-defined 3-D cell size, visually investigating resolution and stacking fold distribution, and generating 2-D cross-section profiles at any user defined angle. I correlated results with fold distribution in contour maps as well as various 3-D images, including slices in X-Y-Z direction and colored parametric surface maps at any depth. I further use this interface to plot 2-D cross-

sections or 3-D images for scattering tomography as well. The usage of this software package is introduced in Appendix B: Manual for CCPscat software package.

6.2.1 1-D Base Model

A 1-D base model is constructed according to previous compiled seismic reflection and refraction data (White et al. 2000) and a standard Earth model (IASP91, Kennett 1991) to compute teleseismic ray geometries and delay-time, to convert the delay-time into depths, and to determine the 3-D geometry of subsurface discontinuities. The model consists of four horizontal layers with a total thickness of 90 km (this depth is extended into 410 km in CCP stacking) over a half-space (see Figure 6.1). The P wave velocity of each layer is obtained by averaging the White et al. (2000) model over each layer, a Possion's ratio of 0.26 and Vp/Vs of 1.81 obtained from IASP91 and local geology are used for generating the S-wave velocity, and density is also assumed according to the IASP91 model.

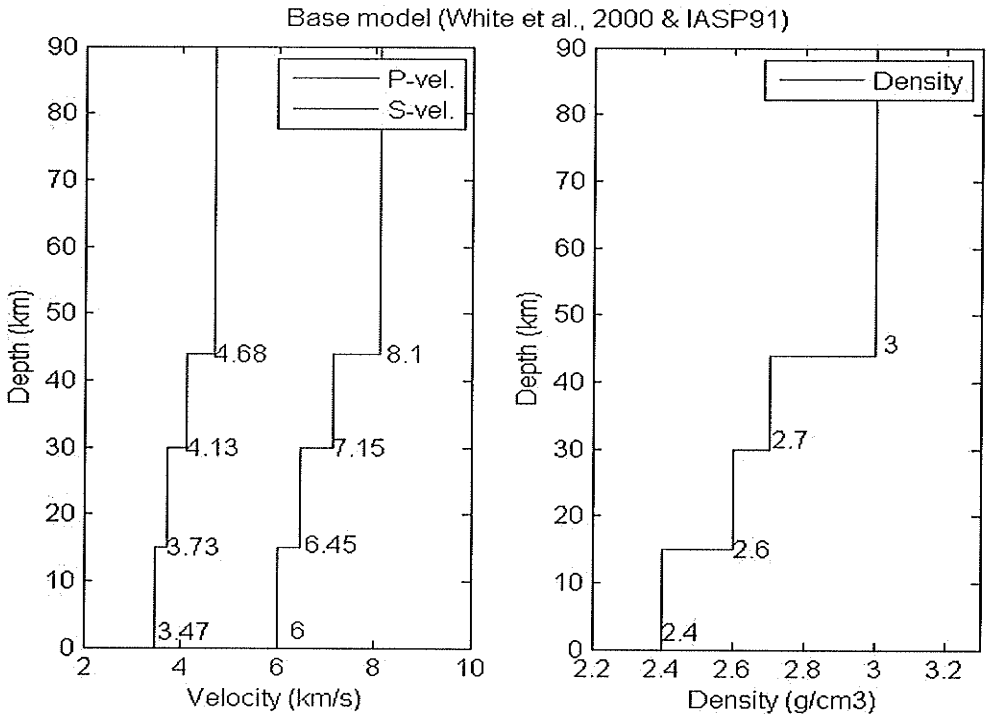

Figure 6.1. 1-D base model used for inversion based on White et al. (2000) and the IASP 91 model (Kennett 1991). Left panel shows average P- and S- velocities in km/s for four model layers, in which the red line is P-velocity, and the blue line denotes S-velocity. Right panel is densities in g/cm^3 for each layer.

6.2.2 CCP Parameters

For CCP stacking, I define a 3-D grid of sample points at 50 km by 50 km lateral spacing and 3-km depth spacing within a 600 km (east-west) by 500 km (south-north) by 420 km (depth) volume, which leads to $12 \times 10 \times 120$ cells in total, the origin being at the surface in the southwest corner. Amplitude in each cell was obtained by assuming all trace energy to be *Ps* conversions, back-projecting using the base model to determine ray paths and stacking all amplitudes arising from a given cell. The effect is to assign all arrivals to points in 3-D space.

Usually the size of each cell is mainly determined by the density of stations and distribution of events and frequency content (particularly vertically), therefore, the cell size and the number of cells should be adjustable given increasing numbers of deployed stations and recorded events in the future. The 3-D CCP program developed in this study provides an interactive interface for users to control any variable parameters and generate updated images immediately.

The station locations and the common conversion points of teleseismic rays at a depth ranging from 0-140 km with interval 30 km are shown in Figure 6.2. From this figure, we can see that the study area is widely sampled in the center by these rays and sparely sampled at the corners, especially the southeast part of the region where there is almost no ray coverage.

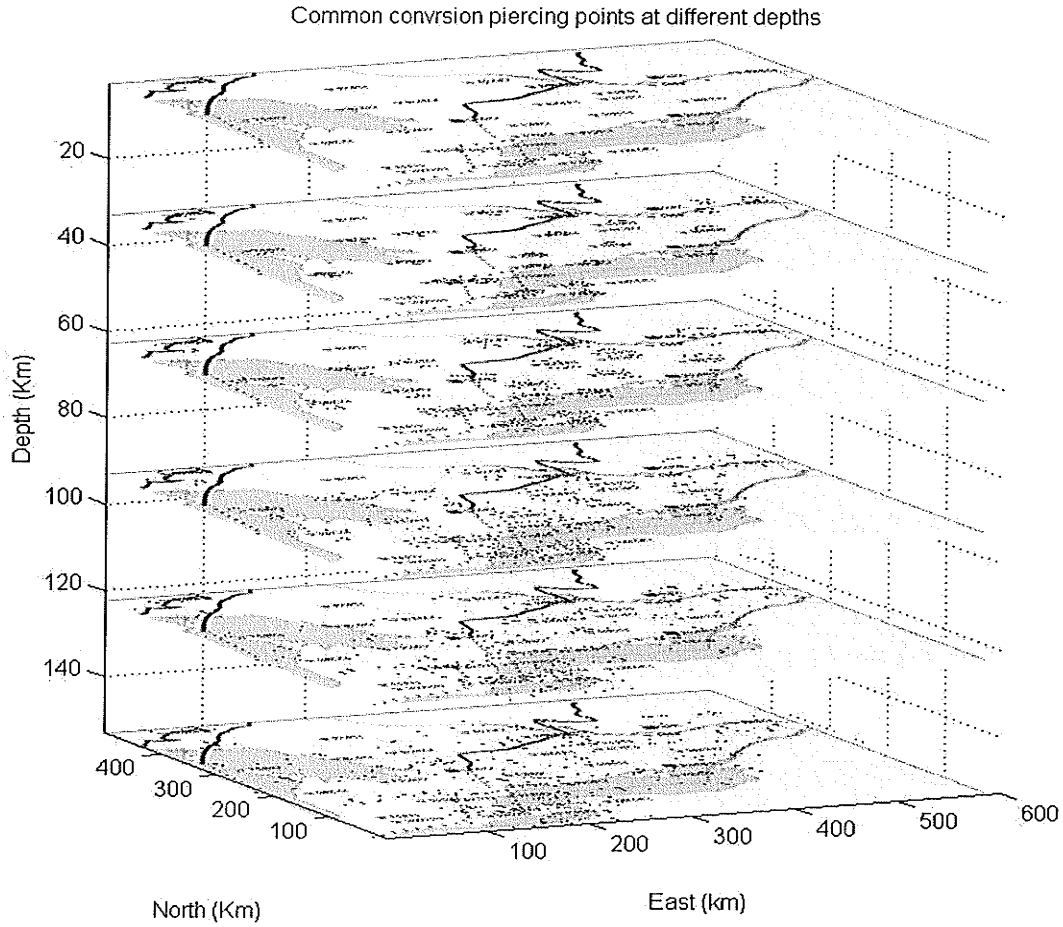

Figure 6.2. 3-D diagram showing P to S common conversion piercing points at depths ranging from 0 (at top) to 140 km (bottom) with interval 30 km superimposed on a local map. Red points denote Ps wave piercing points at each depths. The map covers latitudes and longitudes from (82W, 42.5N) to (74.2 W, 46.8 N).

6.2.3 Resolution

There is a trade-off between the resolution of the image and ray coverage of each stacked common conversion grid cell. As a consequence, the quality of resultant images is directly determined by cell size. A visualization tool is provided in the CCP program to determine an appropriate cell size; thereby, an image with suitable resolution and ray

coverage can be selected by users. Figure 6.3 shows the fold (number of samples contributing to each cell) at different depths with varing cell size. For instance, Figure 6.3 (a) is generated by choosing cell size $30 \times 30 \times 3$ km; the low station density causes many holes in the data volume, so we can expect that the images obtaining from stacking with this cell size will be hard to interpret. I increased the cell size to be a $50 \times 50 \times 3$ km, as shown in figure 6.3 (b). It shows good coverage of the ray path at depths between 20 to 140 km. I further plotted fold slices as deep as 400 km (see figure 6.3 (c) and (d)). As expected, as the depth increases the data density is decreased, and the best imaging would be at depths between 30 to 200 km. Due to lack of stations in the southeast part of the study area, there is no data coverage in this corner for all depths.

As discussed in Chapter 4, the resolution of the CCP method is also restricted by its imaging model based on geometric ray theory, which is only valid in the absence of significant diffraction effects, and for large features, i.e., length scale larger than the first Fresnel zone of the recorded wavefield. The frequency content of the teleseismic waves used in this study is in the range of 0.005 - 0.5 Hz, so the width of first Fresnel zone is on the order of 1 km to 273 km. Spetzler and Snieder (2004) have shown that the first Fresnel zone can be even smaller in heterogeneous media.

Another factor that needs to be taken into account is that the part of the energy in the receiver function produced by multiple P-to-S conversions, for instance, *PpPs* or *PsSs*, will be mapped to incorrect deeper locations by CCP stacking. However, multiples are usually less coherent and weaker than the primary *Ps* conversion due to their longer ray paths in the heterogenous shallow crust and extra reflections at depth. Stacking, on

the other hand, will enhance the primary and suppress noise and multiples (Zhu, 2002). CCP stacking assumes a *Ps* pattern of moveout; non-*Ps* events will stack less coherently.

a)

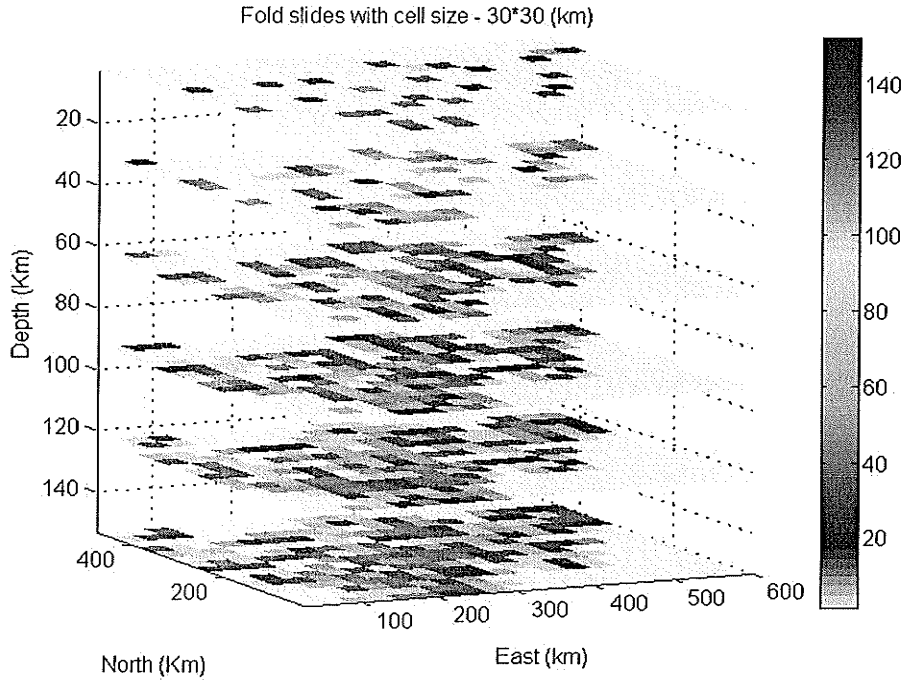

b)

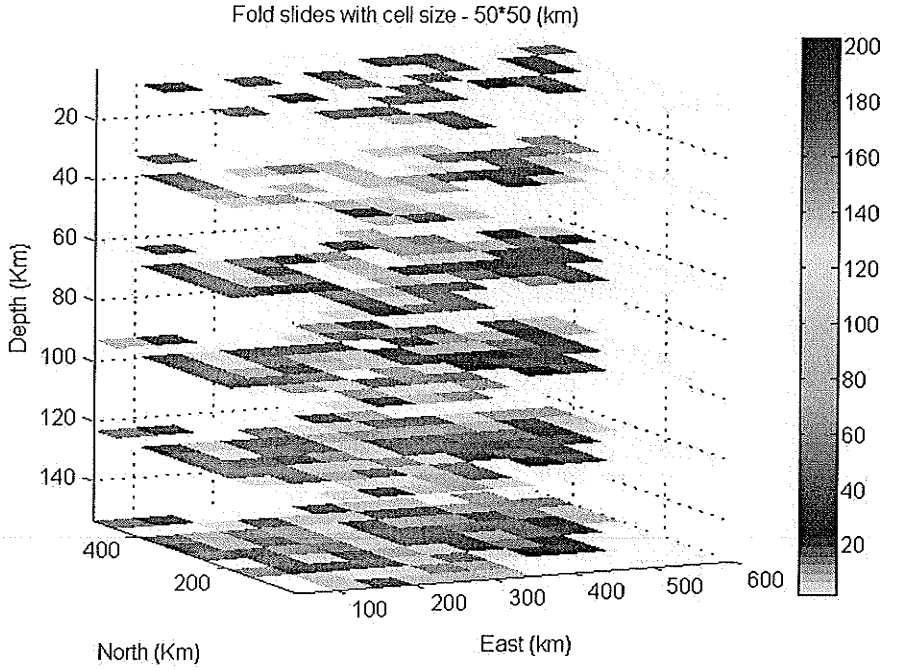

c)

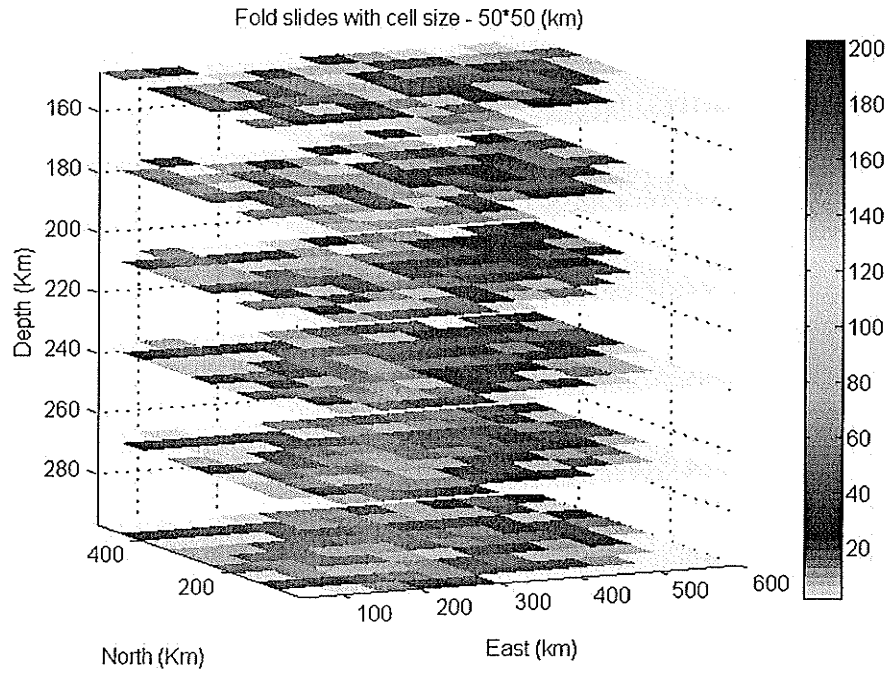

d)

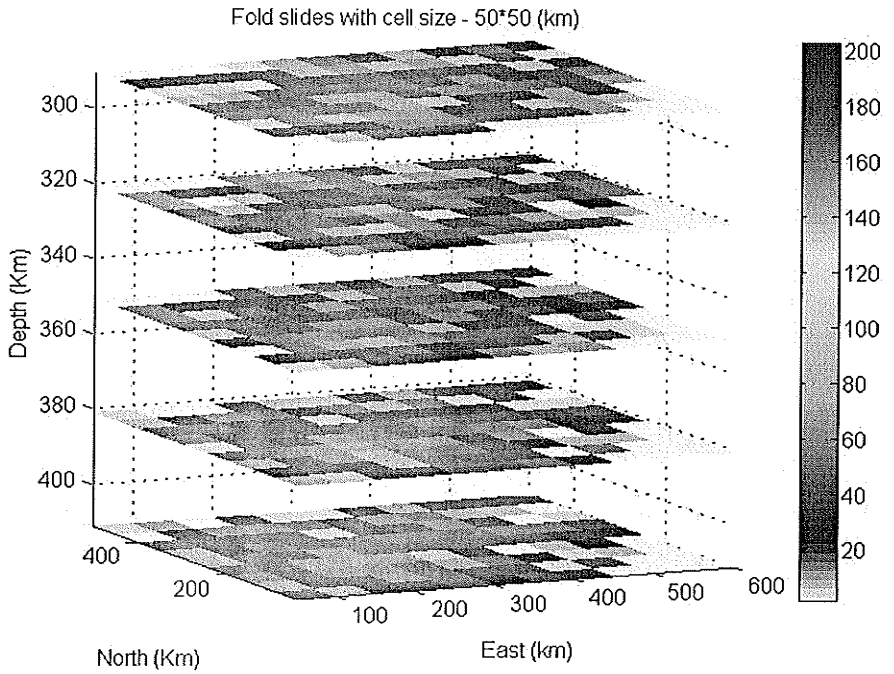

Figure 6.4. Resolution tests showing ray coverage with different cell size. (a) is fold distribution with cell size $30\times30\times3$ km at depth (0-150 km); (b) fold distribution with cell size $50\times50\times3$ km at depth (0-150 km); (c) fold distribution with cell size $50\times50\times3$ km at depth ranging from 165 km to 300 km; (d) fold distribution with cell size $50\times50\times3$ km at depth ranging from 300 km to 410 km.

6.2.4 Major Structures

My initial plots of results show Earth structure starting from 0 km to 420 km, which is consistent with the time window between 0 s and 50 s of the receiver functions (see Figure 6.5). Several features of interest can be seen from these plots. But considering the fact that the fold numbers decrease as the depth increases (see middle panel of Figure 6.5, and see Figure 6.4 (b) for overall fold distribution), uncertainties in interpretation increase in deeper locations. In addition, the deeper portion of the model may be contaminated by mislocated free-surface multiples, such as *PpPs,* by CCP stacking.

Due to above two reasons, I first calculated the range of depth of the first Moho multiple (*PpPs*) arrival time, about 125 km to 149 km. This range was obtained from a time-to-depth calculation given that *PpPs* occurs at approximately at 15 s in our receiver function data. There may be other sources of error within this window, such as features resulting from multiples from lower crustal discontinuities. However, as I mentioned earlier, because the crust-mantle boundary is the biggest discontinuity in the lithosphere, multiples from other interfaces are usually less coherent and weaker compared with the primary *Ps* conversion due to their longer ray paths in the heterogenous shallow crust and extra reflections in the subsurface. And these multiples can be suppressed by stacking. Thus my interpretation mainly focuses on the images ranging from 0 to 120 km.

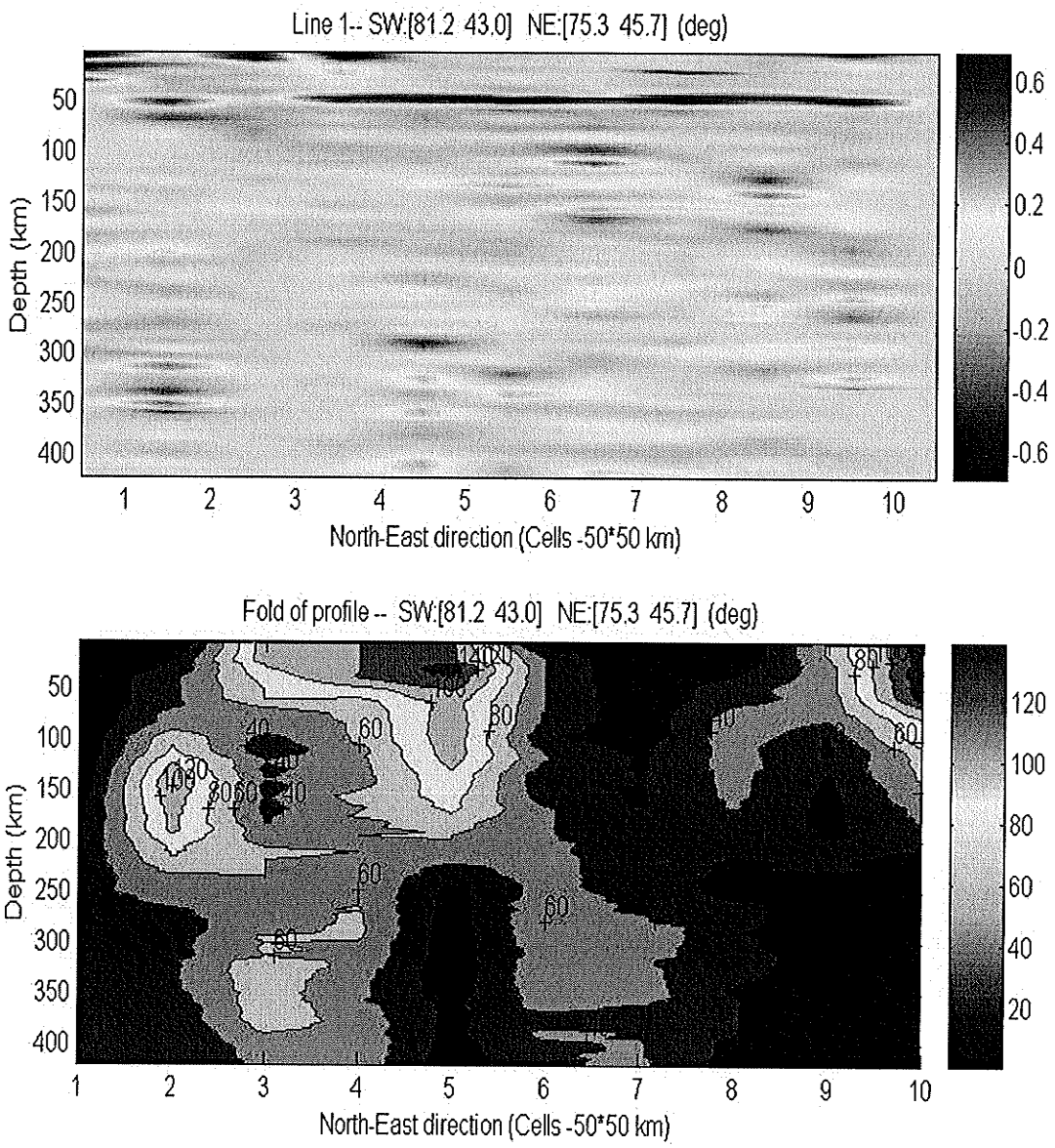

Figure 6.4. Cross-section along Line 1 (figure 6-6) starting from (81.2°W,43.0°N) and ending at (75.3°W, 45.7°N). The top window (panel) shows the stacked amplitude of P-to-S conversions plotted in the range of [0-410] km in depth, and the bottom panel is the contoured fold distribution along this line. The color bar at right is the colormap used for plotting. Note that reddish colors represent positive amplitude in the top panel and high fold for the fold distribution section, while bluish colors are negative for the amplitude variation map and low fold for the bottom panel.

Although the CCP software is able to plot any user-defined cross-section, its ability to resolve structural variations of the whole rectangular area is restricted by the denser station configuration at the centre of the area and the limited number of earthquakes. In order to make full use of available data and to investigate the most interested features, when selecting lines, I try to cross dense station coverage and major tectonic features.

Figure 6.6 to Figure 6.15 (a and b, top and middle panels) are 2-D cross-sections of CCP receiver function stacking images along lines 1 though 10. The first six lines (from south to north, Line-1, 2, 3, 6, 4 and 5) were oriented in SW-NE to West-East manner and extend from the west side of the study area (80°W to 81.5°W) to the east part of the region (75.2°W). From west to east, the other four lines (Line-7, 8, 9 and 10) are oriented in a NW-SE manner, extending from north (45°N) to south (44°N). More specifically, Line-1 and 2 were run through Lake Ontario within the CMB, and across the Ottawa-Bonnechere Graben (OBG) (situated a little south of, and parallel to the Ottawa river); Line-3, 4, and 5 run from the west side of the CGB from around 81.4° West and 43.0°, 44.2°, and 45.1° North respectively, across the CMBbz, through the CMB and across the OBG, ending at the location (75.3°W, 45.8°N) ; Line-6 was run through the southwest part of CGB to the northeast side of the CGB. Line-7, 8, 9 and 10 begin within the CGB, intersect the CMBbz nearly perpendicularly, and end in the CMB. See Figure 6.5 for the locations of these lines.

The top panel in each section (a) shows the stacked amplitude of P-to-S conversions, the middle panel (b) is the stack fold distribution of this line shown as a

contour map, and the bottom panel (c) shows the shear-wave velocity perturbation images obtained from scattering tomography (will be discussed in detail in the section 6.3.4.1). The starting and end location both in latitude and longitude (degrees), names, and major boundaries (CMBbz or OBG) or marked changing features (A or B) of each selected line are labeled on the top of the panel. The color scales of these figures are shown on the right side of the plot. Note: here, reddish color represents positive amplitudes, while negative amplitude for the P-to-S conversion amplitude was plotted in bluish colors for the top panel. For the fold distribution map, reddish colors denote high fold while bluish colors mean low fold. Panel (c) will be discussed in the next section. The interpretations were marked as dashed lines along these cross-sections based on the seismic results, surface geology as well as other geophysical results.

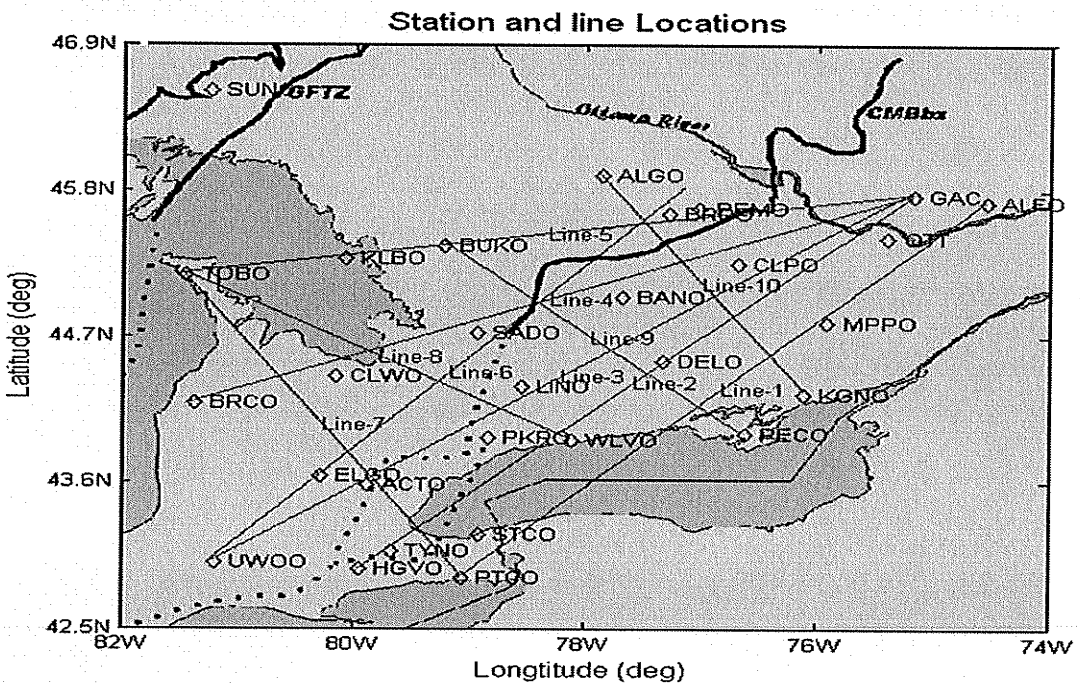

Figure 6.5. Maps showing locations of selected lines used in cross-section in Figure 6.6 to Figure 6.15. Major tectonic boundaries and stations are also shown.

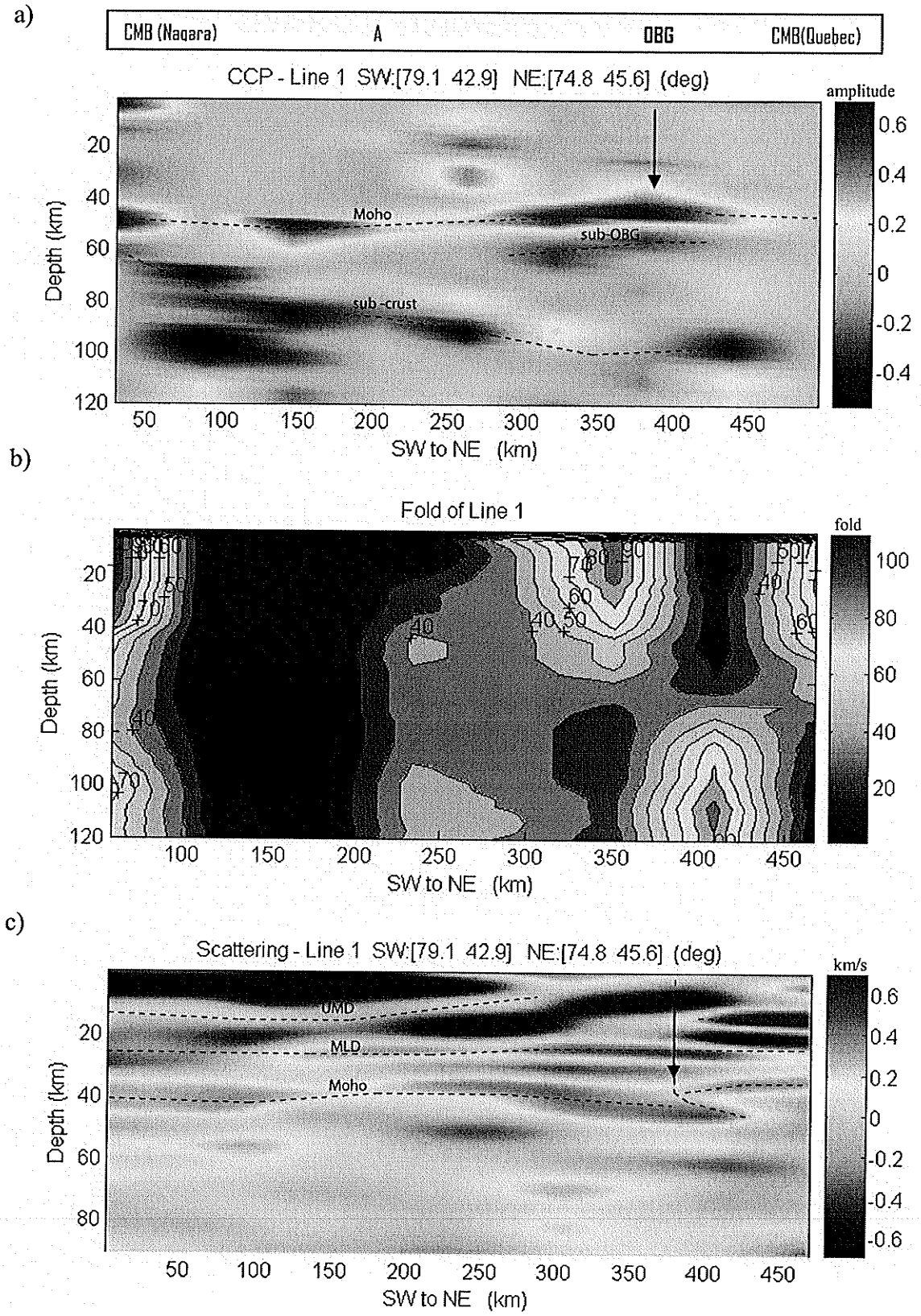

Figure 6.6. Cross-sections along Line 1 (see Figure 6.5 for location) (a) CCP stacking image; (b) fold distribution beneath the line; (c) scattering tomographic image.

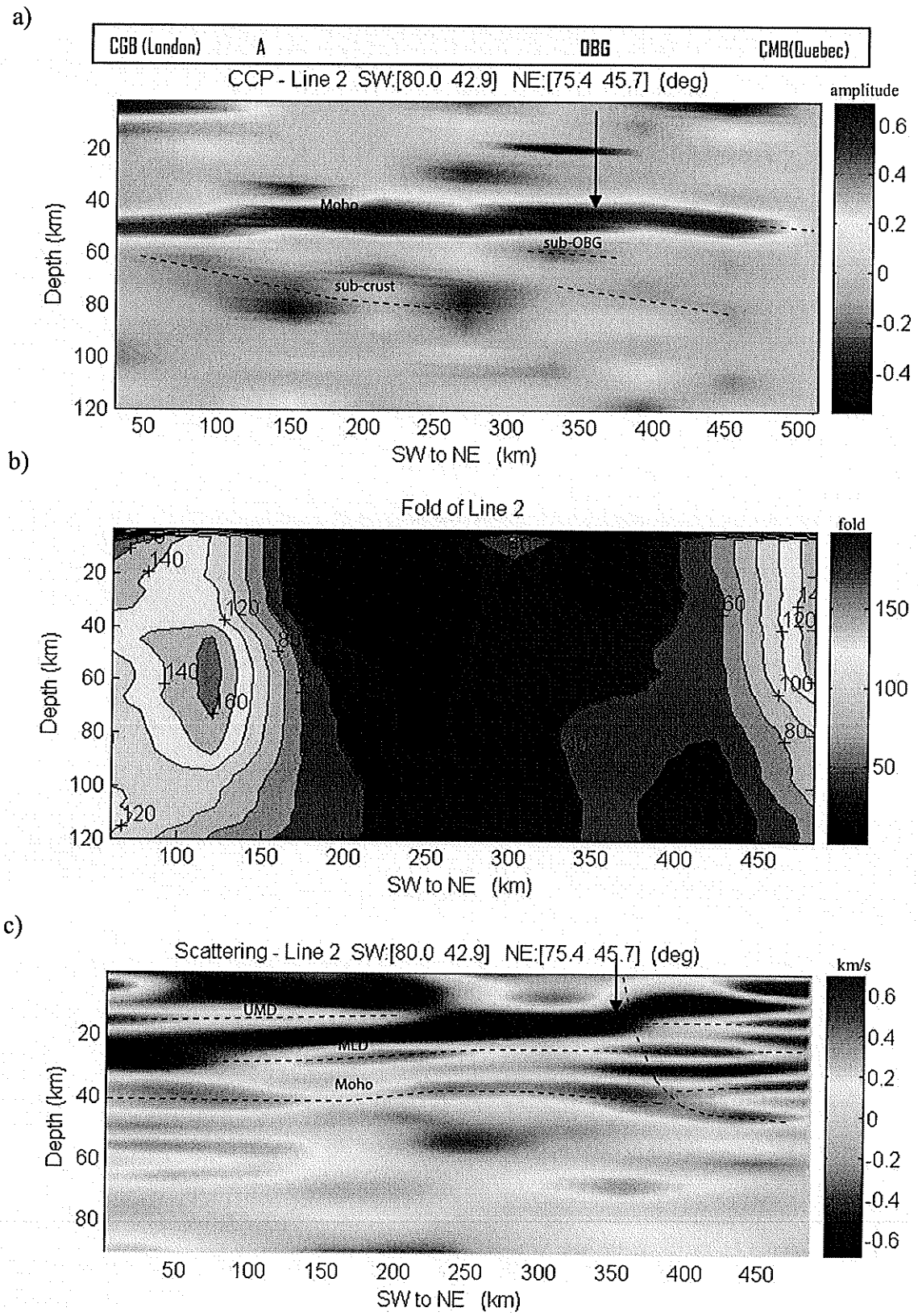

Figure 6.7. Cross-sections along Line 2 (see Figure 6.5 for location) (a) CCP stacking image; (b) fold distribution beneath the line; (c) scattering tomographic image.

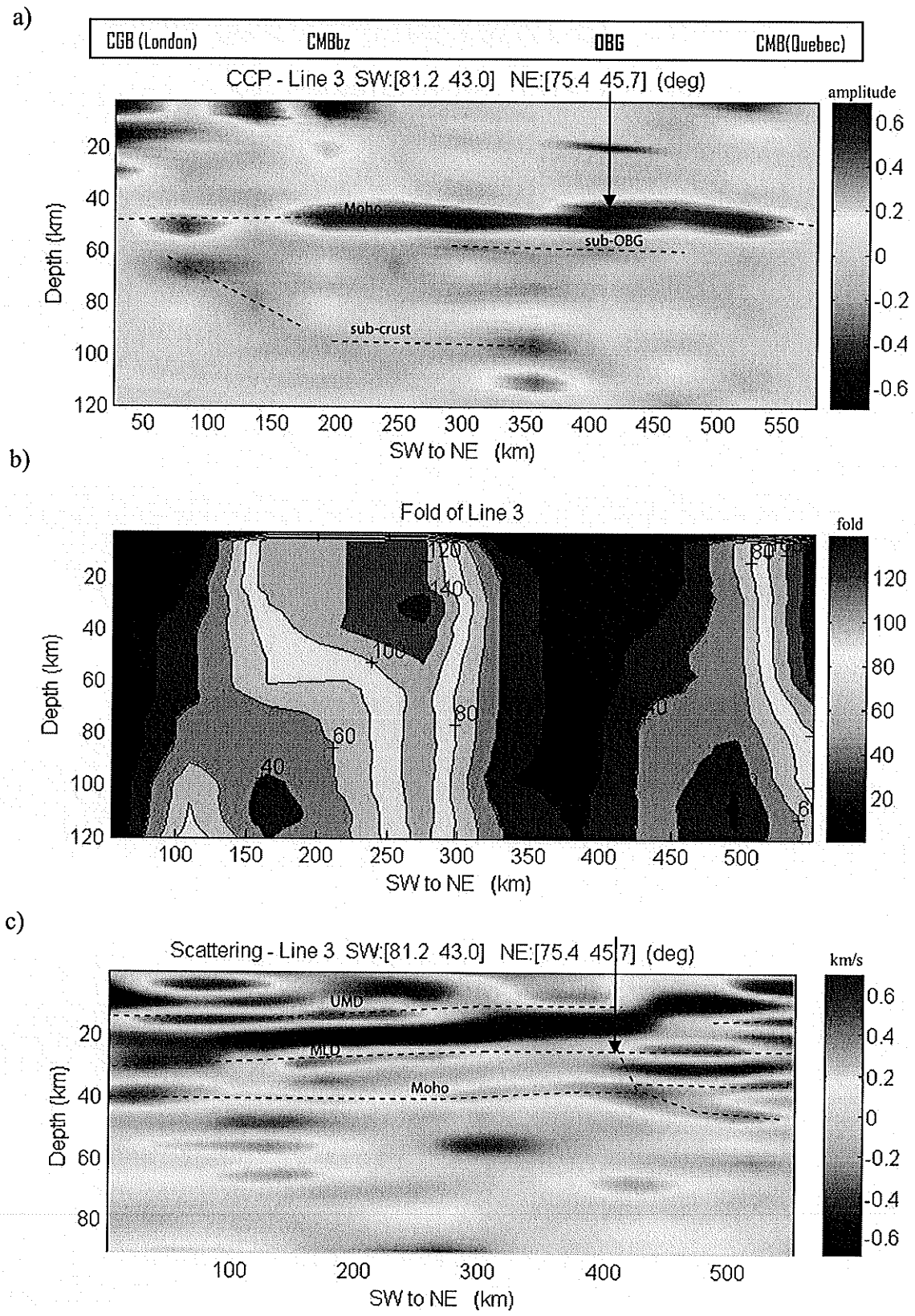

Figure 6.8. Cross-sections along Line 3 (see Figure 6.5 for location) (a) CCP stacking image; (b) fold distribution beneath the line; (c) scattering tomographic image.

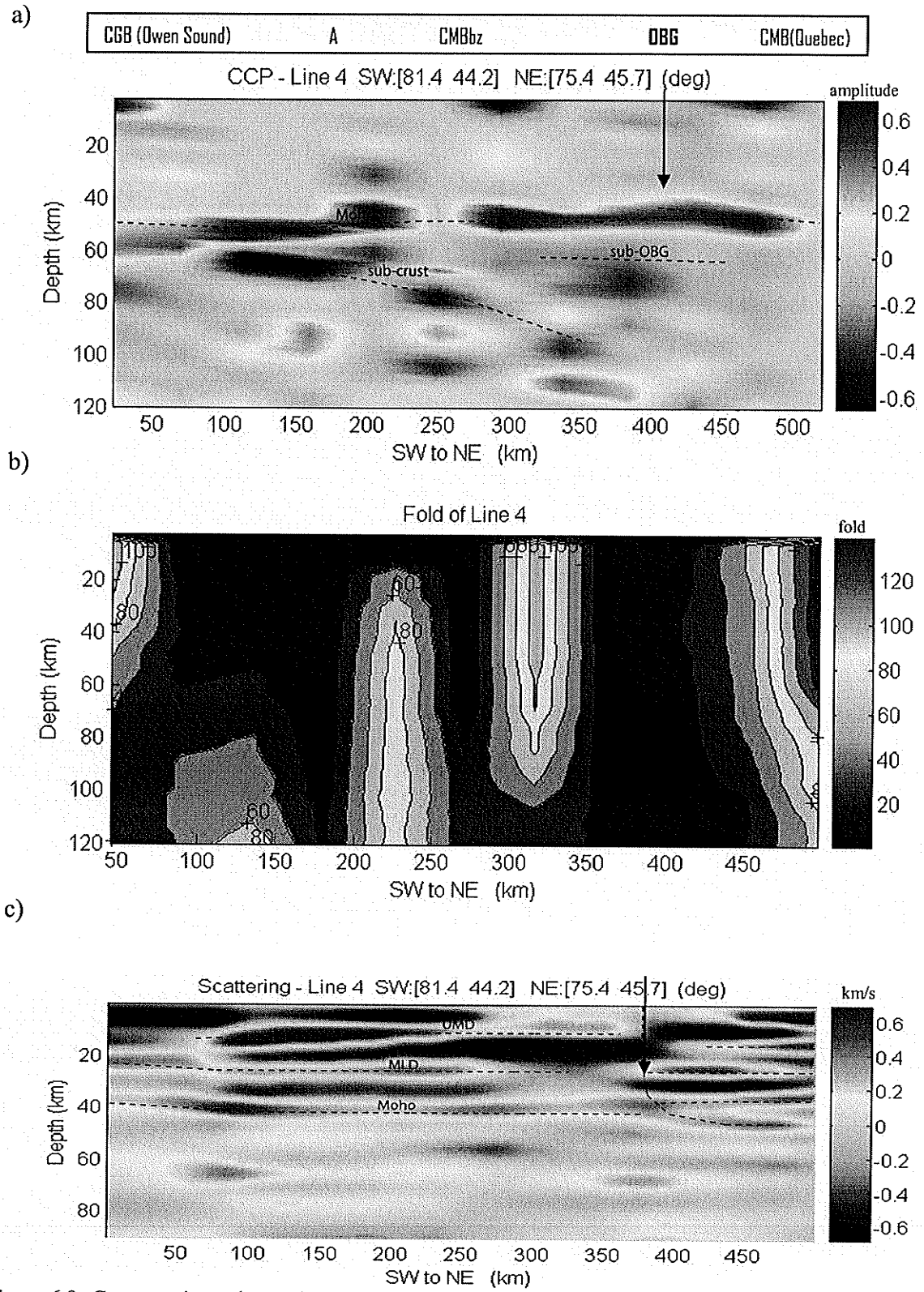

Figure 6.9. Cross-sections along Line 4 (see Figure 6.5 for location) (a) CCP stacking image; (b) fold distribution beneath the line; (c) scattering tomographic image.

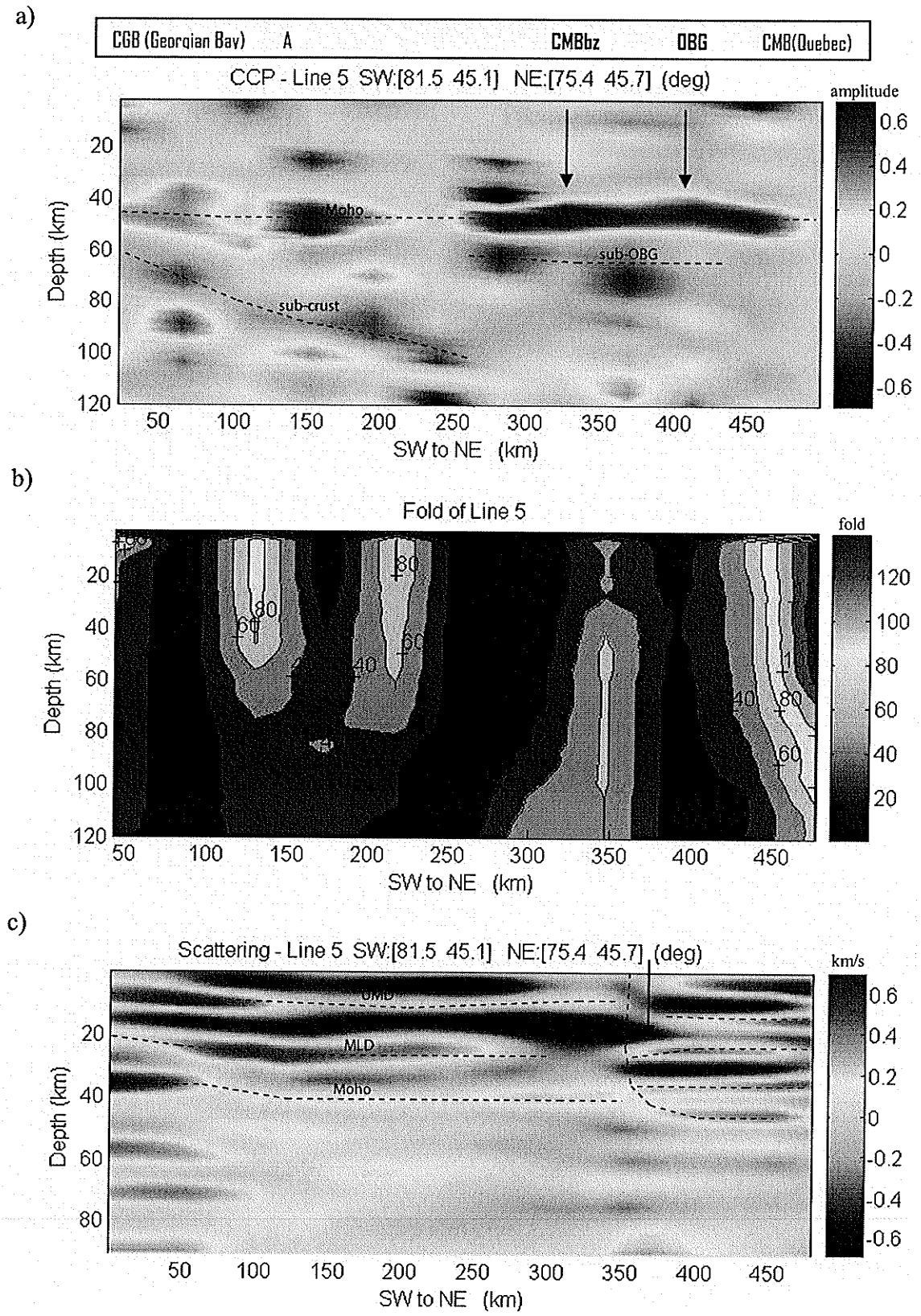

Figure 6.10. Cross-sections along Line 5 (see Figure 6.5 for location) (a) CCP stacking image; (b) fold distribution beneath the line; (c) scattering tomographic image.

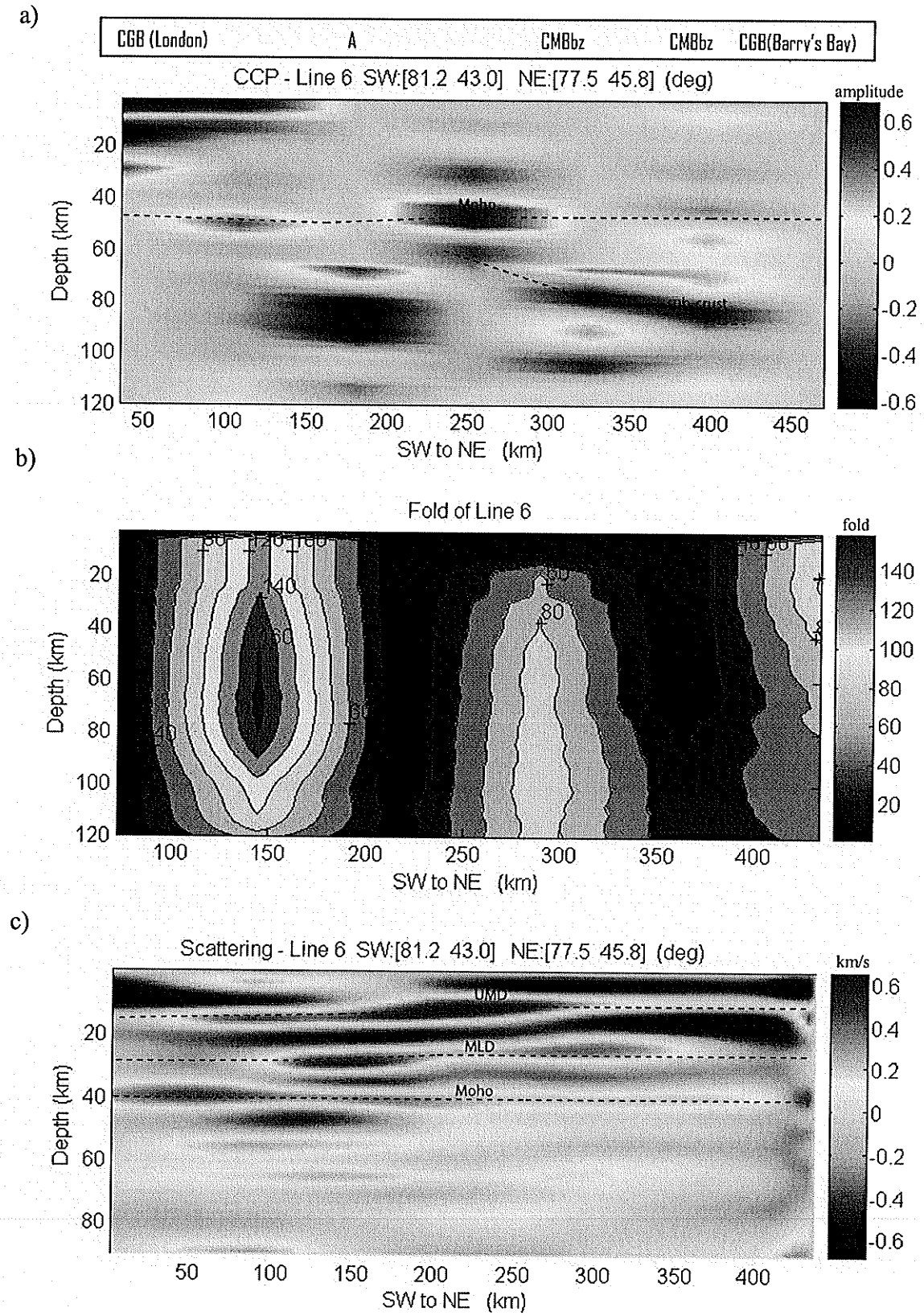

Figure 6.11. Cross-sections along Line 6 (see Figure 6.5 for location) (a) CCP stacking image; (b) fold distribution beneath the line; (c) scattering tomographic image.

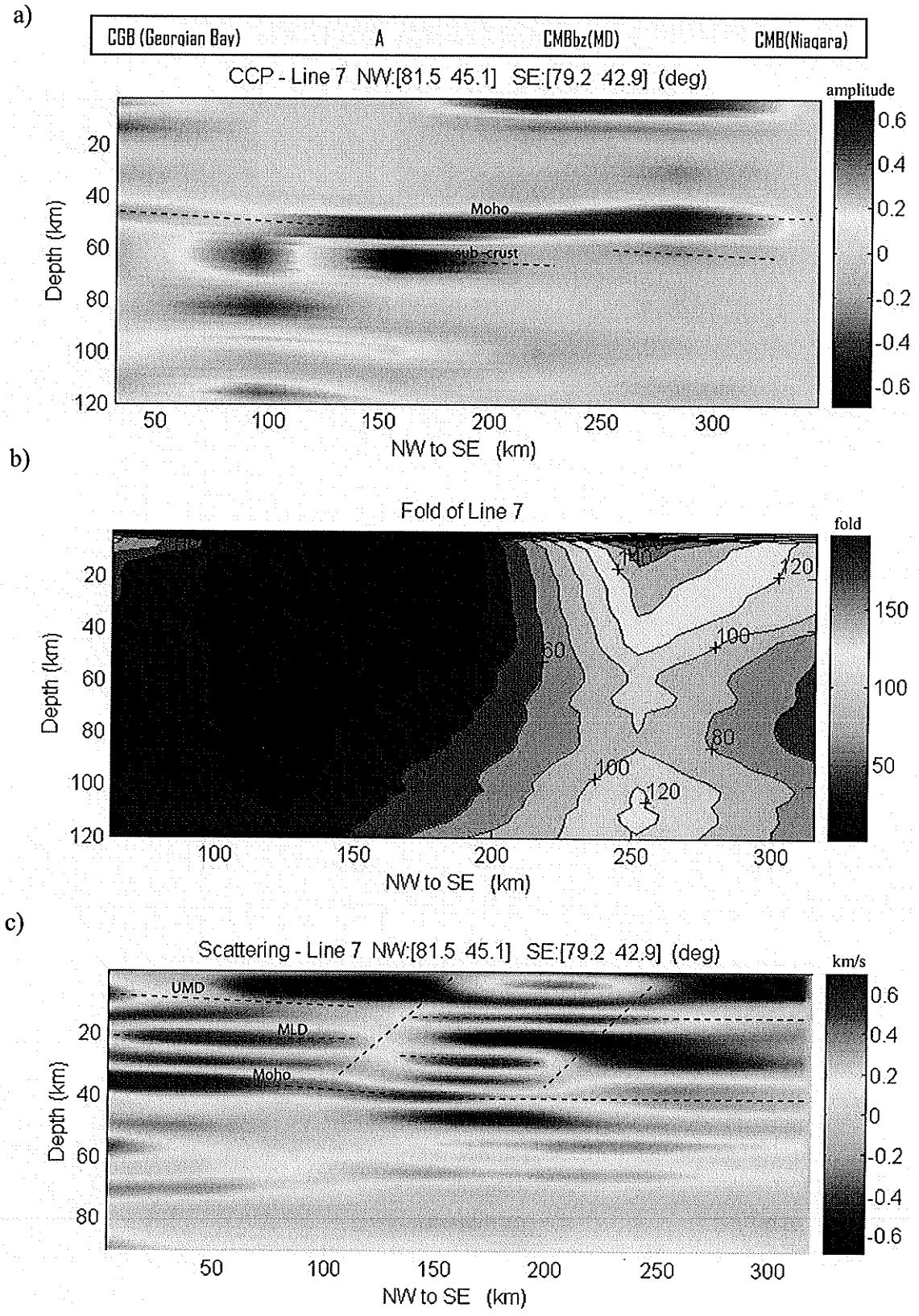

Figure 6.12. Cross-sections along Line 7 (see Figure 6.5 for location) (a) CCP stacking image; (b) fold distribution beneath the line; (c) scattering tomographic image; MD- Mississauga domain.

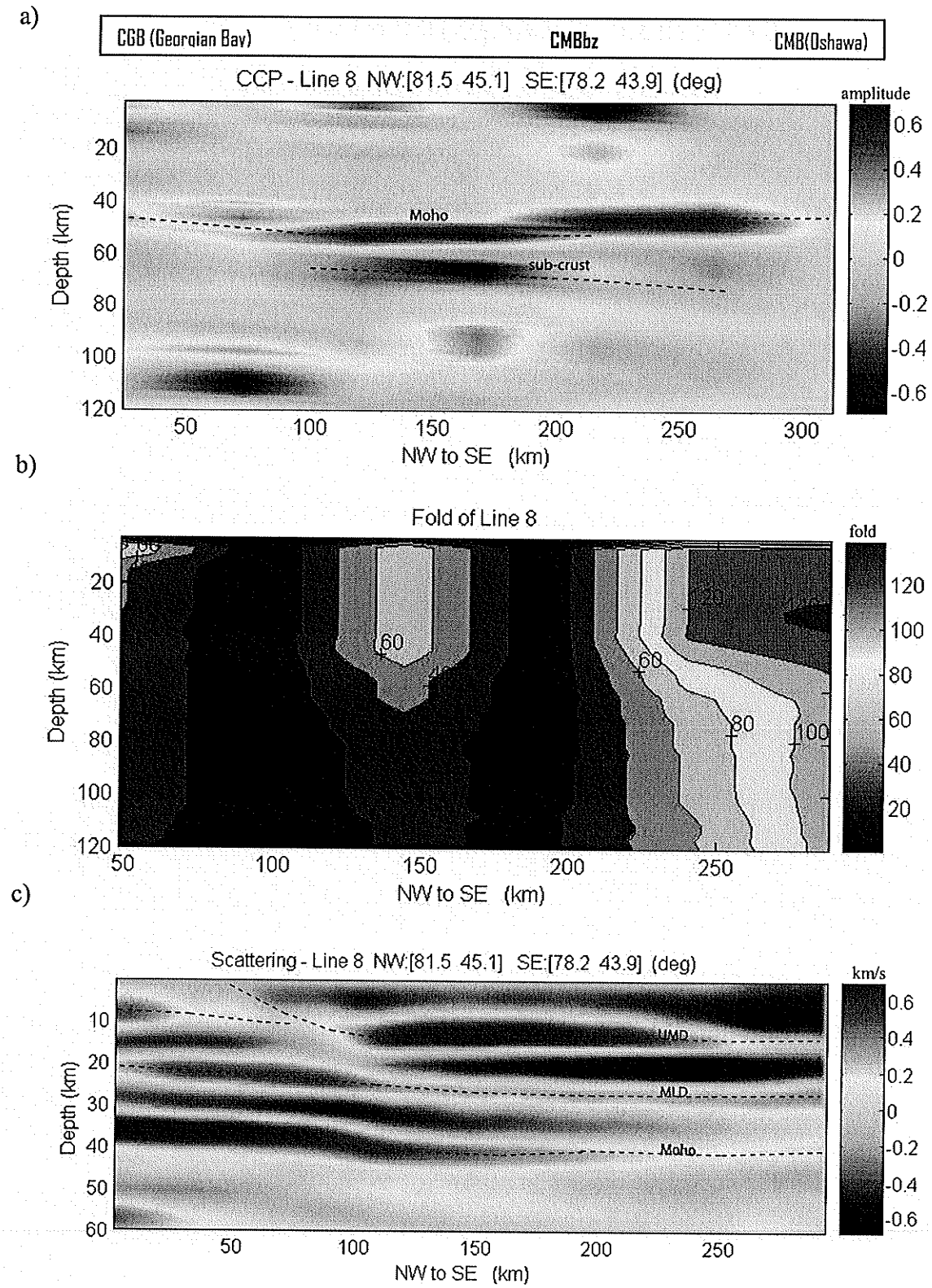

Figure 6.13. Cross-sections along Line 8 (see Figure 6.5 for location) (a) CCP stacking image; (b) fold distribution beneath the line; (c) scattering tomographic image.

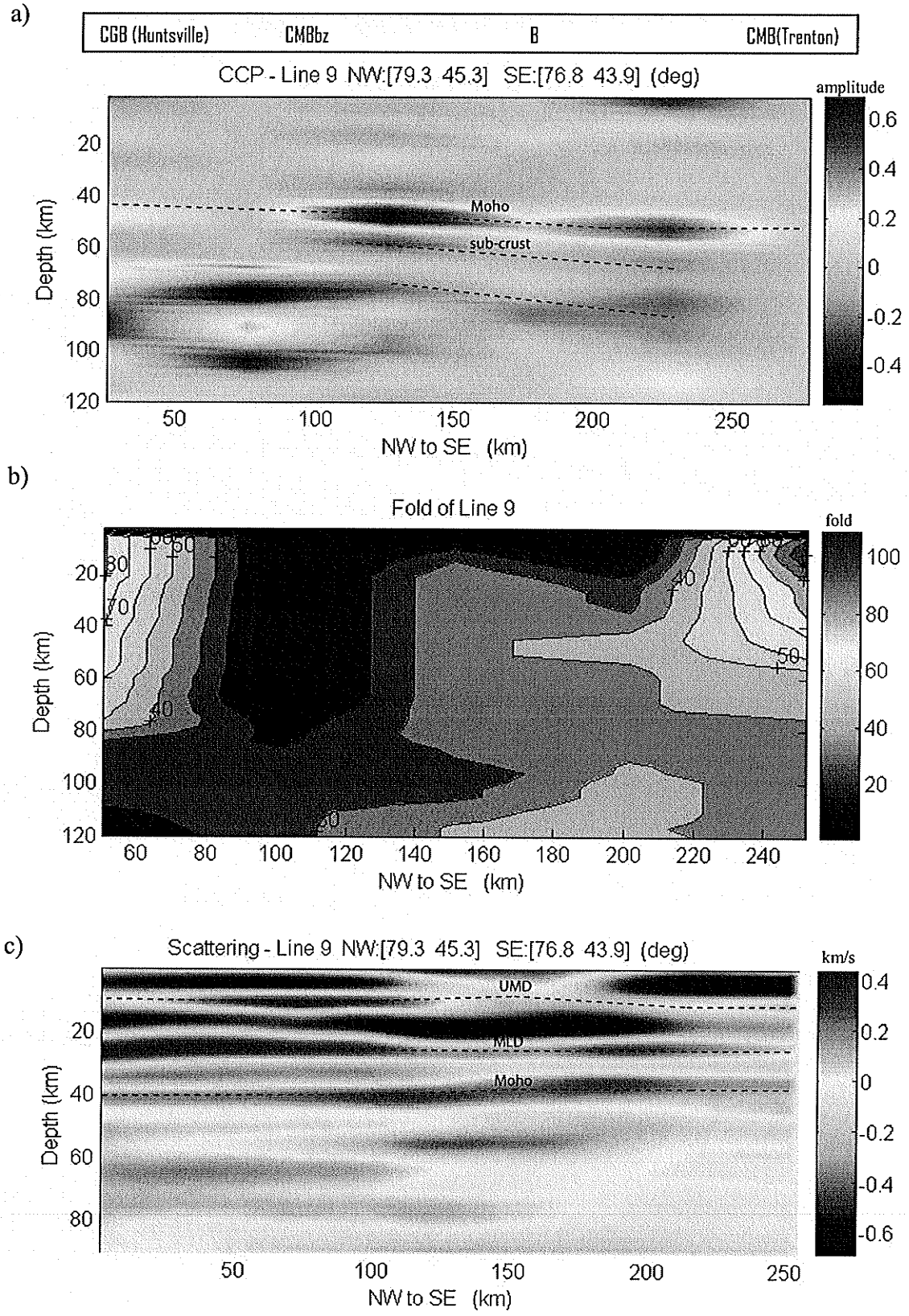

Figure 6.14. Cross-sections along Line 9 (see Figure 6.5 for location) (a) CCP stacking image; (b) fold distribution beneath the line; (c) scattering tomographic image.

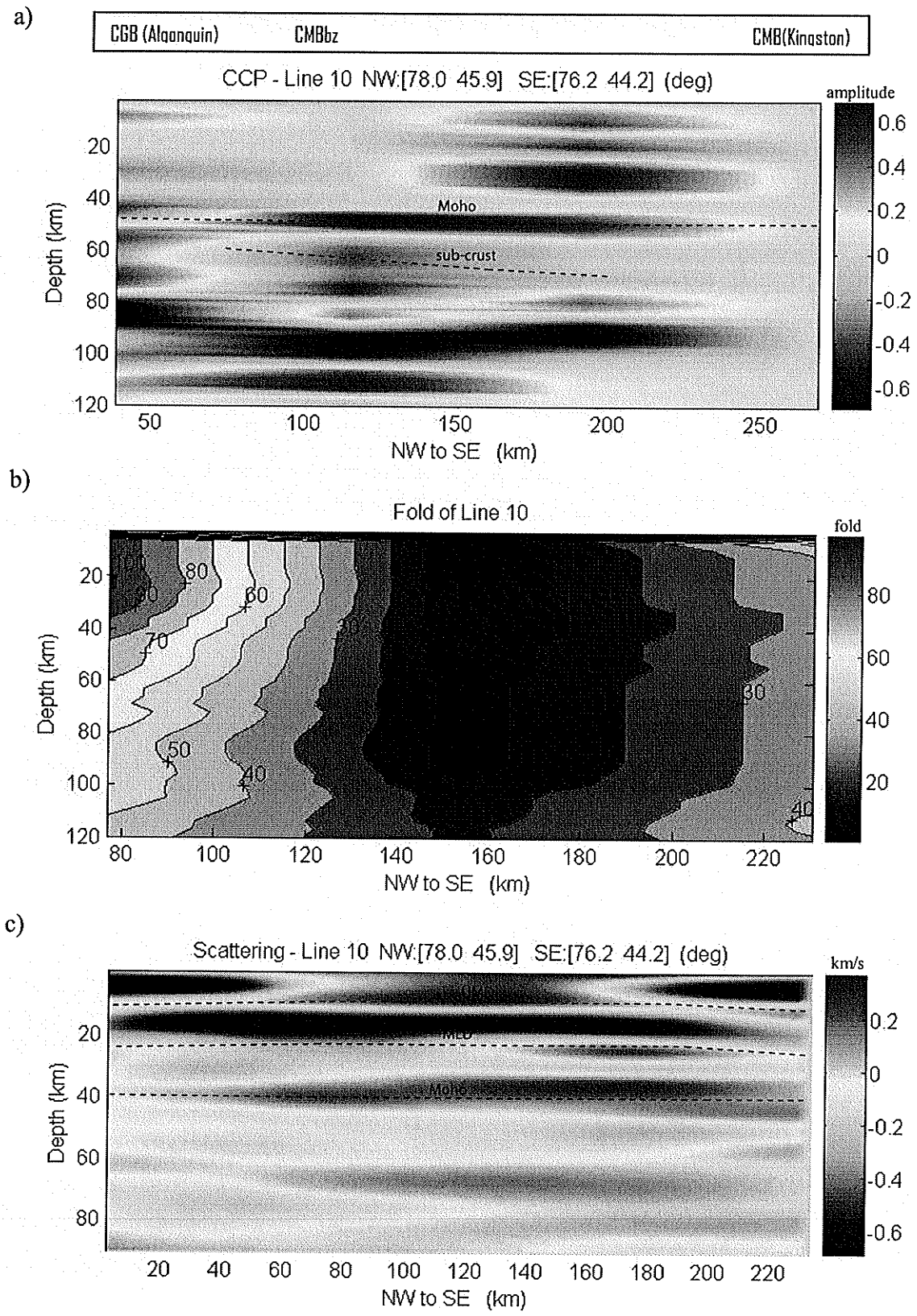

Figure 6.15. Cross-sections along Line 10 (see Figure 6.5 for location) (a) CCP stacking image; (b) fold distribution beneath the line; (c) scattering tomographic image.

1. The Moho depth

The most prominent feature in the CCP stacking images is a positive arrival, at depths ranging from 41 km to 52 km, which is clearly present in all lines. We interpreted it as P-to-S conversions from the Moho discontinuity. Variations in crustal thickness are revealed in the cross-sections. For example, along Line-1, the Moho depth decreases from 49 km in the southwest part of CMB (79.1W, 42.9N) to 41 km at (75°W, 45.4°N) beneath the OBG. This decreasing trend is apparently truncated by normal faults at this point, increasing gradually to 48 km at the end of the profile (northeast of CMB, 74.7W, 45.6N). A similar feature can be observed from Line-2, 3, 4 and 5, probably because these five lines all run in ENE or NE directions across the Ottawa River. However, Line-4 shows greater depth of the Moho, starting at 52 km (the left side of the line), while Line-2 and 3 tend to show a more continuous, nearly flat Moho. This continuous feature is absent in some Lines (1, 3, 4, 5, 6, 9 and 10) which suffer from a lack of ray coverage beneath some area (see middle panel for fold distribution). A less significant difference in crustal thickness is observed along the lines transversing the CGB, the CMBbz and the CMB, i.e., Line 7, 8, 9 and 10. For instance, near one half of Line-8, around (79W, 44.2N), the Moho has been raised by 5 km while elsewhere the crustal thickness tends to be uniform around 42 km to 45 km. The Moho feature appears to be disrupted beneath CMBbz along Line-5 and 8.

The Moho depth variations detected using CCP stacking reveal several features. First, the crustal thickness varies by up to 11 km beneath the study area. Generally, the crust is thicker in the western portion of the region (~79°W-81.5°W), being about 48-52 km. Along the lines transversing the OBG, subparallel to the strike of the CMBbz (Line-

1, 2, 3, 4 and 5), the crust gradually decreases in thickness, reaching a minimum beneath the OBG, and thickening again further to the northeast. Thus the crustal thickness variation along these lines might be due to extension associated with the Ottawa-Bonnechere graben. Secondly, no significant difference in crustal thickness was observed between the southwest portion of the CGB and the southwest portion of the CMB. The crust within the CGB tends to be 44 km to 47 km thick, and about 40 km to 42 km thick within the CMB along Line-7, 8.

2. A sub-crustal negative polarity arrival

Almost all cross-sections had, to some extent, a sub-crustal negative polarity arrival below the Moho (dark blue in cross-sections) with depth ranging from 60 km to 100 km. This negative-polarity feature is slightly to strongly SE dipping varying from 5° to 30° in line 7, 8, 9 and 10 (with ~1.1 to ~1.3 times vertical exaggeration), and it shows a strong NE dip (~ 8° – ~17°) appearing as 15°-35° dips on the cross-sections with ~ 2-2.5 times vertical exaggeration in line 1, 2, 3, 4, 5 and 6. The SE dipping feature can be traced to a depth of ~ 100 km beneath the Hamilton and Niagara Falls area along Line-1, and it tends to be a dominant feature below the Moho along Line-9. As the lines approach to the CMBbz (Line 3, 4, 5 and 6), the upper mantle feature appears to become more complicated, being mottled compared with the features at lines further south (Line 1 and 2), away from the CMBbz. This might indicate that rocks beneath CMBbz and northwest CMB are more heterogeneous than the rocks away from the CMBbz. These negative sub-crustal P-to-S conversions extending the length of orogen might be associated with the formation of tectonic wedges formed through continental collision or intracontinental compression during the Grenvillian orogen (Rondenay, 2000).

3. A sub-OBG negative polarity arrival

The CCP stacking results for lines 1 to 5 all appear to show a negative polarity arrival immediately beneath the positive Moho arrival. This feature is laterally close to the OBG. Although the size of the feature is relatively small, the fact that it is seen on all lines suggests that it is a real feature that might associate with extension of OBG.

6.3 Results from Scattering Tomography Method

To compliment the CCP stacking method, and to generate higher resolution images of heterogeneous crust, another important source of results are obtained by applying the scattering tomography method to the same receiver function data. I use Dr. Frederiksen's code which was developed in Fortran 95 (Frederiksen and Revenaugh, 2004). To do this, a series of preprocessing steps are performed on the receiver function data prior to running scattering tomography programs.

6.3.1 1-D Base Model

I used the same 1-D base model as used in the CCP stacking method for modeling crustal physical properties, i.e., P- , S- velocities and densities (see section 6.2.1).

6.3.2 Scattering Parameters

In this study, we used a grid size of 15×15 km in the depth range 0-90 km to obtain a relatively high resolution image of the southern Ontario ranging from (42.5°N, 82°W) to (46.8°N, 74.2°W), covering a volume of $600 \times 500 \times 90$ km. A total of $40 \times 34 \times 18$ (73440) model cells and 220320 model parameters (3 per cell) are generated

during processing. Due to limitation of the computer memory, a series of preprocessing steps were carried on the receiver function data before performing scattering tomography inversion. These steps can be summarized as follows:

1. resample data to a low rate. The original sample rate of the receiver function data is 0.025 s. Given the frequency content of real data, I resampled the data to a 0.5 s sample rate, reducing the data volume by a factor of 20.
2. cut data into a desired window and mute out primary arrival. Our receiver function data was initially windowed from –10 s to 50 s. I cut the first 12 s and the last 10 s of the data. This not only removes the primary arrival (which is at around 0 s) but also removes the first 2 s of scattered wavefield, to possibly mitigate the effects of spatial aliasing resulting from sparse density of stations as proposed by Poppeliers and Pavlis (2003). Rondenay et al. (2005) have shown that this spatial aliasing effect occurs when the station spacing is larger than 1.8-18 km for the signal with frequencies ranging over the interval 1-0.1 Hz and an average S-velocity of 3.6 km/s. Removing the first 2 s addresses this issue, but will lead to missing the upper 0 to 7 km of structure in the model.
3. split data into subsets to keep the matrix size reasonable. After testing, I split the data into 4 subsets, each having 234 traces (except that the last subset is 233 traces; 935 traces in total). In order to make each subset include multiple widely spaced stations and broad coverage of slowness and back azimuth, I first put all the receiver function waveforms from all single stations together, and randomly picked 234 or 233 traces for each subset.

4. generate grid files. Since deconvolution was used to remove the primary waveform, each trace can be treated as its own event to simplify the problem. Once the traces were divided into subsets with new trace order (step 3), the geometry information including back azimuth and slowness of each trace was written into the grid file with the same trace order as the data.
5. for each subset, generate the inversion sensitivity or partial derivative matrix separately, and then perform the inversion process to produce a model.
6. afterwards, all models are stacked to obtain final results.

Inversion parameters were carefully selected in order to achieve reasonable results and good quality images. The damping parameter value for least-squares inversion is set as 2 based on examination of the trade-off curve of the model norm versus data misfit. This result was obtained by comparing inversion results for damping levels ranging from 0.01, 0.1, 1, 2, 5, 10, 100, 1000 (Figure 6.16). We used a spatial smoothing filter of 3 cells (45 km) in the X (East) direction, 3 cells (45 km) in the Y (North) direction and no smoothing in the Z (vertical) direction to enhance lateral correlation in the lithospheric images.

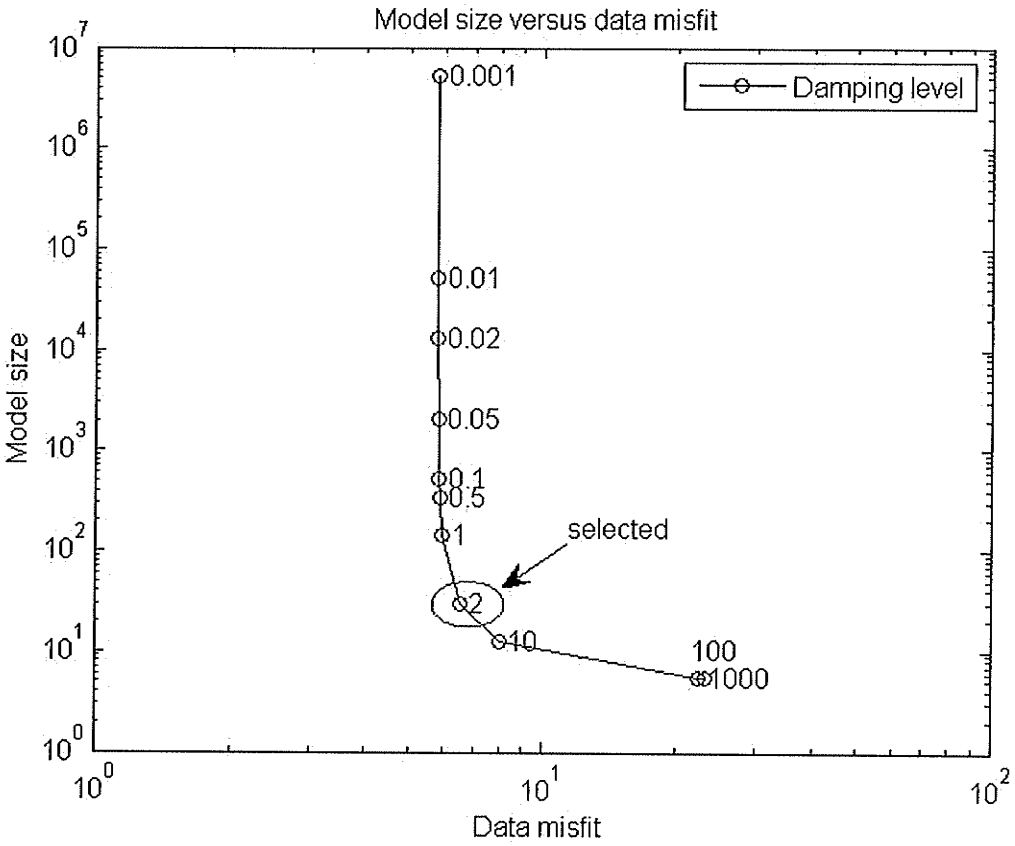

Figure 6.16. Model size versus data misfit, trade-off curve plotted on a logarithmic axis. Numbers on the curves are the damping levels. A damping level of 2 is selected for generating models in this study.

6.3.3 Resolution

A checkerboard resolution test was performed to check the accuracy in recovering models in terms of both the geometry (depth, volume and dip) of discontinuities and the amplitude of associated material property perturbations, which is determined by the combined effects of receiver and earthquake configurations (Rondenay et al 2005). This procedure is similar to the one used by Frederiksen and Revenaugh (2004) in southern California. First, an input model with alternative positive and negative P- and S-anomalies in the even-numbered layers was forward modeled for each subset by using the

partial derivative matrix generated from the real data and source-receiver geometry of the study area. The resultant synthetic data sets are then inverted using the same model parameters as for real data. A final total recovered model is constructed by stacking the four recovered models (one for each subset). Comparing the input model with its recovered model provides a measurement of model resolution, based on the amplitude, location and shape of the P and S velocity anomalies.

This test results are shown in Figure 6.17-6.19. The left column of each figure is an input model for both P and S velocities. In the middle column of the diagram is the recovered P velocity model, and the right column presents the recovered S velocity model. Overall, the P velocity model shows better resolution than S velocity model at greater depth (25-30 km) but the S velocity model has less attenuated perturbation than the P velocity at 15-20 km. All recovered models demonstrate higher resolution in the core and west part of the target area. In contrast, resolution is lost along the edges, especially in the southeast corner, as determined by the station configuration. The anomaly values have been substantially attenuated for both models. For upper crustal structure, there is still some resolution in the core of the S velocity model until below 45 km, while almost no resolution is shown below 40 km in the P model. Based on this resolution test, crustal structures between the middle-lower crustal boundary (below 20 km) to the crust-mantle boundary (above 45 km) larger than ~50 km in the center of the region are expected to be well recovered. After comparing P model and S model images recovered from real data, I chose the S model as the final result for further interpretation, P-velocity perturbation images from scattering tomography can be found in Appendix C.

However, this test may overestimate the actual resolution for several reasons. First, this resolution test did not include noise certain to be present in the real data, even given that the events were carefully selected as described in the previous chapter. The effect of any residual microseismic noise will be to potentially cause inaccuracies of modeling. Secondly, stacking or binning, which was performed on the receiver functions in the process of source estimation, tends to average out small lateral variations, Thirdly, the wavelet is an approximation from the data (Frederiksen and Revenaugh, 2004).

In addition to the above reasons and the direct effects of events and receivers configuration, the resolution might also be affected by departures from assumptions made in its theoretical development. First, the linearalized Born approximation is based on an assumption that the scale length of perturbations is much smaller than the wavelength of the primary wavefield. However, due to limitations of the density of the station distribution and computer memory, the size of 3-D cells in this study is 15 x 15 x 5 km, which may not satisfy the above assumption for features smaller than 100 km. As a consequence, artificial structure in the final images may be generated due to multiple scattering occurred in this medium and small discontinuities. Overly large cells modify the predicted ray kinematics of the wavefield and thereby cause an incomplete focusing of the scattered signal (Rondenay et al., 2005).

Secondly, the first order Born inversion as well as forward modeling was performed based on an isotropic 1-D base model. This is a convenient and commonly employed assumption, as it reduces the number of independent parameters into three unknowns (e.g., $\delta\alpha/\alpha_0$, $\delta\beta/\beta_0$ and $\delta\rho/\rho_0$). However, shear wave splitting and magnetotelluric studies (see review of previous studies in this thesis for references) have

shown that directional variations of elastic and other properties, i.e., anisotropy, are present in the study area, due to mineral fabric orientation and structural features present in the crust and underlying mantle (Eaton et al 2004, Rondenay et al. 2000). This assumption may result in two consequences: first, the structures are mislocated and defocused due to changed ray kinematics; second, recovered scatterers' properties are simplified (compromised) by incorrectly computing the radiation pattern for the scattered waves (Frederiksen and Revenaugh, 2004, Rondenay et al., 2005).

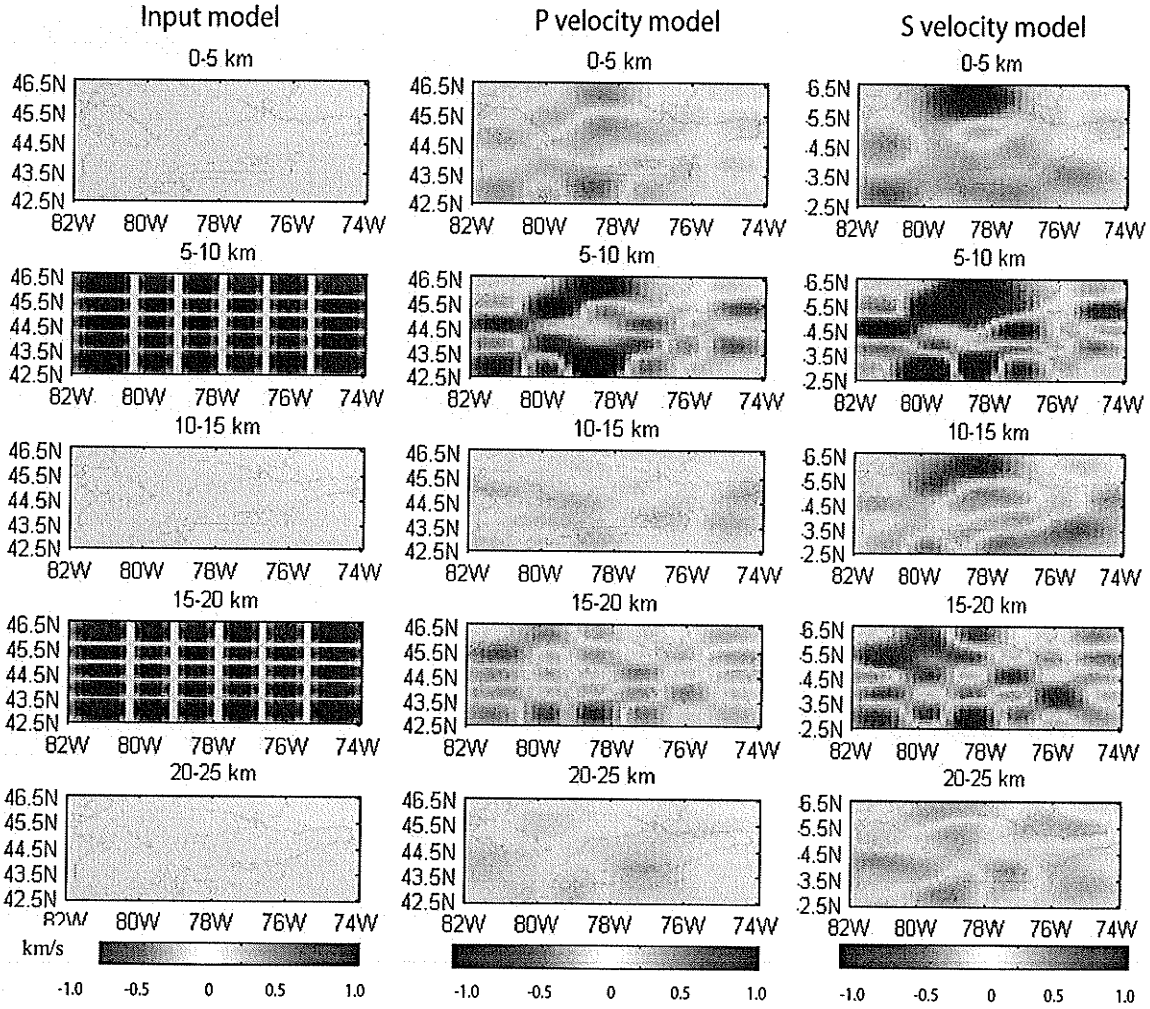

Figure 6.17. Results of resolution test at depths (0-25 km). (a) is an input model with perturbation of ± 1 km/s in the 10-15, 20-25 km layers; (b) stacked recovered P velocity model; and (c) stacked recovered S velocity model.

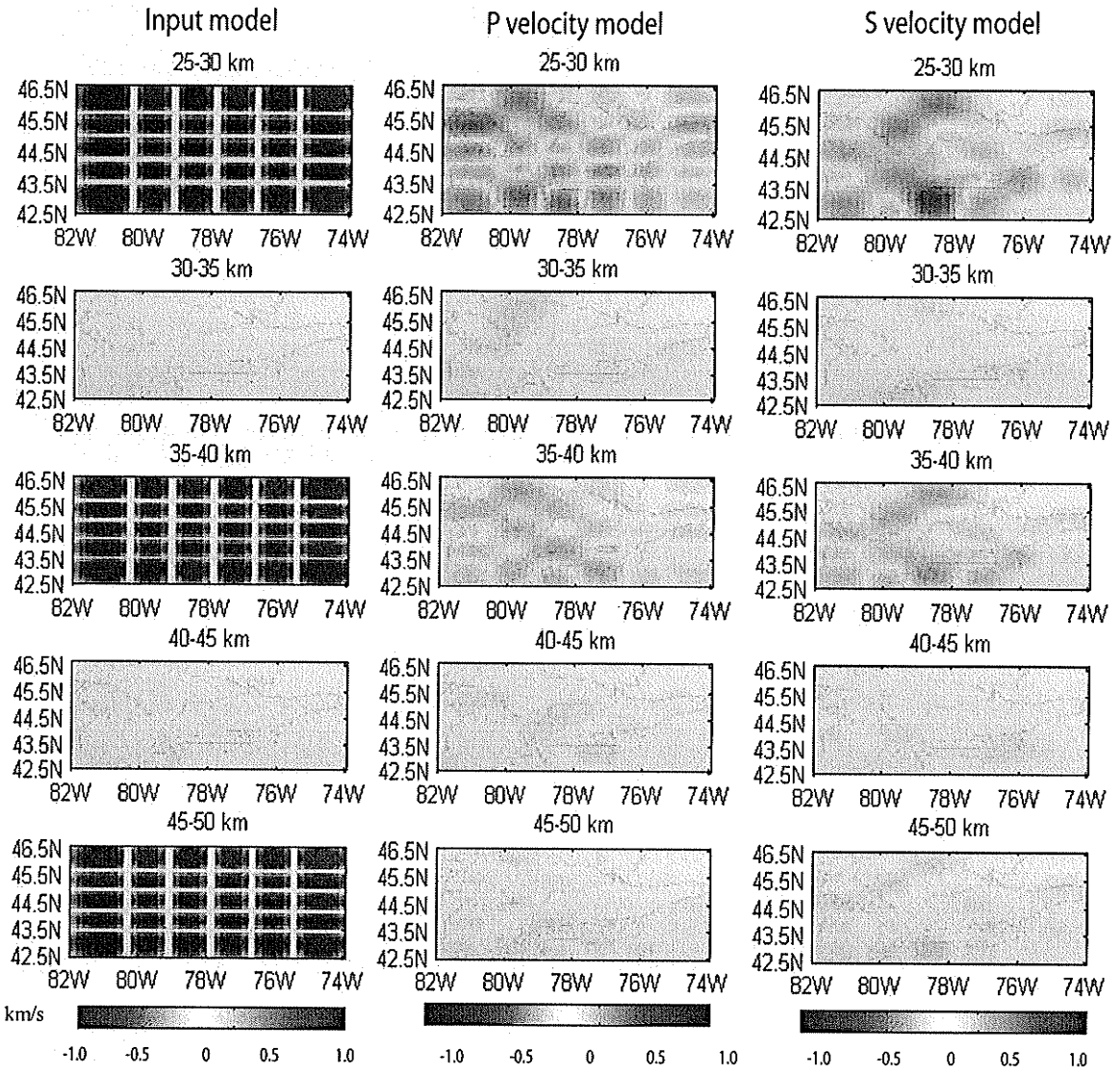

Figure 6.18. Results of resolution test at depths ranging from 25 km to 50 km. (a) an input model with perturbation of ± 1 km/s in the 30-35, 40-45, and 45-50 km layers; (b) stacked recovered P velocity model; and (c) stacked recovered S velocity model.

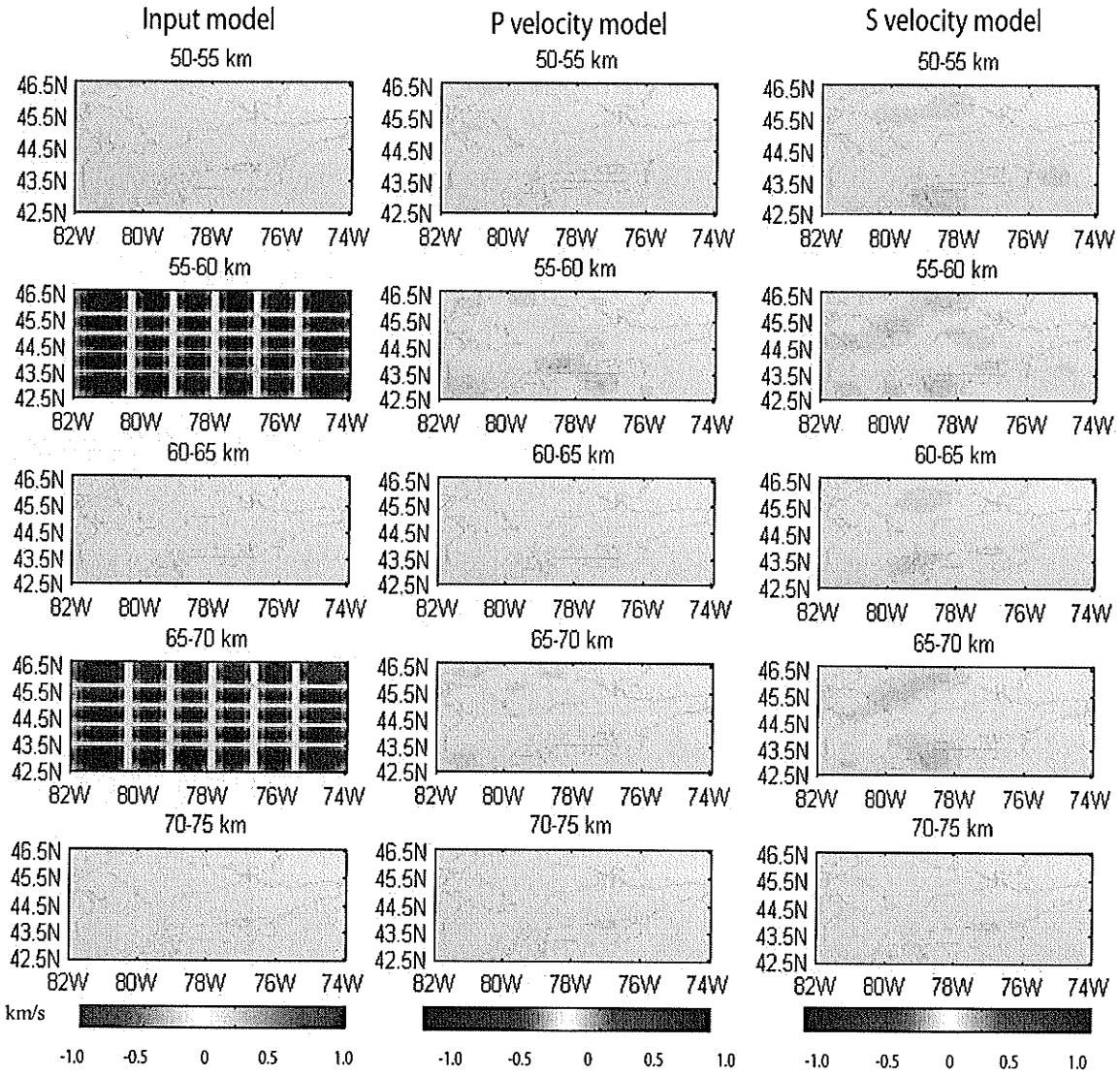

Figure 6.19. Results of resolution test at depths ranging from 50 km to 75 km. (a) an input model with perturbation of ± 1 km/s in the 55-60 and 65-70 km layers; (b) stacked recovered P velocity model; and (c) stacked recovered S velocity model.

6.3.4 Major Structures

The resolution test shows that the available source-receiver geometry is adequate for imaging structures in the range from 5 km depth down to 45 km over the study area. The following two sections will present the images and discuss structures within this range observed on cross-sections and depth slices.

6.3.4.1 Crustal Structures on Cross-sections

The bottom panels (c) of Figures 6.7-6.16 are 2-D cross-section images obtained using scattering tomography along the same lines discussed in the CCP section (see Figure 6.5 for locations). The color scales of these figures are shown on the right side of the plots. Note: here, reddish color represents positive shear wave pertubations, while negative velocity pertubations was plotted in bluish colors. As the sensitivity of scattering tomography decreases with depth, it's only meaningful to compare amplitudes of velocity anomalies within a depth slice. The three most prominent features within this range observed in our model are the positive S velocity perturbations at depths of 10-15 km, 20-30 km and 37-49 km (0.2 to 0.6 km/s) shown in reddish color. These three velocity anomalies appear to be weaker and less continuous within the CMB compared with the anomalies within the adjacent CGB along these ten lines. A large acoustic contrast between CGB units versus CMB units might be correlated with a change in regional metamorphic grade between the CGB and the CMB. CMB rocks also have been intruded by compositionally various plutons of syntectonic, late tectonic and posttectonic age, which may have disrupted crustal structure.

A near surface high-velocity anomaly is visible at depths of 0-10 km (see red and yellow color) in some figures, e.g., Line-1, 2, 3, 6, 7 and 10. This near surface feature will not be interpreted, as it is likely to be an artifact, as the first 2 s of receiver function have been removed before doing inversion as discussed earlier. Therefore the final interpretation is based on features observed from these cross-section lines in the range of 10 km to 45 km.

1. An upper to middle crustal intermediate discontinuity - UMD

The first prominent feature falling into the interpretable range, at depths of between 10 to 15 km, may correspond to the boundary between the upper crust and the middle crust (Mereu 2000; White et al. 2000). It can be observed on all selected cross-section lines. The positive velocity perturbation observed along these ten lines appears to be weaker and less continuous within the CMB compared with the CGB. And this positive discontinuity along NE or WE trending lines (Line-1, 2, 3, 4 and 5) appears to gradually decrease in depth from 15 km in between Lake Erie and Lake Ontario area to ~10 km beneath OBG where it is apparently truncated by normal faults. At the NE end of the profile the UMD shows up strongly at a depth of 15 km beneath Gatineau Park. The UMD appears as a nearly flat feature along Line-9 and 10 at a depth of ~ 10 km, and is a gently sloping feature from 15 km to 10 km depth along Line-6. More interesting features of the UMD can be found along line-7 and 8. Along Line-8, the UMD shows gentle to strong eastward dip one fourth of the way along the profile, where it is apparently truncated and (or) overprinted by a more steeply dipping feature, but is strong and nearly flat thereafter. The UMD on Line-7 is apparently displaced ~ 5 km by possible reverse faulting beneath the Brantford area.

2. A middle to lower crustal discontinuity –MLD

A positive perturbation situated between the middle and lower crust at depths of ~20 to ~30 km is clearly visible along all selected cross-section lines. The velocity perturbation at this discontinuity is in general +0.2 to +0.4 km/s. It emerges at approximately one fourths of the profile, and rises slightly along the Line-1, 2, 3 and 6. The feature tends to be thicker at the ends and thinner in the middle along Line-1, and is broken into two features along Line-2 and 3. A similar feature is observed in the above three lines likely because these lines are close together, running through most of CMB and across the OBG. From the cross-section images run through both CGB and CMB, for example, Line 4, 5, 7, 8 and 9, we can see that this intermediate discontinuity tends to be shallower, at depth of around 20 km, in the northwest side of CGB than in the southeast side of CMB, where it is at a depth of about 25 km.

Some other interesting features of the MLD can be observed from cross-section images along Line-7, 8, 9. Line-7 starts from the edge of the Lake Huron (81.5W, 45.1N), runs through the CGB, across the CMBbz, and ends at the edge of Lake Erie (79.1W, 42.9N) within the CMB. It shows that the MLD jumps by as much as 5 km at the location (80.01W,43.6N) and appears to be absent in the southeast third of the profile. Below the MLD, the Moho discontinuity beyond this point is considerably thicker than in neighboring regions, suggesting an association between MLD and Moho structure. The MLD is disrupted twice under the southeast CMBbz, suggesting that CMBbz splits into two branches. Cross-sections along Line-8 and 9 show a greater SE-dip within the CGB and a nearly flat feature within the CMB.

3. The Moho

The Moho along Line-1 is at a depth of 40 km. It tends to break at one fourth of the profile and appears to split at near the end of the profile, beneath the Ottawa River. This split feature is also shown in Lines 2, 3, 4 and 5 near the Ottawa River (OBG), which might be correlated with boundary faults of the Graben. The Moho depth tends to gradually decrease from beneath Lake Ontario within the CMB (Line-1 and 2) to the Lake Huron area within CGB (Line-4 and 5). For the lines across the major tectonic boundary, CMBbz, i.e., Line-7, 8, 9, 10, the Moho depth increases slightly from 35 km beneath the vicinity of Georgian Bay (west side of CGB) to 40 km near Algonquin Park close to Quebec (east side of CGB). A SE-dipping Moho is obviously observed along Line-7 and 8.

6.3.4.2 Velocity Anomalies on Depth Slices

Figure 6.20 and Figure 6.21 show shear-wave velocity perturbation images in 3-D depth slices at depths ranging from 15 km to 45 km at intervals of 5 km. Figure 6.22 is the same shear-wave velocity model shown in plan view. Variations in shear-wave velocity in the areas at different depths are displayed. From the top layer to bottom layer, the velocity increases as the depth increases (from reddish color to bluish color). There is a sharp change in colors between 35 to 40 km which coincides with the crust-mantle boundary.

Within the crust, the most strong coherent feature observed in this shear-wave velocity perturbation model is a very well defined anomaly elongate in NW-SE direction (around 400 by 125 km). This feature appears a negative velocity perturbation (-1.5 to -0.5 in 10^{-4} km/s, in reddish color) presented beneath the Neoproterozoic Ottawa-

Bonnechere graben at a depth of 20 km (labeled A). The low velocity beneath the OBG may reflect relatively young middle or lower crust which might be correlated with an intrusion of upper-mantle material into the crust during graben formation. Some other elliptical velocity anomalies are visible at this depth, for example, a weaker low-velocity anomaly (labeled B) beneath southeast edge of Lake Huron (~ 81.8°W, ~44°N), and relative high velocity anomalies (0.5 to 1.5 in 10^{-4} km/s, in bluish color), labeled as 'C' and 'D' around the Greater Toronto area, along with two high-velocity anomalies (labeled E and F) located on the east side of study area at ~ 43.5°N, and ~ 45.5°N in longitude, respectively. However, as these features are generally less cohesive, and smaller than the size (100×100 km) used for the resolution test, I will not interpret these features in detail.

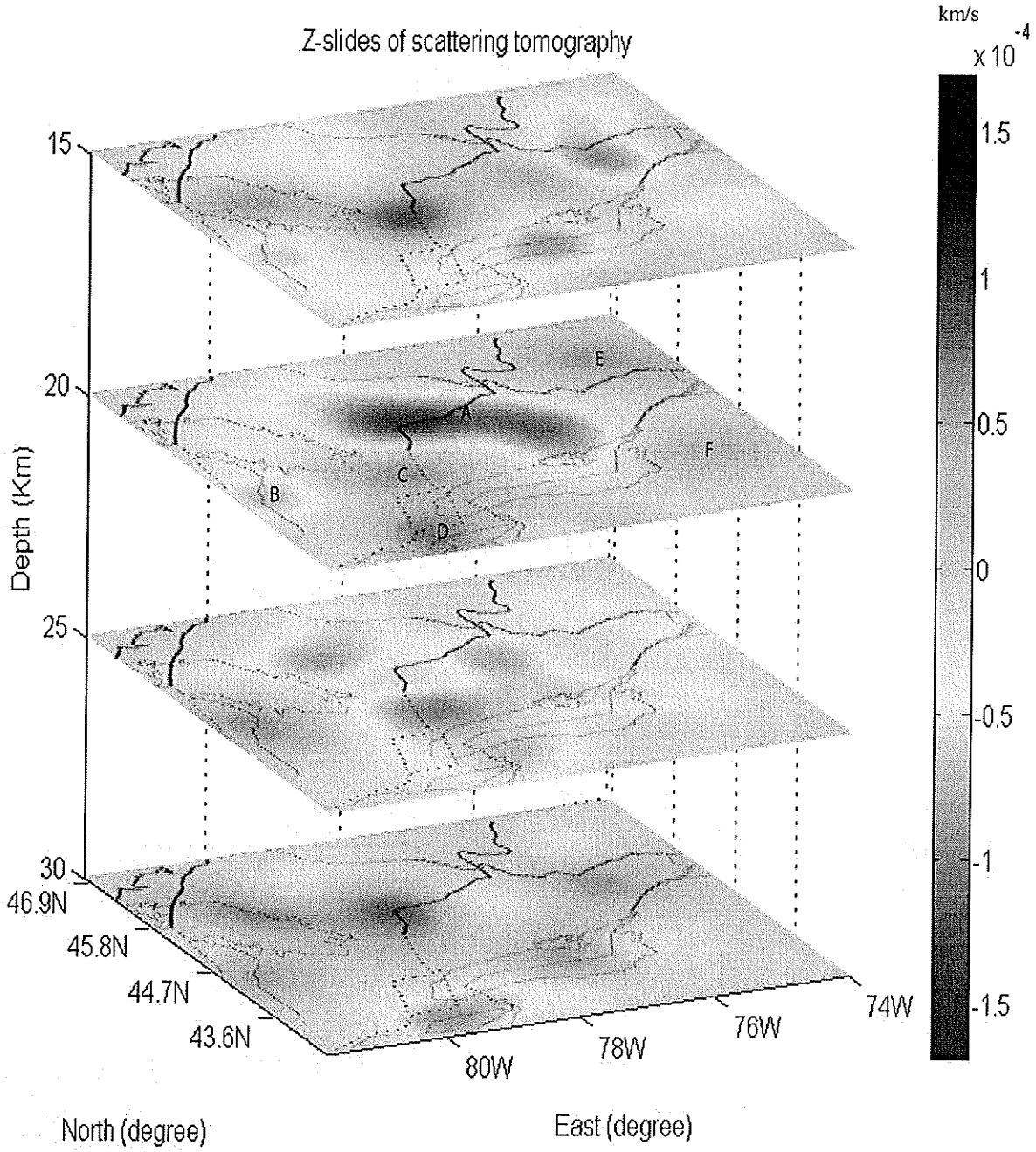

Figure 6.20. Shear-wave velocity perturbation images in 3-D slices superimposed on regional map between 15 km to 30 km with 5 km interval. The colormap represents the velocity perturbation in 10^{-4} km/s, where positive perturbation is shown in bluish color, and negative perturbation is shown in reddish color.

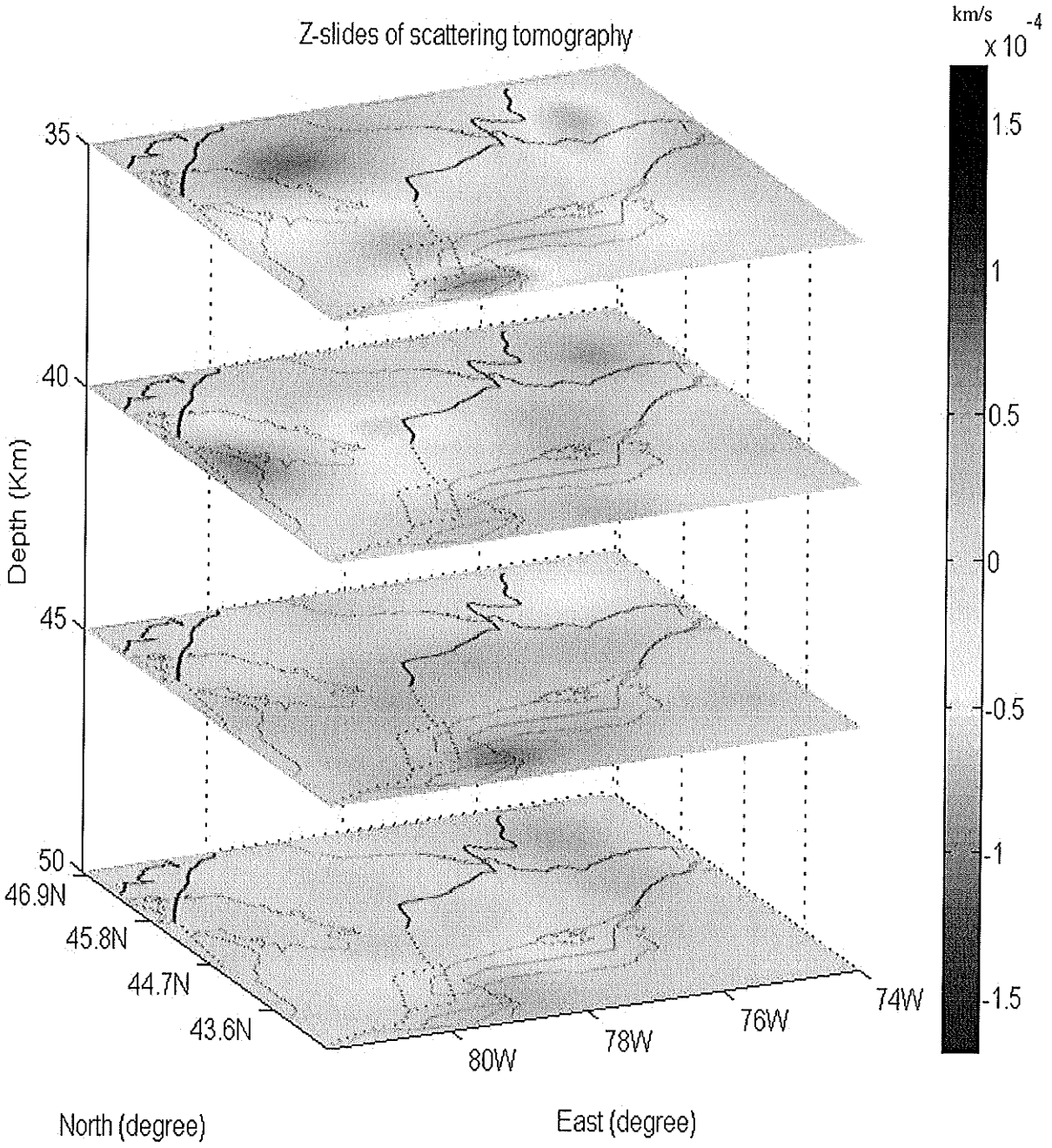

Figure 6.21. Shear-wave velocity perturbation images in 3-D slices superimposed on regional map at depth of between 35 km to 50 km with 5 km interval. The colormap represents the velocity perturbation in 10^{-4} km/s, where positive perturbation is shown in bluish color, and negative perturbation is shown in reddish color.

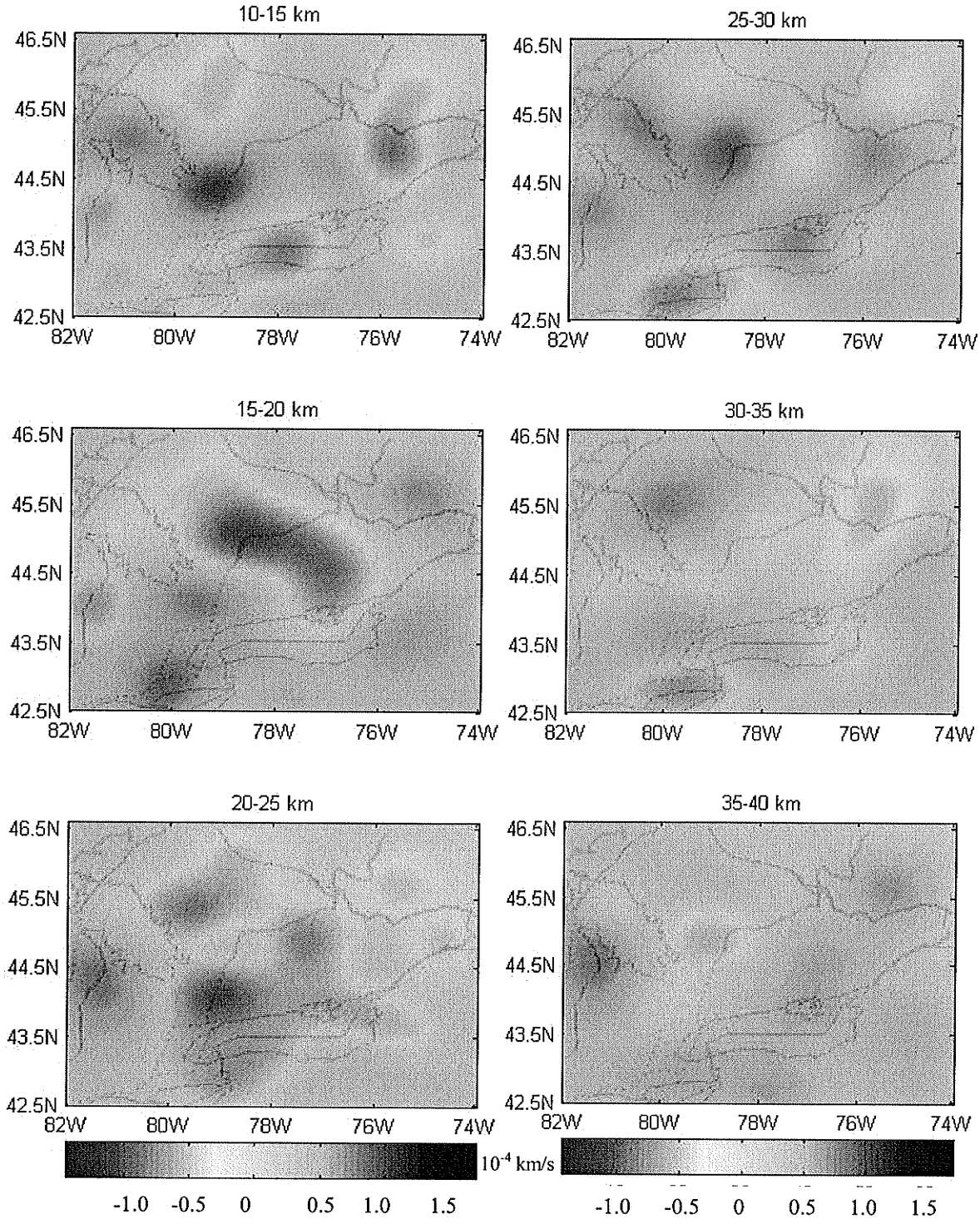

Figure 6.22. Depth slices of shear-wave velocity perturbation at depth of between 10 km to 40 km in plan view. Colormap represents the velocity perturbation in 10^{-4} km/s, where positive perturbation is shown in bluish color, and negative perturbation is shown in reddish color.

6.4 Summary of the Results and Interpretations

In summary, the results and interpretations obtained using CCP stacking and scattering tomography techniques are as follows:

1. CCP stacking method clearly detected the Moho at depth of ~41-52 km. A sub-crustal negative-polarity arrival at depth of ~ 60-100 km, which might correlate with remnants of subduction occurring during orogeny as well as a sub-OBG negative polarity arrival immediately beneath the positive Moho arrival, are visible in lines 1 to 5. The latter feature is laterally close the OBG, indicating that it might be correlated with the extension of the OBG.
2. Higher resolution images of crustal structure were obtained using scattering tomography. Besides the Moho, two other crustal discontinuities, UMD-upper to middle crust discontinuity at depth of ~10-15 km and MLD-middle to lower crust discontinuity at depth of ~20-30 km, respectively, are clearly shown by positive S-wave velocity perturbations.
3. Within the crust, a SE-dipping feature (dipping 25-30 deg) is found beneath and near the Grenville Front Tectonic Zone (GFTZ). The detected feature is consistent with previous interpretations of the GFTZ as a prominent southeast-dipping region of amphibolite-facies rocks that underwent ductile thrusting at ~ ca. 1000 Ma, superimposed on older mylonite in the Killarney Belt. A weaker SE-dipping feature is observed beneath the Central Metasedimentary Belt (CMB) and the Central Metasedimentary Belt boundary zone (CMBbz), which also can be attributed to tectonically imbricated units of the CMB and CMBbz.

4. The CCP and scattering cross-section images show that the crust beneath the Ottawa-Bonnechere Graben (OBG) has been thinned as much as 11 km relative to its neighboring blocks by normal faulting, which further supports that the graben is an ancient rift.
5. A linear, cohesive, NW-striking low velocity S-wave anomaly, oriented parallel to the OBG along its SW edge is clearly shown in a depth slice at 20 km. It is likely to be a graben-related feature.
6. Two lines across the Mississauga domain (MD), SW of the CMBbz were examined in detail. Along Line-7 (oriented NW-SE), the MLD is disrupted twice beneath the MD. However similar disruptions are not found aong Line-2 (oriented SW-NE), indicating that the CMBtz may have formed a strike-slip duplex system oriented parallel to, and west of, Lake Ontario. The CMBbz might be split into two branches beneath this domain.

Chapter 7

Discussion

The following two sections will be introduced in this chapter, first, discussing the differences and similarities between the images obtained using CCP stacking and scattering tomography, finally, comparing results obtained using above two methods in this study with previous studies.

7.1 Comparison of CCP Stacking and Scattering Tomography Results

Both the CCP stacking and scattering tomography methods used in this study imaged the Moho. A comparison of Moho structure as dectected by CCP stacking and scattering tomography along Line 1 through 10 is given in Table 7.1.

Table 7.1. Moho structure comparison between CCP stacking results and scattering tomography results along Line-1 to Line-10. Moho depth is calculated as the mean of the maximum and minimum depth of the Moho along this line. Note that 'decrease' or 'increase' in the table mean decrease or increase in depth.

Line	Structure	CCP stacking	Scattering tomography
1	Moho depth (km)	Min=41, max =51, mean = 46	Min=37, max=47, mean=42
	Crustal thickness variation	Nearly flat to 1/3 (A), begins to decrease in depth to ¾ of the line (OBG), increase hereafter	Nearly flat to 1/3 (A), begins to decrease in depth to ¾ of the line (OBG), increase hereafter
	other features	truncated at ¾ (OBG)	Split feature at ¾ (OBG)
2	Moho depth (km)	Min=42, max=52, mean=47	Min=38, max=48, mean=43
	Crustal thickness variation	Slight decrease in depth to 1/4 (A), nearly flat to 7/10 (OBG), increase hereafter	Slight decrease in depth to 1/4 (A), nearly flat to 7/10 (OBG), increase hereafter
	other features	truncated at 7/10 (OBG)	Split feature at 7/10 (OBG)
3	Moho depth (km)	Min=41, max=51, mean=46	Min=39, max=48, mean=43.5
	Crustal thickness variation	Slightly decrease in depth to ¾ (OBG), increase hereafter	Slightly decrease in depth to ¾ (OBG), increase hereafter
	other features	truncated changes at ¾ (OBG)	Split feature at ¾ (OBG)
4	Moho depth (km)	Min=41, max=50, mean=45.5	Min=38, max=47, mean=42.5
	Crustal thickness variation	Slight decrease in depth to ¾ (OBG), increase hereafter	Slight decrease in depth to ¾ (OBG), increase hereafter
	other features	truncated changes at ¾ (OBG)	Split feature at ¾ (OBG)
5	Moho depth (km)	Min=41, max=51, mean=46	Min=39, max=49, mean=44
	Crustal thickness variation	Slight increase to 3/5 (CMBbz), nearly flat to 4/5 (OBG), increase hereafter	increase to 1/3 (A), nearly flat to 4/5 (OBG), increase hereafter
	other features	Sharp changes at 3/5 (CMBbz), and 4/5 (OBG)	Split feature at 4/5 (OBG)

6	Moho depth (km)	Min=41, max=47, mean=44	Min=38, max=42, mean =40
	Crustal thickness variation	Decrease to 1/3 (A), nearly flat to 2/3 ($CMBbz^1$), increase hereafter	Slight increase to 1/3 (A), nearly flat to 2/3 ($CMBbz^1$), slight decrease hereafter
	other features	break at 1/3 (A), and 2/3 ($CMBbz^1$)	Appear to be break at 1/3 (A), slight change at 2/3 ($CMBbz^1$)
7	Moho depth (km)	Min=40, max=48, mean=44	Min=36, max=42, mean=39
	Crustal thickness variation	Slight increase to 1/3 (A), slight decrease to 2/3 (CMBbz), nearly flat hereafter	jumped 3 km at 1/3 (A), rise 2 km at 2/3 (CMBbz), nearly flat hereafter
	other features	Trend change at 1/3 (A) and 2/3 (CMBbz)	Jump at 1/3 (A) and rise 2/3 (CMBbz)
8	Moho depth (km)	Min=40, max=46, mean=43	Min=36, max=42, mean=39
	Crustal thickness variation	Slight increase to ½ (CMBbz), and slight decrease hereafter	Slight increase to ½ (CMBbz), and slight decrease hereafter
	other features	truncated at ½ (CMBbz)	truncated at ½ (CMBbz)
9	Moho depth (km)	Min=44, max=48, mean=46	Min=39, max=42, mean=40.5
	Crustal thickness variation	Emerges from ¼ (CMBbz), slightly decrease to 5/7 (B), nearly flat hereafter	Nearly flat to 5/7 (B), rise in 2 km and nearly flat hereafter
	other features	Break at 5/7 (B)	rise at 5/7 (B)
10	Moho depth (km)	Mean =44	Mean=40
	Crustal thickness variation	Nearly flat	Nearly flat
	other features	—	—

Comparing ten cross-sections which cover the well-resolved portion of the study area and major tectonic structures, we can see that:

1. Images obtained by using scattering tomography display higher resolution than images generated using CCP stacking. At least three prominent features, including the UMD, MLD and Moho, and more complicated crustal structures are observable in scattering. In contrast, CCP images show simpler structure to greater depth, as deep as 420 km. The Moho is a very well defined as a positive (red) arrival with homogeneous and negative polarity amplitude background (green and bluish color) on the CCP images; on the scattering tomography images, it is a narrower positive perturbation with less lateral continuity. This discrepancy is interpreted to be caused by the different theoretical bases for two methods: CCP stacking is based on ray theory while scattering tomography uses scattering theory. Scattered arrivals are clearly important to detecting detailed crustal structure.
2. The Moho in CCP stacking is at depths between 40 km and 52 km with mean value of about ~ 44 km to ~ 47 km, while the Moho in scattering tomography is at depths between 37 km and 49 km with mean value of ~ 39 km to ~44 km. All structures, including the Moho arrival, are mapped to slightly greater depths in CCP images; the differences is between 2.5 km to 5 km between CCP stacking images and scattering tomographic images. Several reasons may contribute to this difference. First, the vertical cell sizes used for CCP stacking and scattering tomography are different, (3 km in CCP and 5 km in scattering, respectively), which means CCP results are in principle more precise than scattering, but

bearing a ±3 km offset (misfit) in depth prediction. Secondly, because CCP stacking is valid only for non-diffracted energy and is based on an assumption of a horizontally layered Earth. For scattered waves, which occur when $a \approx \lambda$ (<2 km), CCP will mislocate scatterers, while scattering tomography detects scatterers (such as irregularities of the Moho) but smooths them laterally. For example, the travel-time from a point scatterer is larger than from specular conversion points on the same surface, as shown in Figure 7.1, and this will cause CCP stacking to map the scatterer (dark green point) to a greater depth (the light green point), it exaggerating the depths of scatterers. Due to the above reasons, the final values of the Moho depth in this study was obtained by averaging the CCP stacking and scattering results. Finally, there is a strong trade-off between the crustal thickness estimated only from the time delay of Moho Ps phase and crustal Vp/Vs ratio, i.e., the 1-D base model. Both CCP and scattering tomography will return incorrect depths if the base model is incorrect, being particularly sensitive to the Vp/Vs ratio. However changes in the base model do not affect the presense or absence of velocity anomalies (Frederiksen and Revenaugh, 2004). This ambiguity can be reduced significantly by incorporating multiples (Zhu and Kanamori, 2000).

3. The two methods, however, show very consistent lateral variation in the crust. For example, the thinnest crust occurs beneath the OBG, at a depth of ~40 km in CCP results, while at a depth of ~38 km in scattering results; the crust beneath the southwest CMB is thicker (~ 50 km in CCP results, ~46 km in scattering results) than in the northeast CMB (~43 km in CCP results, ~ 38 km in scattering results);

crustal thickness variations of up to 7 km occur between the CGB and CMB along line-7, 8, and 9.

4. Both methods indicate marked changes at some important features. For example, in the vicinity of the OBG, the Moho is apparently truncated by extensional normal faults in CCP, and appears to be a split feature in scattering results which I interpreted as resulting from normal faulting.
5. A sub-crustal negative polarity arrival below the Moho (dark blue in maps) with depth ranging from 60 km to 100 km can be seen in CCP stacking. This negative-polarity feature is slightly to strongly SE dipping varying from 5° to 30° along line 7, 8 and 9, and appears to be NE-dipping (~10°) along line-1, 2, 3, 4 and 5. A similar negative-polarity dipping feature can be also found in scattering but is not as clear as in CCP results.
6. A sub-OBG negative polarity arrival. The CCP stacking results for Lines 1 to 5 all appear to show a negative polarity arrival immediately beneath the positive Moho arrival. This feature is laterally close to the OBG. There is a weaker negative feature in scattering results.

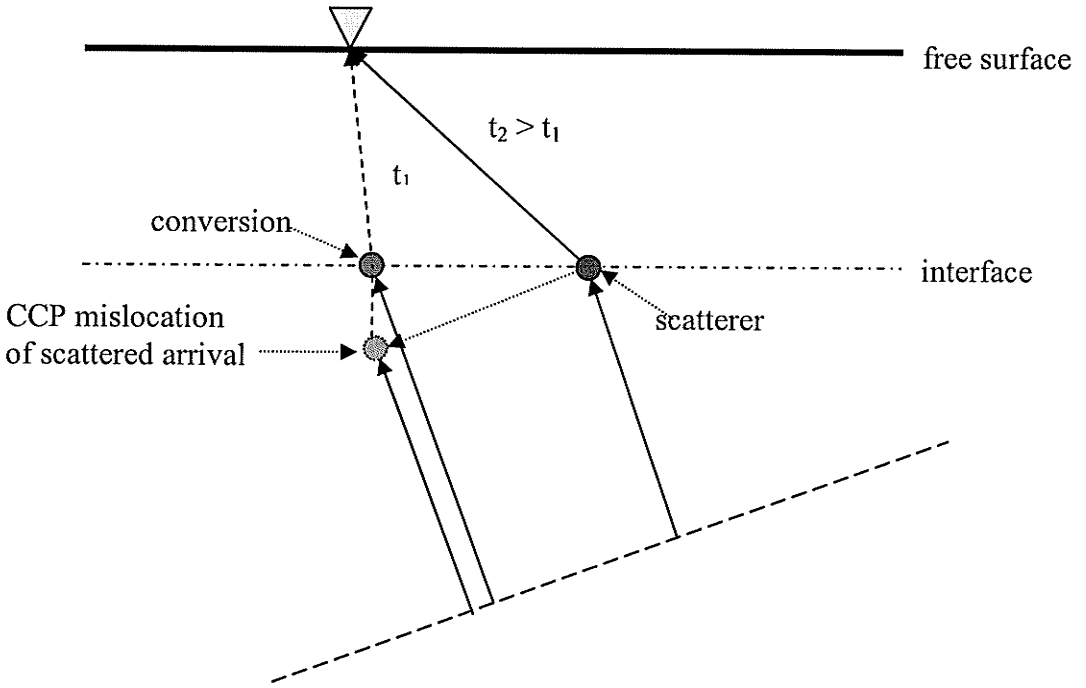

Figure 7.1. Diagram showing mislocation in CCP stacking. Here t_2 represents travel-time from scatterer (filled dark green circle) to the receiver (yellow triangle), t_1 denotes travel-time from conversion point (filled blue circle) to the receiver (yellow triangle) in which $t_2 > t_1$. The scatterer was mislocated to an assumed conversion point (light filled green circle) at greater depth according to Snell's law.

7.2 Comparison with Other Geophysical Studies

I compared the images obtained using CCP stacking and scattering tomography in this study with results interpreted from other geophysical studies, including seismic reflection and refraction, teleseismic, and aeromagnetic studies.

The previous controlled-source seismic reflection and refraction surveys (e.g. CLIMPCE-Line L, Green et al. 1989; AGT90-Line 31, 32 and 33, White et al. 1994; AGT92-Line 15, Kellet et al, 1994) were mostly deployed in the northwest part of the

region focusing on the Grenville Front Tectonic Zone; however teleseismic stations were installed around the CMBbz, and only a few stations situated between them. As a consequence, comparisons drawn between this study and interpreted profiles can only be roughly made by defining the profiles near or parallel to the previous interpreted profiles. Figure 7.2 shows this comparison, in which the compariable lines were highlighted in the same colors. For example, one third to the end of Line-9 may be compared to AGT90-Line 32 and 33 (green); first half of Line-8 may be compared to the second half of GLIMPCE Line-J (blue); one third to one harf of Line-3 to SOSS Line 4 (purple). Two thirds to the end of the Line-3 to COCRUST-82 line-QR (orange) and so on.

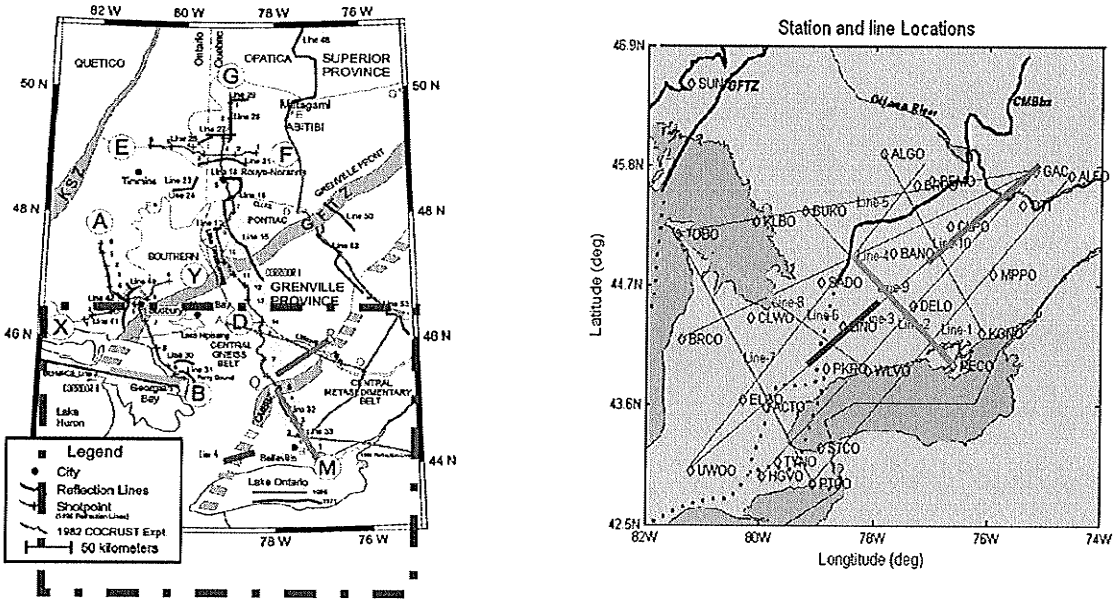

Figure 7.2. Maps show comparisons between previous controlled-source reflection and refraction studies (modified from Roy and Mereu, 2000; left, where right rectangle in this map showing the location of this study area) with this study (right). The comparable lines were highlighted in the same colors. e.g., AGT90-lines 32&33 and part of Line-9 (green); part of GLIMPCE line-J and part of Line-6 (blue); SOSS line 4 (purple) and COCRUST82 Line-QR (orange) and parts of Line-3 (purple and orange).

1. Crustal thickness

Table 7.2 lists the comparision between those comparable lines (this study and previous controlled source seismic studies and another teleseismic receiver function study). The observed crustal thicknesses in this study ranges from 38.5 km to 50.5 km, as obtained by averaging of CCP and scattering results due to the reasons mentioned earlier. Crustal thickness in the central Grenville orogen (700 ×400 km) ranging between ~ 34 km and 52.4 km has been observed by performing a simple semblance-weighted stacking technique using teleseismic receiver functions (Eaton et al. 2005). Eaton et al (2005) also found the thinnest crust (~ 34.5- 37 km) occurring northeast of the OBG and correlated with areas of high intraplate seismicity. Through comparison, we can see that the crustal thicknesses obtained in this study are in good agreement with the Moho depth estimates retrieved by the aforementioned techniques.

Table 7.2. the Moho depth comparison between the results from previous controlled-source seismic, teleseismic studies and results from this study.

This study	**Previous studies**	**Agreement**
Line-9 (1/3->end) ~ 43.5 km	Line 32&33 ~ 44 km	good
Line-8 (Start->1/2) ~ 41 km	GLIMPCE-line-J (1/2->end) ~ 42 km	good
Line-3 (1/3->1/2) ~ 40 km	SOSS Line-4 ~ 39 km	good
Overall ~ 38,5 – 50.5 km, thinnest at OBG	Eaton et al (2005), 700x400 km ~ 34 – 52.4 km, thinnest at OBG	good

2. Crustal structure

Figure 7.2 and Figure 7.3 show two comparable lines. Line-9 and Line-8 obtained using scattering tomography (in figures b) in this study compared with velocity models (in figures a) of AGT90-Line 32 & 33 and GLIMPCE Line-J, respectively, obtained from the respective spatially coincident seismic refraction – wide angle reflection profiles. Besides the crustal-mantle boundary, two other crustal discontinuities are present. The upper to middle crustal discontinuity (UMD) is characterized by a interface between highly variable velocities of 5.6-6.4 $km.s^{-1}$ in the upper crust and relatively uniform with velocities of 6.3-6.6 $km.s^{-1}$ in the middle crust; the middle to lower crustal discontinuity (MLD) is an interface between the velocities in the middle crust (6.3-6.6 $km.s^{-1}$) and the lower crust (6.9-7.4 $km.s^{-1}$), velocity values were from refraction model (White et al., 2000). In our results, these boundaries occur at depths of ~ 11-12 km and ~23-24 km respectively, along Line-9. These depths correlate very well with the nearby seismic refraction velocity model (AGT90-Line 32 and 33, White et al. 2000). A strong lateral variation in crustal interface depths is displayed along Line-8, on the west side of the study area, where the UMD and MLD are almost parallel to each other and both increase in depth from ~10 km (UMD) and ~20 km (MLD) beneath GFTZ to ~14 km and ~ 24 km, respectively, beneath the further east part of Britt Domain and beneath the Shawanaga domain. A similar feature also can be seen in the refraction model along GLIMPCE Line-J, which can be correlated with mainly ~ ca. 1450 Ma Laurentian crustal rocks deformed and transported toward the NW during orogeny (Carr et al., 2000).

3. SE-dipping features

A SE-dipping feature was found in the crust along cross-sections oriented in NW-SE (Line 8 and 9). Along Line-8 (see Figure 7.3 (b)), this feature appears as steeply (25°-30°) to gently dipping (0°-5°) from beneath the GFTZ and nearby northwest of Britt domain to away from the GFTZ (beneath the Shawanaga domain). Previous wide-angle refraction studies (GLIMPCE Line-J, see Figure 7.3 (a)) also displayed similar SE-dipping features and dip angle variation. The detected features are consistent with previous interpretations of the GFTZ as a prominent southeast-dipping region of amphibolite-facies rocks that underwent ductile thrusting at ~ ca. 1000 Ma, superimposed on older mylonite in the Killarney Belt (Davidson 1986a, 1986b; Easton 1992; Bethune 1997, Carr et al. 2000). Compared to Line-8, the SE-dipping features is weaker and smaller-scale in Line-9 (figure 7.2), being observable only in the upper crust, between the UMD and MLD. This characteristic is also consistant with reflection models (AGT90-Line 32 and 33), in which it was attributed to tectonically imbricated units of the CMB and CMBbz (O'Dowd et al, 2004).

a)

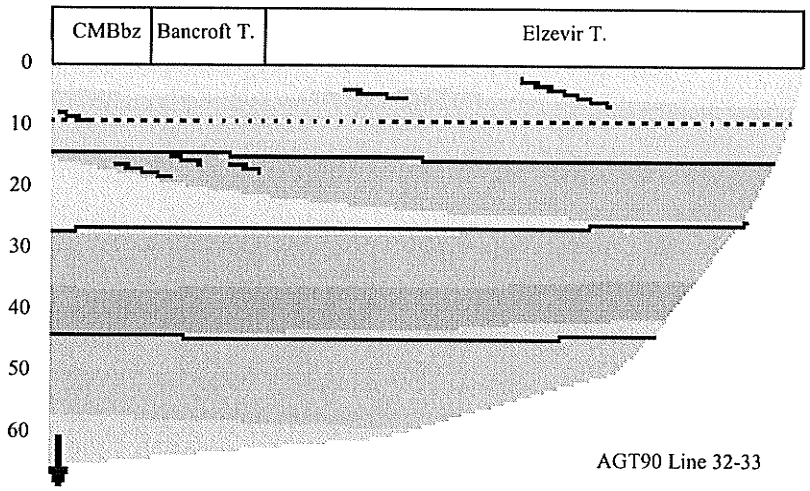

b)

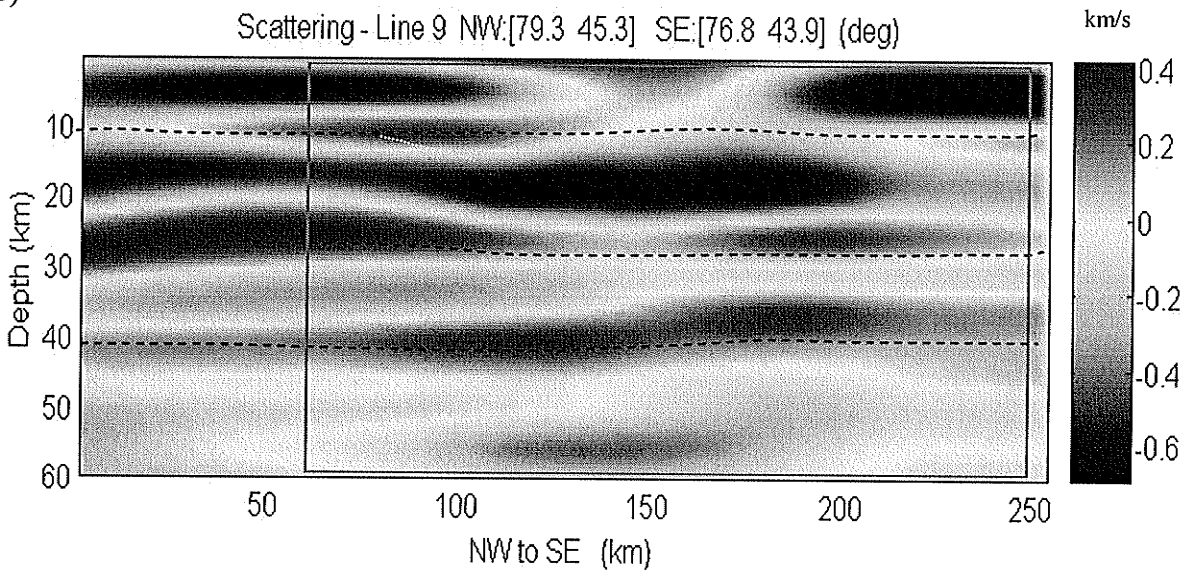

Figure 7.3. Comparison of interpreted seismic refraction model with image obtained in this study, rectangle frame in (b, purple) showing the comparable part of the lines. (a) velocity models from AGT90-Line 32 and 33 obtained from spatially coincident seismic refraction (modified from White et al., 2000); T-terrane; (b) velocity perturbation images along Line-9 obtained using scattering tomography.

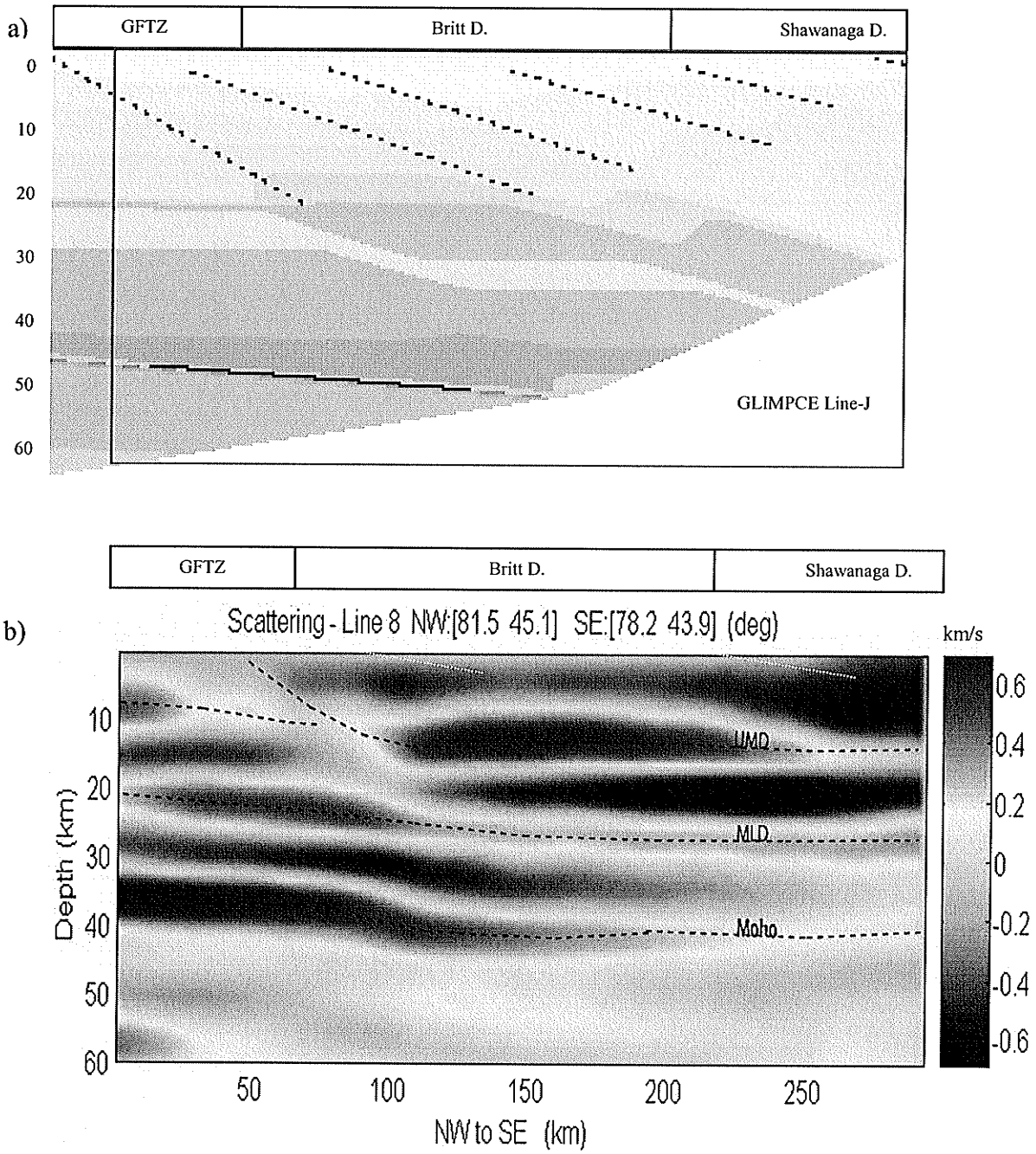

Figure 7.4. Comparison of interpreted seismic refraction model with image obtained in this study, rectangle frame in (a, purple) showing the comparable part of the lines. (a) velocity models from GLIMPCE Line-J, obtained from patially coincident seismic refraction (modified from White et al. 2000); D-domain; (b) velocity perturbation images along Line-8 obtained using scattering tomography; (c) CCP stacked receiver function amplitude.

4. Ottawa-Bonnechere Graben

The cross-sections across the OBG in this study, e.g. Line-3 can be compared with seismic refraction profile-1982 COCRUST line QR (see Figure 7.4). These two lines are almost parallel to each other, though instead of running through the CGB, Line-3 was run through the CMB (see Figure 3.6 and Figure 6.5 for location of lines). Crustal thinning beneath the OBG is clearly visible in both scattering (b) and CCP stacking (c), correlating closely with the interpretation of 1982 COCRUST line-QR (a). This further supports the interpretation that the graben is an ancient rift, affecting the full thickness of the crust.

Another comparison between the results from scattering tomography in this study and travel-time inversion by Aktas and Eaton (2005) is shown in depth-slice in Figure 7.5. S-wave images of the OBG obtained by aforementioned two methods both show a linear, NW-striking, low-velocity anomaly. This low-velocity anomaly is wider, more cohesive, better-defined and located at the south of the Ottawa river (OBG) in scattering image (indicated by arrows in figure b), compared to the travel-time image. The structures in the two models are likely to both be graben-related; this would tend to suggest that the crustal graben imaged in this study is related to the thermomechanically-eroded track of the Great Meteor hotspot through the continental lithosphere, as described by (Rondenay 2000). The OBG feature also correlates well with the western Quebec seismic zone (Ebel, J.E. and Tuttle, M., 2002).

a)

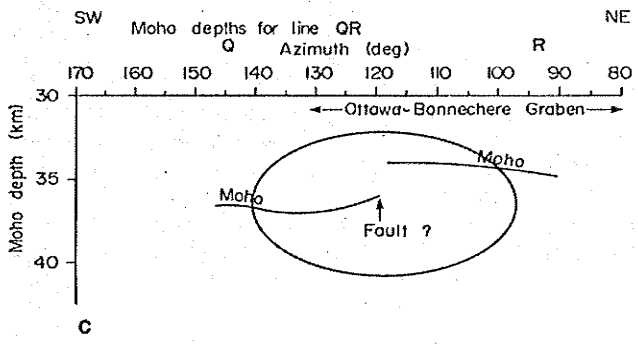

b)

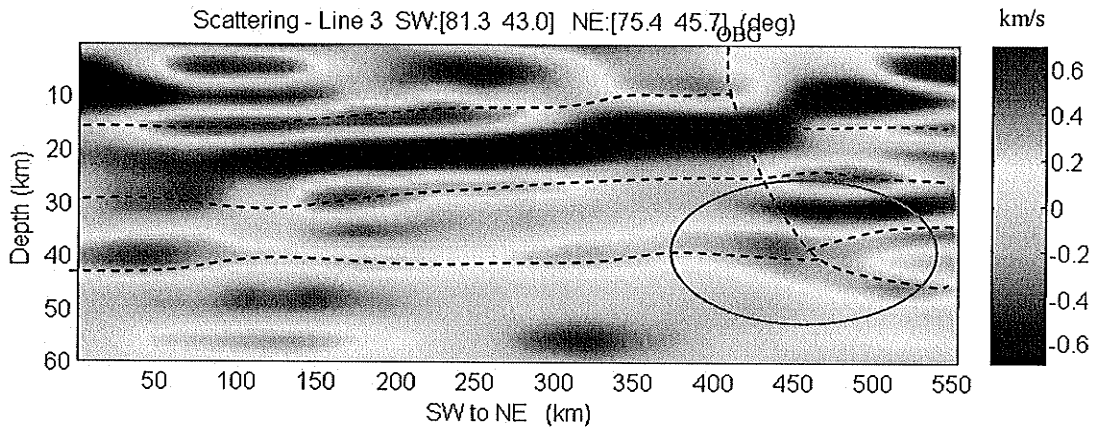

c)

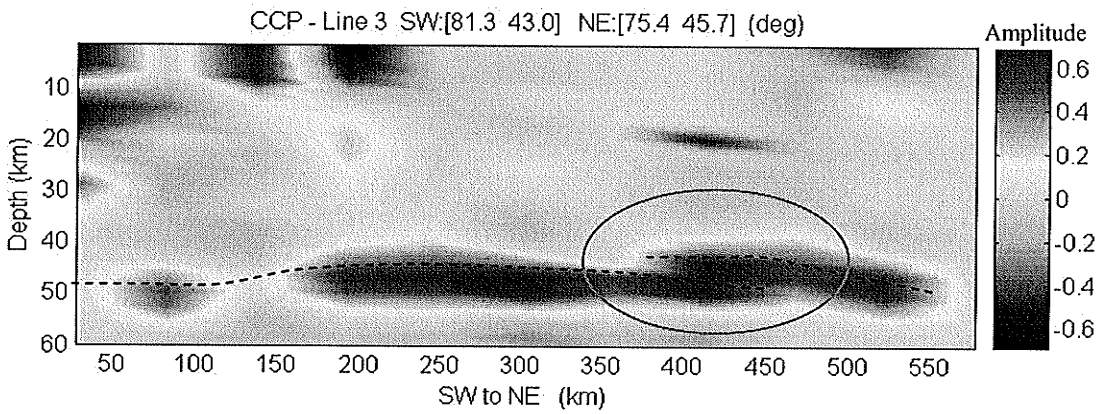

Figure 7.5. Comparison of interpreted seismic refraction model with image obtained in this study. (a) Moho depth profile along Line-QP obtained from the seismic refraction profiles for the 1982 COCRUST seismic survey (modified from Mereu et al, 1986a, Easton 1992); (b) velocity perturbation images along Line-3 obtained using scattering tomography; (c) CCP stacked receiver function amplitude.

a)

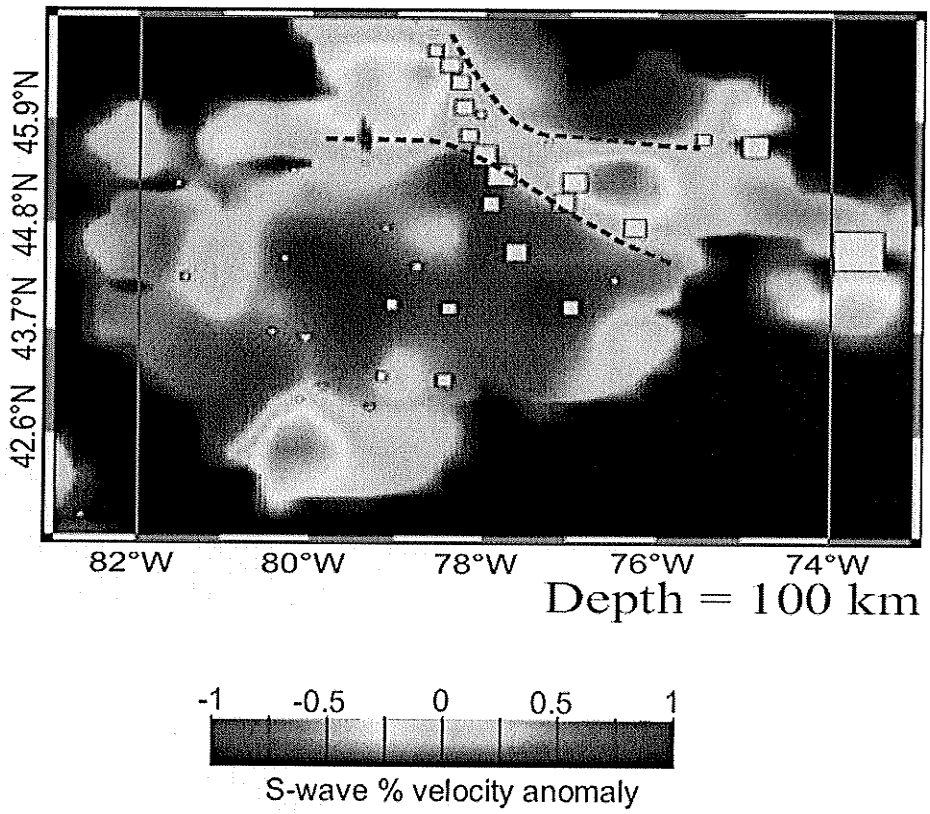

b)

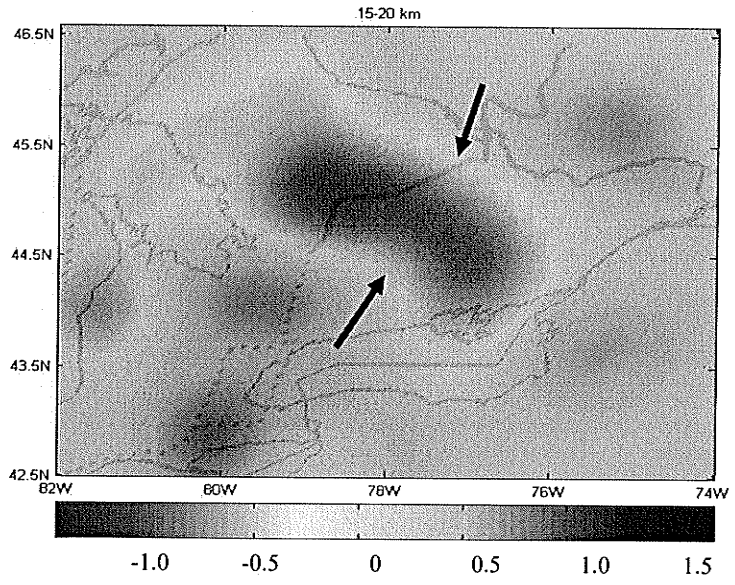

Figure 7.6. Comparison of teleseismic travel-time image with scattering images obtained in this study; rectangle frame showing common part of the study area. (a) S-wave velocity perturbation at depth of 100 km obtained from teleseismic travel-time tomography (Aktas and Eaton, 2005); (b) S-wave velocity perturbation slice at depth of 24 km obtained using scattering tomography in this study.

5. Subduction remnants

As discussed in last chapter, a sequence of sub-crustal negative polarity arrivals, which follow the Moho structure and dip eastward into the mantle from 60 to 100 km can be observed in almost all the CCP stacking cross-sections, especially for the lines parallel to the strike of the major tectonic shear zones (CMBbz and GFTZ). This feature extends to a depth of 100 km in some locations (Line-1, 2, 3, 4, 5, see Figure 5.7-5.12). This feature may be correlated with subduction occurring during the Mesoproterozoic active margin of Laurentia (Rivers and Corrigan, 2000). A number of other studies crossing the vicinity of the Grenville Front (e.g., receiver function images by Eaton et al, 2005; teleseismic travel-time tomography by Rondenay, 2000; seismic refraction by Winardhi and Mereu, 1997; reflection profile by Culotta et al. 1990) all show some evidence of a similar but weaker negative feature; Rondenay (2000) interpreted a relict subduction margin which might be correlated with a reactivation of an underthrust sheet during the Grenvillian orogeny. The dipping features are seen on lines parallel to the strike of the surface features (Line 1, 2, 3, 4 & 5) rather than perpendicular lines (Line 7, 8, 9 and 10), suggesting that the strike of the underthrust sheet is not parallel to the major shear zones and therefore might not be directly related to the formation of the CMBbz and GFTZ.

a)

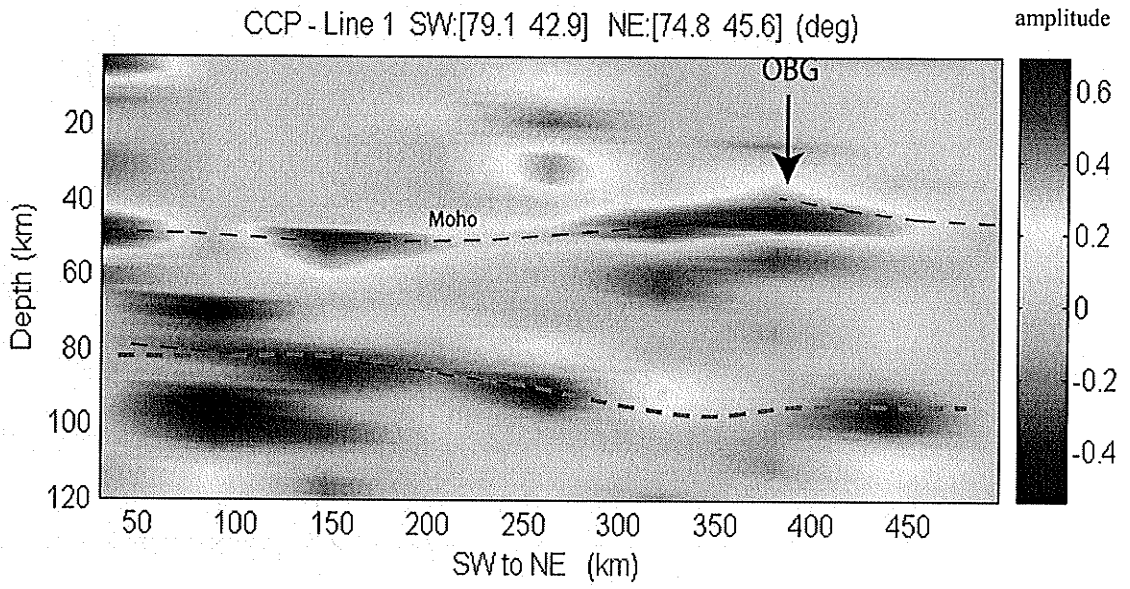

b)

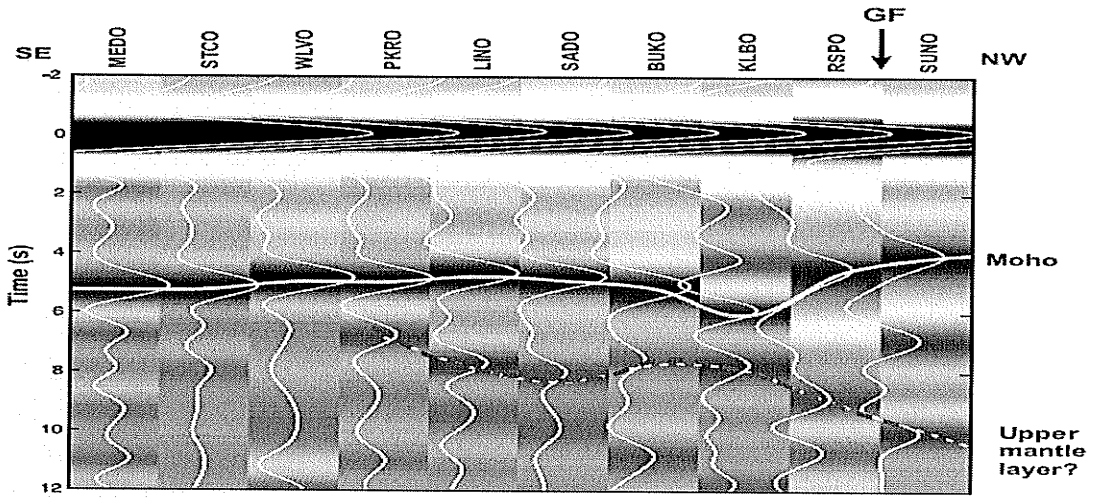

Figure 7.7. Comparison of teleseismic receiver function image (Eaton et al., 2005) with CCP stacking images obtained in this study. (a) CCP stacked receiver function amplitude along Line-1; (b) stacked receiver functions at individual stations (Eaton et al., 2005).

6. A rhomboid-shaped region - the Mississauga domain (MD)

There are two interpretations of the location and geometry of the CMBbz beneath the Toronto region. Some authors suggest that the CMBbz crosses western Lake Ontario in NNE direction, based on seismic reflection profiles and correlating the buried extension of the CMBbz with the Niagara-Pickering linear zone (e.g., Easton and Carter 1995, Wallach et al 1998); Other evidence (magnetic anomalies and new Lithoprobe reflection profile-SOSS line-4, O'Dowd et al 2004) suggests the CMBbz to instead be located west of the distinctive rhomboid shape of the Mississauga domain, suggesting that this domain could have formed within a strike-slip duplex system. Our scattering images across the MD clearly show that upper and middle crust have been truncated by the strike-slip duplex system, strongly supporting the latter interpretation.

This comparison is made in Figure 7.6, showing the scattering tomography images (a, b) along Line-2 and Line-7 obtained in this study and the vertical derivative magnetic map (c) obtained from the final master 200 m aeromagnetic grid for Ontario (Gupta, 1991). This comparison mainly highlights the southwest of the CMBbz, and the Mississauga domain, which is situated beneath the west of Lake Ontario. The magnetic data show an apparently striated fabric with ~N60°E and N13°E trends extrapolated in this domain; the fabric is different from the west side of the CGB and the east side of the CMB (O'Dowd et al, 2004). Along the cross-section (Line-7) across this domain running from NW to SE, the upper to middle crustal discontinuity and middle to lower crustal discontinuity, are displaced twice by reverse-faulting, indicating that bifurcates of the CMBbz might occurr at these two jumping points. However, a similar feature was not observed in Line-2, which also runs through this domain but is oriented almost parallel to

the CMBbz, suggesting that strike-slip might have occurred but that no dip-slip has been applied in this direction. A mixed strike-slip and reverse-slip sense of displacement occurring in the Mississauga domain would correlate well with the oblique geometry of internal magnetic fabrics as well as higher frequency of seismicity in this domain (see Figure 7.6 (d)) than adjacent areas, suggesting that the Mississauga domain is a tectonic active area (Wallach et al., 1998).

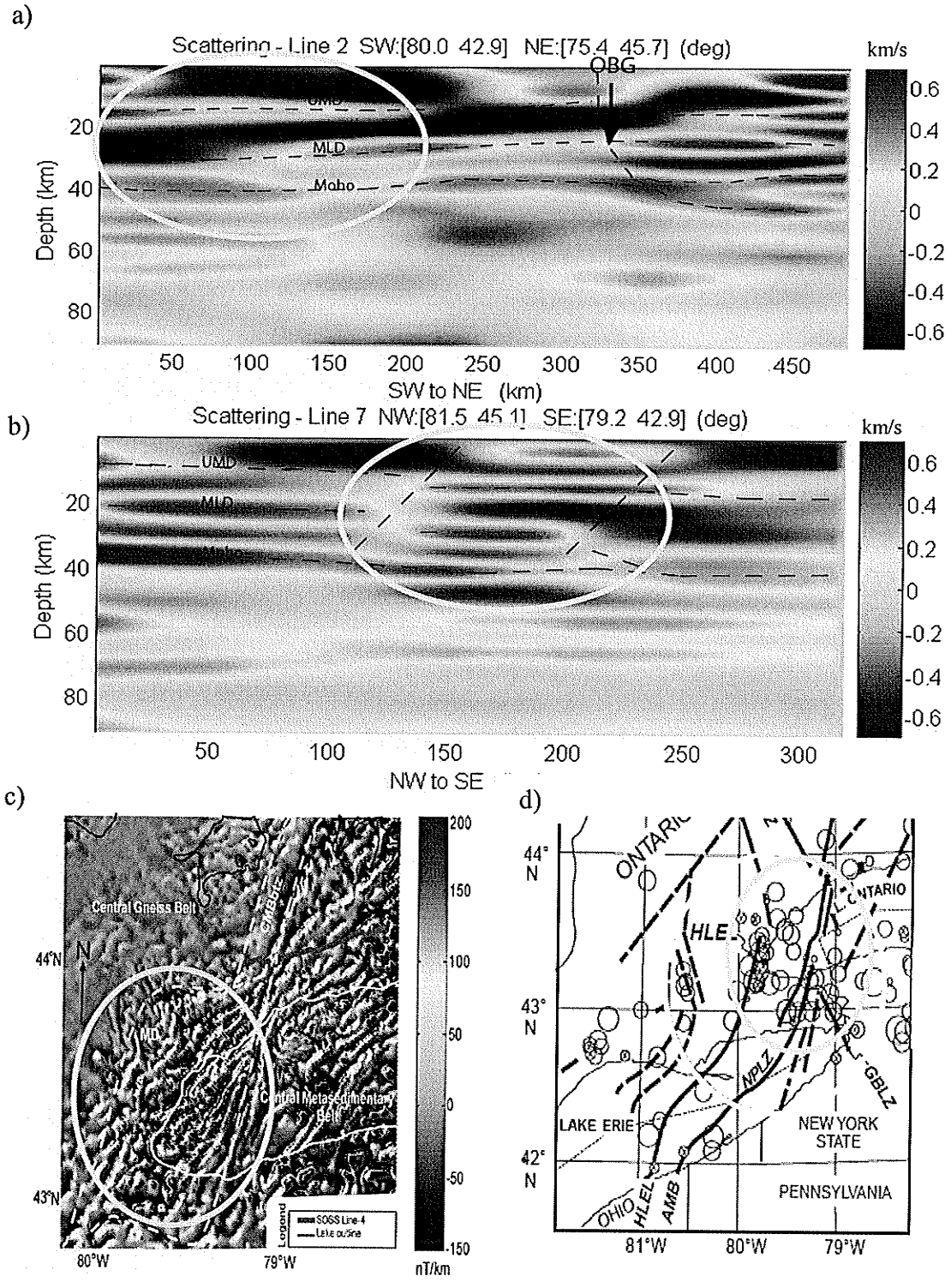

Figure 7.8. shows the comparisons between the scattering tomography images (a) along Line-2, (b) along Line-7, obtained using scattering tomography in this study; a vertical-gradient magnetic map (c) obtained from the final master 200 m aeromagnetic grid for Ontario (Gupta, 1991, O'Dowd et al. 2004); and a seismicity in the MD (d).

Chapter 8

Conclusions

This thesis study has demonstrated that a relatively sparse station deployment can yield interpretable crustal images by using the scattering tomography technique, and that a well-defined Moho structure and greater depth features can be successfully imaged by 3-D CCP stacking. The results and interpretations in this study are mainly based on ten cross-section profiles (CCP stacking and scattering tomography) which cross the major portion of the study area and its major tectonic features, e.g., the Central Metasedimentary belt boundary zone and Ottawa-Bonnechere Graben, These cross-sections are supplemented 3-D depth slices acquired by the '**CCPscat**' software developed in this study using Matlab. These observations and interpretations are summarized as follows.

The Moho discontinuity detected in this study is at depth from 38.5 to 50.5 km (40-52 km in CCP, 37-49 in scattering). The crust is thinnest (~ 40 km in CCP, ~ 37 km in scattering) and changes markedly (apparently truncated in CCP, appears to be a split feature in scattering) beneath the Neoproterozic OBG. This might be due to extension associated with the Ottawa-Bonnechere graben, and is good evidence that the OBG is a crustal-scale feature. No significant difference in crustal thickness was observed between the southwest portion of the CGB and the southwest portion of the CMB. The crust within the CGB tends to be ~44-47 km thick, and ~ 40- 42 km thick within the CMB along Line-7, 8 (in CCP). However, near the CMBbz, within its CGB footwall beneath

Georgian Bay, the crust tends to be thicker than on the other side of the CMB. The thickening of this region might have resulted from convergence along the Laurentian margin during the period 1080-1040 Ma. The crustal thickness detected in this study is consistent with several reflection and refraction studies in near or parallel profiles (AGT90-Line 32 and 33, GLIMPCE Line-J, White et al., 2000; SOSS Line-4, O'Dowd et al, 2004).

A sequence of sub-crustal negative polarity arrivals below the Moho and dipping eastward into the mantle from 60 to 100 km depth can be observed in almost all of the CCP stacking cross-sections. A number of other studies crossing the vicinity of the Grenville Front (e.g., receiver function images by Eaton et al, 2005; teleseismic travel-time tomography by Rondenay, 2000; seismic refraction by Winardhi and Mereu, 1997; reflection profile by Culotta et al. 1990) all show some evidence of a similar but weaker negative feature which Rondenay (2000) correlated with a relict subduction margin, and suggested that may be attributed to reactivation of an underthrust sheet during the Mesoproterozoic active margin of Laurentia (Rondenay, 2000; Rivers and Corrigan, 2000). We found that this feature appears to be eastward dipping only in lines parallel to the strike of the surface geology rather than lines perpendicular major shear zones (CMBbz or GFTZ), suggesting that the subduction might not directly correlate with the forming of the major shear zones. A sub-OBG negative polarity arrival immediately beneath the positive Moho arrival near or beneath the OBG is visible in CCP stacking Lines 1 to 5, and might be correlated with the formation of the graben.

Higher resolution images were achieved in teleseismic scattering tomography. Besides the Moho discontinuity, two other crustal discontinuities, the upper mantle to

middle mantle interface (UMD) at depth of ~10-15 km, and the middle to lower crustal discontinuity (MLD) at depth of ~20-30 km, are clearly shown as positive perturbations in S-wave velocity. In general, UMD and MLD velocity anomalies tend to be weaker and less continuous within the CMB compared with the anomalies within the adjacent CGB, suggesting difference in regional texture and structural style between the CGB and the CMB. The CMB is characterized by polyphase folds, and more complex geometries that are considered to have been at middle to upper crustal levels during the Grenville orogeny, compared with the strongly deformed gniesses of the CGB (White et al., 2000).

SE-dipping features are observed near two major ductile shear zones (CMBbz and GFTZ). Along Line-8, a strongly SE-dipping (25^{o}-30^{o}) feature is found beneath the GFTZ and northwest of Britt domain, while away from GFTZ (benath the Shawanaga domain) it appears to be a nearly flat feature, this SE-dipping feature extends to a depth of 20 km. A similar SE-dipping feature and comparable dip angle variation were detected in GLIMPCE Line-J (White et al. 2000). A weaker and smaller SE-dipping feature is indicated between the UMD and MLD along Line-9, which also agrees well with the previous refraction velocity model (AGT90-Line 32 and 33). The strong SE-dipping feature observed beneath GFTZ is though to be correlated with a prominent southeast dip of amphibolite-facies rocks and northeast trend of cataclastic foliation, related to ductile trusting at ~ ca. 1000 Ma (Davidson 1986a, 1986b; Easton 1992; Bethune 1997, Carr et al. 2000). The weaker SE-dipping feature observed beneath CMB and CMBbz might be attributed to the orientation of tectonically imbricated units of this region (O'Dowd et al, 2004).

Two conspicuous middle-crust (MLD) displacements occur at the southwest end of the tectonic boundaries (CMBbz), beneath the western part of Lake Ontario (the rhomboid shaped Mississauga domain) imaged in scattering tomography along Line-7 (running NW to SE). This feature was not observed in Line-2, which also runs through this domain but is oriented almost parallel to the CMBbz, indicating a mixed strike-slip and reverse-slip sense of displacement occurring in the Mississauga domain, which therefore is characterized as a duplex structure. This finding is consistent with a ENE oblique geometry of internal magnetic anomaly fabrics extended in this domain (Gupta, 1991) as well as high frequency of seismicity in this domain, suggesting that the Mississauga domain is a tectonic active area (Wallach et al., 1998), which strongly support that the buried trace of CMBbz is located parallel to, and west of Lake Ontario (O'Dowd et al, 2004). Other authors have interpreted the CMBbz as crossing western Lake Ontario in NNE direction (e.g., Easton and Carter 1995, Wallach et al 1998), an interpretation not supported by this study.

The Ottawa-Bonnechere Graben is another interesting feature within the study area and has been investigated by many authors using different geophysical methods (e.g., teleseismic travel-time by Aktas and Eaton (2005); the 1982 COCRUST seismic survey by Mereu et al, 1986a, Easton 1992). The cross-section images (Line-1, 2, 3, 4 and 5, both in CCP and in scattering) show that the crust beneath the OBG has been raised up as much as 11 km relative to its neighboring blocks by downward normal faulting, an observation that agrees well with the 1982 COCRUST refraction model. This feature appears in depth slice (at 20 km) in the scattering image as a linear, cohesive, very well-defined, NW-striking low-velocity S-wave anomaly, oriented parallel to the OBG

along its SW edge, which consists with western Quebec seismic zone. A similar feature is visible in the travel-time model of Aktas and Eaton (2005) at much greater depth, suggesting that the graben is associated with a mantle structure possibly attributed to the Great Meteor hotspot track (Rondenay 2000).

On the basis of this thesis research, crust and upper mantle structures across the Grenville orogen in southern Ontario have been investigated in detail, which correlate well with previous geophysical works and surface geology, and support previous interpretations made in the same or nearby area. However, due to the limited area of good resoltuion, which was mainly determined by station configuration, it is not able to characterize detailed features of the northeast part of the region, or Grenville Front Tectonic Zone. Better coverage of these areas will depend on future teleseismic deployments, though images could also be improved by use of an accurate 3-D base model of the region.

References

Achenbach, J.D., Gautesen, A.K., and McMaken, H., 1982, Ray methods for waves in elastic solids, with application to scattering by cracks: Pitman Learning.

Adams, J., and Basham, P., 1991, The seismicity and seismotectonics of eastern Canada. In: Slemmons, D.B., Engdahl, E.R., Zoback, M.D., Blackwell, D.D. (Eds.), Neotectonices of North America, vol, 1. Geological Society of America, Boulder, CO, 261-276.

Aki, K., and Richards, P.G. 1980. Quantitative seismology. W.H. Freeman and Company, 577 p.

Ammon, C.J., 1991, The isolation of receiver function effects from teleseismic P waveforms, Bull. Seismol. Soc. Am., **81**, 2504-2510.

Atkas, K., and Eaton, D.W., 2005, Upper-mantle velocity structure of the lower Great Lake region, submitted to Tectonophysics.

Bailey, R.C., Craven, J.A., Macnae, J.C., and Polzer, B.D., 1989, Imaging of deep fluids in Archean crust. Nature, **340**, 136-138.

Bank, C., Eaton, D. and Aktas, K., 2005, Moho topography and lower crustal density in Southern Ontario from linearized gravity inversion, 2005 AGU spring meeting 23-27 May, New Orleans, poster, T43D-04.

Bath, M. and Steffanson, R., 1966, S-P conversion from the base of the crust, Ann. Geophys., **19**, 119-130.

Bethune, K.M., 1997, The subury dyke swarm and its bearing on the tectonic

development of the Grenville Front, Ontario, Canada, Precambrian Research, **85**, 117-146.

Boerner, D.E., Kurtz, R.D., and Graven, J.A., 2000, A summary of electromagnetic studies on the Abitibi-Grenville transect, Canadian J. Earth Sci., **37**, 427-437.

Boland, A.V., and Ellis, R.M., 1989, Velocity structure of the Kapuskasing uplift, northern Ontario, from seismic refraction studies. J. Geophys. Res., **94**, 7189-7204.

Bostock, M.S. and Rondenay, S., 1999, Migration of scattered teleseismic body waves, Geophys. J. Int. **137**, 732-746.

Carr, S.D., Easton, R.M., Jamieson, R.A., and Culshaw, N.G., 2000, Geologic transect across the Grenville orogen of Ontario and New York, Can. J. Earth Sci., **37**, 193-216.

Carter, T.R. and Easton, R.M., 1990, Extension of Grenville basement beneath southwestern Ontario: Lithology and tectonic boundaries; in Subsurface Geology of Southwestern Ontario: A Core Workshop, Core Workshop Volume, 1990, Ontario Petroleum Institute, London, Ontario, 9-28.

Cassidy, J.F., Adams, J., Atkinson, G., Bostock, M.G., Eaton, D, Ferguson, I.J., Snyder, D. and Unsworth, M., 2003, POLARIS: Portable Obeservations for Lithospheric Analysis and Research Investigating Seismicity- new opportunities in Canada, Geophysical Research Abstracts, **5**, 13206.

Castle, J.C., and Creager, K.C., 1999, A steeply dipping discontinuity in the lower mantle beneath Izu-Bonin, J. Geophys. Res., 104, 7279-7292.

Culotta, R.C., Pratt, T., and Oliver, J., 1990, A tale of two sutures: COCORP's deep

seismic surveys of the Grenville province in the eastern U.S. mid-continent, Geology, **18**, 646-649.

Davidson, A., 1984a, Identification of ductile shear zones in the southwestern Grenville Province of the Canadian Shield; in Precambrian Tectonics Illustrated, E. Schweizerbart' sche Verlagsbuchhandlung, Stuttgart, 263-279.

Davidson, A., 1986a, New interpretations in the southwestern Grenville province. In the Grenville Province. Edited by Moore, J.M., Davidson, A. and Baer, A.J., Geological Association of Canada, Special paper **31**, 61-74.

Davidson, A., 1986b, Grenville Front relationships near Killarney, Ontario; in The Grenville Province, Geological Association of Canada, Specail paper **31**, 107-118.

Davidson, A., 1986c, A new look at the Grenville Front in Ontario, Geological Association of Canada-Mineralogical Association of Canada, Ottwa '86, Field Trip Guidebook **15**, 31.

Dickin, A.P. and McNutt, R.H., 1989a, Nd model age mapping of the southeast margin of the Archean foreland in the Grenville Province of Ontario; Geology, **17**, 299-303.

Dickin, A.P., McNutt, R.H. and Clifford, P.M., 1990, A neodymium isotope study of plutons near the Grenville front in Ontario, Canada; Chemical Geology, **83**, 315-324.

Dressler, B., 1979, Geology of McNish and Janes townships; Ontario Geological Survey, Report **191**, 91.

Dueker, K.G. and Sheehan, A.F., 1997, Mantle discontinuity structure from midpoint stacking of converted P to S waves across the Yellowstone hotspot track, J. Geophys., Res., **102/B4**, 8313-8327.

Easton, R.M., 1986, Geochronology of the Grenville Province; in The Grenville

Province, Geological Association of Canada, Special Paper **31**, 127-173.

Easton, R.M., 1992, The Grenville Province and the Proterozoic history of central and southern Ontario, Geology of Ontario, **19**, 715-886.

Easton, R.M., and Carter, T.R., 1995: Geology of the Precambrian basement beneath the Paleozoic of southwestern Ontario, In: Ojakangas, R.W., Dickas, A.B. and Green, J.C. (editors), Proceedings of the International Conference on Basement Tectonics, **10**: 221-264.

Eaton, D., 2005, Ontario POLARIS project – seismology research, Annual report to Ontario parks 2004 field activities and earthquake research, U. of Western Ontario, London, Ontario.

Eaton, D., Dineva, S. and Ferguson, I., 2000, Science plan for the Ontario Polaris Array; Seismic risk to Canada's economic core, U of Western Ontario, London, ON, U of Manitoba, Winnipeg, MB.

Eaton, D., Frederiksen, A. and Miong, S.K., 2004, Shear-wave splitting observations in the lower Great Lakes region: Evidence for regional anisotropic domains and keel-modified asthenospheric flow, Geophys. Res. Lett., **31**, L07610.

Eaton, D., Dineva, S. and Mereu, R., 2005, Crustal thickness and Vp/Vs variations in the centeral Grenville orogen (Ontario, Canada) from analysis of teleseismic receiver functions, Manuscript in preparation for Tectonophysics.

Ebel, J.E. and Tuttle, M, 2002, Earthquakes in the Eastern Great Lakes Basin from a regional perspective, Tectonophysics, **353**, 17-30.

Fehler, M. and Aki, K., 1978, Numerical study of diffraction of plane elastic waves by a

finite crack with application to location of magma lens; Bull. Seism. Soc. Am., **68**, 573-598.

Fouch, M.J., Fischer, K.M., Parmentier, E.M., Wysession, M.E., and Clarke, T.J., 2000, Shear wave splitting, continental keels, and patterns of mantle flow, J. Geophys. Res., **105**, 6255-6275.

Forsyth, D.A., Milkereit, B., Zelt, C.A., White, D.J, Easton, R.M., and Hutchinson, D.R., 1994, Deep structure beneath Lake Ontario: crustal-scale Grenville subdivisions, Can. J. of Earth Sci., **31**, 255-270.

Frederiksen, A.W., and Bostock, M.G., 2000, Modelling teleseismic waves in dipping anisotropic structures. Geophys. J. Int., **141**, 401-412.

Frederisken, A.W. and Revenaugh, J., 2004, Lithospheric imaging via teleseismic scattering tomography, Geophys. J. Int. **159**, 1-13.

Frederiksen, A.W., Ferguson, I.J., Eaton, D., Miong, S.K., Gowan, E., 2005, Mantle fabric at multiple scales across an Archean-Proterozoic boundary, Eastern Ontario, Canada, submitted to Phys. Earth Planet. Int.

Gilbert, H.J., and Sheehan, A.F., 2004, Images of crustal variations in the intermountain west, J. of Geophys. Res., 109, B03306, doi:10.1029/2003JB002730.

Golub, G.H., Heath, M. and Wahba, G., 1979, Generalized cross-validation as a method for choosing a good ridge parameter, Technometrics, **21**, 215-223.

Green, A.G., Cannon, W.F., Milkereit, B., Hutchinson, D.R., Davidson, A., Behrendt, J.C., Spencer, C., Lee, M.W., Morel-a-l'Huissier, P. and Agena, W.F., 1989, A "Glimpce" of the deep crust beneath the Great Lakes; in Properties and Processes of Earth's Lower Crust, American Geophysical Union, Monograph **51**, 65-80.

Green, A.G., Milkereit, B., Mayrand, L.J., Ludden, J.N., Hubert, C., Jackson, S.L., Sutcliffe, R.H., West, G.F., Verpaselst, P., and Simard, A., 1990, Deep structure of an Archean greenstone terrane, Nature (London), **344**, 327-330.

Gupta, V.K., 1991, Shaded image of total magnetic field of Ontario, southern sheet, Ontario Geological Survey, Map 2587, scale 1:1000000.

Gurrola, H., Naker, G.E. and Minster, J.B., 1995, Simultaneous time-domain deconvolution with application to the computation of receiver functions, Geophys. J. Int., **120**, 537-543.

Ham, S., Niu, F., Levander, A., Obayashi, M., 2004, Mantle discontinuities beneath Japan determined from CCP stacking of receiver functions, AGU Fall meeting, 13-17 December, San Francisco, California, USA.

Harper, C.T., 1967, On the interpretation of potassium-argon ages from Precambrian shields and Phanerozoic orogens; Earth and Planetary Science Letters, **3**, 128-132.

Hoffman, P.F., 1989, Precambrian geology and tectonic history of North America. 447-512, In, The geology of North America; an overview, Bally, A.W. (ed.), Geological Society of America, Boulder, U.S.A.

Ji. S., Rondenay, S., Mareschal, M., and Senechal, G., 1996, Obliquity between seismic and electrical anisotropies as a potential indicator of movement sense for ductile shear zones in the upper mantle, Geology, **24** (11), 1033-1036.

Karason, H., and van der Hilst, R.D. 2001, Tomographic imaging of the lowermost mantle with differntial times of refracted and diffracted core phases (PKP, P_{diff}), J. Geophys. Res., **106**, 6569-6587.

Kellett, R.L., Barnes, A.E., and River, M. 1994, The deep structure of the Grenville

Front: a new perspective from western Quebec, Can. J. Earth Sci., **31**, 282-292.

Kennett, B., 1991, The removal of free surface interactions from three-component seismograms, Geophys. J. Int., **104**, 153-163.

Kind, R., Kosarev, G.L. and Peterson, N.V., 1995, Receiver functions at the stations of the German Regional Seismic Network (GRSN), Geophys. J. Int., **121**, 191-202.

Kinsman, A. and Parrish, R.R., 1990, U-Pb age of detrital zircons from five quartzites in the Central Metasedimentary Belt of the Grenville Province; in Program with abstracts, Geological Association of Canada-Mineralogical Association of Canada, **15**, A70.

Knapmeyer, M. and Harjes, H.P., 2000, Imaging crustal discontinuities and the downgoing slab beneath western Crete, Geophys. J. Int., **143**, 1-21.

Kruger, F., Baumann, M., Scherbaum, F. and Weber, M., 2001, Midmantle scatters near the Mariana slab detected with a double array method, Geophys. Res. Lett., **28**, 667-670.

Kurtz, R.D., 1982, Magnetotelluric interpretation of crustal and mantle structure in the Grenville Province, Geophys.J.R.astr.Soc., **70**, 373-397.

Kurtz, R.D., Craven, J.A., Niblett, E.R., and Stevens, R.A., 1993, The conductivity of the crust and upper mantle beneath the Kapuskasing Uplift: electrical anisotropy in the upper mantle, Geophys. J. Int., **113**, 483-498.

Langston, C.A., 1979, Structure under Mount Rainier, Washington, inferred from teleseismic body waves, J. Geophys. Res., **84**, 4749-4762.

Lowrie, W., 1997, Fundamentals of Geophysics, Cambridge University Press, Cambridge.

Lumbers, S.B., 1975, Geology of the Bruwash area: Ontario division of mines, Geological Report, **116**, 160.

Lumbers, S.B., 1978, Geology of the Grenville front tectonic zone in Ontario; in Toronto '78, Field Trips Guidebook, Geological society of America-Geological association of Canada-Mineralogical Association of Canada, 347-361.

Lysmer, J. and Drake, L.A., 1972, A finite element method for seismology. In Alder, B. Fernbach, S. and Bolt, B.A., editors, Methods in Computational Physics, **11**, chapter 6. Academic Press, New York.

Mareschal, M., Kurtz, R.D., Chouteau, M., and Chakridi, 1991, A magnetotelluric survey on Manitoulin Island and Bruce Peninsular along GLIMPCE seismic line J: black shales mask the Grenville Front, Geophys. J. Int., **105**, 173-183.

Mareschal, M., Kellett, R.L., Kurtz, R.D., Ludden, J.N., Ji, S., and Bailey, R.C., 1995, Archaean cratonic roots, mantle shear zones and deep electrical anisotropy, Nature, **375**, 134-137.

Mareschai, J.C., Jaupart, C., Gariepy, C., Cheng, L.Z., Guillou-Frottier, L., Bienfait, G., and Lapointe, R., 2000, Heat flow and deep thermal structure near the southeast edge of the Canadian Shield, Can. J. Earth Sci, **37**, 399-414.

Menke, W., 1989, Geophysical Data Analysis: Discrete Inverse Theory (Revised Edition), Academic Press, San Diego, CA, 285 p.

Mereu, R.F., 2000, The complexity of the crust and Moho under the southeastern Superior and Grenville provinces of the Canadian Shield from seismic refraction-wide-angle reflection data, Can. J. Earth Sci. **37**, 439-458.

Mereu, R.F., Wang, D., Kuhn, O. and Forsyth, D.A., 1986a, Summary of the results of

the 1982 Cocrust long-range seismic experiment across the Ottawa-Bonnechere Graben and western Grenville Front; in The Grenville Province, Geological Association of Canada, Special paper **31**, 235-240.

Mereu, R.F., Wang, D., Kuhn, O., Forsyth, D.A., Green, A.G., Morel, P., Crossley, D., Schwartz, E., Duberger, R., Brooks, C. and Clowes, R. 1986b, The 1982 Cocrust seismic experiment across the Ottawa-Bonnechere Graben and Grenville Front in Ontario and Quebec; Royal Astron. Soc. Geophys. J., **84**, 491-514.

Miller, R.R., 1983, Age and petrological relationships of some igneous-textured and gneissic alkaline rocks in the Haliburton-Bancroft area; unpublished PhD thesis, University of Toronto, Toronto, Ontario, pp345.

Mohan G. and Rai SS., 1992, Imaging of seismic scatters beneath the Gauribidanaur (GBA) array, Phys. Earth Planet. Inter., **71**, 36-45.

Musacchio, G., Mooney, W.D., Luetgert, J.H., and Christensen, N.I., 1997, Composition of the crust in the Grenville and Appalachian Provinces of North America based on V_p/V_s ratio, J. Geophys. Res., **102**, 15225-15242.

Neugerg, J. and Ponter, T., 1995, Modelling seismic refelections from D" using the Kirchoff method; Phys. Earth Planet. Inter, **90**, 273-281.

O'Dowd, C.R., Easton, D., Forsyth, D. and Asmis, H.W., 2004, Structural fabric of the Central Metasedimentary Belt of southern Ontario, Canada, from deep seismic profiling, Tectonophysics, **388**, 145-159.

Oldenburg, D.W., 1981, A comprehensive solution to the linear deconvolution problem, Geophys. J.R. Astron. Soc., **65**, 331-337.

Owens, T.J., Zandt, G. and Talor, S.R., 1984, Seismic evidence for ancient rift beneath

the Cumberland plateau, Tennessee: A detailed analysis of broadband teleseismic P waveforms, J. Geophys. Res., **89**, 7783-7795.

Paige, C. and Saunders, M., 1975, Solution of Sparse Indefinite Systems of Linear Equations, SIAM J. Numer. Anal. **12**, 617-629.

Poppeliers, C., and Pavlis, G.L., 2003, Three-dimensional, prestack, plane wave migration of teleseismic P-to-S converted phases: 2. Stacking multiple events, J. Geophys. Res., 108(B5), **2267**, doi:10.1029/2001JB001583.

Pratt, T., Culota, R., Hauser, E., Nelson, D., Brown, L., Kaufman, S., Oliver, J. and Hinze, W. 1989. Major Proterozoic basement features of the eastern mid-continent of North America revealed by recent COCORP profiling; Geology, **17**, 505-509.

Reading, A., Kennett, B. and Sambridge, M., 2003, Improved inversion for seismic structure using transformed, S-wavevector receiver functions: Removing the effect of the free surface, Geophys. Res. Lett., **30(19)**, 1981. doi:10.1029/2003GL018090.

Revenaugh, J., 1995b, A scattered-wave image of subduction beneath the Transverse Ranges, California, Science, **268**, 1888-1892.

Rivers, T. and Corrigan, D., 2000, Convergent margin on southeastern Laurentia during the Mesoproterozoic: tectonic implications, Can. J. Earth Sci., **37**, 359-383.

Rivers, T., Martingole, J., Grower, C.F. and Davidson, A. 1989, New tectonic subdivisions of the Grenville Pronvince, southeast Canadian Shield; Tectonics, **8**, 63-84.

Rondenay, S., 2000, Teleseismic imaging of the southeastern Canadian Shield and cascadia subduciton zone, Ph.D thesis, the University of British Columbia, 117 p.

Rondenay, S., Bostock, M.G., Hearn, T.M., White, D.J., Wu, H., Senechal, G., Ji, S. and

Mareschal, M., 2000, Teleseismic studies of the lithosphere below the Abitibi-Grenville Lithoprobe transect, Can. J. Earth Sci., **37**, 415-426.

Rondenay, S., Bostock, M.G., and Shragge, J., 2001, Multiparameter two-dimensional inversion of scattered teleseismic body waves, 3: Application to the Cascadia 1993 data set, J. Geophys. Res., **106**, No.12, 30795-30807.

Rondenay, S, Bostock, M.G. and Fischer, K.M., 2005, Multichannel inversion of scattered teleseismic body waves: practical considerations and applicability, Dept. of Geological Sciences, Brown Univ, Providence, Rhode Island, USA, Dept. of Earth and Ocean Sciences, Univ of Bristish Columbia, Vancourver, BC, Canada.

Rost, S. and Thomas, C., 2002, Array Seismology: methods and applications, Rev. Geophys., **40**, 3/2, 1-25.

Roy, B. and Mereu, R.F., 2000, Applications of seismic pattern recognition and gravity inversion techniques to obtain enhanced subsurface images of the Earth's crust under the Central Metasedimentary Belt, Grenville Province, Ontario, Geophys. J. Int. **143**, 735-751.

Schultz, A., Kurtz, R.D., Chave, A.D., and Jones, A.G., 1993, Conductivity discontinuities in the upper mantle beneath a stable craton, Geophys. Res. Lett., **20**, 2941-2944.

Sheriff, R.E. and Geldart, L.P., 1982, Exploration Seismology, Cambridge University Press, Cambridge, 475 p.

Silver, P.G., and Chan, W.W., 1991, Shear wave splitting and subcontinental mantle deformation, J. Geophys. Res., **96**, 16429-16454.

Spetzier, J. and Snieder, R., 2004, The Fresnel volume and transmitted waves,

Geophysics, Vol, **69**, No. 3, 653-663.

Stockwell, C.H., 1964, Forth report on structural provinces, orogenies and time-classification of rocks of the Canadian Precambrian Shield; Geological Survey of Canada, Paper 64-17, II, 21.

Van der Hijden, J.H.M.T., and Neerhoff, F.L., 1984a, Scattering of elastic waves by a plane crack of finite width: J. App.Mech., **51**, 646-651.

Van der Lee, S., 2002, High-resolution estimates of lithospheric thickness from Missouri to Massachusetts, USA, Earth planet. Sci. Lett., **203**, 15-23.

Vidale, J, E., and Earlie, P.S., 2000, Fine-scale heterogeneity in the Earth's inner core, Nature, **404**, 273-275.

Wallach, J.L., Mohajer, A.A., Thomas, R.L., 1998, Linear zones, seismicity, and the possibility of a major earthquake in the intraplate western Lake Ontario area of eastern North America, Can. J. Earth Sci., **35**, 762-786.

White, D., Davidson, A., Forsyth, D., Green, A. and Milkereit, B., 1991a, Seismic images from the Central Metasedimentary Belt, Southern Ontario; Abitibi-Grenville Lithoprobe Workshop III, 19-20 November 1991, Montreal, Abstracts, 67.

White, D.J., Easton, R.M., Culshaw, N.G., Milkereit, B., Forsyth, D.A., Carr, S., Green, A.G. and Davidson, A., 1994, Seismic image of the Grenville Orogen in Ontario, Can. J. Earth Sci., **31**, 293-307.

White, D., Forsyth, D., Davidson, A., Milkereit, B. and Easton, R.M. 1992, Seismic images of the crustal structure from the western Central Metasedimentary Belt; 1992 Grenville Workshop, Abstracts, 60.

White, D.J., Forsyth, D.A., Asudeh, I.A., Carr, S.D., Wu, H., Easton, R.M., and Mereu,

R.F., 2000, A seismic-based cross-section of the Grenville Orogen in Southern Ontario and western Quebec, Can. J. Earth Sci., **37**, 183-192.

Williams, H.R., Stott, G.M., Thurston, P.C., Sutcliffe, R.H., Bennett, G., Easton, R.M. and Armstrong, D.K., 1992, Tectonic evolution of Ontario: summary and synthesis, Geology of Ontario, **25**, 1255-1346.

Winardhi, S. and Mereu, R. F., 1997, Crustal velocity structure of the Superior and Grenville Provinces of the Southeastern Canadian Shield, Can. J. Earth Sci. **34**, 1167-1184.

Wu, R.S. and K. Aki, 1985, Scattering characteristics of elastic waves by an elastic heterogeneity, Geophysics, **50**, 582–595.

Wynne-Edwards, H.R. 1972, The Grenville Province; in variations in tectonic styles in Canada, Geological Association of Canada, Special Paper **5**, 163-182.

York, D., Smith, P., Easton, R.M. and Layer, P., 1991, A laser 40Ar/39Ar study of single crystals of biotite and hornblende across the Grenville Front; in Program with abstracts, Geological Association of Canada-Mineralogical Association of Canada-Society of Economic Geologist, **16**, A136.

Zhu, L., 2000, Crustal structure across the San Andreas Fault, Southern California from teleseismic converted waves, Earth Planet. Sci. Lett., **179**, 183-190.

Zhu, L., 2002, Deformation for lower crust and downward extent of the San Andreas Fault as revealed by teleseismic waveforms, Earth Planets Space, **54**, 1005-1010.

Appendix A

List of Earthquakes Used in This Study

Table A1. List of earthquakes recorded by Polaris Network

Date	Time	Latitude	Longitude	Depth	Magnitude	Distance	B.azimuth
'2002/03/03'	'12:08:19'	36.5	70.48	225.6	6.3	95.9	3.5
'2002/03/28'	'04:56:22'	-21.66	-68.33	125.1	6.5	65.8	68
'2002/04/01'	'19:59:32'	-29.67	-71.38	71	6.4	73.4	72.1
'2002/04/18'	'05:02:46'	16.98	-100.86	24.9	6.8	31.9	20.1
'2002/04/18'	'16:08:36'	-27.54	-70.59	62	6.7	72.1	69.9
'2002/05/25'	'05:36:31'	53.81	-161.12	33	6.4	51.7	11.7
'2002/06/16'	'02:46:14'	8.78	-83.99	35	6.4	34.9	86.8
'2002/06/18'	'13:56:22'	-30.8	-71.12	54	6.6	74.5	72
'2002/06/22'	'02:58:21'	35.63	49.05	10	6.5	88.6	9.2
'2002/06/28'	'17:19:30'	43.75	130.67	566	7.3	88.8	38.3
'2002/07/31'	'00:16:44'	7.93	-82.79	10	6.5	35.6	84.6
'2002/09/15'	'08:39:32'	44.83	129.92	586.3	6.4	88	39.2
'2002/09/24'	'03:57:22'	-31.52	-69.2	119.6	6.3	75.4	70.4
'2002/10/03'	'16:08:29'	23.32	-108.53	10	6.5	31	38.4
'2002/10/12'	'20:09:11'	-8.29	-71.74	534.3	6.9	52.2	69.6
'2002/11/03'	'22:12:41'	63.51	-147.45	4.2	7.2	42.3	22.1
'2002/11/17'	'04:53:53'	47.82	146.21	459.1	5.8	80.2	30.4
'2003/01/21'	'02:46:47'	13.63	-90.77	24	6.5	31.3	0.4
'2003/01/22'	'02:06:34'	18.77	-104.1	24	7.6	32	26.8
'2003/02/19'	'03:32:36'	53.65	-164.64	19	6.6	53.6	12.6
'2003/03/12'	'23:41:30'	26.34	-110.64	10	6.4	30.2	45.2
'2003/03/17'	'16:36:16'	51.4	177.94	33	7.1	63.8	16.9
'2003/03/17'	'18:55:47'	51.36	177.82	33	6.2	63.9	17
'2003/04/27'	'22:57:44'	-8.21	-71.64	560.2	6	52.1	69.4
'2003/05/01'	'00:27:04'	39.01	40.51	10	6.4	81.8	2.7
'2003/05/14'	'06:03:35'	18.24	-58.67	41.1	6.7	31.1	37.8
'2003/05/21'	'18:44:19'	36.98	3.67	10	6.8	61.6	4.8
'2003/05/26'	'09:24:33'	38.89	141.51	69.2	7	89.7	28.8
'2003/06/15'	'19:24:33'	51.55	176.92	20	6.5	64.2	17.5
'2003/06/16'	'22:08:01'	55.49	159.94	173.6	6.9	69	28.1
'2003/06/20'	'06:19:38'	-7.54	-71.62	555.8	7.1	51.5	69.3
'2003/06/20'	'13:30:41'	-30.53	-71.37	32	6.8	74.2	72.2
'2003/06/23'	'12:12:34'	51.42	176.79	18	6.9	64.4	17.4
'2003/08/14'	'05:14:55'	39.19	20.74	10	6.3	70.9	3.9
'2003/08/31'	'23:08:00'	43.41	132.23	480.8	6.2	88.7	37.1
'2003/09/25'	'19:50:07'	41.86	143.79	33	8.3	86.2	28.8
'2003/09/27'	'11:33:25'	50.04	87.77	18.1	7.3	86.1	0.8

Table A1. (continue ½)

'2003/09/27'	'18:52:47'	50.08	87.79	14.8	6.4	86.1	0.8
'2003/09/29'	'02:36:54'	42.45	144.39	33	6.5	85.5	28.7
'2003/10/01'	'01:03:25'	50.21	87.66	10	6.7	86	0.9
'2003/10/08'	'09:06:55'	42.65	144.57	32	6.7	85.3	28.7
'2003/10/31'	'01:06:28'	37.81	142.62	10	7	90.2	27.5
'2003/11/12'	'08:26:43'	33.17	137.07	384.9	6.4	96.4	29.4
'2003/11/17'	'06:43:06'	51.15	178.65	33	7.8	63.6	16.4
'2003/12/05'	'21:26:09'	55.54	165.78	10	6.7	66.6	25.6
'2003/12/22'	'19:15:56'	35.7	-121.1	7.3	6.5	32.3	70
'2003/12/25'	'07:11:11'	8.42	-82.82	33	6.5	35.1	84.8
'2003/12/26'	'01:56:52'	29	58.31	10	6.6	98.3	6
'1998/08/04'	'18:59:20'	35.18	-3.9	12.6	6.4	57.6	0.5
'1998/08/23'	'13:57:15'	-21.12	-65.59	289.8	6.1	65.8	65.2
'1999/01/28'	'08:10:05'	36.51	71.03	187.1	6.6	96	3.1
'1999/03/31'	'05:54:42'	55.23	162.66	51.3	6.2	68.1	26.7
'1999/04/03'	'06:17:18'	-37.7	-73.41	21	6.6	81.2	74.7
'1999/05/05'	'22:41:30'	14.46	-90.73	124.6	5.7	30.5	0.7
'1999/06/06'	'07:08:05'	34.23	141.39	16	6.5	93.8	26.7
'1999/08/20'	'10:02:21'	55.68	160	188.6	6.9	68.8	28.2
'1999/08/22'	'09:35:39'	-21.25	-68.37	115.4	5.7	65.4	68
'1999/08/28'	'12:40:06'	55.01	-134.38	15.5	6.8	36.3	7.8
'1999/09/15'	'03:01:24'	47.2	151.29	128.3	6.4	78.9	27.1
'1999/12/06'	'23:12:36'	49.68	-126.94	22	6.4	32.3	97.5
'2001/06/26'	'04:18:31'	17.2	-95.22	100.9	5.9	29.3	10.7
'2001/07/07'	'09:38:43'	39.63	141.96	69.7	5.7	88.9	28.9
'2001/07/24'	'05:00:09'	16.43	-94.94	62.9	5.9	33.6	16.5
'2001/08/02'	'23:41:06'	-34.93	-70.39	1	6.5	78.7	71.9
'2001/08/13'	'20:11:23'	33.07	136.62	14	7.2	96.7	29.7
'2002/03/28'	'04:56:22'	33.18	137.07	10	7.4	96.4	29.4
'2002/06/18'	'13:56:22'	33.2	137.23	10	6.7	96.3	29.3
'2002/06/22'	'02:58:21'	-28.57	-65.84	22.3	6.4	73	66.9
'2002/09/24'	'03:57:22'	33.14	137.2	21.2	6.2	96.4	33.4
'2002/10/12'	'20:09:11'	52.2	174.03	25	6.2	65.2	19.3
'2002/11/17'	'04:53:53'	12.03	-86.49	87.3	5.6	32	92
'2003/05/14'	'06:03:35'	36.42	26.79	128.9	5.5	76.3	2.6
'2003/05/21'	'18:44:19'	11.45	-86.64	35	6.9	32.5	92.1
'2003/05/26'	'09:24:33'	37.24	138.73	16	6.6	92.2	30
'2003/06/16'	'22:08:01'	37.3	138.8	10	6.3	92.1	30
'2003/06/20'	'06:19:38'	45.79	26.63	95.8	5.9	69.8	5.6
'2003/06/20'	'13:30:41'	49.3	-128.78	10	6.7	33.6	97.2
'2003/06/23'	'12:12:34'	43.61	146.8	61.6	5.9	83.7	30.9
'2003/08/14'	'05:14:55'	47.96	144.43	472.7	6.2	80.8	31.5
'2003/09/25'	'19:50:07'	42.1	144.3	40.2	6.1	85.9	31.9
'2003/09/27'	'11:33:25'	-26.65	-63.23	568	6.1	71.6	64.2
'2003/09/27'	'18:52:47'	4.63	-77.54	10	7.2	38.9	76
'2003/10/01'	'01:03:25'	9.6	-84.17	16	6.4	34.1	87.2
'2003/11/17'	'06:43:06'	13.38	-90.06	40.6	6.3	31.3	99

Table A1. (continue 2/2)

'2003/12/22'	'19:15:56'	15.68	-61.71	14	6.3	31.9	45
'2003/12/25'	'07:11:11'	-26.52	-113.83	10	6.6	76.4	10.8
'2004/02/24'	'02:27:48'	43.01	145.12	39	7	84.7	28.5
'2004/04/05'	'21:24:04'	42.9	145.23	35	6.8	84.8	28.4
'2004/05/03'	'04:36:50'	18.96	-81.41	10	6.8	24.6	83.1
'2004/05/03'	'05:12:40'	48.84	156.31	11	6.2	75.5	25.4
'2004/06/10'	'15:19:57'	53.22	-173.79	252.7	5.8	58.6	15.3
'2004/07/08'	'10:30:49'	-0.88	-21.19	10	6.8	68.6	13.2
'2004/07/19'	'08:01:49'	42.95	144.87	42	6.3	84.9	28.6
'2004/08/07'	'11:49:12'	34.06	141.49	27.8	6.5	84.9	18.2
'2004/08/28'	'13:41:27'	-1.36	-80.78	16.9	6.1	44.8	81
'2004/09/05'	'10:07:07'	-1.18	-81.5	10	6.1	44.6	82
'2004/09/05'	'14:57:18'	-1.09	-81.16	10	6.2	44.5	81.6
'2004/09/07'	'11:53:06'	26.09	144	24	6.3	100.3	25
'2004/10/23'	'08:56:00'	-10.93	-76.1	126.2	5.5	56.3	81.4
'2004/10/27'	'20:34:36'	30.74	56.83	14	6.4	96.1	6.3
'2004/11/02'	'10:02:12'	38.11	72.71	114.9	5.7	95	1.2
'2004/11/12'	'06:36:16'	84.95	99.39	10	6.2	51.7	0
'2004/11/15'	'09:06:56'	15.14	-91.38	197.4	6.2	30	2.3
'2004/11/20'	'08:07:22'	33.81	130.08	10	6.6	97.8	39.2
'2004/11/20'	'22:01:45'	-24.98	-63.47	579.1	6.9	69.9	64
'2004/11/21'	'11:41:07'	-24.72	-63.5	570.1	6.4	69.7	64
'2004/11/28'	'18:32:14'	78.58	6.05	10	6.2	43.9	6.5
'2004/12/06'	'14:15:11'	-7.37	-77.89	130.3	6	50.8	77.2
'2004/12/14'	'23:20:13'	-17.38	-69.47	117.3	5.8	61.5	68.5
'2005/03/17'	'13:37:37'	29.63	138.87	426.8	5.9	89.8	17.8
'2005/03/21'	'12:23:54'	5.72	-82.84	10	6.5	37.8	84.5
'2005/04/11'	'14:54:06'	-3.29	-80.85	39.1	6.4	46.7	81.1

Table A2. List of earthquakes recorded by GAC station (CNSN network)

Date	Time	Latitude	Longitude	Depth	Magnitude	Distance	B.azimuth
'1994/01/10'	'15:53:50'	-13.34	-69.45	596	6.9	59	73.1
'1994/04/29'	'07:11:29'	-28.3	-63.25	561.5	6.9	74.5	68.8
'1994/05/10'	'06:36:28'	-28.5	-63.1	600.5	6.9	74.7	68.7
'1994/06/06'	'20:47:40'	2.92	-76.06	12.1	6.6	42.6	80.9
'1994/06/09'	'00:33:16'	-13.84	-67.55	631.3	8.2	59.7	71.1
'1994/07/21'	'18:36:31'	42.34	132.87	471.4	7.3	88.8	39.4
'1994/08/19'	'10:02:51'	-26.64	-63.42	563.6	6.5	72.8	68.7
'1994/09/01'	'15:15:53'	40.4	-125.68	10	6.6	36.6	80
'1994/10/04'	'13:22:55'	43.77	147.32	14	8.1	83.1	30.3
'1994/10/09'	'07:55:39'	43.91	147.92	33	7.1	82.8	30
'1994/12/10'	'16:17:38'	18.14	-101.38	48.1	6.6	34.9	26.6
'1995/01/06'	'22:37:34'	40.25	142.18	26.9	6.7	88	32.1
'1995/01/19'	'15:05:03'	5.05	-72.92	17.3	6.6	40.6	76.1
'1995/04/23'	'02:55:55'	51.33	179.71	16.9	6.5	63.7	17.4
'1995/05/27'	'13:03:52'	52.63	142.83	11	6.7	76.7	37.2
'1995/07/30'	'05:11:23'	-23.34	-70.29	45.6	6.6	68.9	74.9
'1995/08/19'	'21:43:31'	5.14	-75.58	119.6	6.6	40.4	80.2
'1995/09/14'	'14:04:31'	16.78	-98.6	23	7.4	34.7	21.3
'1995/09/23'	'22:31:56'	-10.68	-78.58	59.9	6.5	56.2	83.7
'1995/10/03'	'01:51:23'	-2.75	-77.88	24.4	7	48.3	83.2
'1995/10/09'	'15:35:53'	19.05	-104.2	33	8	35.6	31.3
'1995/10/21'	'02:38:57'	16.84	-93.47	159.3	7.2	32.5	13.4
'1995/11/22'	'04:15:11'	28.83	34.8	10	7.2	82.6	6.1
'1995/12/03'	'18:01:08'	44.66	149.3	33	7.9	81.7	29.5
'1996/02/21'	'12:51:01'	-9.59	-79.59	10	7.5	55.2	84.9
'1996/02/25'	'03:08:15'	15.98	-98.07	21.1	7.1	35.2	19.9
'1996/03/03'	'14:55:11'	11.66	-86.86	33	6.8	35.3	99.5
'1996/03/03'	'16:37:31'	11.9	-86.77	33	6.8	35	99.5
'1996/04/19'	'00:19:31'	-23.94	-70.09	49.5	6.6	69.5	74.7
'1996/06/02'	'02:52:09'	10.8	-42.25	10	7	44.9	30.3
'1996/06/10'	'15:24:56'	51.48	-176.85	26.3	7.3	61.9	16
'1996/06/21'	'13:57:10'	51.57	159.12	20	7	72.3	27.7
'1996/07/15'	'21:23:34'	17.6	-100.97	18.3	6.8	35.1	25.5
'1996/09/05'	'08:14:14'	-22.12	-113.44	10	6.9	75.8	16
'1996/11/12'	'16:59:44'	-14.99	-75.67	33	7.7	60.4	80.2
'1997/01/11'	'20:28:26'	18.22	-102.76	33	7.2	35.5	28.5
'1997/01/23'	'02:15:22'	-22	-65.72	276.2	7.1	68	70.2
'1997/07/06'	'09:54:00'	-30.06	-71.87	19	6.8	75.5	76.8
'1997/09/02'	'12:13:22'	3.85	-75.75	198.7	6.8	41.7	80.4
'1997/10/15'	'01:03:33'	-30.93	-71.22	58	7.1	76.4	76.2
'1997/10/28'	'06:15:17'	-4.37	-76.68	112	7.2	49.9	81.6
'1997/11/09'	'22:56:42'	13.85	-88.81	176.4	6.5	33.7	3.8
'1997/11/28'	'22:53:41'	-13.74	-68.79	586	6.7	59.5	72.4
'1998/01/30'	'12:16:08'	-23.91	-70.21	42	7.1	69.4	74.8
'1998/04/01'	'22:42:56'	-40.32	-74.87	9	6.7	85.6	79.5
'1998/04/03'	'22:01:48'	-8.15	-74.24	164.6	6.6	53.6	78.5

Table A2. (continue ½)

'1998/07/09'	'05:19:07'	38.65	-28.63	10	6.2	35	4.6
'1998/07/29'	'07:14:24'	-32.31	-71.29	51.1	6.4	77.7	76.4
'1998/08/04'	'18:59:20'	-0.59	-80.39	33	7.2	46.3	86.8
'1998/08/23'	'13:57:15'	11.66	-88.04	54.6	6.7	35.6	1.5
'1999/01/28'	'08:10:05'	52.89	-169.12	67.2	6.6	57.3	14
'1999/03/31'	'05:54:42'	5.83	-82.62	10	7	40.2	91
'1999/04/03'	'06:17:18'	-16.66	-72.66	87.2	6.8	62.1	76.9
'1999/05/05'	'22:41:30'	14.36	-94.67	33	6.3	35.2	13.6
'1999/06/06'	'07:08:05'	13.9	-90.77	33	6.3	34.2	7.1
'1999/08/20'	'10:02:21'	9.04	-84.16	20	6.9	37.3	94.2
'1999/08/22'	'09:35:39'	-40.51	-74.76	33	6.4	85.8	79.4
'1999/08/28'	'12:40:06'	-1.29	-77.55	196.4	6.3	46.8	82.8
'1999/09/15'	'03:01:24'	-20.93	-67.28	218	6.4	66.7	71.7
'1999/12/06'	'23:12:36'	57.51	-154.67	45.8	6.8	47.8	14.3
'2001/06/26'	'04:18:31'	-17.75	-71.65	24	6.7	63.2	75.9
'2001/07/07'	'09:38:43'	-17.54	-72.08	33	7.6	63	76.4
'2001/07/24'	'05:00:09'	-19.45	-69.25	33	6.4	65.1	73.5
'2001/08/02'	'23:41:06'	56.26	163.79	14	6.3	66.9	28.6
'2001/08/13'	'20:11:23'	41.05	142.31	38	6.4	87.3	32.4
'2002/03/28'	'04:56:22'	-21.66	-68.33	125.1	6.5	67.4	72.8
'2002/06/18'	'13:56:22'	-30.8	-71.12	54	6.6	76.2	76.1
'2002/06/22'	'02:58:21'	35.63	49.05	10	6.5	84.8	2.4
'2002/09/24'	'03:57:22'	-31.52	-69.2	119.6	6.3	77.1	74.5
'2002/10/12'	'20:09:11'	-8.29	-71.74	534.3	6.9	53.9	75.4
'2002/11/17'	'04:53:53'	47.82	146.21	459.1	5.8	80	32.9
'2003/05/14'	'06:03:35'	18.24	-58.67	41.1	6.7	30.7	47.5
'2003/05/21'	'18:44:19'	36.98	3.67	10	6.8	57.8	8.4
'2003/05/26'	'09:24:33'	38.89	141.51	69.2	7	89.5	32
'2003/06/16'	'22:08:01'	55.49	159.94	173.6	6.9	68.9	29.8
'2003/06/20'	'06:19:38'	-7.54	-71.62	555.8	7.1	53.1	75.2
'2003/06/20'	'13:30:41'	-30.53	-71.37	32	6.8	76	76.3
'2003/06/23'	'12:12:34'	51.42	176.79	18	6.9	65	18.8
'2003/08/14'	'05:14:55'	39.19	20.74	10	6.3	67	7
'2003/09/25'	'19:50:07'	41.86	143.79	33	8.3	86	31.7
'2003/09/27'	'11:33:25'	50.04	87.77	18.1	7.3	83.5	0.8
'2003/09/27'	'18:52:47'	50.08	87.79	14.8	6.4	83.5	0.8
'2003/10/01'	'01:03:25'	50.21	87.72	10	6.7	83.4	0.8
'2003/11/17'	'06:43:06'	51.15	178.65	33	7.8	64.3	17.8
'2003/12/22'	'19:15:56'	35.7	-121.1	7.3	6.5	35.6	70.1
'2003/12/25'	'07:11:11'	8.42	-82.82	33	6.5	37.7	91.9
'2004/02/24'	'02:27:48'	35.18	-3.9	12.6	6.4	53.8	4.4
'2004/04/05'	'21:24:04'	36.51	71.03	187.1	6.6	92.8	6.4
'2004/05/03'	'04:36:50'	-37.7	-73.41	21	6.6	83	78.3
'2004/05/03'	'05:12:40'	14.46	-90.73	124.6	5.7	33.7	7.3
'2004/06/10'	'15:19:57'	55.68	160	188.6	6.9	68.7	29.9
'2004/07/08'	'10:30:49'	47.2	151.3	128.5	6.4	78.8	29.6
'2004/07/19'	'08:01:49'	49.62	-126.97	23.7	6.4	34.3	95.6
'2004/08/07'	'11:49:12'	17.2	-95.22	100.9	5.9	32.9	16.5

Table A2. (continue 2/2)

'2004/08/28'	'13:41:27'	-34.93	-70.39	1	6.5	80.4	75.8
'2004/09/05'	'10:07:07'	33.07	136.62	14	7.2	96.4	33.3
'2004/09/05'	'14:57:18'	33.18	137.07	10	7.4	96.1	33
'2004/09/07'	'11:53:06'	-28.57	-65.84	22.3	6.4	74.4	71.2
'2004/10/23'	'08:56:00'	37.24	138.73	16	6.6	91.9	33.3
'2004/10/27'	'20:34:36'	45.79	26.63	95.8	5.9	66	8.5
'2004/11/02'	'10:02:12'	49.3	-128.78	10	6.7	35.6	95.5
'2004/11/12'	'06:36:16'	-26.65	-63.23	568	6.1	72.9	68.5
'2004/11/15'	'09:06:56'	4.7	-77.51	15	7.2	40.9	83.1
'2004/11/20'	'08:07:22'	9.6	-84.17	16	6.4	36.7	94.4
'2004/11/20'	'22:01:45'	13.38	-90.06	40.6	6.3	34.5	5.6
'2004/11/21'	'11:41:07'	15.68	-61.71	14	6.3	32.1	54.4
'2004/11/28'	'18:32:14'	43.01	145.12	39	7	84.6	31.3
'2004/12/06'	'14:15:11'	42.9	145.23	35	6.8	84.6	31.2
'2004/12/14'	'23:20:13'	18.96	-81.41	10	6.8	27.1	92.4
'2005/03/17'	'13:37:37'	15.14	-91.38	197.4	6.2	33.3	8.8
'2005/03/21'	'12:23:54'	-24.98	-63.47	579.1	6.9	71.2	68.5
'2005/04/11'	'14:54:06'	-7.37	-77.89	130.3	6	52.9	83
'2005/05/05'	'19:12:20'	5.72	-82.84	10	6.5	40.3	91.4
'2005/05/21'	'05:11:34'	-3.29	-80.85	39.1	6.4	49	87.1

Table A3. List of earthquakes recorded by SADO (CNSN network)

Date	Time	Latitude	Longitude	Depth	Magnitude	Distance	B.azimuth
'1996/11/12'	'16:59:44'	-14.99	-75.67	33	7.7	59.6	76.1
'1997/01/11'	'20:28:26'	18.22	-102.76	33	7.2	33	24.3
'1997/05/01'	'11:37:36'	18.99	-107.35	33	6.9	34.8	31.6
'1997/09/02'	'12:13:22'	3.85	-75.75	198.7	6.8	40.9	74.8
'1997/10/15'	'01:03:33'	-30.93	-71.22	58	7.1	75.7	73
'1997/10/28'	'06:15:17'	-4.37	-76.68	112	7.2	49	76.7
'1997/11/28'	'22:53:41'	-13.74	-68.79	586	6.7	59	68.2
'1997/12/05'	'11:26:54'	54.84	162.03	33	7.8	68	26.9
'1998/01/12'	'10:14:07'	-30.98	-71.41	34.8	6.6	75.7	73.2
'1998/01/30'	'12:16:08'	-23.91	-70.21	42	7.1	68.8	71.2
'1998/03/29'	'19:48:16'	-17.55	-179.09	537.2	7.2	109.1	64.1
'1998/05/03'	'23:30:21'	22.31	125.31	33	7.5	109.6	36
'1998/06/01'	'05:34:03'	52.89	160.07	43.7	6.9	70.3	26.4
'1998/08/04'	'18:59:20'	-0.59	-80.39	33	7.2	45.2	81.8
'1998/08/20'	'06:40:55'	28.93	139.33	440.5	7.1	98.7	26.5
'1999/01/28'	'08:10:05'	52.89	-169.12	67.2	6.6	56.1	13.1
'1999/04/03'	'06:17:18'	-16.66	-72.66	87.2	6.8	61.4	72.9
'1999/04/08'	'13:10:34'	43.61	130.35	565.7	7.1	88.2	39
'1999/08/20'	'10:02:21'	9.04	-84.16	20	6.9	35.9	88.5
'1999/09/20'	'17:47:18'	23.77	120.98	33	7.7	109.4	40.5
'1999/12/06'	'23:12:36'	57.51	-154.67	45.8	6.8	46.6	14
'2000/01/28'	'14:21:07'	43.05	146.84	61.1	6.8	83.4	28
'2000/03/28'	'11:00:22'	22.34	143.73	126.5	7.6	102.6	19.8
'2000/05/12'	'18:43:18'	-23.55	-66.45	225	7.2	69	67.5
'2000/07/11'	'01:32:28'	57.37	-154.21	43.6	6.3	46.4	13.7
'2000/12/06'	'17:11:06'	39.57	54.8	30	7	86.4	3.9
'2001/01/13'	'17:33:32'	13.05	-88.66	60	7.7	32.6	97.4
'2001/03/15'	'13:02:42'	-32.32	-71.49	37	6	77	73.4
'2001/04/09'	'09:00:57'	-32.67	-73.11	11	6.7	77.3	74.8
'2001/05/25'	'00:40:50'	44.27	148.39	33	6.7	81.8	27.6
'2001/07/05'	'13:53:48'	-16.09	-73.99	62	6.6	60.7	74.3
'2001/07/07'	'09:38:43'	-17.54	-72.08	33	7.6	62.3	72.4
'2001/07/24'	'05:00:09'	-19.45	-69.25	33	6.4	64.5	69.7
'2001/07/28'	'07:32:43'	59.02	-155.12	131.3	6.3	46.4	16.1
'2001/08/13'	'20:11:23'	41.05	142.31	38	6.4	86.8	29.9
'2001/12/02'	'13:01:53'	39.4	141.09	123.8	6.5	88.7	30
'2002/03/03'	'12:08:07'	36.43	70.44	209	6.3	94.6	4.2
'2002/03/03'	'12:08:19'	36.5	70.48	225.6	6.3	94.6	4.1
'2002/03/26'	'03:45:48'	23.35	124.09	33	6.4	109	37.5
'2002/03/28'	'04:56:22'	-21.66	-68.33	125.1	6.5	66.8	69.1
'2002/03/31'	'06:52:50'	24.28	122.18	32.8	7.1	108.6	39.5
'2002/04/01'	'19:59:32'	-29.67	-71.38	71	6.4	74.4	73
'2002/04/18'	'16:08:36'	-27.54	-70.59	62	6.7	72.4	72
'2002/06/16'	'02:46:14'	8.78	-83.99	35	6.4	36.1	88.2
'2002/06/18'	'13:56:22'	-30.8	-71.12	54	6.6	75.6	72.9
'2002/06/28'	'17:19:30'	43.75	130.67	566	7.3	87.9	38.9

Table A3. (continue ½)

'2002/07/31'	'00:16:44'	7.99	-82.78	10	6.5	36.8	86
'2002/09/24'	'03:57:22'	-31.52	-69.2	119.6	6.3	76.5	71.3
'2004/02/24'	'02:27:48'	23.32	-108.53	10	6.5	32.1	38
'2004/03/17'	'03:21:07'	-8.29	-71.74	534.3	6.9	53.2	70.8
'2004/04/05'	'21:24:04'	63.51	-147.45	4.2	7.2	41.8	21.3
'2004/04/14'	'01:54:09'	47.82	146.21	459.1	5.8	79.6	30.8
'2004/05/03'	'04:36:50'	13.63	-90.77	24	6.5	32.6	1.3
'2004/05/03'	'05:12:40'	18.77	-104.1	24	7.6	33.2	26.8
'2004/05/29'	'20:56:09'	53.65	-164.64	19	6.6	53.3	12.3
'2004/06/10'	'15:19:57'	26.56	-110.59	10	6.4	31.1	44.8
'2004/06/17'	'01:16:01'	51.27	177.98	33	7.1	63.5	16.8
'2004/06/28'	'09:49:47'	-8.21	-71.64	560.2	6	53.2	70.7
'2004/07/08'	'10:30:49'	18.24	-58.67	41.1	6.7	31.5	40.5
'2004/07/19'	'08:01:48'	36.98	3.67	10	6.8	60.5	5.8
'2004/08/07'	'11:49:12'	38.89	141.51	69.2	7	89	29.4
'2004/08/10'	'06:13:33'	55.49	159.94	173.6	6.9	68.4	28.3
'2004/08/18'	'09:03:10'	-7.54	-71.62	555.8	7.1	52.5	70.6
'2004/08/28'	'13:41:27'	-30.53	-71.37	32	6.8	75.3	73.1
'2004/09/05'	'10:07:07'	51.42	176.79	18	6.9	64	17.5
'2004/09/05'	'14:57:18'	39.19	20.74	10	6.3	69.7	4.7
'2004/09/06'	'23:29:35'	41.86	143.79	33	8.3	85.6	29.3
'2004/09/07'	'11:53:06'	50.04	87.77	18.1	7.3	84.9	0.4
'2004/09/08'	'14:58:25'	50.08	87.79	14.8	6.4	84.9	0.4
'2004/09/19'	'20:26:04'	42.45	144.39	33	6.5	84.9	29.2
'2004/10/01'	'08:01:01'	50.21	87.72	10	6.7	84.7	0.4
'2004/10/07'	'01:05:12'	51.15	178.65	33	7.8	63.2	16.4
'2004/10/09'	'21:26:53'	55.54	165.78	10	6.7	66.1	25.7
'2004/10/23'	'08:56:00'	35.7	-121.1	7.3	6.5	33	68.9
'2004/10/23'	'09:34:04'	8.42	-82.82	33	6.5	36.4	86.2
'2004/10/27'	'20:34:36'	35.18	-3.9	12.6	6.4	56.5	1.7
'2004/11/02'	'10:02:12'	-21.12	-65.59	289.8	6.1	66.7	66.2
'2004/11/04'	'14:03:11'	36.51	71.03	187.1	6.6	94.7	3.7
'2004/11/07'	'02:02:25'	55.23	162.66	51.3	6.2	67.5	26.9
'2004/11/11'	'10:02:47'	-37.7	-73.41	21	6.6	82.2	75.4
'2004/11/12'	'06:36:16'	14.46	-90.73	124.6	5.7	31.8	1.7
'2004/11/15'	'09:06:55'	55.68	160	188.6	6.9	68.2	28.4
'2004/11/20'	'08:07:22'	54.8	-134.25	20	6.8	36.1	6.3
'2004/11/20'	'22:01:45'	47.2	151.3	128.5	6.4	78.2	27.5
'2004/11/21'	'11:41:07'	49.62	-126.97	23.7	6.4	32.4	96
'2004/11/28'	'02:35:13'	17.2	-95.22	100.9	5.9	30.6	11.3
'2004/11/28'	'18:32:14'	16.43	-94.94	62.9	5.9	31.2	10.3
'2004/12/06'	'14:15:11'	-34.93	-70.39	1	6.5	79.7	72.7
'2004/12/14'	'23:20:13'	33.07	136.62	14	7.2	96	30.4
'2004/12/18'	'06:46:19'	33.18	137.07	10	7.4	95.7	30.1
'2004/12/28'	'21:07:36'	33.2	137.23	10	6.7	95.6	30
'2005/01/12'	'08:40:03'	-28.57	-65.84	22.3	6.4	74	67.8
'2005/01/18'	'14:09:06'	11.45	-86.64	35	6.9	33.8	93.3

Table A3. (continue 2/2)

'2005/01/19'	'06:11:36'	37.24	138.73	16	6.6	91.5	30.7
'2005/01/24'	'23:23:26'	45.79	26.63	95.8	5.9	68.5	6.4
'2005/01/28'	'09:26:18'	49.3	-128.78	10	6.7	33.6	95.8
'2005/01/28'	'15:46:45'	4.7	-77.51	15	7.2	39.9	77.5
'2005/02/09'	'18:46:09'	9.6	-84.17	16	6.4	35.3	88.6
'2005/02/17'	'03:12:46'	13.38	-90.06	40.6	6.3	32.6	100
'2005/02/22'	'02:25:22'	15.68	-61.71	14	6.3	32.5	47.5
'2005/02/25'	'23:04:04'	43.01	145.12	39	7	84.1	29
'2005/03/06'	'05:21:43'	42.9	145.23	35	6.8	84.2	28.9
'2005/03/17'	'13:37:37'	18.96	-81.41	10	6.8	25.8	84.9
'2005/03/20'	'01:53:41'	84.95	99.39	10	6.2	50.5	0.2
'2005/03/21'	'12:23:54'	15.14	-91.38	197.4	6.2	31.3	3.2
'2005/03/21'	'12:43:12'	-24.98	-63.47	579.1	6.9	70.9	65
'2005/04/02'	'12:52:36'	78.58	6.05	10	6.2	45.6	6.1
'2005/04/11'	'14:54:06'	-7.37	-77.89	130.3	6	51.9	78.4
'2005/04/16'	'22:41:16'	5.72	-82.84	10	6.5	39	85.8
'2005/04/19'	'01:46:56'	-3.29	-80.85	39.1	6.4	47.9	82.3

Appendix B

CCPscat Software Package User Guide

DESCRIPTION

CCPscat is an interactive software package developed by Jinling Zhang using Matlab, for computing P-to-S Common Conversion Points based on teleseismic receiver functions; analyzing the stacking fold distribution; and generating 2-D or 3-D plots. More specifically it comprises the following main functions:

1. computing and stacking P-to-S common converted phases according to user-defined 3-D cell size and available receiver function data
2. determining the 3-D stacking fold distribution accordingly
3. generating user-defined 2-D cross-section profiles and correlated fold distribution in contour maps at any angle
4. plotting user-defined 3-D slices in X-Y-Z or (East-North-Depth) directions
5. plotting user-defined depth slices
6. plotting the colored parametric surface at any depth.
7. this software is also able to plot 2-D or 3-D images of P velocity, S velocity, or density model resulted from scattering tomography (Fortran 95 code by Andrew Frederiksen)

GUI LAYOUT

The user graphical interface consists of four sub-windows (Figure B.1)

- the left top panel, '**Station and line Locations**', is an on-screen display and operation window. It shows station location which can be superimposed by regional geological maps (Southern Ontario Maps) and it is also used for defining cross-section profiles by using the mouse.
- '**Status window**' at left middle, a real-time display and monitor mouse position in X-Y (km) and West and North (degree of latitude and longitude)
- The left bottom window includes 'Print' and 'Exit' selections
- The right panels, **function window**, contains standard drop-down menus, slides, text edits and push buttons used to access other functions. These operations include:

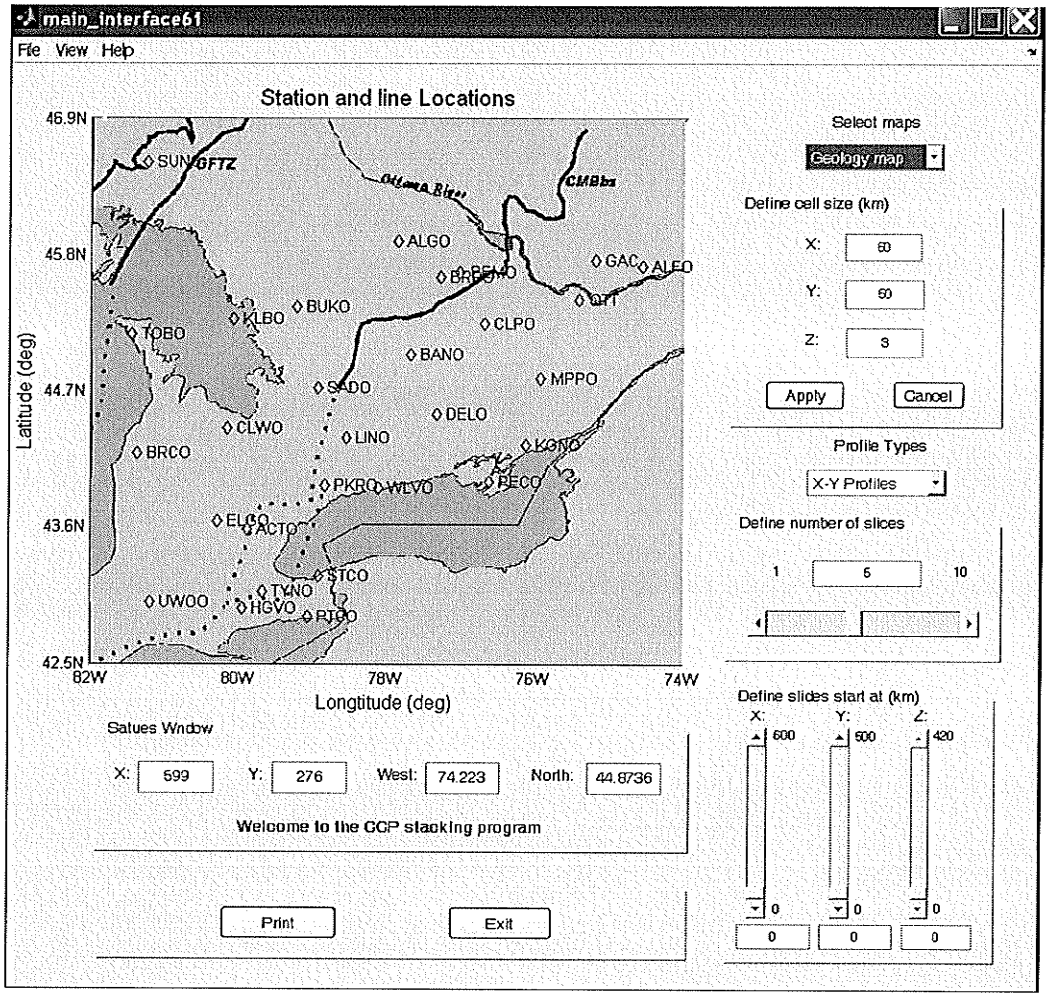

Figure B.1. Main interface of CCPscat software package.

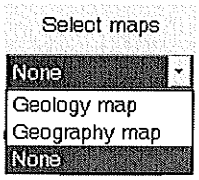

Select maps – this drop-down menu changes the display of station location window superimposed with or without a base map.

- Geology map- add geology map on station location window, default selection
- Geography map – add a geography map on station location window

- None – do not add any base map (as Figure B.2 showing)

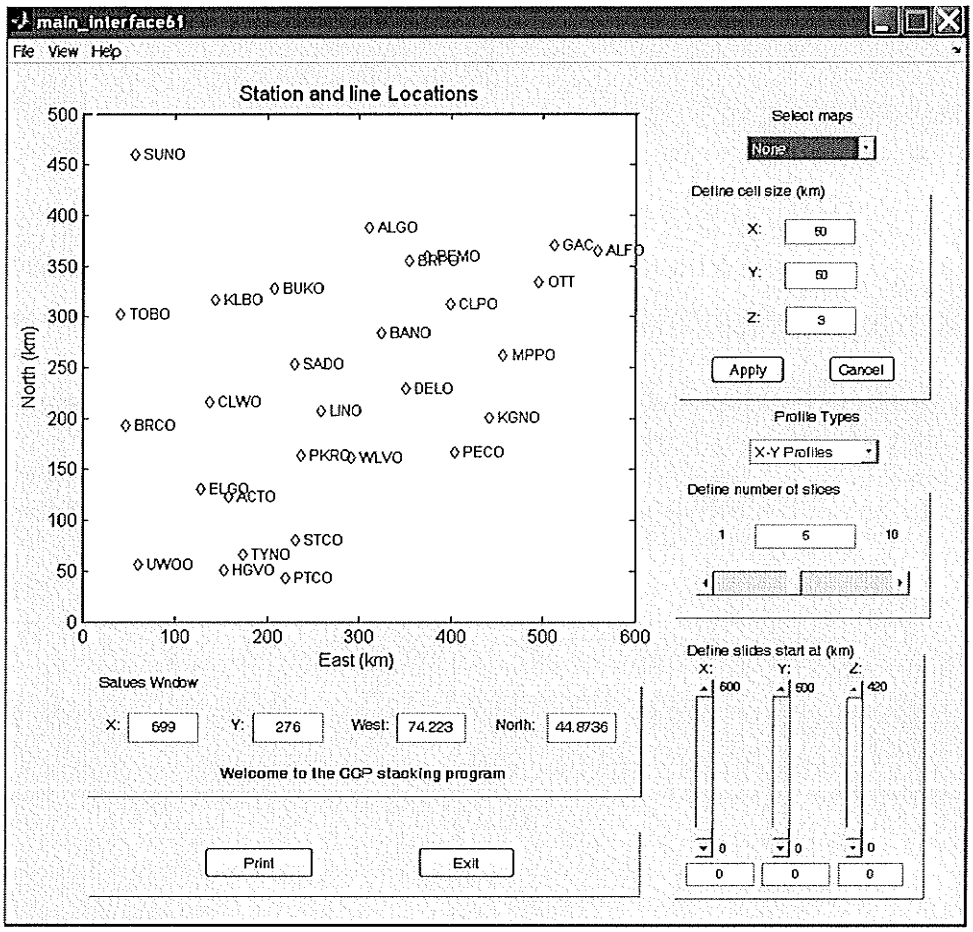

Figure B.2. Main interface without showing basemap.

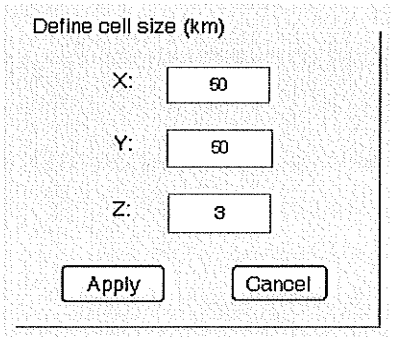

Define cell size (km) – defines 3-D cell size in km

- Apply – re-stacking and re-computing the P-to-S CCP according to user-input cell size
- Cancel – cancel this action

Profile Types – drop-down menu, five options provided

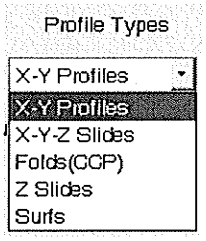

- X-Y Profiles – use mouse to choose start and end point of the cross-section profile on station location window, and selected lines' location will show up immediately in the station window as second point select (Figure B.3), and popup cross-sections (CCP stacking (stacking results on the top, fold distribution on the bottom and scattering tomography, Figure B.4 and B.5) along selected lines.

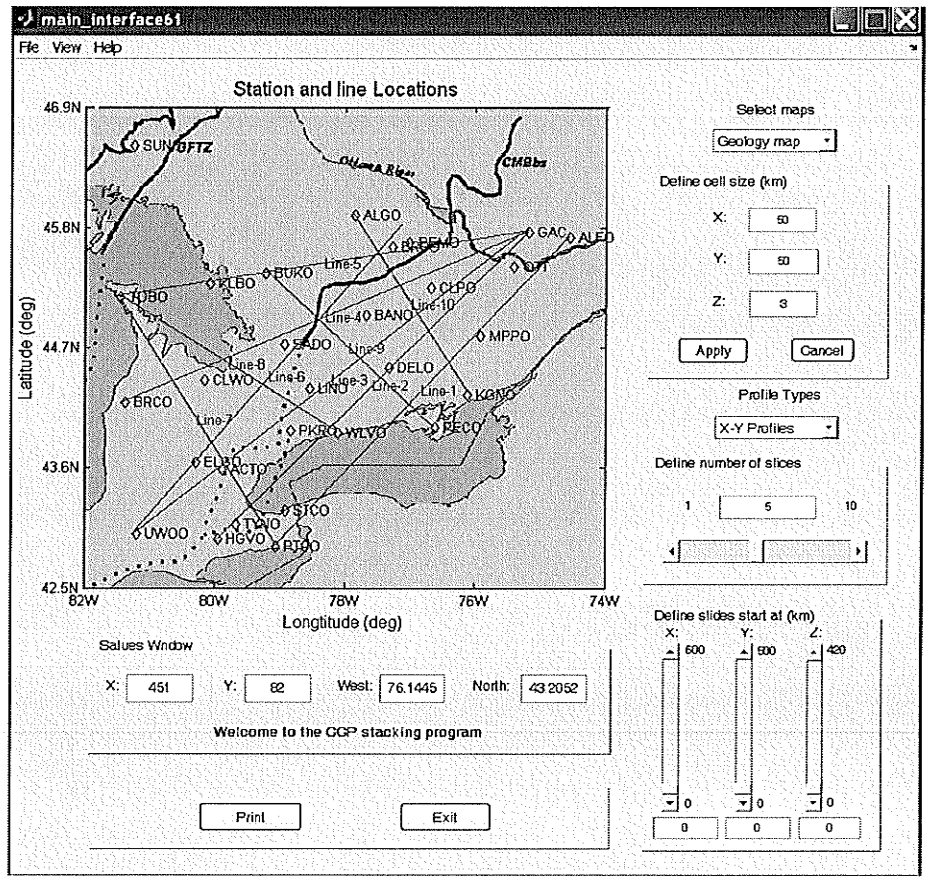

Figure B.3. Main interface showing Line location.

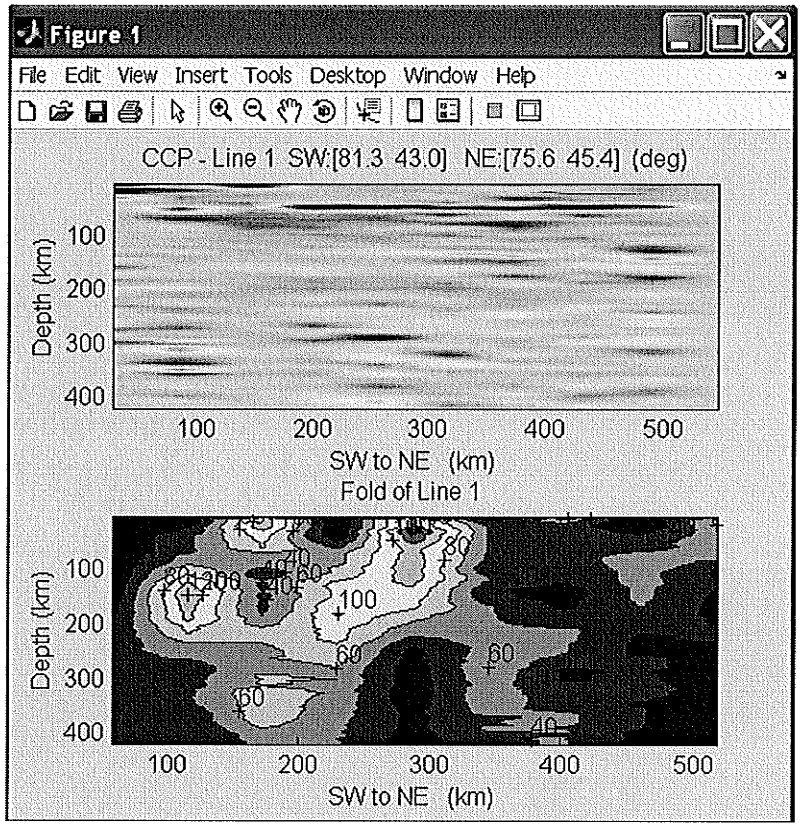

Figure B.4. X-Y profiles of CCP stacking, (top) stacking cross-section, (bottom) fold distribution along this line.

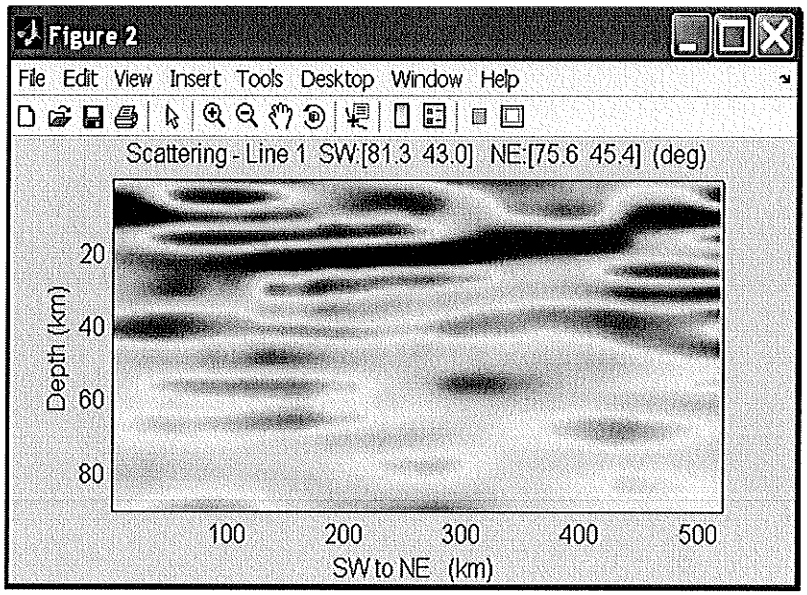

Figure B.5. X-Y profiles of scattering tomography along selected lines.

- X-Y-Z Slides – first at the panel of 'Define slices start at (km)' define the location (X, Y ,Z) you want to draw, and then select this function to display the slides in X-Y-Z direction in three sub-windows (Figure B.6).

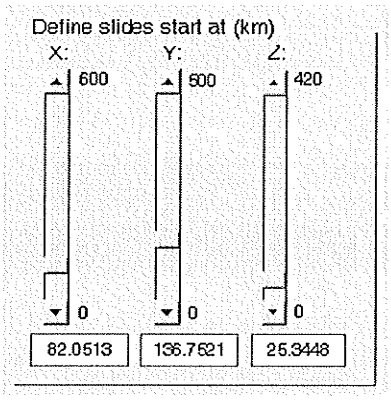

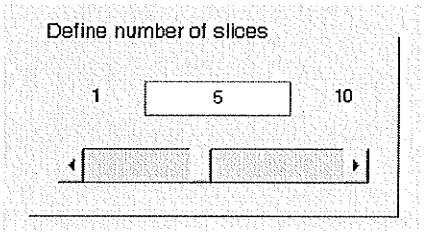

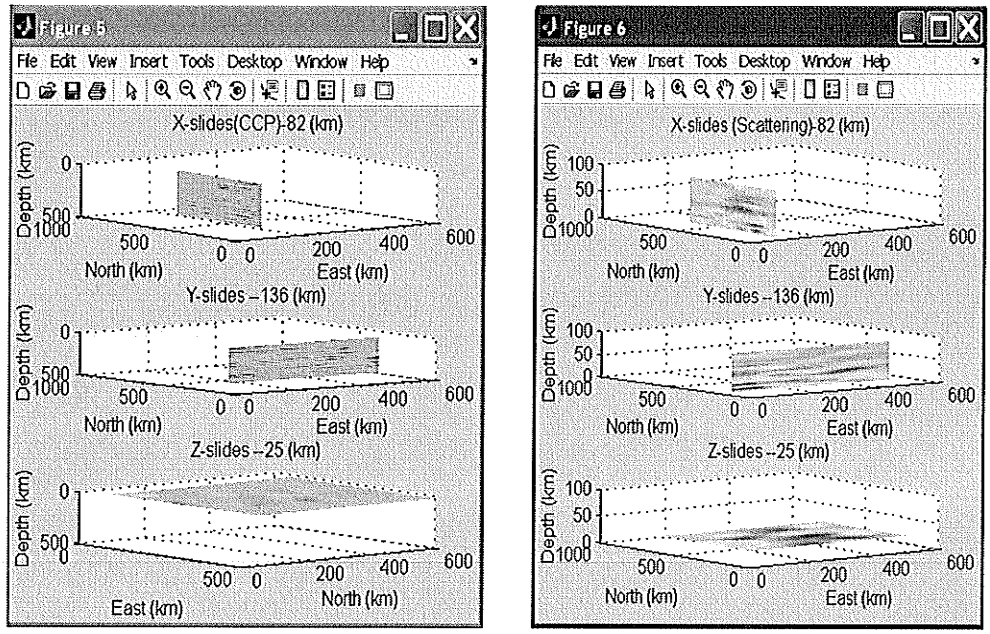

Figure B.6. X-Y-Z slices of CCP (left) and scattering (right).

- Fold (CCP) – first at the panel of 'Define slices start at (km)' defined the depth (Z) you want to start to plot, and then, at the panel of 'Define number of slices' (above) select number of layers you want to display, finally select 'Folds(CCP)' to display CCP stacking fold distribution at different depths according to selected 3-D cell size (Figure B.7).

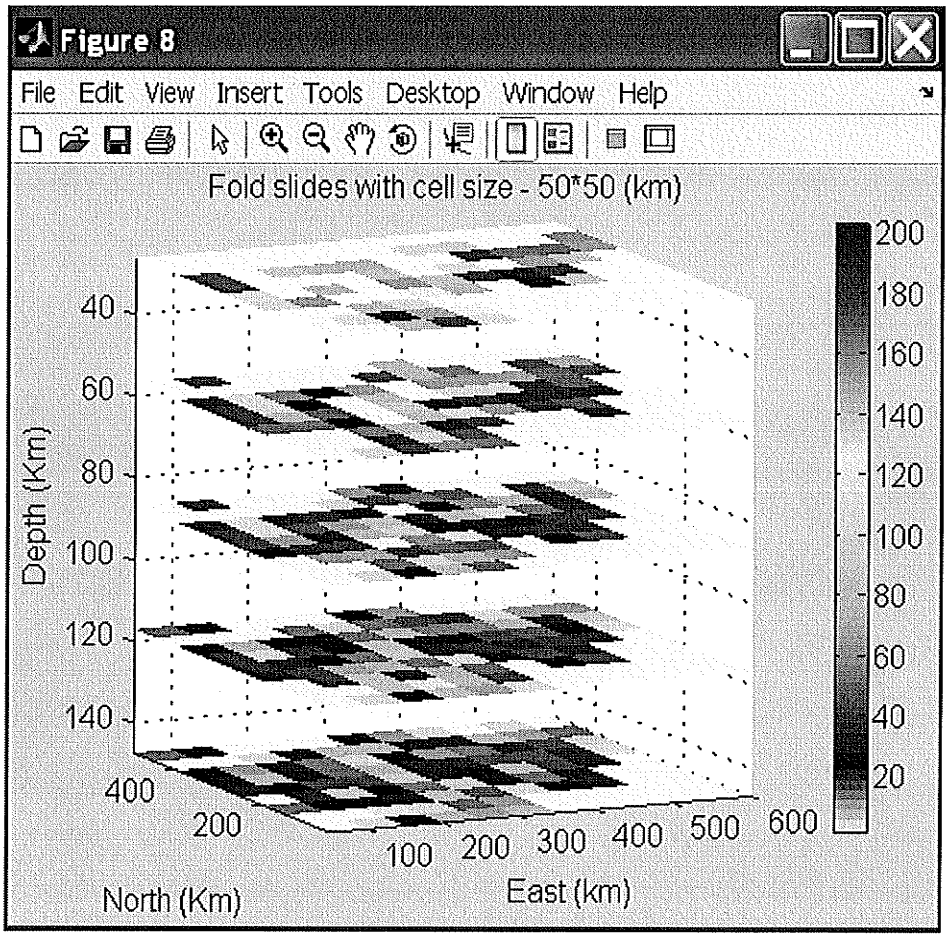

Figure B.7. 3-D CCP stacking fold distribution

- Z Slides – same as 'Folds (CCP)', except for the last step selecting 'Z Slides' rather than 'Folds(CCP)' to draw slices at defined depth of CCP and scattering (Figure B.8)

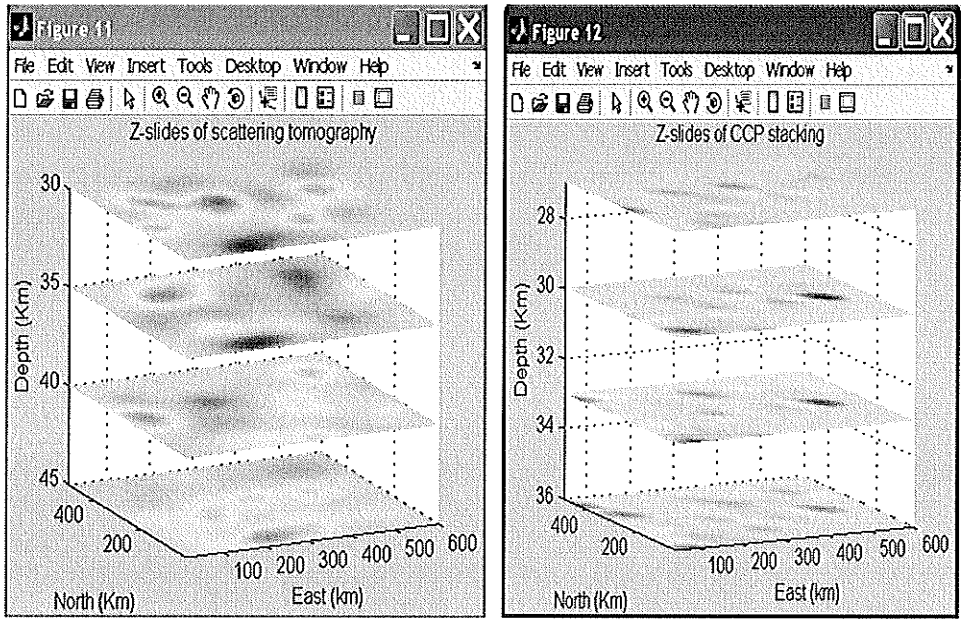

Figure B.8. 3-D depth slices of CCP stacking (right) and scattering (left).

- Surfs – first at the panel of 'Define slices start at (km)' defined the depth (Z) you want to start to plot, and then select 'Surfs' to plots the colored parametric surface (CCP and scattering, see Figure B.9).

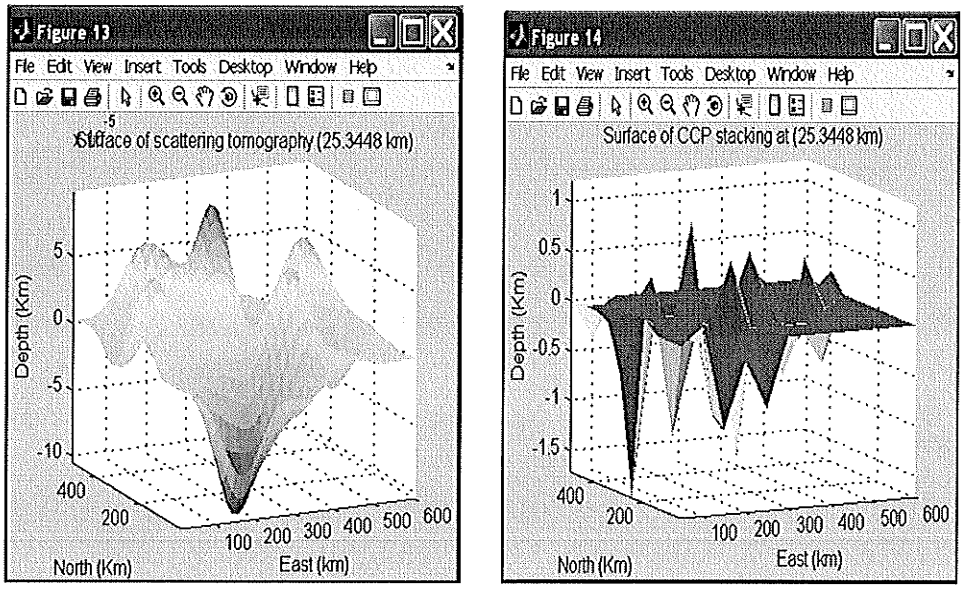

Figure B.9. Surface plot at defined depth, scattering is on the left and CCP is on the right.

- Note that, generated figures are adjustable by operating the menus on the figures' window, for example, axes, colors and so on, provided in Matlab (see Matlab manual for these functions).

Appendix C

P-Velocity Perturbation Images from Scattering Tomography

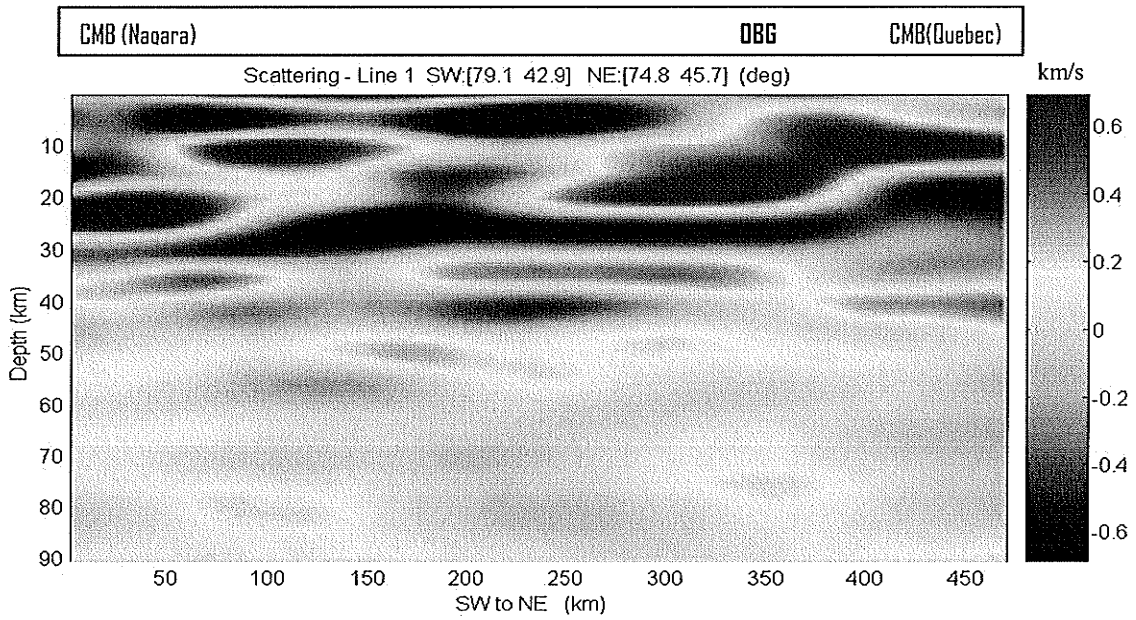

Fig C.1. P-velocity anomaly image from scattering tomography along Line-1.

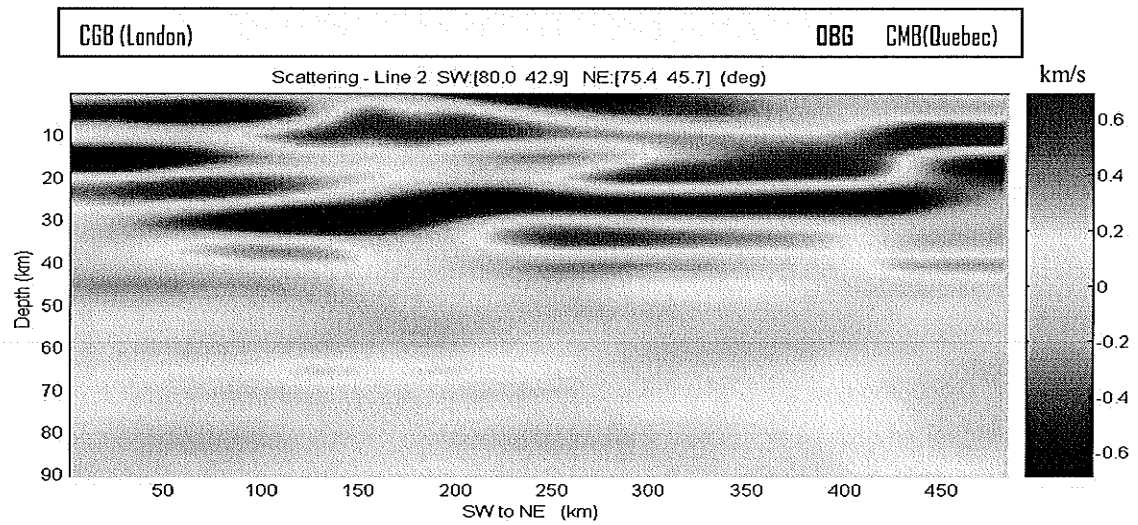

Fig C.2. P-velocity anomaly image from scattering tomography along Line-2.

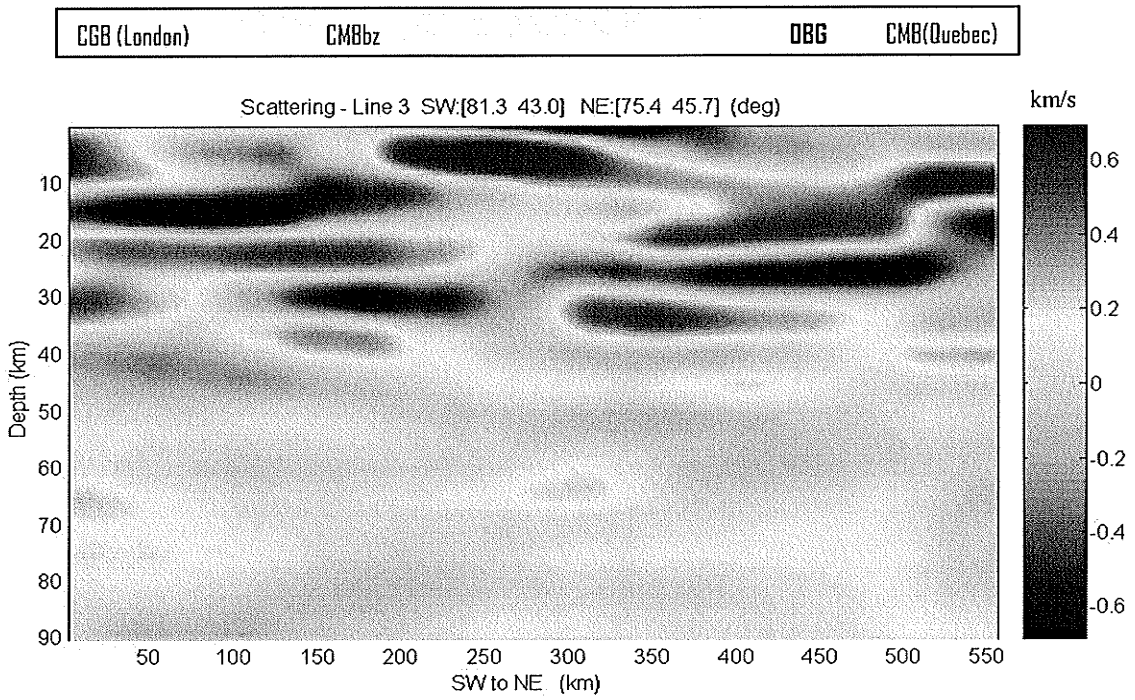

Fig C.3. P-velocity anomaly image from scattering tomography along Line-3.

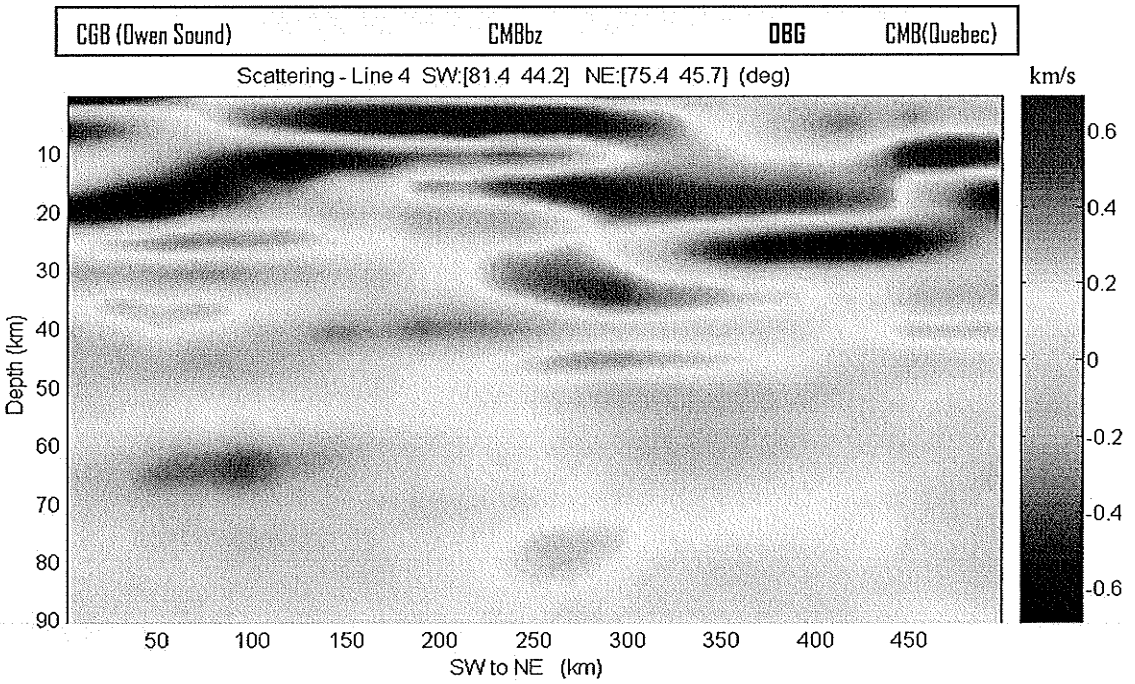

Fig C.4. P-velocity anomaly image from scattering tomography along Line-4.

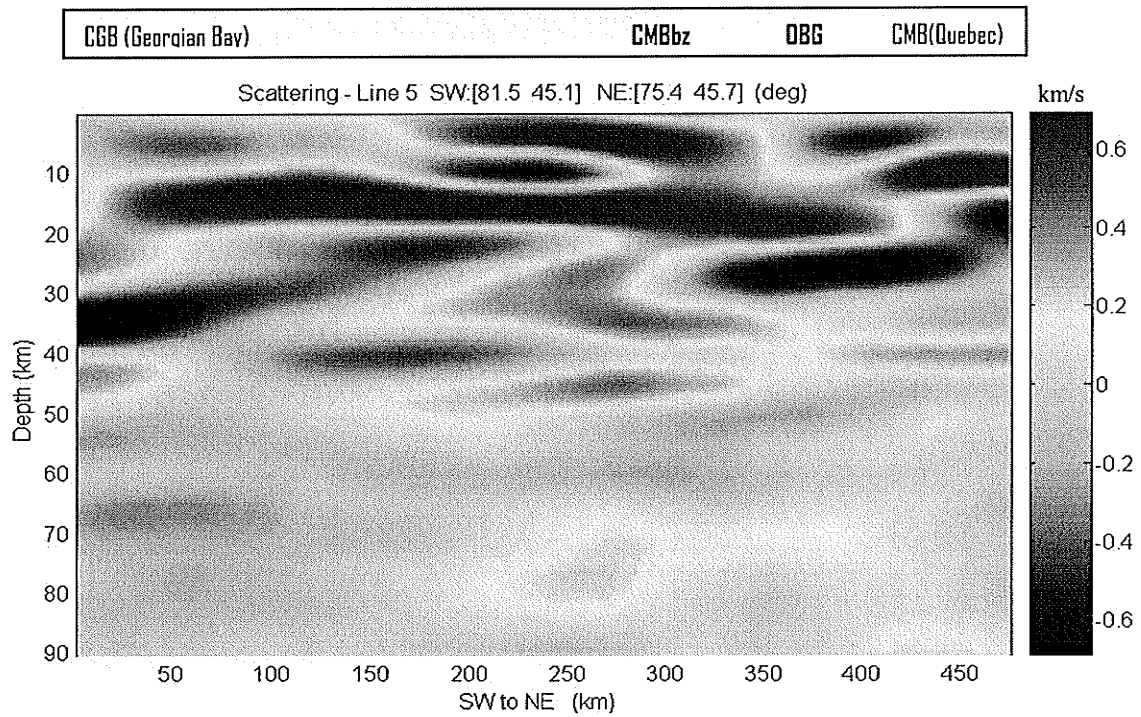

Fig C.5. P-velocity anomaly image from scattering tomography along Line-5.

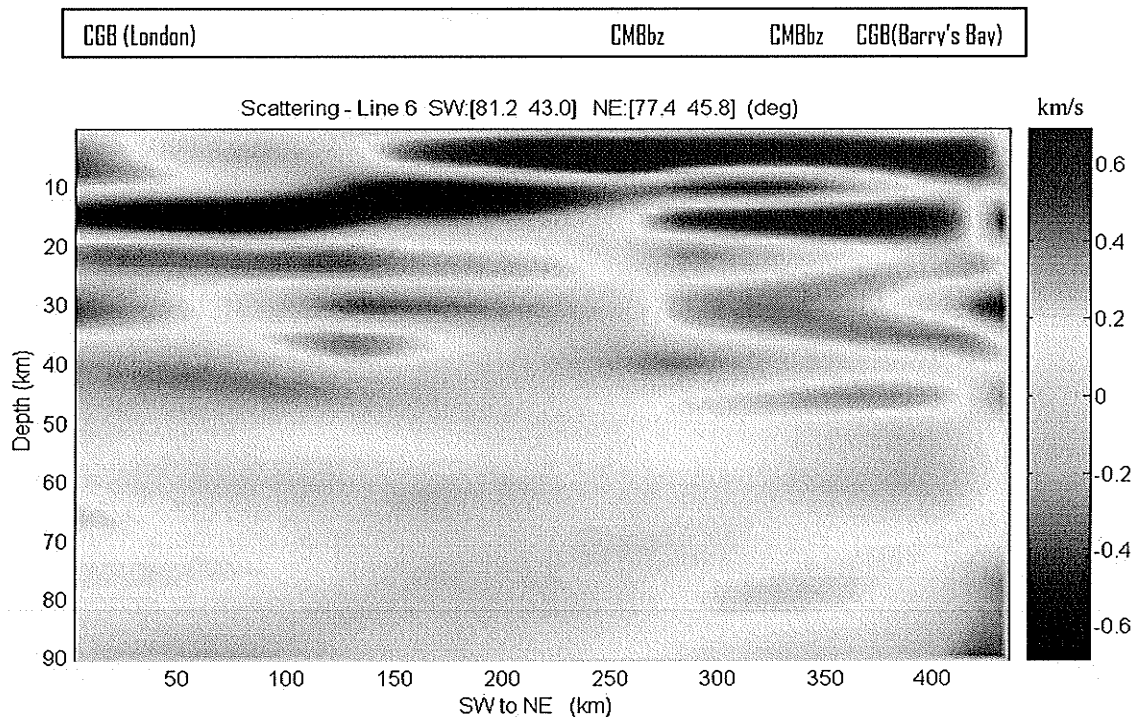

Fig C.6. P-velocity anomaly image from scattering tomography along Line-6.

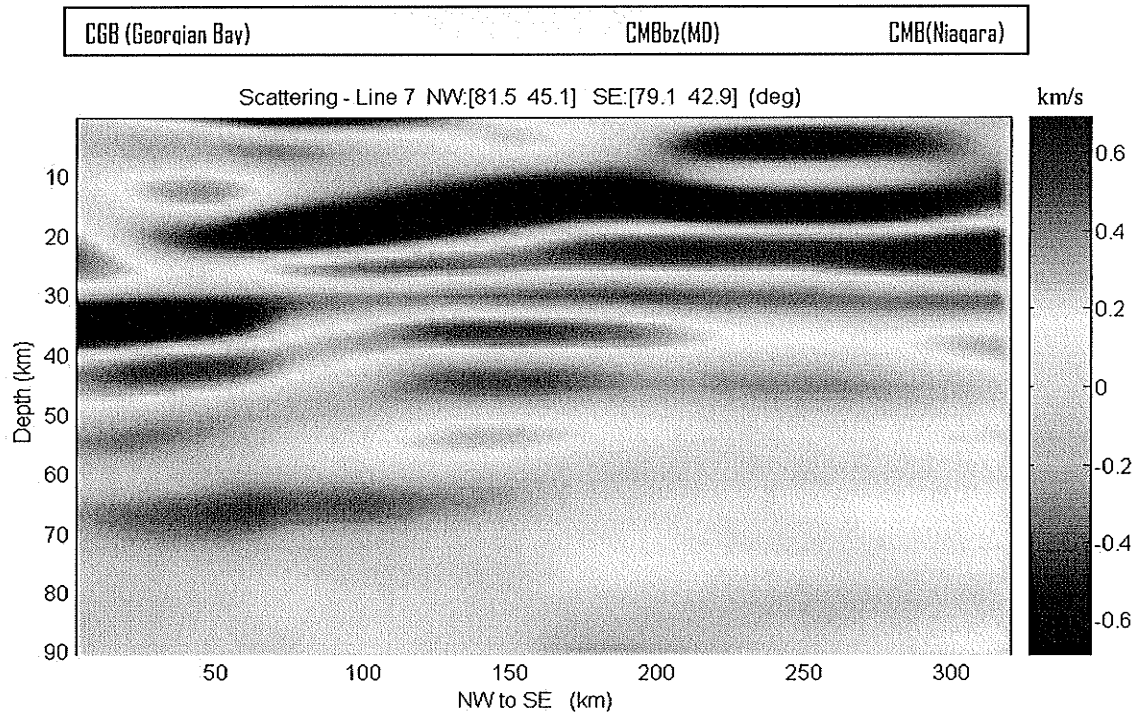

Fig C.7. P-velocity anomaly image from scattering tomography along Line-7.

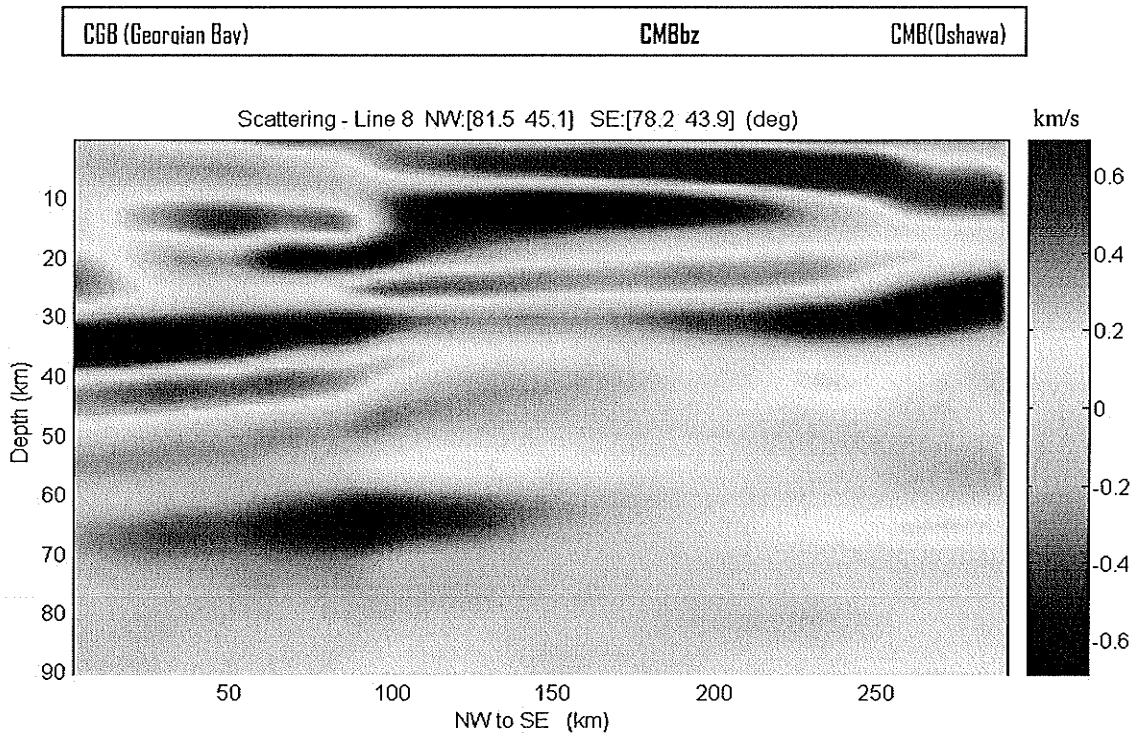

Fig C.8. P-velocity anomaly image from scattering tomography along Line-8.

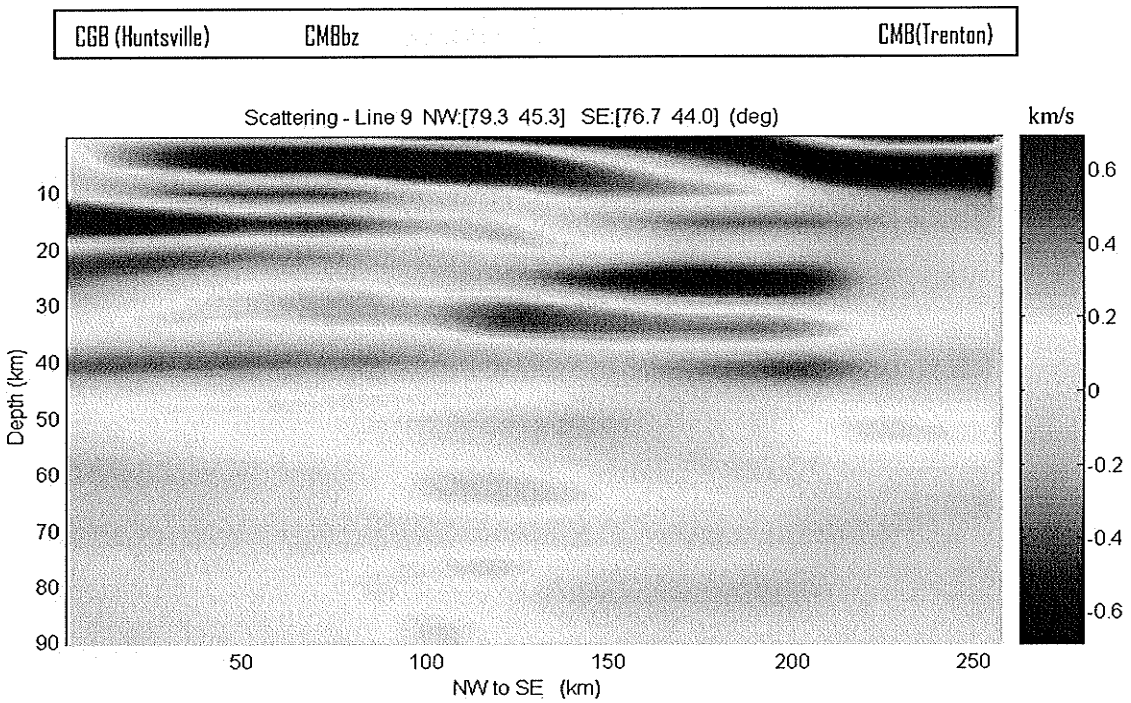

Fig C.9. P-velocity anomaly image from scattering tomography along Line-9.

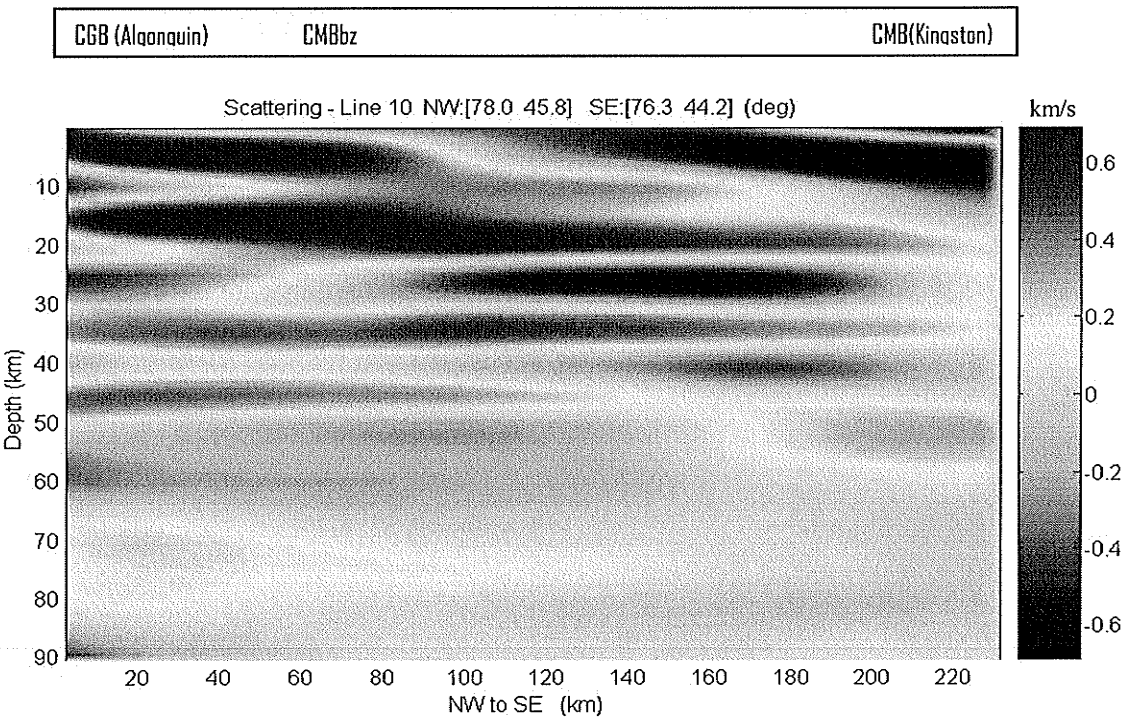

Fig C.10. P-velocity anomaly image from scattering tomography along Line-10.